Study on

Development of General Radar Polarimetry Methods for Fully Polarimetric Synthetic Aperture Radar Data Utilization to Monitor the Earth

Gulab Singh

Development of General Radar Polarimetry Methods for Fully Polarimetric Synthetic Aperture Radar Data Utilization to Monitor the Earth

Gulab Singh

Doctoral Program in Electrical and Information Engineering

Graduate School of Science and Technology, Niigata University

Niigata-shi, Japan

March 2013

I dedicate this dissertation to my father Mr. Ram Pal Singh.

* * *

His wisdom, courage,
and patience for tackling the
problems are an inspiration to me.

Preface

The Earth surface parameter observations play a crucial role in predicting and modeling ecological processes and economical optimization procedures. A rapid growth of population, its impact on the environment, and limited available resources on our planet, the need for monitoring the environmental processes and managing our resources is unequivocal. Since natural disaster have frequently occurred causing significant loss of life and devastating damage to property and infrastructure, the monitoring of the disaster damages over the globe is also an urgent need.

Earth parameter data collections by conventional and ground-based methods are cumbersome, both in terms of cost effective considerations and sporadic occurrences. Even when available, Earth parameter data represent only point measurements which may or may not be representative of a large area or region. Due to the strong spatial and time dependent dynamics of the Earth surface parameters, frequent observations are necessary. Satellite remote sensing has great potential in the study of dynamically changing environments due to its repetitive capability and synoptic coverage.

Microwave radar sensors are ideally suited for space imaging because those are almost weather independent, and microwaves propagate through the atmosphere with little deteriorating effects due to clouds, storms, rain, fog and haze. Globally humidity, haze and cloudiness are increasing at a rather rapid pace for irreversible reasons due to expansive aerosol build-up within the tropical/subtropical belts. Thus, optical remote sensing from space especially in the tropical and sub-tropical vegetated belts will become rather ineffective, and microwave remote sensing technology must now be advanced strongly and most rapidly hand in hand with digital communications technology because operationally radar sensing is more rapidly tractable especially for disaster mitigation assistance.

In particular, remote sensing with polarimetric radar offers an efficient and reliable means of collecting information required to extract geophysical and biophysical parameters from Earth's surface. Moreover, there is a rapidly increasing interest in the application of radar polarimetry with its increased information extraction for Earth observation due to availability of steadily more advanced polarimetric space-borne radar sensors, such as ALOS-PALSAR radar sensors, such as ALOS-PALSAR (L-band, Japan), TerraSAR-X (X-band, Germany), and RADARSAT-2 (C-band, Canada), and follow-up tandem satellite sensor systems for all of these novel fully polarimetric sensors. In today's dynamic Earth context, fully polarimetric SAR data utilization has a crucial role in understanding the Earth surface parameters and monitoring rapid changes whether they are naturally occurring changes or due to natural disaster and man-induced crisis.

Radar polarimetry with its sensitivity to the dielectric and geometric characteristics of objects, and potential to acquire subsurface information, is one of the most promising approaches for achieving the goal. However, although retrieval of Earth surface parameters using radar polarimetry methods were investigated for the last two decades, simple and robust algorithm/methodology is still lacking, which can be directly applied without restrictions for monitoring of the terrestrial covers. In this thesis, the focus is directed towards research on development of general radar remote sensing techniques using fully polarimetric information for several Earth's surface parameters retrieval such as land cover classification, snowpack and ice parameter estimation and vegetation parameters estimation, etc. Moreover, both natural and man-made disaster monitoring techniques are presented.

Furthermore, this thesis proposes to reduce the complexity and to develop efficient approaches by using SAR polarimetry techniques for Earth surface parameter estimation. New target decomposition methods are also developed for fully polarimetric SAR (FULL-POL-SAR) data utilization. Based on newly developed decomposition methods, the innovative algorithms are developed for Earth surface parameter monitoring. Finally, this thesis attempts to bridge the intellectual gap at the radar polarimetry method terminus, where radar polarimetry theories/methods development traditionally ends, and the Earth surface parameter monitoring traditionally begins.

More specifically, this thesis focuses on the following subtasks

1. Needs for physical scattering mechanism model-based decomposition of FULL-POL-SAR
2. Effects of volume scattering selection on decomposition and the results of decomposition components
3. Incorporation of FULL-POL-SAR information in scattering power decomposition
4. Decomposition components as information repositories for the Earth surface parameter retrieval modelling

The complete detailed formulations of the various subtasks of this dissertation study are presented in the Chapters 2 - 8. Chapter 9 covers overall conclusions.

Chapter 2 provides an overview of the utilization of the original Yamaguchi four-component decomposition (Y4O) for terrain classification in the cold mountainous region. In addition, this chapter assesses the Y4O method suitability as compared to the Freeman and Durden three-component decomposition (FDD) method for the identification of glaciated terrain features. A new methodology has been proposed by combining the complex Wishart distribution and Y4O method for glaciated terrain classification. Chapter 3 evaluates the modified Yamaguchi four-component decomposition with rotation of coherency matrix (Y4R). It is shown that improvement can clearly be achieved in the highly rugged glacier region by using Y4R as compared to Y4O (Chapter 2). Chapter 4 presents a new volume scattering model that accounts for the cross-polarized (*HV*) component caused by double-bounce structures. This model reduces the volume scattering power and enhances the double-bounce scattering power within man-made structures, leading to an improvement in the four-component scattering power decomposition, denoted as S4R. An improved hybrid decomposition scheme is presented in Chapter 5. As shown in Chapter 4, the classification between vegetation and the buildings becomes inconclusive when based on *HV* components caused by dipole scattering. Therefore, it is proposed to use an extended volume scattering model suited for oriented urban buildings (i.e., oriented dihedral model) to mitigate the overestimated volume scattering problem. This proposed method shows the advancements in a 3-component hybrid decomposition scheme for resolving the discrimination ambiguity of oriented dihedral objects from vegetation, by implementing the extended volume scattering model and the concept of rotation about line of sight. The general four-component scattering power decomposition with unitary transformation of coherency matrix (G4U) is presented in Chapter 6. This chapter also describes the utilization for 100% independent polarimetric parameters of the coherency matrix in the four-component decomposition. Chapter 7 describes the application of the G4U scheme to a set of fully polarimetric synthetic aperture radar images acquired before and after the **Tohoku** “110311” off-shore earthquake and resultant tsunami for extracting spatial information of the scene. Change detection has been analyzed based on G4U parameters. Chapter 8 deals with the development of a generalized fully polarimetric synthetic aperture radar (FULL-POL-SAR) decomposition scheme over wet snow areas. This decomposition accounts for all independent parameters of the coherency matrix. In the proposed decomposition scheme, a generalized spheroidal (ellipsoid) shape is chosen for volume scattering model derivation. Furthermore, the generalized Cloude volume and the Freeman surface parameter methods have been derived over wet snow areas, which account for all independent relative polarimetric phase parameters of the coherency matrix.

Furthermore, key findings under various subtasks and linkages of this thesis are summarized in Chapter 9.

Contents

List of Figures

List of Tables

Abbreviations and Acronyms

A-ERS	Active Earth Remote Sensing
AIRSAR	Airborne Synthetic Aperture Radar
ALOS	Advanced Land Observing Satellite
ALOS-AVNIR-2	Advanced Land Observing Satellite-Advanced visible near infrared radiometer -2
ASTER-GDEM	Advanced Spaceborne Thermal Emission and Reflection Radiometer-Global Digital Elevation Map
BK	Bhagirath Kharak
CTD	Coherent Target Decomposition
CWD	Complex Wishart Distribution
dB	Decibel
DCG	Debris covered glacier
DEM	Digital Elevation model
DLR	Deutschen Zentrums für Luft- und Raumfahrt (German Aerospace Center)
DN	Digital Number
EM	Electromagnetic Wave
ESA	European Space Agency
$F3H_c$	Three-component original hybrid Freeman / eigenvalue decomposition, as proposed by Cloude
FCC	False Color Composite
FDD	Freeman and Durden Decomposition
F-SAR	Flugzeug-Synthetic Aperture Radar
FSI	Forest Survey of India
FULL-POL-SAR	Fully Polarimetric SAR
G4U	General Four-Component Scattering Power Decomposition with Unitary Transformation of Coherency Matrix
$G4U_w$	The optimization of the $Y4O_w$ method for G4U
GCP	Ground Control Point
GDEM	Global Digital Elevation Map
GHz	Gigahertz
GIS	Geographical Information system
GPS	Global Positioning System
GSI	Association of Japanese Geographers, and Geospatial Information, Authority of Japan
HH	Horizontal transmit, Horizontal receive
HV	Horizontal transmit, Vertical receive
ICTD	Incoherent Target Decomposition
IEEE	Institute of Electrical and Electronics Engineers
IRS-P6-AWiFS	Indian Remote Sensing Satellite P6 -Advanced Wide Field Sensor
JAXA	Japan Aerospace Exploration Agency
MRS	Microwave Remote Sensing
NASA/JPL	National Aeronautics and Space Administration/Jet Propulsion Laboratory
N-E	North-East
NPA	Japanese National Police Agency report
N-W	North-West
ONERA	Office National d’Etudes et Recherches Aérospatiales

PALSAR	Phase Array L-band Synthetic Aprature Radar
Ph.D.	Doctoral of Philosophy
Pi-SAR	Polarimetric and Interferometric SAR
POL-SAR	Polarimetric SAR
POL-SAR	Polarimetric Synthetic Aperture Radar
PPD	Polarimetric Phase Difference
RADAR	Radio Detection and Ranging
RADARSAT-2	Radar Satellite-2
RAMSES	Radar Aéroporté Multi-Spectral d'Etudes de Signatures
RGB	Red-Blue-Green
RSI	Radar Snow Index
RVI	Radar Vegetation Index
S3H	Three-component hybrid scattering model-based / eigenvalue decomposition with extended volume scattering model
S3H$_w$	The optimization of the Y4O$_w$ method for S3H
S4R	Four-component decomposition with a rotation about the line of sight to set Re(T_{23})=0 rotation and the remaining *HV* contribution due to scattering from either a dihedral or a dipole distribution
S4R$_w$	The optimization of the Y4O$_w$ method for S4R
SAR	Synthetic Aperture Radar
S-E	South-East
SETHI	Système Expérimental de Télédétection Hyperfréquence Imageur
SHAPE -TC	Supreme Headquarters Allied Powers Europe, Technical Centre
SIR-C	Shuttle Imaging Radars-C
SLC	Single Look Complex
SOI	Survey of India
SRTM	Shuttle Radar Topography Mission
SSC	Single Look Slant Range Complex
S-W	South-West
TanDEM-X	TerraSAR-X add-on for Digital Elevation Measurements
TerraSAR-X	Versatile X-band SAR satellite with active phased array antenna technology
TP	Total Power
TSX	TerraSAR-X
VH	Vertical transmit, Horizontal receive
VHR	Very-High-Resolution
VV	Vertical transmit, Vertical receive
Y4O	Original Yamaguchi Four-component Decomposition
Y4O$_w$	A new glaciated terrain classification method by combining Y4O method with the Wishart supervised classifier
Y4R	Yamaguchi Four-component Decomposition with Rotation of Coherency Matrix
Y4R$_w$	The optimization of the Y4O$_w$ method for Y4R

Chapter 1 Introduction

The radar remote sensing pathologists and radiologists of Earth and Planetary covers - W.-M. Boerner

After briefly summarizing some selected major contributions on principles of radar polarimetry, the motivation and aims of the thesis are described in this chapter.

1.1 Background of Radar Polarimetry

Radar polarimetry is the merging of the technological concept of Radar (radio detection and ranging) with the fundamental property of the full vector nature of polarized (vector) electromagnetic waves imaging.

1.1.1 Historical Development of Radar Polarimetry (from 1940'ies to 1980'ies)

Radar polarimetry is concerned with the utilization of polarimetry in radar applications as reviewed most recently by Boerner (2003). Whereas polarimetry invention, development and advancement have a long history (Boerner 2003), development on specific radar polarimetry started during the late 1940'ies. First work on specific radar polarimetry is introduced by G. B. Sinclair. It is known that the fully polarimetric radar measurements can be rearranged in matrix form. This coherent matrix is known as scattering matrix or Sinclair matrix. In this way, a single data set is a 2x2 complex scattering matrix, whose elements are the measured radar reflectivities for the four combinations of transmitted-received polarization states in an orthogonal basis (Sinclair 1950). Later, the radar polarimetry fundamentals were developed, primarily by E.M. Kennaugh with the formulation of the coherent radar scattering matrix theory in the late forties at the Antenna Laboratory, Ohio State University (Kennaugh 1952). Kennaugh's fundamental polarization radar optimal null postulates of 1952 were verified by Poelman in the early 1970'ies with developing the first dual polarimetric radar at the Supreme Headquarters Allied Powers Europe, Technical Centre (SHAPE-TC) (Poelman and Guy 1985) , but only a few notable contributions (Bickel 1965; Bickel and Ormsby 1965; Copeland 1960; Deschamps 1951; Graves 1956) were made in radar polarimetry until Huynen's milestone dissertation of 1970, being the starting point of Poelman's first dual polarization high power meteorological surveillance radar system at SHAPE-TC in Scheveningen. Huynen's dissertation, which was discovered by W-M Boerner in 1978, renewed the interest of the remote sensing community on radar polarimetry. Huynen's work was based squarely on Kennaugh's target decomposition theory (Huynen 1970) as was shown by W-M Boerner as early as 1979. W.-M. Boerner was and is still one of the prime promoters of modern SAR polarimetry who first re-discovered and realized the importance of Kennaugh's and Huynen's works (Huynen 1970; Kennaugh 1952), which were essentially unknown or forgotten by others until the early 1980. Since 1978, W.-M. Boerner and his collaborators critically assessed the works of Kennaugh and Huynen (Chaudhuri and Boerner 1987; Davidovitz and Boerner 1986; Kostinski and Boerner 1986; Kostinski and Boerner 1987; Kostinski *et al.* 1988). Chaudhuri and Boerner (1986) used the first order polarization correction to physical optics for validation analysis of Huynen's target-descriptor interpretations of the Kennaugh matrix elements which was first attempted by Huynen himself in Huynen (1992)), and Agrawal and Boerner (1989) transferred the Optimal Polarization state concept from the Poincare sphere surface on to the azimuth/elipticity planar maps in 1985, later on known as the vanZyl power density plots. Since radar polarimetry requires advanced hardware devices, which have not been available in the late 1940's and the 1950's, radar polarimetry remained only a hypothetical concept and its practical use for civil applications was not really recognized. This situation changed at the latest in the early 1980's with the availability of polarimetric Synthetic Aperture Radar (SAR) data from the NASA/JPL airborne AIRSAR system, which allowed in practice the implementation of more recent works by Kennaugh (1952), Huynen (1970), and Boerner (Agrawal and Boerner 1986; Chaudhuri and Boerner 1987; Davidovitz and Boerner 1986; Kostinski and Boerner 1986).

1.1.2 Recent Development of Radar Polarimetry (from 1980'ies to present)

The most important concept on polarization power density signatures in radar polarimetry was introduced by Agrawal (1986), and made known by default as the vanZyl power density signatures - at a time when fully polarimetric SAR (FULL-POL-SAR) data acquisition arrived and made possible in 1980'ies. During the past 30 years, radar polarimetry has been applied to remote sensing and other fields, and splendid results were achieved. More recently, the contribution of Boerner, Cloude, Durden & Freeman, Krogager, Lee, Mott, Pottier, Touzi, vanZyl, Yamaguchi (Boerner *et al.*1985; Boerner *et al.*1992; Boerner 2003; Boerner 1981; Boerner 1995; Boerner and Xi 1990; Boerner *et al.*1987; Boerner *et al.*1981; Boerner *et al.*1998; Cloude 1985; Cloude 1986; Cloude 2009; Cloude and Pottier 1997; Cloude 1992; Cloude 1990; Cloude *et al.* 2002; Durden *et al.* 1989; Durden *et al.* 1990; Freeman and Durden 1998; Krogager 1990; Krogager and Boerner 1996; Lee and Ainsworth 2011; Lee and Pottier 2009; Mott 1992; Mott 2007; Mott and Boerner 1992; Mott and Boerner 1997; Pottier 1998; Touzi 2007; Touzi and Charbonneau 2002; vanZyl 1985; vanZyl 1989; vanZyl *et al.* 2008; vanZyl and Kim 2010; Yamaguchi 2007; Yamaguchi *et al.* 2005; Yamaguchi *et al.* 2006;Yamaguchi *et al.* 2011) on various scattering, covariance and coherency matrix decomposition theory stand out which finally culminated in the fully polarimetric scattering matrix feature identification and extraction methods vanZyl & Arii (Arii *et al.* 2011), Yamaguchi & Singh (Yamaguchi *et al.* 2012) and Singh *et al*. (2013b).

1.2 Target Decomposition

Polarimetric target decomposition techniques split a received signal into a sum of various scattering contributions. This information can be used for extracting the corresponding target types in the image. Chandrasekhar published the first documented work about the decomposition (Chandrasekhar 1960). He proposed to decompose the scattering from a cloud of small anisotropic particles into a sum of terms governed by Rayleigh scattering plus a noise term due to the anisotropy of the particles. Ten years after Chandrasekhar's work, Huynen (1970) proposed the generalization of target decomposition approaches to other scattering problems. Since Huynen deliberations stimulated the great interest in the formulation of target decomposition theory for establishing a unified approach of polarimetric SAR (POL-SAR) data analysis, various decomposition techniques have been proposed (Arii *et al.* 2011; Barnes 1988; Cameron *et al.* 1996; Cloude 1985; Cloude 1992; Cloude 2009; Cloude and Pottier 1997; Cloude *et al.* 2002; Corr and Rodrigues 2002; Freeman and Durden 1998; Holm and Barnes 1988; Krogager 1990; Krogager and Boerner 1996; Lee and Pottier 2009; Lee and Ainsworth 2011; Pottier 1998; Touzi 2007; Touzi and Charbonneau 2002; vanZyl *et al*. 2008; vanZyl and Kim 2010; Yamaguchi 2007; Yamaguchi *et al.* 2005; Yamaguchi *et al.* 2006; Yajima *et al.* 2008;Yamaguchi *et al.* 2011; Yang 1999). The compressive overviews are described in Boerner *et al.* (1998), Cloude and Pottier (1996), Lee and Pottier (2009), and Touzi *et al.* (2004).

Target decomposition techniques are divided into two main groups, depending on whether of coherent or incoherent type, respectively; and on the decomposition procedures carried out on the matrices. A brief description of each group as well as their most outstanding contributions is summarized in the following:

1.2.1 Coherent Decomposition Theory

This approach was developed to characterize completely polarized scattered waves for which the fully polarimetric information is contained in the scattering matrix for isolated point scatterers. To do this, the scattering matrix is expressed as a sum of elemental scattering matrices by using coherent averaging. The drawback of averaging coherently the scattered fields is the existence of interference among all the contributions, which results in a type of noise known as *speckle* (Lee and Pottier 2009).

The main work of this type of target decomposition was introduced by Krogager (1990), and Krogager and Boerner (1996), where it was proposed that the scattering matrix could be separated into a sum of the contributions from a sphere, a helix and a diplane. Many other coherent target decomposition methods were published in Cameron *et al.* (1996), Corr and Rodrigues (2002), and Touzi and Charbonneau (2002).

1.2.2 Incoherent Decomposition Theory

Most of the targets at earth surface are natural distributed heterogeneous scatterer ensembles, thus incoherent target decomposition methods may provide good results. Therefore, incoherent target decomposition models have been chosen in this thesis. This type of target decomposition makes use of the covariance or the coherency matrix formulations, which are equivalent to the Mueller matrix. The scattering matrix is expressed by means of a linear combination of elementary Mueller scattering matrices, which correspond to the predominant scattering mechanisms contained in the scene.

Eigenvalue/Eigenvector Decomposition

In 1985 Cloude extended Wiener's wave 2 × 2 Coherency matrix representation of light polarization to a 4 × 4 target coherency matrix that is decomposed into four orthogonal rank-1 matrices representing the eigenvalue-weighted behavior of four deterministic targets (Cloude 1985; Cloude 1986). For backscatter geometries, by application of the reciprocity principle, the analysis is reduced to 3 × 3 complex target coherency matrix and the four targets theorem becomes a three targets decomposition (Cloude 1992). In 1997, Cloude and Pottier proposed a solid physical interpretation of the scattering behaviour of natural targets by the use of the well-known eigenvalue entropy and eigenvector mean-alpha parameters (Cloude and Pottier 1997). In the last 15 years, the Cloude–Pottier decomposition has found an enormous success utilizing the more rigorous properties of such a mathematical approach and useful usage of the von Neuman entropy (H), the anisotropy (A), as well as the eigenvector parameters for a plethora of remote sensing investigations (Singh 2010; Singh and Venkataraman 2012; Singh *et al.* 2008; Singh *et al.* 2013a). In 2007, Touzi has pointed out that the average eigen-parameters are a non-unique set that can allow confusion between some target classes and proposed an eigen-decomposition of the nine parameters target coherency matrix in term of 15 orientation invariant features (Touzi 2007) intrinsically following the Kennaugh-Huynen incoherent decomposition formulation of the Mueller backscattering matrix (Huynen, 1970; Touzi *et al.* 2004).

Model-Based Decomposition

Several authors have proposed decompositions of measured polarimetric coherency or covariance matrices into the weighted sums of individual covariance matrices that represent known scattering models. These types of methods (Arii *et al.* 2011; Freeman and Durden 1998; Lee and Ainsworth 2011; Singh *et al.* 2013b; Yamaguchi *et al.* 2005; Yamaguchi *et al.*

2011) provide straightforward implementation of such sub-matrices for which the decomposition powers correspond to physical scattering mechanisms and the resulting color-coded images are directly recognizable and straightforward for relating to physical characteristics. The original three-component scattering power decomposition was proposed by Freeman and Durden (1998) under reflection symmetry condition (e.g. HV=VH in H and V polarization basis). Here, it is essential to note that the color-coding of the SAR scattering components were standardized in coordination with NASA/JPL's AIRSAR demonstrations as HH (red), HV or VH (green) and VV (blue) and for implementing Pauli-based decompositions as HH-VV (red) , HV+VH (green) and HH+VV (blue) after considerable earlier confusion was therewith eliminated. This means that the FDD (the Freeman and Durden Decomposition) accounts five independent parameters out of nine independent parameters of coherency matrix. Next important steps were taken by Yamaguchi *et al.* (2005). They proposed four-component power scattering decomposition and subject to this alteration Yamaguchi *et al.* (2005) succeeded to account for six independent parameters out of nine independent parameters of the coherency matrix in the original Yamaguchi four-component decomposition (Y4O). Yajima *et al*. (2008) noticed that there is no guarantee of non-negative power occurrence in Y4O. The solutions of the negative power problem were also discussed by Yajima *et al*. (2008). Lee and Ainsworth (2011) have investigated the orientation dependence of the model-based and FDD and Y4O, whereas Yamaguchi *et al.* (2011) have responded by proposing an orientation independent, four-component decomposition. By using Huynen's deorientation concept in Y4O, they achieved 75% polarimetric information in the Yamaguchi decomposition with rotation of the coherency matrix (Y4R) scheme and reduced the negative power occurrence. Interesting model-based decompositions have also been published by Arii *et al.* (2011). More recently, Singh *et al.* (2013b) proposed the scheme of general four-component decomposition with unitary transformation of coherency matrix (G4U). Finally, with this most recent improvement, Singh *et al.* (2013b) in G4U were able to account for 100% polarimetric phase information of the coherency matrix, and improved considerably the 3D images as compared to other existing model based decompositions schemes.

Hybrid Eigenvalue/Model-Based Decompositions

Using model-based schemes, interpretations are simple and straightforward; however there is no guarantee of non-negative power occurrence. The solutions of the negative power problem were discussed by Yajima *et al.* (2008) and vanZyl *et al.* (2008). vanZyl *et al.* (2008) proposed a hybrid decomposition method to overcome negative power fatal deficiencies. Thereupon, Cloude (2009) proposed a generalized hybrid Freeman/eigenvalue decomposition method for dealing with the negative power problems. The hybrid Freeman/eigenvalue decomposition is a mathematically and computationally very simple approach. The main idea of this approach is to use orthogonality for reducing the number of unknowns. In addition, the reformulation and simplified computation of this approach enables a clearer demonstration of the effectiveness of the new scattering mechanism model (Singh *et al.* 2013c).

1.3 Motivation

The Earth's surface parameters are of crucial importance in climate models. Many Scientists throughout the world are monitoring the Earth's surface parameters. Since monitoring of Earth's surface parameters is an important application of Microwave Remote Sensing (MRS), SAR Polarimetry represents an active area of research in Active Earth Remote Sensing (A-ERS).

The motivation of this work arises from my previous Indian Ph.D. Thesis entitle “*SAR Polarimetry Techniques for Snow Parameters Estimation*” and one of the quotations of the prime promoter of the Modern SAR Polarimetry Sir Wolfgang-Martin Boerner — “*Terrestrial remote sensing with polarimetric SAR is the radiology with diagnostics of the health of the Earth at all weather and volcanic conditions and at day and night*”**.** Moreover, there is a rapidly increasing interest in the application of SAR polarimetry for Earth observations due to increasing availability of polarimetric space-borne radar sensors, such as ALOS-PALSAR (L-band, Japan), TerraSAR-X and TanDEM-X (X-band, Germany), and RADARSAT-2 (C-band, Canada), and follow-up satellite sensor systems for all of these novel fully polarimetric sensors. FULL-POL-SAR also allows a discrimination of different types of scattering mechanisms. This becomes possible because the received power depends strongly on the actual scattering process. Certain polarimetric scattering models indeed provide direct physical interpretation of the scattering process, allowing an estimation of physical ground parameters like soil moisture and surface roughness, as well as unsupervised classification methods with automatic identification of different scatterer characteristics and target types. Here, we note that in addition to polarization diversity, a wide range of incidence angles is required which will be overcome with the novel beam-shaping concepts currently pioneered at DLR.

The problem of the physical interpretation of a measured radar return is, consequently, of growing importance. In the absence of a physical model describing a given sample, its experimental measured fully polarimetric scattering matrix with second order statistics can still be phenomenologically interpreted by decomposing it algebraically into simpler components having a direct physical meaning. With polarimetric decomposition techniques, a received signal can be split into a sum of various scattering contributions with polarimetric signatures. The polarimetric target decomposition methods of a measured coherency or covariance or Mueller matrix into several simpler ones, representing basic polarization components (partial polarizers, wave-plates and depolarizers), often allow one to obtain an improved insight into the physics underlying the original matrix. Decomposition methods can be used for extracting the corresponding target type in the image.

SAR polarimetry additionally offers some limited capability for separating multiple scattering mechanisms occurring inside the same resolution cell and can be deemed as a first step in resolving the ambiguous scattering problem in SAR, as mentioned above.

Understanding and quantitatively retrieving information from POL-SAR signatures of the terrain surfaces have become a key issue for the SAR remote sensing applications. Remote sensing with POL-SAR offers an efficient and reliable means of collecting information required to extract geophysical and biophysical parameters from Earth’s surface. This remote sensing technique has found many successful applications in crop monitoring and damage assessment, forestry clear cut mapping, deforestation mapping, land surface structure, land use and land cover, hydrology (soil moisture, flood delineation), sea ice monitoring, snow and glacier monitoring, natural disaster monitoring, ocean and coastal monitoring, etc.

Besides, the understanding of FULL-POL-SAR remote sensing of earth surface features’ behaviour, investigated for the last decades; yet simple and robust decomposition schemes are still lacking, which can be directly applied for monitoring of land cover information. This thesis also proposes new FULL-POL-SAR decompositions, which can be utilized further for interpreting the FULL-POL-SAR images, automatic land cover classification/segmentation and scattering parameters inversion for geo-/bio-physical parameters estimation.

1.4 Aim of Thesis

The main aim of the thesis is to bridge the intellectual gap at the radar polarimetry method terminus—where radar polarimetry theories/methods developments traditionally ends — and earth surface parameters monitoring traditionally begins. Fittingly, those engaged in this kind of research are members of both disciplines and show an interest in the effective applications of radar polarimetry. This thesis therefore intends to focus upon the following as elementary subtasks to meet the goal:

1. **Needs for physical scattering mechanism model-based decomposition of FULL-POL-SAR**: Why is the scattering model based decomposition required in POL-SAR data interpretation? How can the model based decomposition be utilized in terrain features categorization? How can the model based decomposition be aided in improvement of the terrain classification results?

2. **Effects of volume scattering selection on decomposition and the results of decomposition components**: How will dipole, oriented dihedral and spheroid volume scattering models effect the decomposition results? How does the response vary in different scattering models?

3. **Incorporation of FULL-POL-SAR information in scattering power decomposition**: How can the complete FULL-POL-SAR information be utilized in decomposition models? How can decomposition performance be improved?

4. **Decomposition components as information repositories for earth surface parameters retrieval modelling**: What kind of information can be extracted from decompositions that can aid earth surface parameters retrieval modelling? How can decomposition components help to constrain model parameters or provide model input?

The questions under the above mentioned subtasks that guide to organize the research works of [P1]–[P8] and for which answers were sought, are discussed in this thesis.

1.5 Scope and Organization of the Thesis

FULL-POL-SAR remote sensing offers an efficient and reliable means of collecting information required to develop methodology, and lead to a significant improvement in understanding, qualitatively and quantitatively retrieving information of the earth surface key parameters. Hence, the main scope of this thesis is to establish an approach for monitoring, modeling and planning of the earth surface key parameter retrieval. This thesis discusses closing this gap of the absence of suitable methodologies for retrieving the earth surface key parameters. Under this thesis, suitable methodologies/algorithms are developed for earth surface parameter related studies, which can be directly applied to monitor the earth and there is potential for earth surface parameters to become an operational product. This thesis is also basic for understanding the potential of FULL-POL-SAR remote sensing for earth surface parameter estimation and can lead to development of geo-/bio-physical properties as operational products with the aid of current radar space-borne missions such as RADARSAT-2 (C-band) and near-future radar space-borne missions such as ALOS-PALSAR-2 (L-band). Upon assessing the state-of-the-art on the pertinent literature on radar remote sensing of the earth, the decomposition method of the Yamaguchi team was selected and also a new decomposition model has been developed to analyze the problems of the earth surface parameter estimation and to provide an accurate assessment. The complete detailed formulations of the various subtasks of this dissertation study are outlined in the introduction of the respective chapters and are summarized at the end of each chapter.

The subject matter of the thesis is presented in the following nine chapters:

Chapter 2 presents the methodology and results on utilization of Y4O for complex glaciated terrain classification;

Chapter 3 presents the evaluation of Y4R;

Chapters 4, 5, and 6 introduce new developments in target decomposition theory of FULL-POL-SAR data;

Chapter 7 provides disaster monitoring applications;

Chapter 8 focuses on the development of generalized FULL-POL-SAR decomposition scheme over wet snow area;

Chapter 9 covers overall conclusions.

Here, it should be emphasized that by integrating all coherency matrix components, we are essentially increasing the implementation of ever more polarimetric relative phase information intrinsically contained in the coherency matrix, which for the simpler models is not included and is lost. This observation applies also to Touzi's alternative formulations.

More specifically, Chapter 2 assesses the utilization of the original Yamaguchi four-component decomposition (Y4O) for terrain classification in the cold mountainous regions. In addition, this chapter presents the Y4O method suitability as compared to the FDD method for glaciated terrain features identification. A new methodology has been discussed by combining the complex Wishart distribution (Wishart 1928) and Y4O method for glaciated terrain classification. This work is published in the journal *Geocarto International* [P1].

Chapter 3 evaluates the modified Yamaguchi four-component decomposition with rotation of coherency matrix (Y4R). It is shown that improvement can be clearly seen in the highly rugged glacier region by using Y4R as compared to Y4O (Chapter 2). The results are also published in *Geocarto International* [P2].

Chapter 4 presents a new volume scattering model that accounts for the *HV* component caused by double-bounce structures. This model reduces the volume scattering power and enhances the double-bounce scattering power within man-made structures, leading to an improvement in the four-component scattering power decomposition. This method accounts for 6 parameters out of 8 independent observable polarimetric parameters, for which the maximum accountable number is 6 up to now. The results are published in the *IEEE Geoscience and Remote Sensing Letter* [P3].

An improved hybrid decomposition scheme is presented in Chapter 5. As seen in Chapter 4, the classification between vegetation and the buildings becomes inconclusive. Therefore, it is proposed to use an extended volume scattering model suited for oriented urban buildings (i.e., oriented dihedral model) to mitigate the overestimation volume scattering problem. This proposed method shows the advancements in a three-component hybrid decomposition scheme (Cloude 2009) for resolving the discrimination ambiguity of oriented dihedral objects from vegetation, by implementing the extended volume scattering model and the concept of rotation about line of sight. The results are published in the *IEEE Geoscience and Remote Sensing Letter* [P4].

General four-component scattering power decomposition with unitary transformation of coherency matrix (G4U) is presented in Chapter 6. This chapter also describes the utilization for 7 parameters out of 7 independent polarimetric parameters of the coherency matrix in the four-component decomposition. The results are published in the *IEEE Transactions Geoscience and Remote Sensing* [P5].

Chapter 7 describes the application of the G4U scheme (Chapter 6) to a set of fully polarimetric synthetic aperture radar images acquired before and after the Tohoku earthquake and resultant tsunami for extracting spatial information of the scene. Change detection has been analysed based on G4U parameters. The results are being published in *the Proceedings of the IEEE* [P6].

Chapter 8 deals the development of a generalized FULL-POL-SAR decomposition scheme over wet snow area. This decomposition accounts for all independent parameters of the coherency matrix. In the proposed decomposition scheme, a generalized spheroidal (ellipsoid) shape is considered for the volume scattering model derivation. Furthermore, the generalized Cloude volume and the Freeman surface parameters have been derived over wet snow areas, which account for all independent parameters of the coherency matrix. The results are the part of Papers [P7] and [P8]. Here, it should be re-emphasized that by integrating all coherency matrix components, we are essentially increasing the implementation of ever more polarimetric relative phase information intrinsically contained in the coherency matrix, which for the simpler models is not included and is lost which also holds for Touzi’s methods.

Chapter 2 Utilization of Four-Component Scattering Power Decomposition Y4O Method for Glaciated Terrain Classification

Science is deeply embedded in Nature

2.1 Abstract

Glaciated terrain classification is important for hydrological and climate change modelling. For this purpose, fully polarimetric Advanced Land Observation Satellite-Phase Array L-band Synthetic Aperture Radar (ALOS-PALSAR) data sets have been used over the Indian Himalayan glaciated region. PALSAR data sets have been analyzed based on the three- and four-component scattering decomposition methods for glaciated terrain classification. These methods have been applied on multi-looked 3×3 coherency matrix sets of ALOS-PALSAR data. The analysis of these methods shows that the Freeman and Durden three-component scattering power decomposition (FDD) method suffers from an over-estimation problem for the volume backscattering component as compared to the Yamaguchi four-component scattering power decomposition (Y4O) method, here considered in greater detail. In addition, is applied for POL-SAR data classification over the Indian Himalayan glaciated terrain. However, by implementing the Wishart supervised classifier, an overall accuracy of 93.38% has been achieved but discrimination between vegetation and glacier snow/ice classes was not properly accomplished. To overcome this ambiguity, the Y4O method has been combined with the complex Wishart distribution for supervised classification of ALOS-PALSAR image, here denoted as $Y4O_{w.}$ The new feature of $Y4O_w$ is that the probability difference between surface backscattering and volume backscattering has been introduced as a next step in the altered Wishart classification procedure which will be assessed in this Chapter 2.

2.2 Introduction

Satellite remote sensing promises great potential in the study of dynamically changing environments related to the high altitude cold regions mainly because of its repetitive capability and synoptic coverage. The land-covered features have unique reflectance characteristics in different spectral bands of optical sensors, which may provide information on physical properties as well as the areal extent of glaciated terrain features under cloud-free conditions. However, they have some difficulty in rugged high mountainous area: 1) optical images are often affected by clouds in mountainous glacier areas; and the Himalayan region is strongly affected by monsoons and cloud cover is quite common, especially during the summer months: The glaciated terrain classification is indeed hindered in the Himalayan region due to a lack of cloud-free optical images for most of time and during all seasons; 2) the mountain shadow makes it difficult to discriminate between glacier areas and non-glacier areas; and 3) an ambiguity between snow and ice exists because both have similar optical properties in glacial areas (Racoviteanu 2009). Due to the strong spatial and time dependent dynamics of glaciated terrain, regular and frequent mapping is necessary to monitor glaciated terrain, and requires sensors that are time and weather independent.

SAR remote sensing with its all-weather capability, cloud penetration, and quasi independence of sun illumination (in case angle of incidence is neglected) can add considerable robustness to classify the glaciated terrain (Rott 1994; Singh and Venkataraman 2008). In case of monostatic FULL-POL-SAR data, point targets are characterized by five parameters (three amplitude and two relative phases) for the assumed reciprocal symmetric formulation. Therefore, SAR full-polarimetry techniques can lead to a significant improvement in the quality of classification and segmentation results in comparison to conventional single-channel SAR. FULL-POL-SAR also allows discrimination of different types of scattering mechanisms. This becomes possible because the received power depends strongly on the actual backscattering process. Received backscattering power can be divided into a sum of various backscattering contributions by using polarimetric target decomposition methods (Cloude and Pottier 1996). Thus, polarimetric decomposition methods can be utilized for extracting the corresponding target type in fully polarimetric ALSO-PALSAR images over glaciated terrain.

In the literatures (Boerner *et al.* 1998; Cloude 2009; Cloude and Pottier 1996; Freeman and Durden 1998; Lee and Pottier 2009; Touzi 2007; vanZyl and Kim 2010; Yamaguchi 2007; Yamaguchi *et al.* 2005), polarimetric target decomposition methods are categorized into two types (see Section 1.2 in Chapter 1): the first type is coherent decomposition methods that are directly performed on the complex scattering matrix. The second type is incoherent decomposition methods based on the second order statistics of polarimetric information, e.g. the coherency matrix and intrinsically applied to the 4x4 real Mueller or Kennaugh matrices. The incoherent decomposition methods (Freeman and Durden 1998; Yajima *et al.* 2008; Yamaguchi *et al.* 2005) expand the coherency matrix into the incoherent sum of scattering power components of a distributed target. Since most of the targets are distributed in natural earth environments, this type of target can only be characterized statistically. Singh (2010) proved that incoherent decomposition provides sufficient information for classification of glaciated terrain features such as "*debris covered glacier (DCG)*", snow, barren rock, etc, using fully polarimetric data (Singh and Venkataraman 2012; Singh *et al.* 2013a).

In this Chapter 2, the Y4O method (Yamaguchi 2007; Yajima *et al.* 2008; Yamaguchi *et al.* 2005) is applied to identify glaciated terrain features in part of Indian Himalaya. The Y4O method decomposes polarimetric radar power into surface, double-bounce, volume, and helix power scattering. This Y4O method is a first extension of the FDD method (Freeman and Durden 1998) to the more general scattering case with non-reflection symmetry condition, for which the resulting Y4O method has been the following advantages: 1) straightforward implementation; 2) scattering power calculations are straight-forward; 3) the decomposed powers correspond to physical scattering mechanisms resembling those in nature most closely, i.e., surface scattering, double-bounce scattering, volume scattering, helix (circular polarization) scattering; 4) output color-coded images are directly recognizable and easy to understand because the selected color-coding does indeed resemble nature most closely in comparison to other color-coding choices. Moreover, this chapter assesses the Y4O method (Yajima *et al.* 2008; Yamaguchi *et al.* 2005) suitability as compared to the FDD method (Freeman and Durden 1998) for glaciated terrain features identification. A new methodology, here denoted as $Y4O_w$, has been discussed by combining the complex Wishart distribution (Wishart 1928; Lee and Pottier 2009) and the Y4O method for glaciated terrain classification.

2.3. Study Area

The location map is shown in Fig.2.1, introducing the Alaknanda river catchment, Uttarakhand, India, consisting many glaciers. Satopanth and Bhagirath Kharak glaciers are the major glaciers among them in this catchment. The Satopanth and Bhagirath Kharak glaciers are approximately 13 and 18.5 km long with an average width of 750–850 m, covering an area of 21.17 and 31.17 km^2, respectively. The upper Alaknanda river catchment covers an area of 1544.08 km^2, out of which 70.70 and 107.22 km^2 are covered by the Satopanth and Bhagirath Kharak sub-watersheds, respectively (Nainwal *et al.* 2008).

The elevation ranges between 2000 m and 7000 m The Alaknanda river, which is the main tributary of Ganga river, originates at the snout of the Satopanth glacier. The area lies between latitude 30^0 40’ N and 30^0 50’ N and longitude between 79^0 15’ E and 79^0 28’ E. Satopanth and Bhagirath Kharak glaciers are shown in Fig. 2.2(a) to (c). This glaciated region includes snow, debris-covered glacier (DCG), and barren rocks targets.

2.4. Data Used

In this study, we acquired the Phased-Array-type L-band Synthetic Aperture Radar (PALSAR) fully polarimetric, single look complex, level 1.1 data sets of May 12, 2007 with fixed 21.5^0 incident angle and nominal pixel spacing (azimuth × range) 3.54 (m) × 9.36 (m). PALSAR fully polarimetric sensor, on-board the Advanced Land Observing Satellite (ALOS), was launched on 24 January 2006 by the Japan Aerospace Exploration Agency (JAXA) at Tanegashima. It operates in the L-band frequency at 1.27 GHz (23.6 cm wavelength). It is well known that L-band microwave signals penetrate through dry snowpack with negligible volume backscatter from snow. However, if snowpack is wet, the situation becomes different. If the moisture exceeds 1% in highly accumulated snowpack, L-band frequency suffers from attenuation in the snowpack while reflection or backscatter from the snowpack is enchanced (Abe *et al.* 1990). In general, snow cover area becomes wet in the month of May (early summer) over Himalayan snow bound areas with significant melting. The magnitude of backscatter depends on the snow density and water content, and the depth of snowpack. Since the snowpack on May 06, 2007 is wet due to the beginning of snow melting, the snowpack contains water and is not so transparent at L-band frequency. Snowpack is also heterogeneous with snow grain particles compressed during winter season and contains high density due to snow accumulation and melting cycle. The co-polarization backscatter components (*HH* and *VV*) increase with snow volume, while the cross-polarization backscatter (*HV*) remains small as compared to co-polarization. Since the *HV* components contribute only to volume scattering in the Y4O, the main polarimetric response from snowpack becomes surface scattering in the Y4O results by using L-band POL-SAR measurements (see Section 2.6).

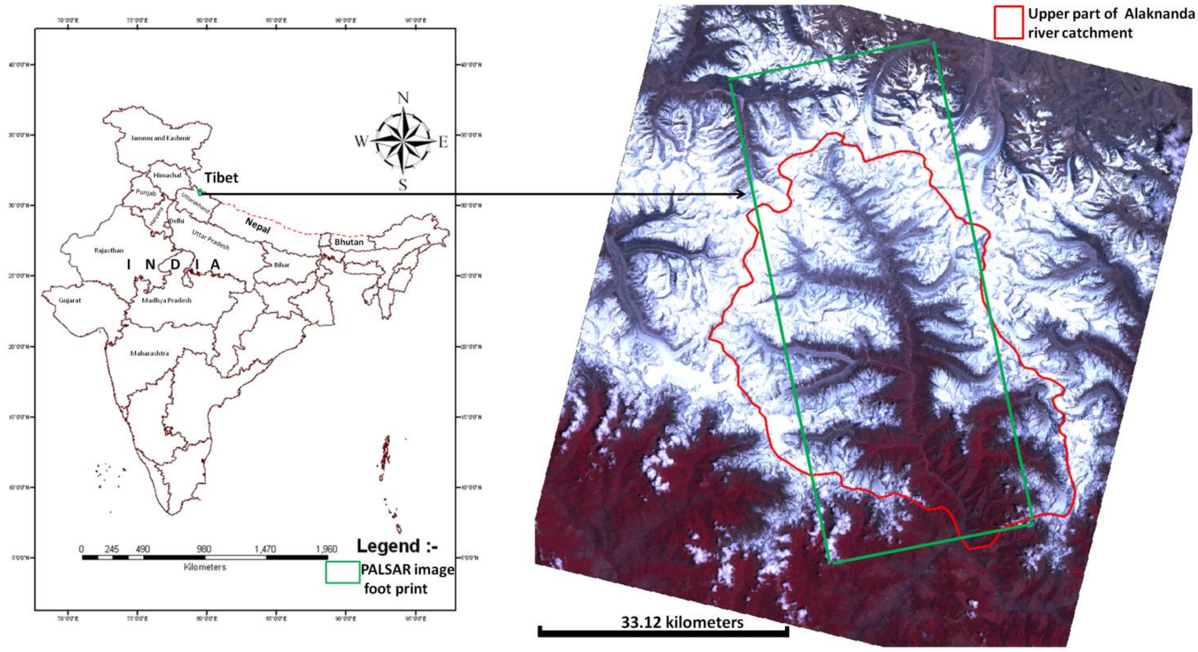

Fig. 2.1. Location map of study area.

Fig. 2.2(b) shows the Pauli color composite image (May 12, 2007) which provides the clear information about single scattering (snow cover area over glacier and non-glacier), double-bounce (dihedral features) and volume scattering (debris-covered glacier) in the study area.

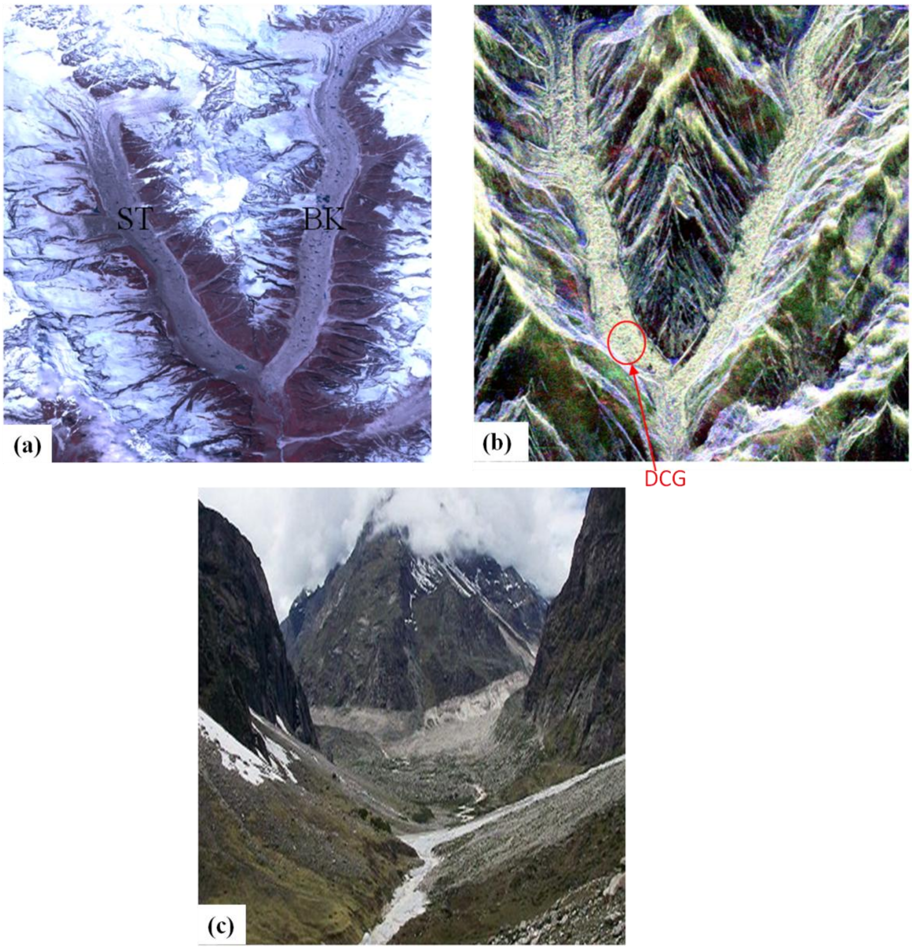

Fig.2.2. (a) Cloud free ALOS-AVNIR-2 image of 24 May 2010. (b) Pauli RGB HH-VV (red), 2HV (green), HH+VV (blue) image of PALSAR of 12 May 2007. (c) Photo of Satopanth (ST) and Bhagirath Kharak (BK) entrance.

2.5. Method and Technique

2.5.1 Scattering Matrix

Backscattered electric field $\boldsymbol{E}^{\boldsymbol{S}}$ received at POL-SAR antenna (see Fig. 2.3) can be expressed as linear transformation of incident electric field $\boldsymbol{E}^{\boldsymbol{t}}$ upon target:

$$\boldsymbol{E}^{\boldsymbol{S}} = \frac{e^{-jk_w r}}{r} \boldsymbol{S}\, \boldsymbol{E}^{\boldsymbol{t}} \tag{2.1}$$

where $\boldsymbol{S}$ is backscattering matrix, k_w is wave number and r is slant range distance.

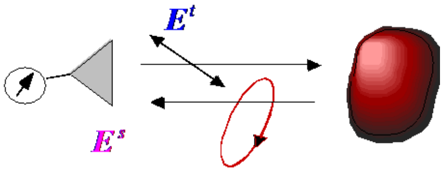

Fig.2.3. Interaction of the polarized radar signal with an object.

The calibrated complex 2×2 backscattering matrix $\boldsymbol{S}$ of POL-SAR in horizontal-vertical basis is expressed as

$$\boldsymbol{S} = CF\begin{bmatrix} S_{HH} & S_{HV} \\ S_{VH} & S_{VV} \end{bmatrix} \tag{2.2}$$

where *CF* is calibration factor (e.g. ALOS-PALSAR's $CF = 10^{-86/10}$), and the elements of scattering matrix S_{HH}, S_{VV}, S_{HV}, S_{VH} are called complex backscattering coefficients. The elements S_{HH} and S_{VV} produce the power return in co-polarized channel and the elements S_{HV} and S_{VH} produce the power in the cross-polarization channels.

In practical cases of backscattering, reciprocity of electric field ($S_{HV} = S_{VH}$, monostatic case) may be assumed for which the scattering matrix can be rewritten as

$$\boldsymbol{S} = CF\begin{bmatrix} S_{HH} & S_{HV} \\ S_{HV} & S_{VV} \end{bmatrix} \tag{2.3}$$

Due to the reason that the measured scattering matrix is often affected by the noise-like speckle, incoherent analysis making use of the second-order statistics such as the coherency and covariance is often used (Arii *et al.* 2011; Freeman and Freeman 1998;Yamaguchi *et al.* 2005). These polarization matrices involve nine independent polarimetric measurements. Covariance matrix $\langle[\boldsymbol{C}]\rangle$ represents the physical elements associated with power. On the other hand, the coherency matrix $\langle[\boldsymbol{T}]\rangle$ has the advantage of providing mathematical representation (i.e. easy to formulate and rotate) and of describing the physical scattering nature representation. However, the preference of particular covariance versus coherency matrix formulation is a matter of personal choice. The coherency matrix based analysis is treated in this chapter as well as in rest part of this thesis.

2.5.2 Coherency Matrix

Once the calibrated scattering matrix $\boldsymbol{S}$ is acquired with a fully polarimetric radar, we can define the scattering vector $\boldsymbol{k}$ for the Pauli presentation as (Cloude 2009; Lee and Pottier 2009; Yamaguchi 2007)

$$\boldsymbol{k} = \frac{1}{\sqrt{2}}\begin{bmatrix} S_{HH} + S_{VV} \\ S_{HH} - S_{VV} \\ S_{HV} \end{bmatrix} \tag{2.4}$$

The coherency matrix is then given as

$$\langle[\boldsymbol{T}]\rangle = \langle \boldsymbol{k}\boldsymbol{k}^{\dagger}\rangle = \begin{bmatrix} T_{11} & T_{12} & T_{13} \\ T_{21} & T_{22} & T_{23} \\ T_{31} & T_{32} & T_{33} \end{bmatrix}$$

$$= \frac{1}{2}\begin{bmatrix} \langle |S_{HH} - S_{VV}|^2\rangle & \langle (S_{HH} + S_{VV})(S_{HH} - S_{VV})^*\rangle & 2\langle (S_{HH} + S_{VV})S_{HV}^*\rangle \\ \langle (S_{HH} - S_{VV})(S_{HH} + S_{VV})^*\rangle & \langle |S_{HH} - S_{VV}|^2\rangle & 2\langle (S_{HH}\ S_{VV})S_{HV}^*\rangle \\ 2\langle S_{HV}(S_{HH} + S_{VV})^*\rangle & 2\langle S_{HV}(S_{HH} - S_{VV})^*\rangle & \langle |S_{HV}|^2\rangle \end{bmatrix} \tag{2.5}$$

where † denotes complex conjugation and transposition, and $\langle . \rangle$ denotes ensemble average in an imaging window.

2.5.3 Four-Component Decomposition Method Y4O according to Yamaguchi

The Yamaguchi four-component scattering power decomposition method divides the measured coherency matrix into 4 sub-matrices representing physical scattering mechanisms Yajima *et al.* 2008; Yamaguchi *et al.* 2005; Yamaguchi *et al.* 2006)

$$\langle[T]\rangle = f_s\langle[T]\rangle_{\mathrm{surface}} + f_d\,\langle[T]\rangle_{\mathrm{double}} + f_v\,\langle[T]\rangle_{\mathrm{vol}} + f_c\langle[T]\rangle_{\mathrm{helix}} \qquad (2.6)$$

where f_s, f_d, f_v and f_c are coefficients to be determined. $\langle[T]\rangle_{\mathrm{surface}}$, $\langle[T]\rangle_{\mathrm{double}}$, $\langle[T]\rangle_{\mathrm{vol}}$ and $\langle[T]\rangle_{\mathrm{helix}}$ are expansion coherency matrices corresponding to surface, double-bounce, volume, and helix scattering, respectively. The Yamaguchi four-component decomposition Y4O works subject to the non-reflection symmetric case to accommodate the more general scattering case encountered in complicated geometric scattering structures.

The single-bounce scattering model is represented by surface scattering phenomena from slightly rough surfaces for which the cross-polarized component is negligible. The expansion coherency matrix for surface scattering is

$$\langle[T]\rangle_{\mathrm{surface}} = \begin{bmatrix} 1 & \beta^* & 0 \\ \beta & |\beta|^2 & 0 \\ 0 & 0 & 0 \end{bmatrix}, \beta = \frac{\alpha_{HH} - \alpha_{VV}}{\alpha_{HH} + \alpha_{VV}}, |\beta| < 1 \qquad (2.7)$$

where α_{HH} and α_{VV} are reflection coefficients for *HH* and *VV* polarization respectively.

The double-bounce scattering model is based on the hypothesis of double reflections from right-angled structures. Double-bounce structures include road-surfaces, building-walls, ground-trees, and man-made targets, etc.. The expanded coherency matrix for double-bounce scattering is

$$\langle[T]\rangle_{\mathrm{double}} = \begin{bmatrix} |\alpha|^2 & \alpha & 0 \\ \alpha^* & 1 & 0 \\ 0 & 0 & 0 \end{bmatrix}, \alpha = \frac{e^{2j\delta_{HH}}\alpha_{HH}^{D}\alpha_{HH}^{S} + e^{2j\delta_{VV}}\alpha_{VV}^{D}\alpha_{VV}^{S}}{e^{2j\delta_{HH}}\alpha_{HH}^{D}\alpha_{HH}^{S} - e^{2j\delta_{VV}}\alpha_{VV}^{D}\alpha_{VV}^{S}}, |\alpha| < 1 \qquad (2.8)$$

where α_{HH}^{D} and α_{VV}^{D} are reflection coefficients of vertical surface for *HH* and *VV* polarization, respectively; α_{HH}^{S} and α_{VV}^{S} are reflection coefficients of horizontal ground surface for *HH* and *VV* polarization, respectively; and δ_{HH} and δ_{VV} represent the propagation and phase change effects.

Volume scattering can be observed if the SAR antenna-beam penetrates into a medium. Scattering by trees or branches, subsurface or snow/ice layers etc. are examples of volume scattering. For the volume scattering model, Yamaguchi (2007) has proposed the following volume coherency matrices according to the magnitude balance of $\langle|S_{HH}|^2\rangle$ and $\langle|S_{VV}|^2\rangle$ (Yamaguchi *et al.* 2005), in case

When $10\log(\langle|S_{VV}|^2\rangle/\langle|S_{HH}|^2\rangle) \geq 2\ dB$

$$\langle[T]\rangle_{\mathrm{vol}} = \frac{1}{30}\begin{bmatrix} 15 & -5 & 0 \\ -5 & 7 & 0 \\ 0 & 0 & 8 \end{bmatrix} \qquad (2.9)$$

When $-2\ dB < 10\log(\langle|S_{VV}|^2\rangle/\langle|S_{HH}|^2\rangle) < 2\ dB$

$$\langle[T]\rangle_{\text{vol}} = \frac{1}{4}\begin{bmatrix} 2 & 0 & 0 \\ 0 & 1 & 0 \\ 0 & 0 & 1 \end{bmatrix} \tag{2.10}$$

When $10\log(\langle|S_{VV}|^2\rangle/\langle|S_{HH}|^2\rangle) \le -2\ dB$

$$\langle[T]\rangle_{\text{vol}} = \frac{1}{30}\begin{bmatrix} 15 & 5 & 0 \\ 5 & 7 & 0 \\ 0 & 0 & 8 \end{bmatrix} \tag{2.11}$$

Helix scattering power is equivalent to circular polarization power. This term appears in urban and mountainous area for L-band data. The helix scattering expansion matrix, which takes into account of non-reflection symmetry condition, is

$$\langle[T]\rangle_{\text{helix}} = \frac{1}{2}\begin{bmatrix} 0 & 0 & 0 \\ 0 & 1 & \pm j \\ 0 & \mp j & 1 \end{bmatrix} \tag{2.12}$$

The corresponding scattering powers (the surface scattering power P_s, the double-bounce scattering P_d, the volume scattering power P_v and the helix scattering power P_c) are directly obtained from the expansion coefficients by implementing the decomposition. The decomposition takes account of an imbalance of the co-polarized channel power. For the case of $-2\ dB < 10\log(\langle|S_{VV}|^2\rangle/\langle|S_{HH}|^2\rangle) < 2\ dB$, the decomposed power expression becomes as (Yamaguchi 2007):

$$P_c = f_c = \ 2\ |\text{Im}\{T_{23}\}| \tag{2.13}$$

$$P_v = f_v = 2\ [2\ T_{33}(\theta) - f_c] \tag{2.14}$$

$$P_s = f_s(1 + |\beta|^2) \tag{2.17}$$

$$P_d = f_s(1 + |\alpha|^2) \tag{2.16}$$

2.5.4. Complex Wishart Classifier

The complex Wishart distribution is expressed as (Wishart 1928)

$$P(\langle[T]\rangle/[T_m]) = \frac{L^{Ln}|\langle[T]\rangle|^{L-n}e^{-n\,Tr([T_m]^{-1}\langle[T]\rangle)}}{\pi^{\frac{n(n-1)}{2}}\Gamma(L)..\Gamma(L-n+1)[T_m]} \tag{2.17}$$

where L is the number of looks and n is the polarimetric dimension; and the class coherency matrix, denotes as $[T_m]$ for defined class, is estimated from using training samples. Using the complex Wishart distribution of the coherency matrix $\langle[T]\rangle$, an appropriate distance measure, d, can then be calculated according to Bayes maximum likelihood classification as (Lee and Pottier 2009)

$$d_m(\langle[T]\rangle) = L\ Tr([T_m]^{-1}\langle[T]\rangle) + L\ ln([T_m]\ ) - ln(P[T_m]) + K \tag{2.18}$$

Thus leading to a minimum distance classification independent of the number of looks used to form the multi-looked coherency matrix $\langle[T]\rangle$ (Lee and Pottier 2009):

$$\langle[T]\rangle \in [T_m] \quad if \quad d_m(\langle[T]\rangle) < \ d_j(\langle[T]\rangle) \ \ \forall\, j \neq m \tag{2.19}$$

2.5.5. Decomposition Scattering Power Probabilities

The Y4O method splits total backscattering power into surface scattering (P_s), double-bounce backscattering (P_d), volume backscattering (P_v), and helix backscattering (P_c). Total backscattering power (TP) can be defined as

$$TP = P_s + P_d + P_v + P_c \tag{2.20}$$

With the help of (2.20), we can define the probability of surface backscattering and volume backscattering decomposed components as

$$\text{Probability of surface backscattering power,} \qquad p_s = \frac{P_s}{TP} \tag{2.21}$$

$$\text{Probability of volume backscattering power ,} \qquad p_v = \frac{P_v}{TP} \tag{2.22}$$

Therefore from (2.21) and (2.22)

$$-1 \leq \Delta p_{s-v} = p_s - p_v \leq 1 \tag{2.23}$$

Equation (2.23) helps us to determine the dominated scattering component from surface scattering and volume scattering in the Y4O method's decomposition image. If Δp_{s-v} is positive, we determine that surface scattering is the dominant contribution. On the other hand, if Δp_{s-v} is negative, we determine that volume scattering is the dominant contribution. The threshold does not begin from zero because we need to take into account the noise variation in case that both the probabilities are close to zero.

2.5.6 Classification Procedure Y4O$_w$

Using Y4O method and Complex Wishart Distribution (CWD), a supervised classification methodology has been presented for FULL-POL-SAR images classification, denoted as Y4O$_w$. The flow chart of developed methodology is shown in Fig. 2.4.

The sequence of this procedure is followed as:

1. First of all, a multi-looked (6 times in azimuth direction and 1 times in range direction) coherency matrix has been generated.
2. For reducing the speckle noise of the POL-SAR data, the polarimetrically refined Lee filter (Lee *et al.* 1999) with window size 7×7 has been applied on the coherency matrix.
3. The Y4O method has been applied on the de-speckled coherency matrix and Y4O method false color composite (FCC) image has been generated. In the FCC image of the Y4O method as shown in Fig. 2.5, red color is assigned to double-bounce scattering, green color is assigned to volume scattering, and blue color is assigned to surface scattering. Training samples have been allotted on the basis of visually comparing four-component color composite image with AVNIR-2 snow cover image and field information, resembling natural scenes rather closely.
4. CWD has been applied on de-speckled coherency matrix and computed for the averaged coherency matrices from the assigned classes. These computed mean matrices have been used as the class centers. All pixels are classified based on their Wishart distance measure and criteria ((2.18) and (2.19)) from class centers.

5. Finally based on conditional approach (2.24), as explained below, the probability difference (Δp_{s-v}) has been used for resolving volume scattering ambiguity from vegetation and glacier snow/ice.

   The conditional approach criteria (CAC) of Y4O$_w$ for improving the Wishart supervised classified map is defined as

$$\text{CAC} = \begin{cases} \text{Glacier snow/ice class IF } \Delta p_{s-v} \geq 0.05 \text{ and vegetation class ;} \\ \text{Wishart supervised classified classes OTHERW ISE} \end{cases} \quad (2.24)$$

   i.e. an additional class (glacier snow/ice class) has been added to the supervised classified image (Figure), where is, the probability difference (Δp_{s-v}) image has ≥0.05 value but the supervised classified image shows vegetation class. Otherwise Wishart supervised classified pixels remain same in the final improved classified image.

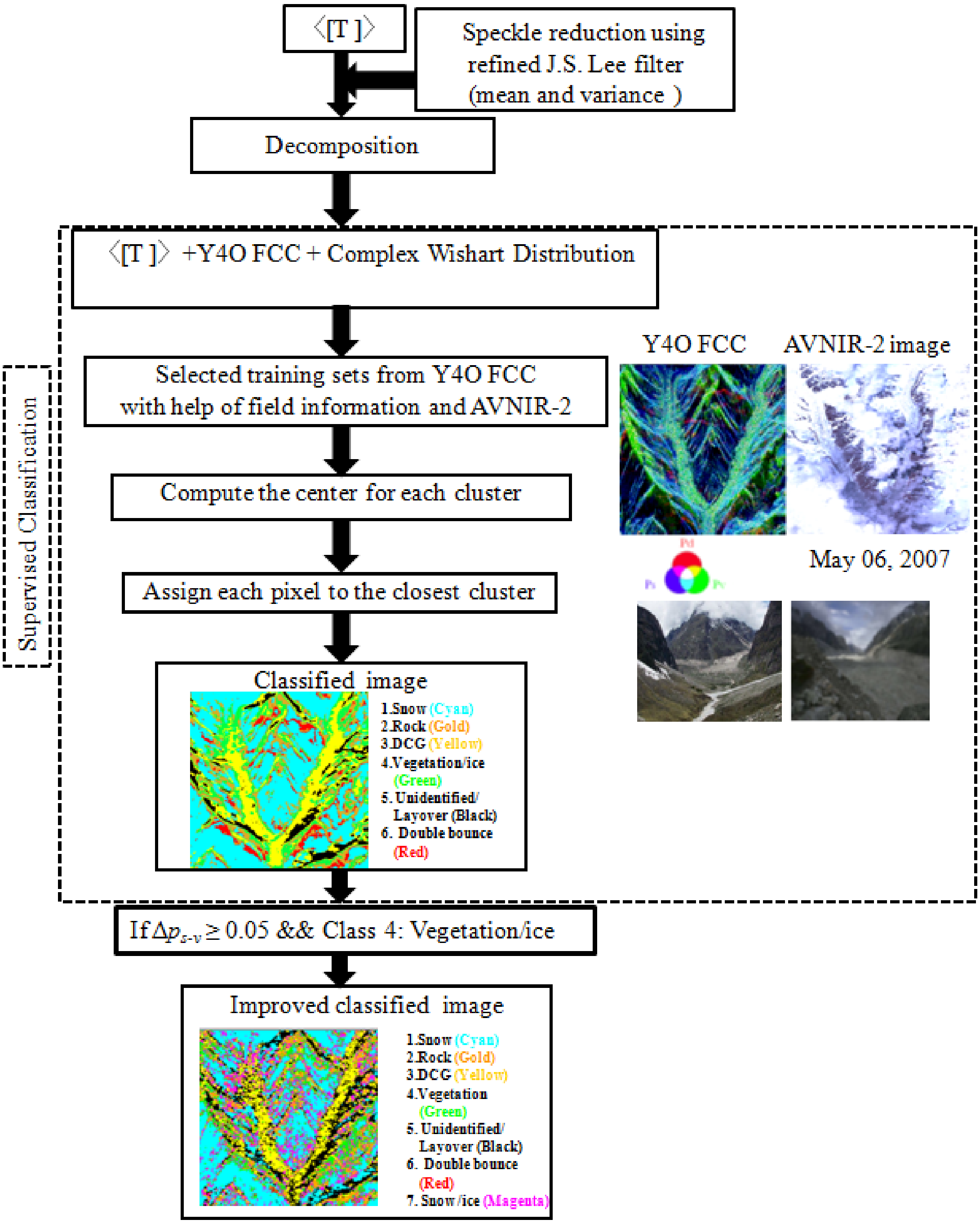

Fig.2.4. Flow chart of the Y4O$_w$ method for the POL-SAR image classification.

2.6. Results and Discussion

The FDD and Y4O plus the Y4O$_w$ methods have been applied on L-band PALSAR data over the Satopanth and Bhagirath Kharak glaciated region. FDD and Y4O methods False Color Composite (FCC) images are shown in Fig.2.5. For the FDD and Y4O methods, FCC images of PALSAR data over Satopanth glacier region (Fig. 2.5), the following color-coding scheme has been adopted: blue color represents surface scattering from snow cover over glacier area (accumulation zone) and permanent snow cover at mountains peaks; red color represents double-bounce or dihedral scattering mechanism; debris-covered glaciers (ablation area) are shown in green color. Glacier moraines dammed lakes appear in deep blue color.

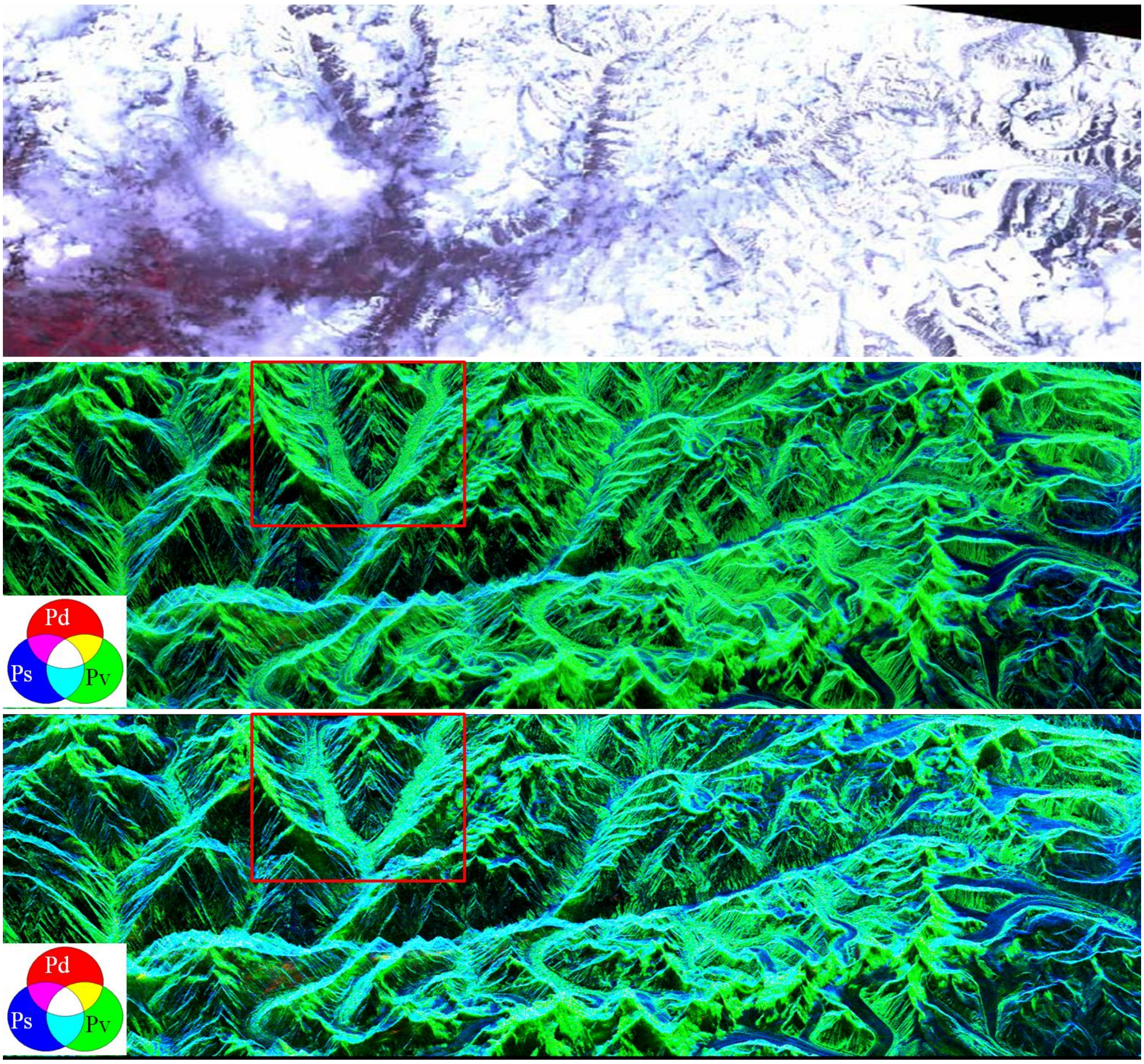

Fig.2.5. (**Upper**) ALOS-AVNIR-2 image of 6 May 2007. (**Middle**) FDD method FCC of 12 May 2007 PALSAR data. (**Bottom**) Y4O method FCC of 12 May 2007 PALSAR data. Enlarged view for red color rectangular on the Y4O and FDD methods FCCs are shown in Fig.2.6.

The comparison of visual interpretation has been done for both decomposition FCCs with the Pauli RGB (Fig. 2.2(b)) and AVNIR-2 (Fig.2.5) image. The differences are clearly seen between FDD and Y4O methods for the FCCs in Fig.2.6 (enlarged part of red color rectangular area in Fig. 2.5). Most of the differences can be visibly identified in double-bounce and surface scattering components; and these components are clearly exposed (Fig. 2.6(b)) in the FCC of the Y4O method. Some of these differences are indicated by yellow circles no. 1, 2 and 3 in Fig. 2.6(b) (FDD FCC) correspond to yellow color circles no. 1, 2 and 3 in Fig. 2.6(a) (FDD FCC), respectively. Furthermore, the Y4O method gives very sharp information about dihedral features in the study area as compared to FDD method and Pauli RGB images. Therefore, the fourth component of four-component scattering decomposition (Y4O) method represents the helical scattering phenomena, which occurs due to slope surface of target. It has been seen in Fig.2.7 that the helix (Pc) scattering component shows high value (greater than -10 dB) at steep slope and low values (less than -20 dB) are found over snow-covered area. The Himalayan topography has gentle to steep slopes, which behaves like oriented targets from the direction of radar; and an oriented target does not satisfy the reflection symmetry condition for which the FDD method works, which causes the over estimation of volume scattering in the FDD method. But for the Y4O method, volume scattering is reduced by the fourth component in which case volume scattering supersedes helix scattering. The main reason for the reduction of the volume component for the Y4O method is due to the reflection symmetric space where the Y4O method works. In other words, it corrects for rotation about the line of sight while it decomposes. Therefore, a Y4O method is suitable for fully polarimetric PALSAR data decomposition over Himalayan glaciated terrain as compared to the FDD method.

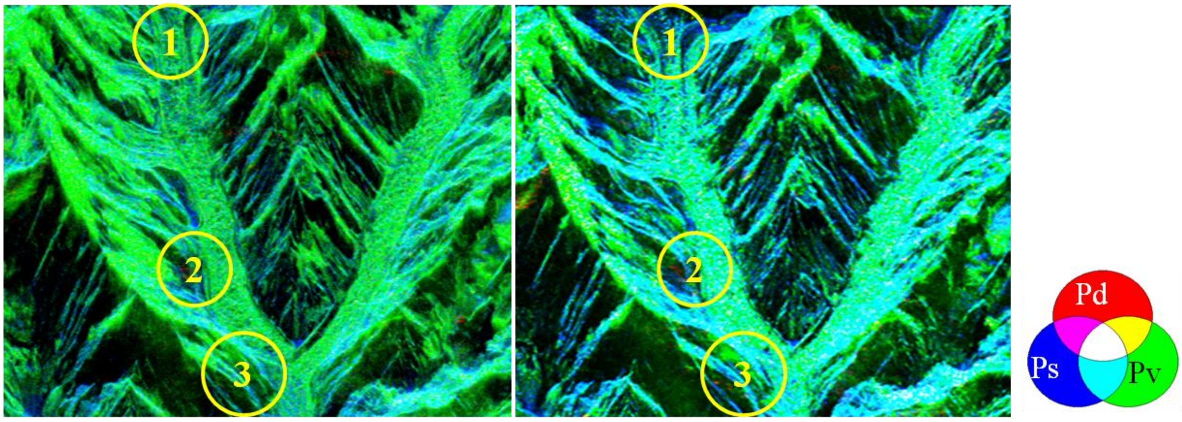

(a) (b)

Fig.2.6. (a) FDD method FCC of 12 May 2007 PALSAR data. (b) Y4O method FCC of 12 May 2007 PALSAR data.

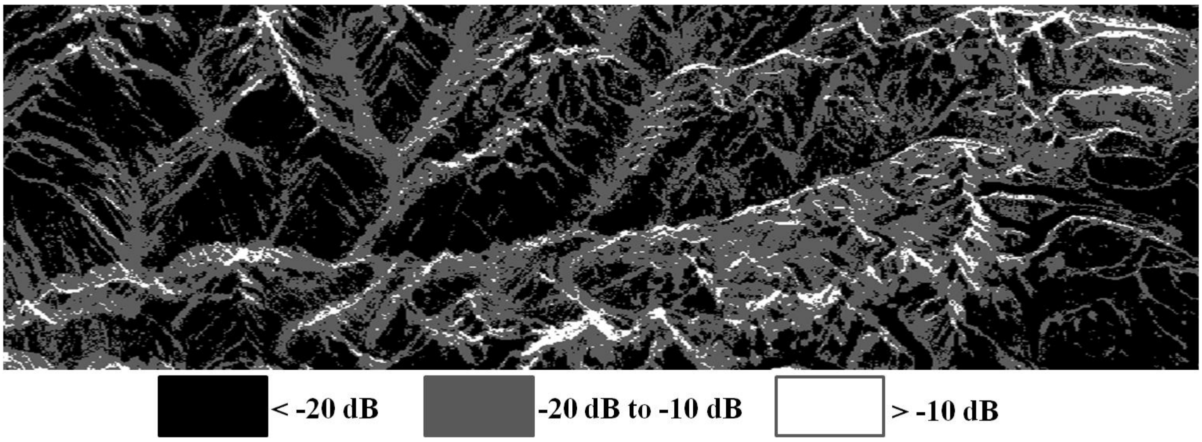

Fig. 2.7. Helix scattering (P_c) component of the Y4O for PALSAR image of 12 May 2007.

Moreover, using Wishart supervised classification scheme, ALOS-PALSAR data was classified into six major classes (e.g. snow, non-snow and unidentified/layover, Fig. 2.8). The most common tool used for assessing the classification accuracy is the confusion (or error) matrix (Table 2.1). The columns in a confusion matrix (Table 2.1) represent test data that have been collected via field observation and interpretation of Y4O method FCC and ALOS-AVNIR-2 images, while rows represent the labels assigned by the classifier. The main diagonal entries of the Table 2.1 represent the number of pixels that are correctly classified. By this way, overall classification accuracy has been found to be 93.38%, but vegetation class from glacier snow/ice could not discriminated properly by using alone complex Wishart classifier with defined training samples. Therefore, new $Y4O_w$ classification procedure was developed and applied on coherency matrix to improve Wishart supervised classification results. The $Y4O_w$ classification method introduces the utilization of the probability difference image (Δp_{s-v}) images of the model-based decomposition method (e.g. Y4O) for separating the misclassified classes properly. The probability difference image shows low value over vegetation area and high value over glacier snow/ice area. By using the $Y4O_w$ classification technique, it is possible to resolve the ambiguity between vegetation class (Fig.2.8) and glacier snow/ice (Fig. 2.9).

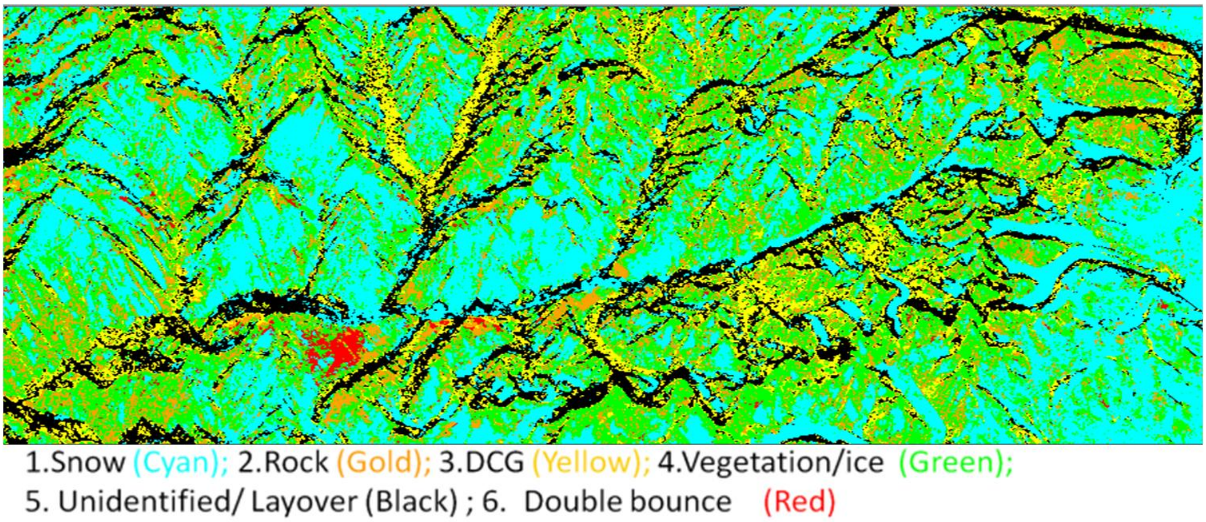

Fig.2.8. PALSAR classified image of 12 May 2007.

Table 2.1. A confusion (or error) matrix composed of six glaciated terrain classes (the number of pixels in percent belonging to the test area).

	Snow	Rock	DCG	Double-bounce /Settlement	Vegetation/ice	Layover
Snow	**98.55**	0.33	0.36	0.00	0.43	0.32
Rock	5.26	**79.25**	0.00	1.45	14.04	0.00
DCG	0.00	0.00	**86.58**	0.00	2.24	11.18
Double-bounce/Settlement	0.00	8.75	0.00	**89.96**	1.28	0.00
Vegetation/ice	0.00	12.60	5.91	0.00	**81.14**	0.35
Layover	0.00	0.00	4.14	0.00	0.00	**95.38**
Overall Accuracy = 93.38%						

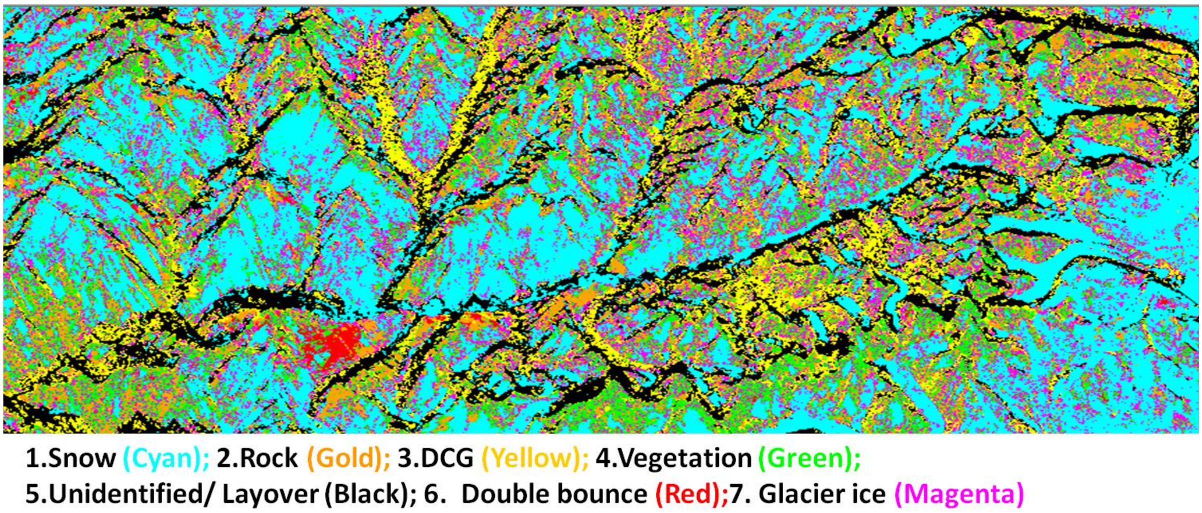

Fig.2.9. Vegetation and ice separating in PALSAR classified image of 12 May 2007 by using probability difference between surface scattering and volume scattering probabilities.

2.7. Summary and Conclusions

In this Chapter 2, fully polarimetric PALSAR data sets of high altitude glaciated terrain in Himalayan region have been analyzed based on the FDD and Y4O methods and information of various terrain features have been extracted. It has been found that the Y4O method discriminates better terrain features such as snow cover, dihedral (double-bounce) and glacier features as compared to the FDD method.

Moreover, Wishart supervised classification and proposed Y4O$_{w}$ classification techniques have been implemented. The Wishart supervised classification procedure shows over all accuracy 93.38%, but the ambiguity of separating the vegetation from glacier snow/ice has been also found in classified image. However, the ambiguities for separating the vegetation area from glacier snow/ice areas are well resolved by implemented Y4O$_{w}$. In future work, this methodology will be assessed with more time series data to check the resolving capability of the ambiguity between vegetation and glacier snow/ice. Finally, the Y4O$_{w}$ can also be optimized and/or improved by introducing the Δp_{s-v} form the Y4R (Chapter 3), S4R (Chapter 4), S3H (Chapter 5), and G4U (Chapter 6) decomposition methods for the Y4R$_{w}$, S4R$_{w}$, S4R$_{w}$, S3H$_{w}$, and G4U$_{w}$ methods, respectively. These optimized methods (Y4R$_{w}$, S4R$_{w}$, S4R$_{w}$, S3H$_{w}$, and G4U$_{w}$) will be evaluated in near future work.

Chapter 3 Evaluation of Modified Four-Component Scattering Power Decomposition Y4R Method over Highly Rugged Glaciated Terrain

Science is bound by certain laws of the Nature

3.1 Abstract

In recent years, there has been increased utilization of FULL-POL-SAR data to study glaciated terrain features for glaciological and climate change modeling. This chapter is concerned with more accurate results and an appropriate analysis of POL-SAR data over a highly rugged glaciated area of the Himalayan region. For this purpose, the modified Yamaguchi four-component scattering power decomposition method Y4R with a rotation concept of the 3 × 3 coherency matrix $\langle[T]\rangle$ about the line of sight is evaluated. It has been found that the modified Yamaguchi four-component scattering power decomposition (Y4R) method significantly improved the decomposition results as compared to Y4O by minimizing the cross-polarized (*HV*) components. This Y4R leads to enhancement in the double-bounce scattering and surface scattering components and also avoids the overestimation problem in the volume scattering component as compared to the Y4O and Y4O_w from the sloped terrain. The significant reductions of the negative power occurrence in the surface scattering (3.9%) and the double-bounce scattering (19.7%) components have also been noticed as compared with the Y4O method over the glaciated area in the selected part of the Indian Himalaya.

3.2. Introduction

Detection of glaciated terrain features are important for hydrological and climate change modeling. Optical and near-infrared remote sensing techniques are very sensitive to cloud cover and different weather conditions, although they are promising for glaciated terrain mapping (Dozier 1989; Mohite *et al.* 2007; Rott 1994). MRS using active sensing with SAR has advantages such as cloud penetration, all-weather capability and quasi independence of sun illumination. SAR information adds considerable robustness to identify the glaciated terrain (Singh and Venkataraman 2008; Singh *et al.* 2011) and potentially allows the retrieval of additional snow parameters associated with surface roughness and wetness, as well as internal snow structure and glacier movement (Michal and Rignot 1999; Partington 1998; Shi and Dozier 1995; Shi and Dozier 2000). Fully polarimetric capabilities of newer generation space-borne SAR sensors are expected to lead to significant improvements in an automated glaciated terrain feature identification method based on the polarimetric scattering decomposition method (Singh 2010; Singh and Venkataraman 2012; Singh *et al.* 2008; Singh *et al.* 2013a). The main purpose of implementing scattering decomposition methods is to extract different scattering contributions in the polarimetric backscattering signature within the resolution cell. POL-SAR data decompositions are also important to interpret or segment the glaciated terrain features and to develop the methodology for the retrieval of glacier parameters.

Several incoherent decomposition methods were published (Cloude and Pottier 1996; Freeman and Durden 1998; Yajima *et al.* 2008; Yamaguchi *et al.* 2005), of which several incoherent decomposition methods and scattering power decomposition methods are attractive. These methods (Freeman and Durden 1998; Yajima *et al.* 2008; Yamaguchi *et al.* 2005) provide straightforward implementation of which the decomposition scattering powers correspond to physical scattering mechanisms and the corresponding output color-coded images are directly recognizable and easy to understand as discussed in previous Chapter 2. Mountainous region topography has gentle to steep slopes, which behave like oriented surface as seen from the direction of radar illumination, and oriented surface do not suffice the reflection symmetry condition for which the FDD method works, which then causes the overestimation of volume scattering in the FDD. It was expected that the overestimated volume scattering power is reduced by the fourth component in the Y4O method subject to the non-reflection condition (Singh *et al.* 2011). However, it has been found that the Y4O still does not eliminate over estimation in the volume scattering power (Singh *et al.* 2010). Hence, this chapter presents the results by using further modification of the Y4R method on glaciated terrain features as evaluated for the Satopanth glacier region in Himalaya (Yamaguchi *et al.* 2011). It is shown that improvement can be clearly verified for the highly rugged glacier region.

3.3. Study Area and Data Used

Satopanth and Bhagirath Kharak (BK) glaciers are the main glacier system of the Alaknanda river catchment, Uttarakhand, India. The elevation ranges between 2000 m and 7000 m. The Alaknanda river, which is the main tributary of the Ganga (*Ganges*) river, originates at the snout of the Satopanth glacier. The area is located between latitude 30^0 40’ N and 30^0 50’ N and longitude between 79^0 15’ E and 79^0 28’ E. Satopanth and Bhagirath Karak glaciated region, for which details are given in previous Chapter 2, Section 2.3.

In this Chapter 3, the fully polarimetric PALSAR, single look complex, level 1.1 data of May 12, 2007 with 21.5^0 off-nadir angle of incidence and nominal pixel spacing (azimuth × range) 3.54m × 9.36m has been used (www.eorc.jaxa.jp/ALOS/en/about/palsar.htm; www.palsar.ersdac.or.jp/e/index.html). The data sets have been multi-looked six times in azimuth direction and one time in range direction for generating the coherency matrix elements. After generating the multi-looked coherency matrix, speckle noise was reduced by using the refined Lee filter (Lee and Pottier 2009) with a window size of 5×5.

The Snow-covered area becomes wet in May (early summer) over the Himalayan snow bound area with significant melting, and the wet snowpack is no longer transparent for the L-band frequency (Singh *et al.* 2011). The co-polarization backscatters (*HH* and *VV*) responses are nearly 10 times larger than the cross-polarization backscatter (*HV* or *VH*) responses (Singh 2010). Since the *HV* components contribute to volume scattering power in the Y4O and Y4R, the main polarimetric response of the Y4O, $\mathrm{Y4O_w}$ and/or Y4R, $\mathrm{Y4R_w}$ ($\mathrm{Y4R_w}$ is an optimization of $\mathrm{Y4O_w}$ with Y4R method) from snowpack will lead to surface scattering components in the L-band (Abe *et al.* 1990; Singh *et al.* 2011).

3.4. Method and Technique

3.4.1 Y4O

As seen in Section 2.5 of Chapter 2, the measured coherency matrix can be expanded into four sub-matrices which correspond to surface scattering, double-bounce scattering, volume scattering, and helix scattering mechanisms. The expression of Y4O is given in equation (1.6) in Section 2.5 of Chapter 2.

3.4.2 Concept of $\langle[T]\rangle$ Rotation

Himalayan topography has gentle to very steep slopes, and these slopes vary in azimuth as well as in range direction. In general, an appreciable distortion occurs in backscattering encountered for the Himalayan region as compared with the horizontal flat surface. It is pointed out (Lee *et al.* 2000; Lee *et al.* 2002) that the polarization orientation shift (or, equivalently, the cross-polarized component S_{HV}) is induced due to the azimuthally sloped surface. In addition, the amount of the induced polarization orientation shift is a function of the radar look angle and slope angle in range direction. These effects in highly topographically irregular surfaces can be reduced with the help of polarization orientation compensation or minimization of the cross-polarized component. Since the T_{33} element of coherency matrix is synonymous with the cross-polarized component S_{HV} in the coherent Sinclair scattering matrix, a method of rotating the coherency matrix to minimize its T_{33} element has been adopted. The idea of minimization of the T_{33} element is also known as Deorientation (Huynen 1970; Xu and Jin 2005)

A general form of rotation of the coherency matrix about the radar line of sight can be written as (Yamaguchi *et al.* 2011)

$$\langle [T\ (\theta)] \rangle = \begin{bmatrix} 1 & 0 & 0 \\ 0 & \cos 2\theta & \sin 2\theta \\ 0 & -\sin 2\theta & \cos 2\theta \end{bmatrix} \langle [T\ ] \rangle \begin{bmatrix} 1 & 0 & 0 \\ 0 & \cos 2\theta & -\sin 2\theta \\ 0 & \sin 2\theta & \cos 2\theta \end{bmatrix} \tag{3.1}$$

The rotated coherency matrix (Yamaguchi *et al.* 2011) is denoted as

$$\langle [T\ (\theta)] \rangle = \begin{bmatrix} T_{11}(\theta) & T_{12}(\theta) & T_{13}(\theta) \\ T_{21}(\theta) & T_{22}(\theta) & T_{23}(\theta) \\ T_{31}(\theta) & T_{32}(\theta) & T_{33}(\theta) \end{bmatrix} \tag{3.2}$$

where

$$T_{33}(\theta) = T_{33}\cos^2 2\theta + T_{22}\sin^2 2\theta - \mathrm{Re}(T_{23})\sin 4\theta. \tag{3.3}$$

An attempt has been made to minimize the $T_{33}(\theta)$ term by rotation (Yamaguchi *et al.* 2011). The rotation angle can be found from

$$\frac{d}{d\theta} T_{33}(\theta) = 0 \tag{3.4}$$

$$\tan 4\theta = \frac{4\mathrm{Re}\langle S_{HV}^{*}\ \ (S_{HH} - S_{vv}) \rangle}{\langle |S_{HH} - S_{vv}|^2 \rangle - 4\langle |S_{Hv}|^2 \rangle} = \frac{4\mathrm{Re}\langle S_{HV}^{*}\ \ (S_{HH} - S_{vv}) \rangle}{\langle |S_{HH} - S_{vv}|^2 \rangle - 4\langle |S_{Hv}|^2 \rangle} \tag{3.5}$$

$$2\theta = \frac{1}{2}\tan^{-1}\left(\frac{2\mathrm{Re}\ \{T_{23}\}}{T_{22} - T_{33}} \right) \tag{3.6}$$

This rotation angle is the same as the phase angle between two co-circular (left-left and right-right) polarization channels used to estimate azimuthal slope angle (Krogager and Boerner 1996; Lee and Pottier 2009). Thus, the minimization of the $T_{33}(\theta)$ element yields the same angle.

After this rotation (3.1), the elements of the coherency matrix become

$$T_{11}(\theta) = T_{11}$$

$$T_{12}(\theta) = T_{21}^{*}(\theta) = T_{12}\cos 2\theta + T_{13}\sin 2\theta$$

$$T_{13}(\theta) = T_{31}^{*}(\theta) = T_{13}\cos 2\theta - T_{12}\sin 2\theta$$

$$T_{22}(\theta) = T_{22}\cos^2 2\theta + T_{33}\sin^2 2\theta + \mathrm{Re}(T_{23})\sin 4\theta$$

$$T_{23}(\theta) = T_{32}^{*}(\theta) = j\ \mathrm{Im}\ \{T_{23}\}$$

$$T_{33}(\theta) = T_{33}\cos^2 2\theta + T_{22}\sin^2 2\theta - \mathrm{Re}(T_{23})\sin 4\theta. \tag{3.7}$$

The angle in (3.6) will serve for more accurate decomposition results over highly topographically irregular mountainous areas in comparison with the original coherency matrix method (Yajima *et al.* 2008; Yamaguchi *et al.* 2006). It is understood by virtue of the diagonal terms that $T_{33}(\theta)$ decreases by $\mathrm{Re}(T_{23})\sin 4\theta$ and that $T_{22}(\theta)$ increases by the same amount, while $T_{11}(\theta)$ remains the same. It should be noted that $T_{23}(\theta)$ becomes purely imaginary which exactly fits the helix scattering model for the non-reflection symmetry condition (Yamaguchi *et al.* 2005) as a roll-invariant parameter (Huynen 1970; Lee and Ainsworth 2011). The Y4O method with the rotation of coherency matrix, denoted as Y4R, was used hitherto for POL-SAR data decomposition more frequently.

3.4.3 Yamaguchi Four-Component Decomposition with Rotation of Coherency Matrix (Y4R)

After the rotation of the measured coherency matrix, the Y4O method is applied to the rotated coherency matrix (3.1) for obtaining the improved results of POL-SAR data decomposition. The expression of Y4R (after deorientation in POL-SAR measurements) is expressed as

$$\langle[T\ (\theta)]\rangle = f_s\langle[T]\rangle_{\text{surface}} + f_d\ \langle[T]\rangle_{\text{double}} + f_v\ \langle[T]\rangle_{\text{vol}} + f_c\langle[T]\rangle_{\text{helix}} \tag{3.8}$$

where f_s, f_d, f_v and f_c are coefficients to be determined. The expansion coherency matrices $\langle[T]\rangle_{\text{surface}}$, $\langle[T]\rangle_{\text{double}}$, $\langle[T]\rangle_{\text{vol}}$ and $\langle[T]\rangle_{\text{helix}}$ are same as of Section 2.5 in Chapter 2. The Y4R algorithm in terms of rotated coherency matrix elements is shown in the flow-chart of Fig. 3.1 (Yamaguchi 2007).

3.5 Results and Discussion

First, the Y4O method (Yamaguchi *et al.* 2006) is applied to L-band PALSAR data sets over the Satopanth and BK glaciated region. The decomposition powers of surface scattering (P_s), double-bounce scattering (P_d), volume scattering (P_v) and helix scattering (P_c) are shown in Fig. 3.2.

In order to examine the decomposition results of Fig. 3.2 quantitatively, the elevation map in this area is shown in Fig. 3.3(a), the slope angle map in Fig. 3.3(b) and aspect (direction of slope) in Fig. 3.3(c), respectively. These topographic parameters are derived based using the on Advanced Space-borne Thermal Emission and Reflection Radiometer - Global Digital Elevation Map (ASTER-GDEM) with 30-m resolution (www.gdem.aster.ersdac.or.jp).

The angle derived by (3.6) is shown in Fig. 3.3(d). The rotation angle varies from -45^0 to +45^0. Noisy angle distributions have been seen in steep slope areas. The reason why we have prepared Fig. 3.3(d), is to examine a relation between the angle and negative power problem.

Percentages of pixels with negative powers in surface scattering (P_s) and double-bounce scattering component of the Y4O method become 11.6% and 29.5%, respectively. It is seen in surface scattering (P_s) of Fig. 3.2(a) that the occurrences of negative power (black color) are less where slopes are gentle and that the negative power occurrences are more pronounced at steep slopes. Most of negative powers in P_s occurred on the back side of the slope area (N-E and S-E facing slope), i.e. in the radar shadowing area.

On the other hand, for the double-bounce power (P_d) image of Fig. 3.2(b), most of negative powers appear (black color) in the layover region yielding noisier images. The volume (P_v) and helix (P_c) scattering components are dominated at steeper slope fore-slope area (N-W and

S-W facing slope) and low values are found over snow-covered area and back slope areas (Fig. 3.2(c) and Fig. 3.2(d)), respectively.

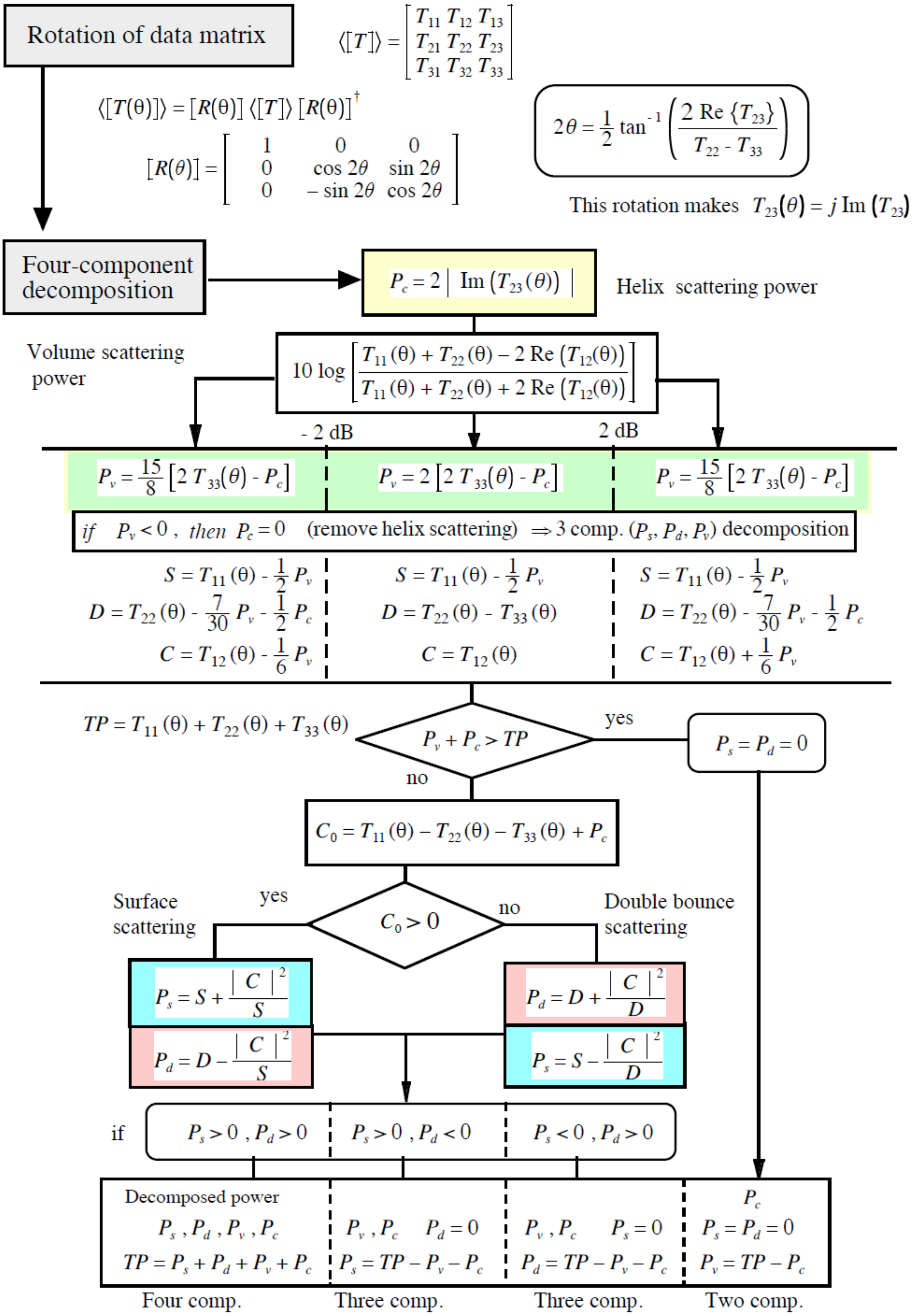

Fig.3.1 Four-component scattering power decomposition algorithm using rotated coherency matrix for Y4O => Y4R.

Then the resulting Y4R method (Yamaguchi *et al.* 2011) is applied to the same area in order to see the effect of the rotation (Fig.3.4). This method reduces the percentages of pixels with negative powers in Ps and Pd. Pixels with negative power in Ps and Pd remained at 7.7% and 9.8%, respectively. It can be noticed subject to T_{33} rotation that the negative power occurrences are reduced 3.9% in Ps (Fig. 3.4(a)) and 19.7% in Pd (Fig. 3.4(b)) by the modified method Y4R as compared to original method Y4O.

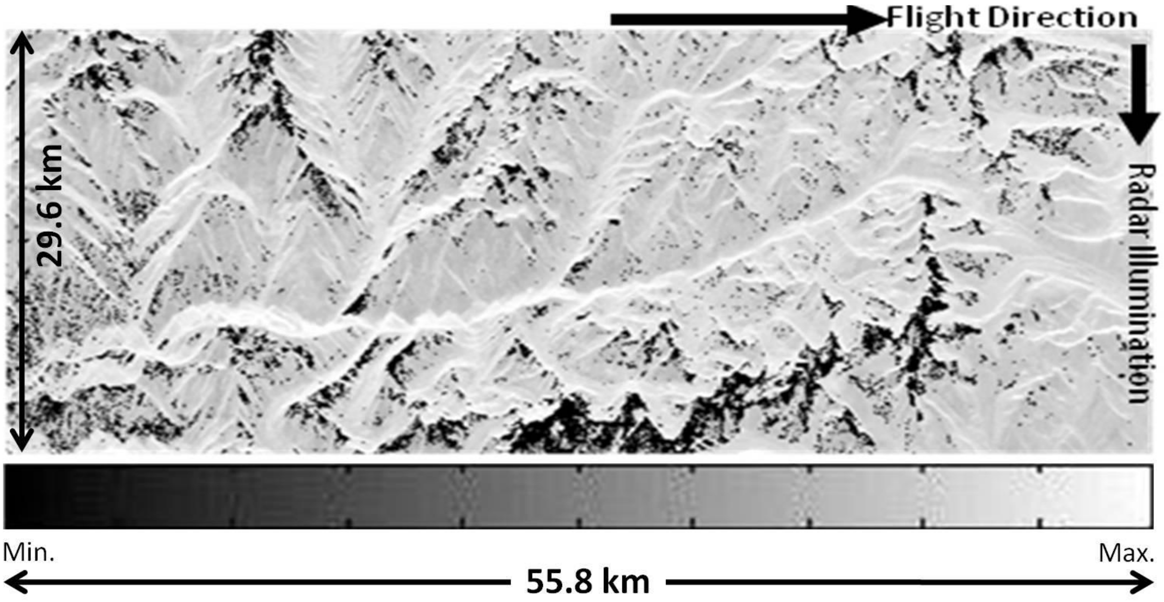

(a)

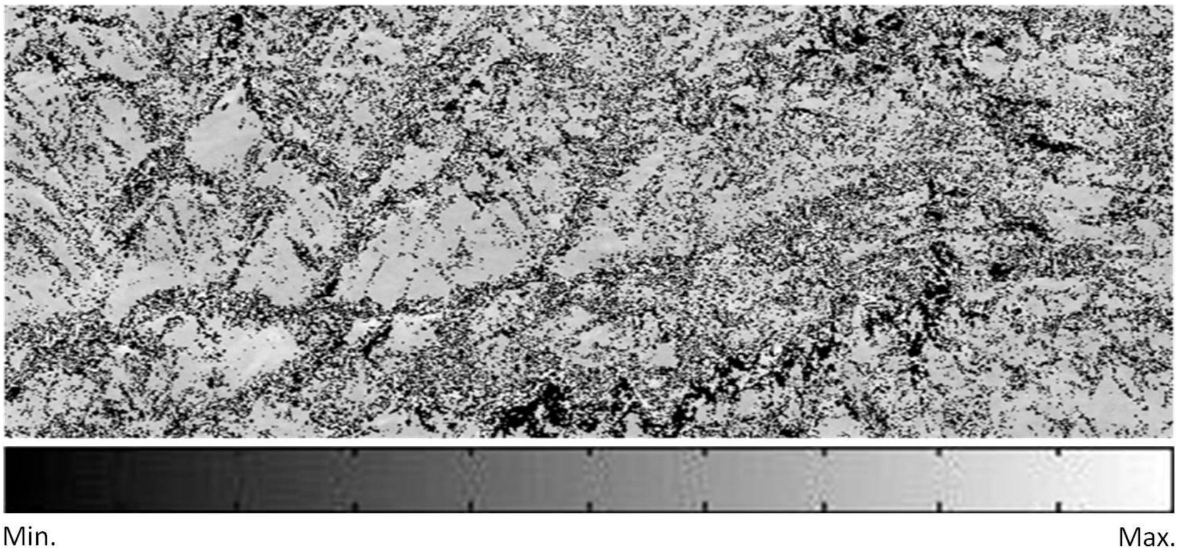

(b)

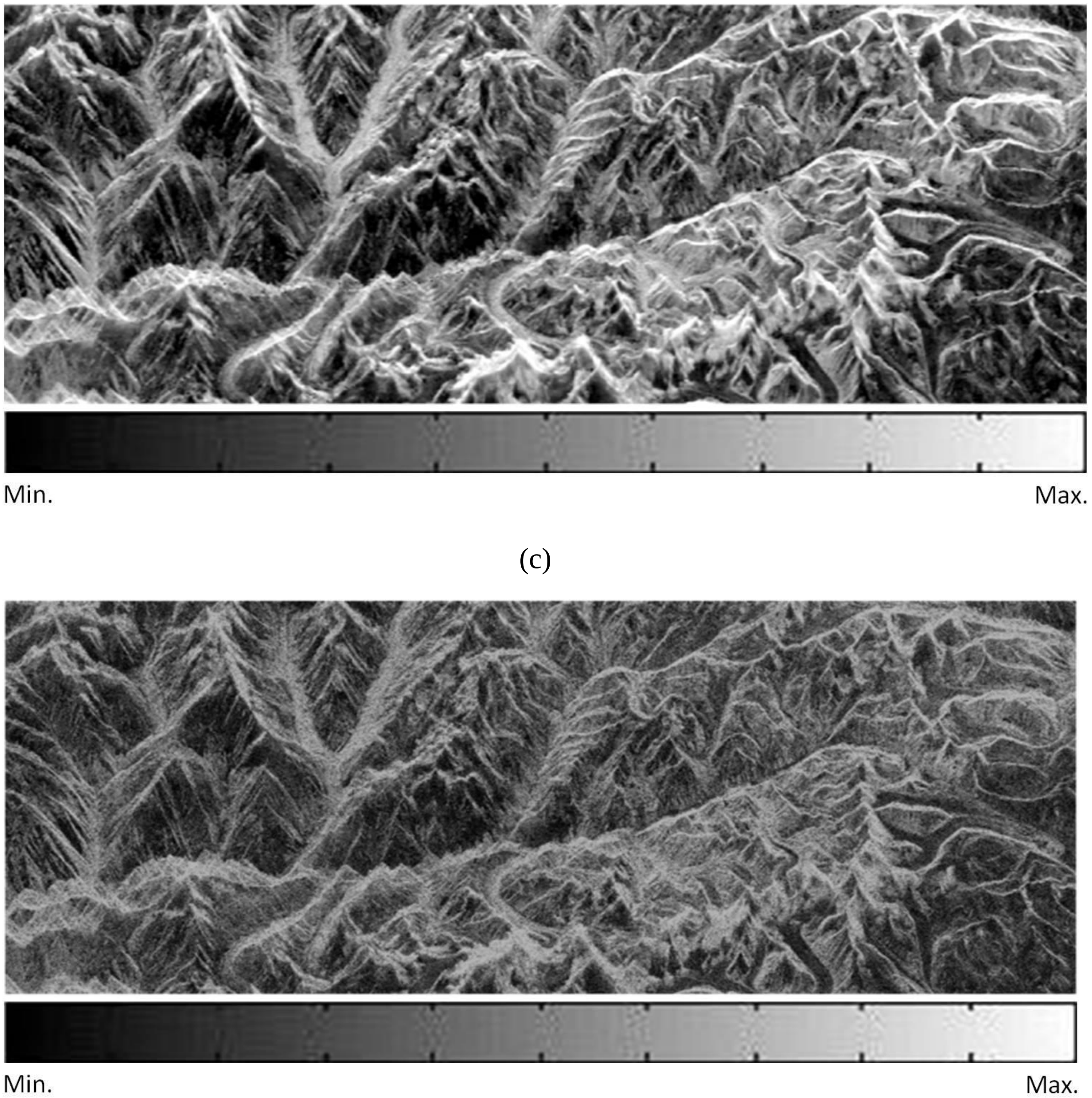

(c)

(d)

Fig. 3.2. Original Y4O method decomposed powers (a) P_s, (b) P_d, (c) P_v, and (d) P_c. Black areas are 11.6% in P_s image (a) and are 29.5% in P_d image (b), respectively; indicating that negative power occurred in the respective pixels.

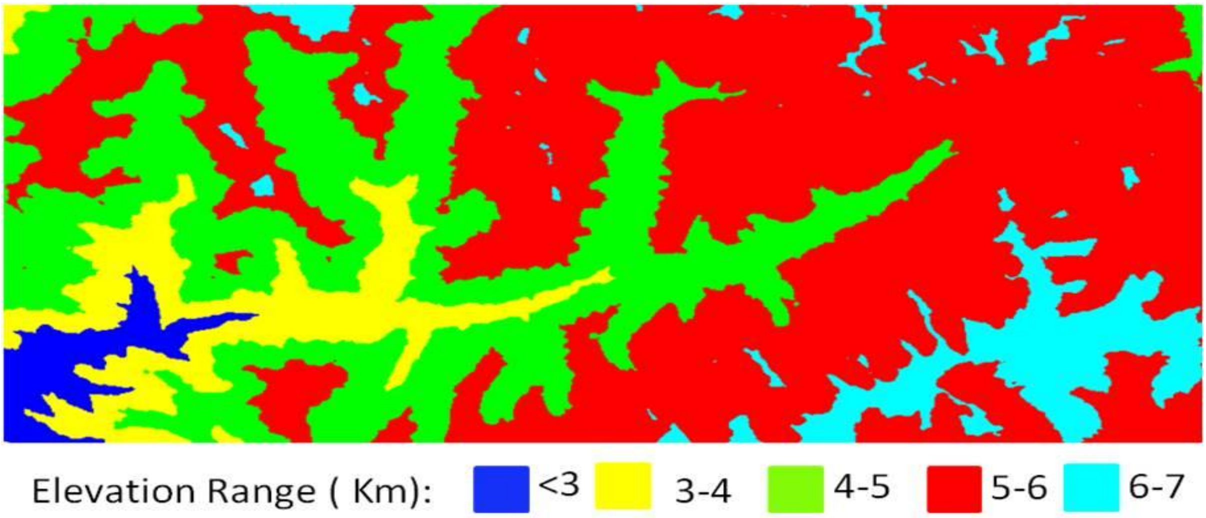
Elevation Range (Km):
<3
3-4
4-5
5-6
6-7

(a)

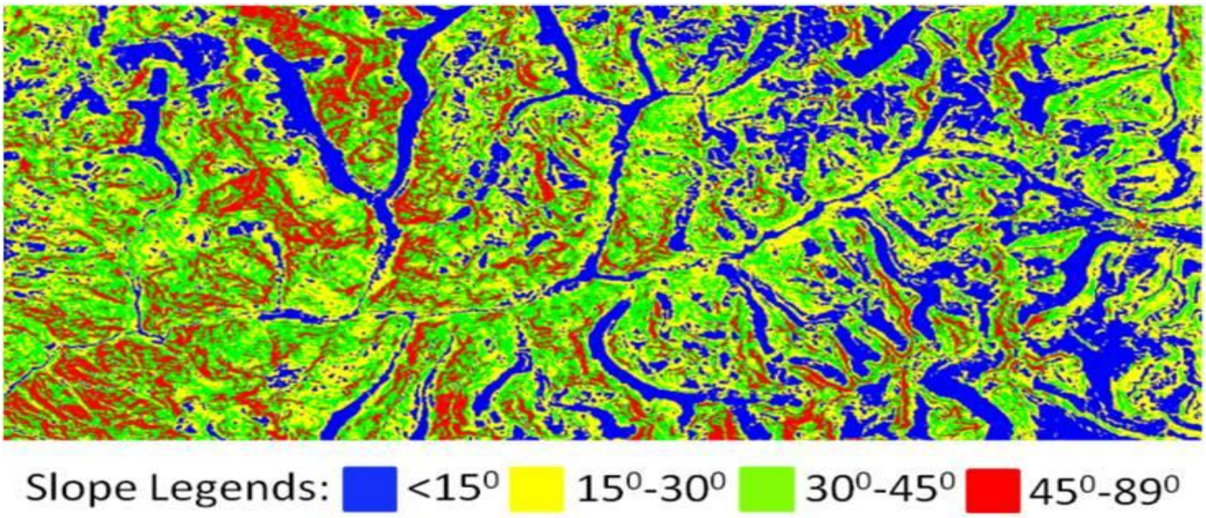
Slope Legends:
<15⁰
15⁰-30⁰
30⁰-45⁰
45⁰-89⁰

(b)

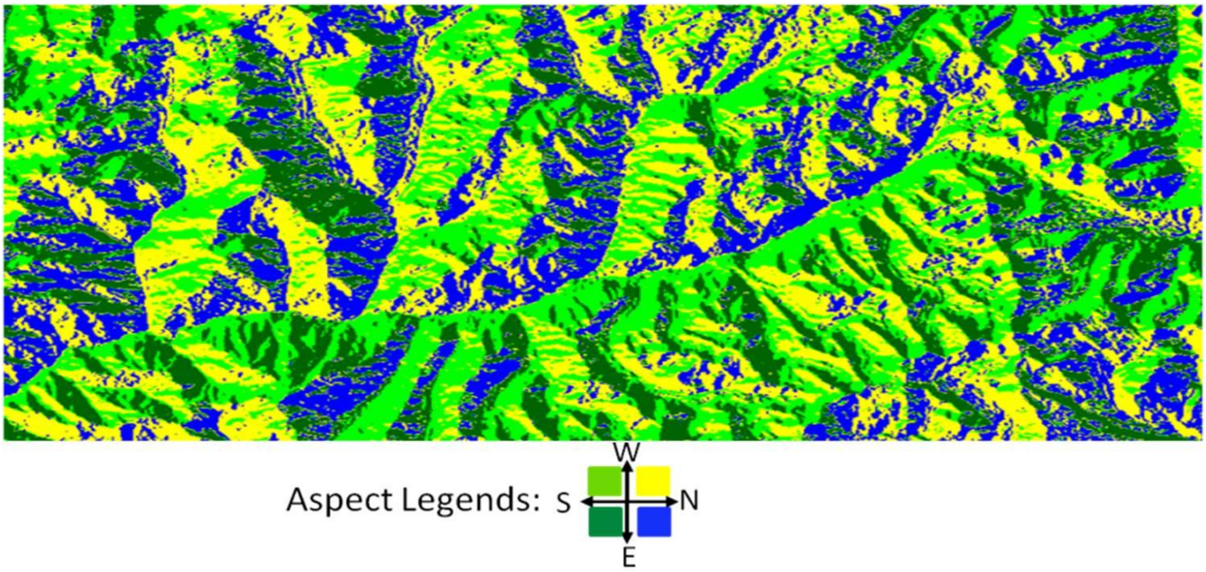
Aspect Legends:
W
S
N
E

(c)

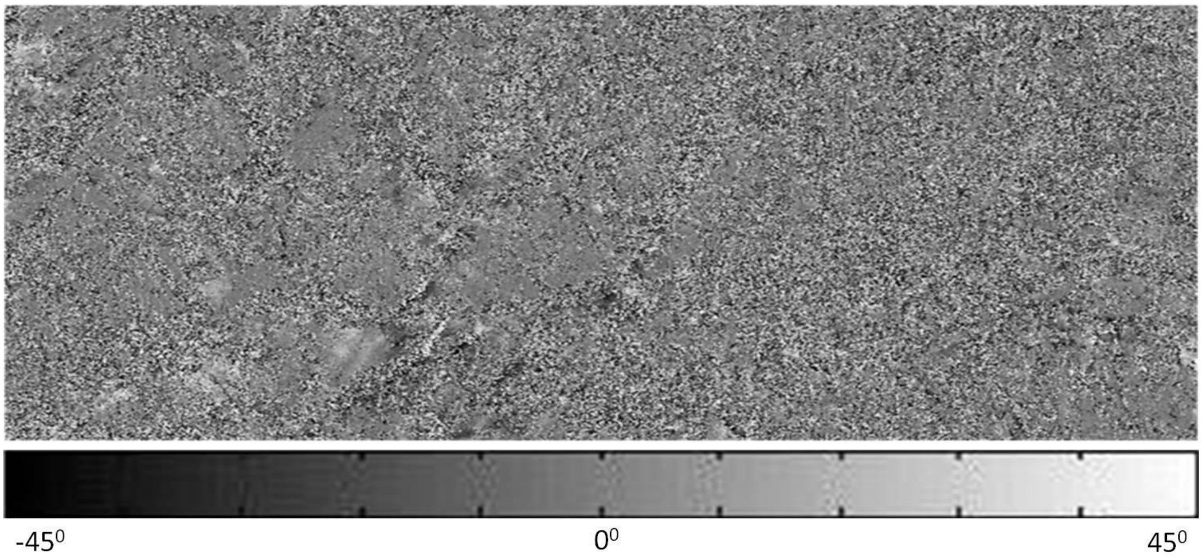

(d)

Fig. 3.3 (a) ASTER-GDEM. (b) Slope map. (c) Aspect (direction of slope). (d) Noisy rotation angle, derived by (3.6), at steep slope areas.

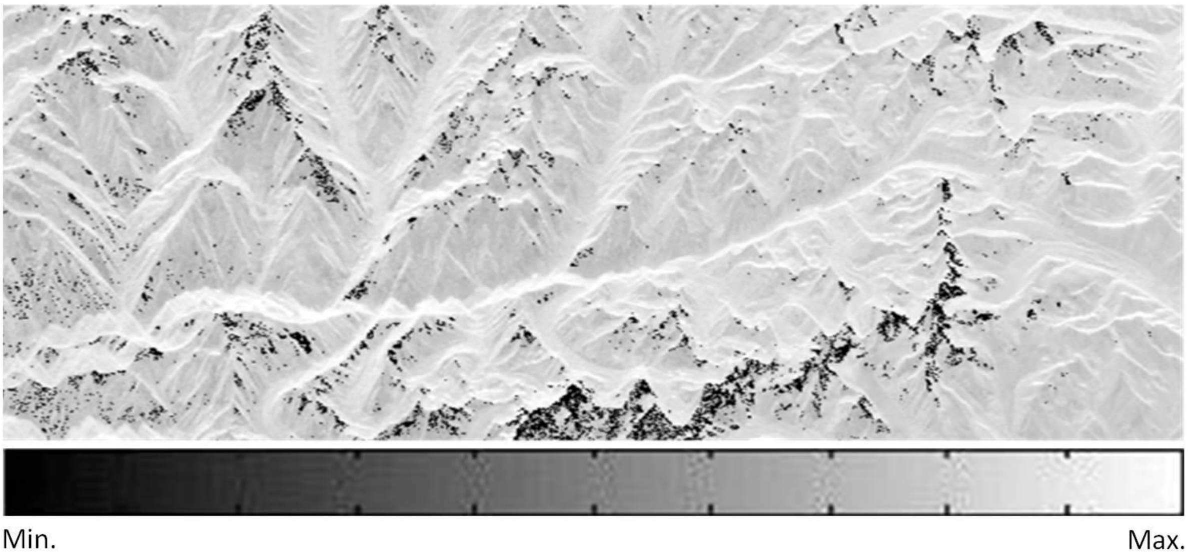

(a)

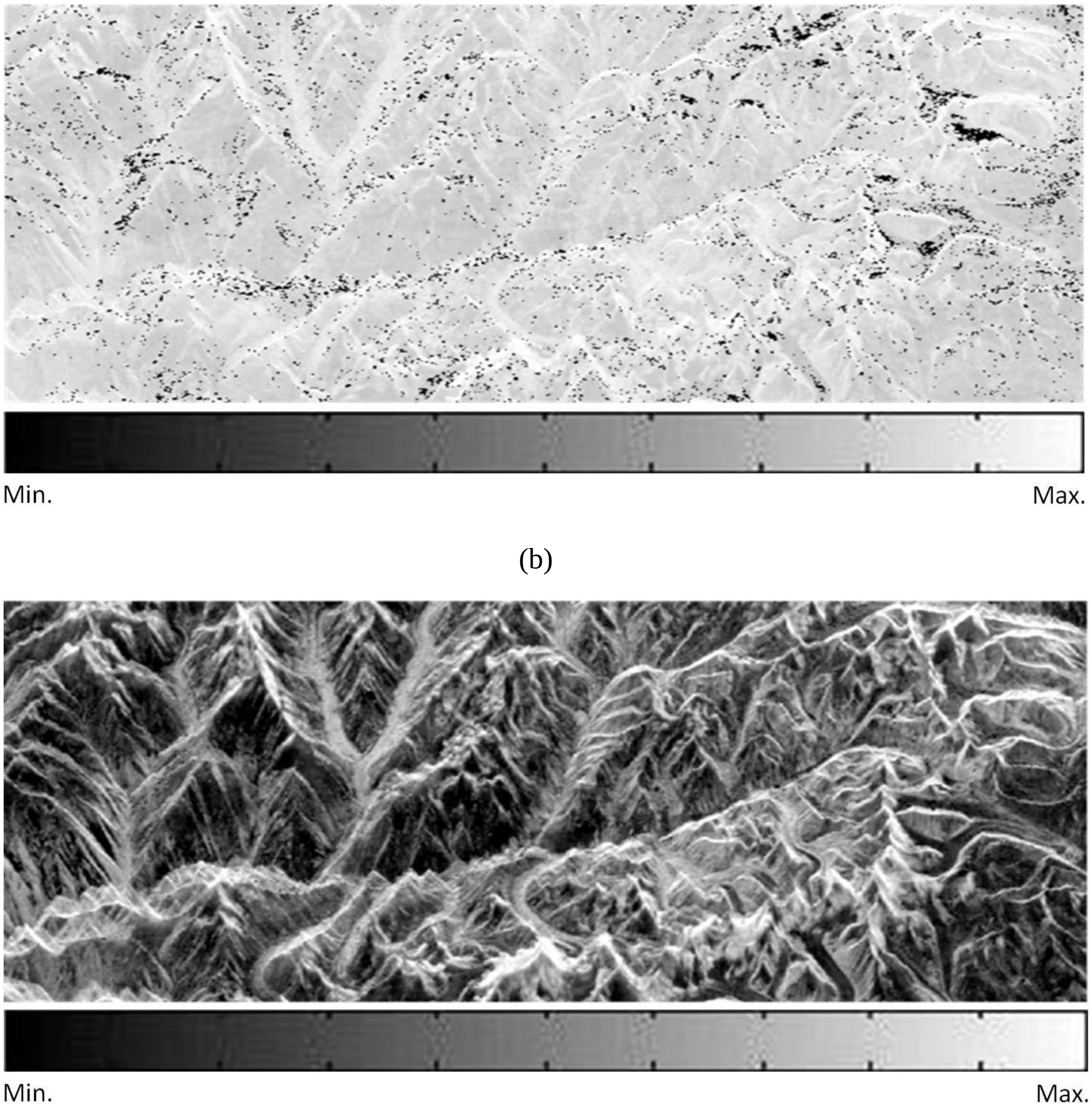

(b)

(c)

Fig. 3.4. Y4R method component powers (a) P_s (b) P_d (c) P_v. Black areas in P_s image are 7.7% and in P_d image are 9.8%, which indicate that negative power occurred in respective pixels.

The decomposition power profiles are shown in Fig.3.5 (a)-(c), along a transect over the Satopanth glacier valley (see the transect in Fig. 3.5(a), 501 pixels profile on Y4R with FCC image in yellow color) for quantitative comparison of the original Y4O method *vs.* the modified Y4R method. The ablation area of glaciers is highly crevassed and covered with moraine and debris material, which constitutes a very rough surface and generates multiple scattering; and this property displays high values of P_v in the respective profile.

In these profiles, values of less than -20dB represent the negative power occurring pixels. Significant improvement in the negative power problem can be seen in Fig. 3.5 subject to the rotation of the coherency matrix. Since Himalayan topography has gentle to steep slope, which behave like oriented surface from the direction of radar illumination that causes the over estimation volume scattering in the original Y4O method. But the modified Y4R method compensates for the orientation changes along the line of sight while it decomposes the POL-SAR data. The value of P_v is decreasing over the Satopanth glacier area, which is consistent with other experimental evidence (Yamaguchi *et al.* 2011) avoiding over-estimation of the cross-polarized component. The values of P_s and P_d components increase after rotation and are not fluctuating compared to the original case. Since the imaginary part T_{23} is roll-invariant (Lee and Ainsworth 2011) which is main source of the helix power P_c in Y4O (Yamaguchi *et al.* 2006). Therefore, the value of Pc remains unchanged in the modified Y4R decomposition results. In addition, it can be seen that some of negative powers also appear after rotation (7.7% in P_s image and 9.8% in P_d image). These observations are inconsistent with the prevailing physical phenomena. Even though there are significant improvements in reduction of negative powers, it is difficult to avoid elimination of all negative powers by the modified method Y4R. The conditions of negative power occurrence in Y4O are described in Yajima *et al.* (2008).

Furthermore, the technique of Yajima *et al.* (2008) has been adopted to avoid the remaining negative powers in decomposition results before making FCC images. These RGB false color composite images with surface scattering (Blue), double-bounce scattering (Red), and volume scattering (Green) are shown in Fig.3.6. In general, RGB false color composite images over Satopanth glacier region represent blue to deep blue color due to single scattering from snow cover over glacier areas (accumulation zone) and permanently snow-covered mountain peak areas. Red color represents double-bounce or dihedral scattering mechanism. The DCG (ablation area) corresponds to green color area, where as dam-lakes of glacier moraines are elucidated in deep blue color.

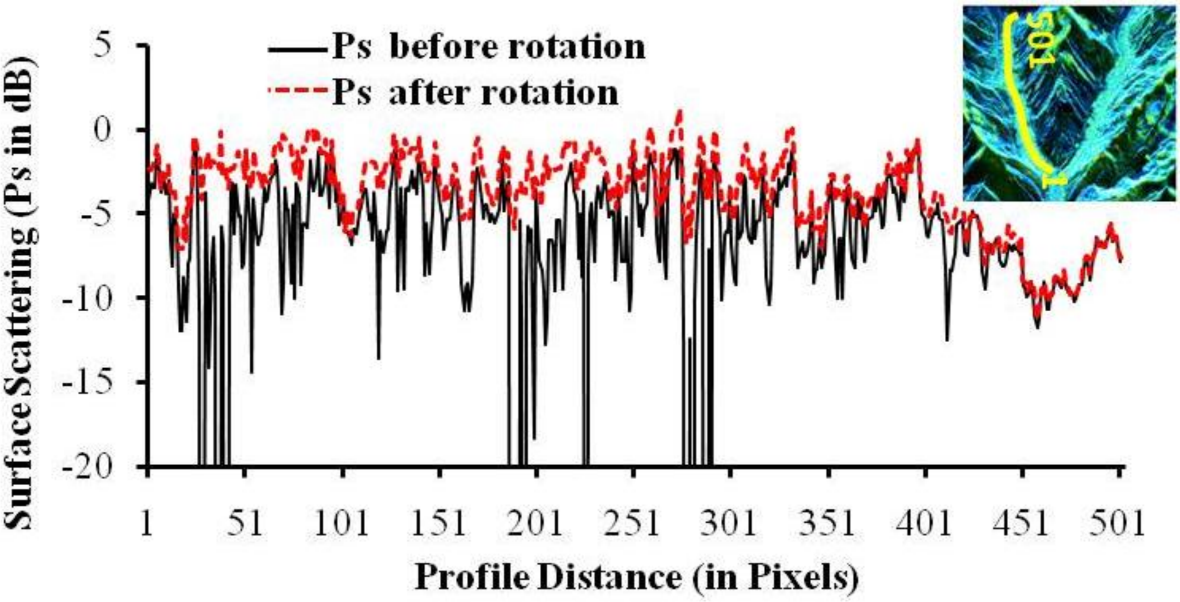

(a)

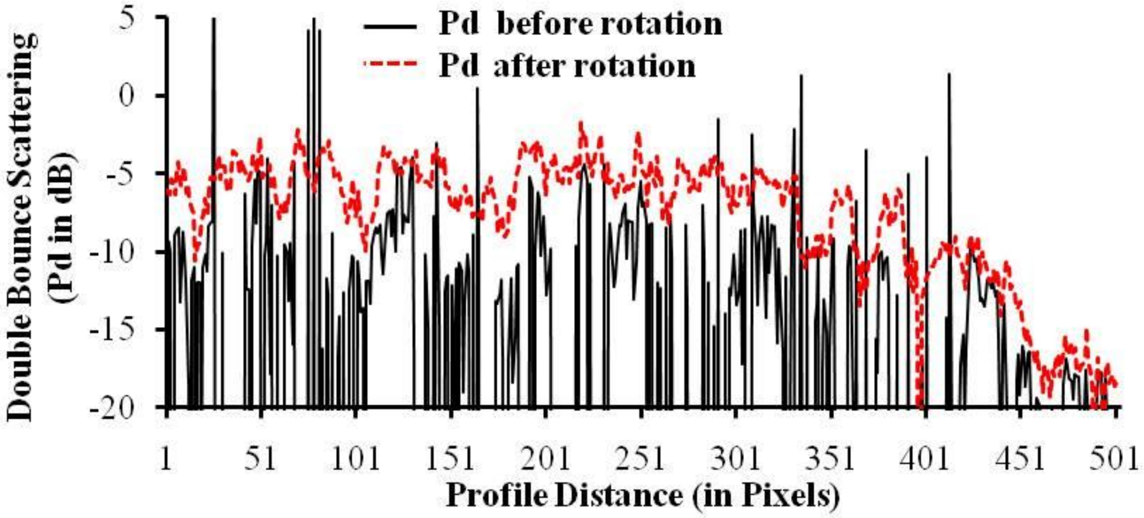

(b)

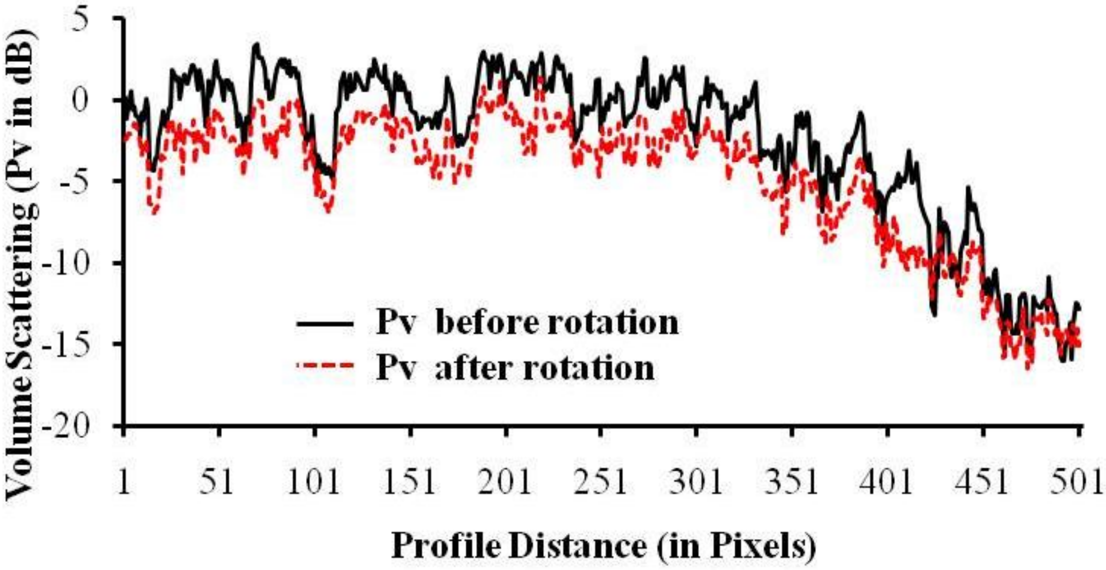

(c)

Fig.3.5. These profiles show the original Y4O and modified Y4R methods scattering components over Satopanth Glacier (a) P_s (b) P_d and (c) P_v.

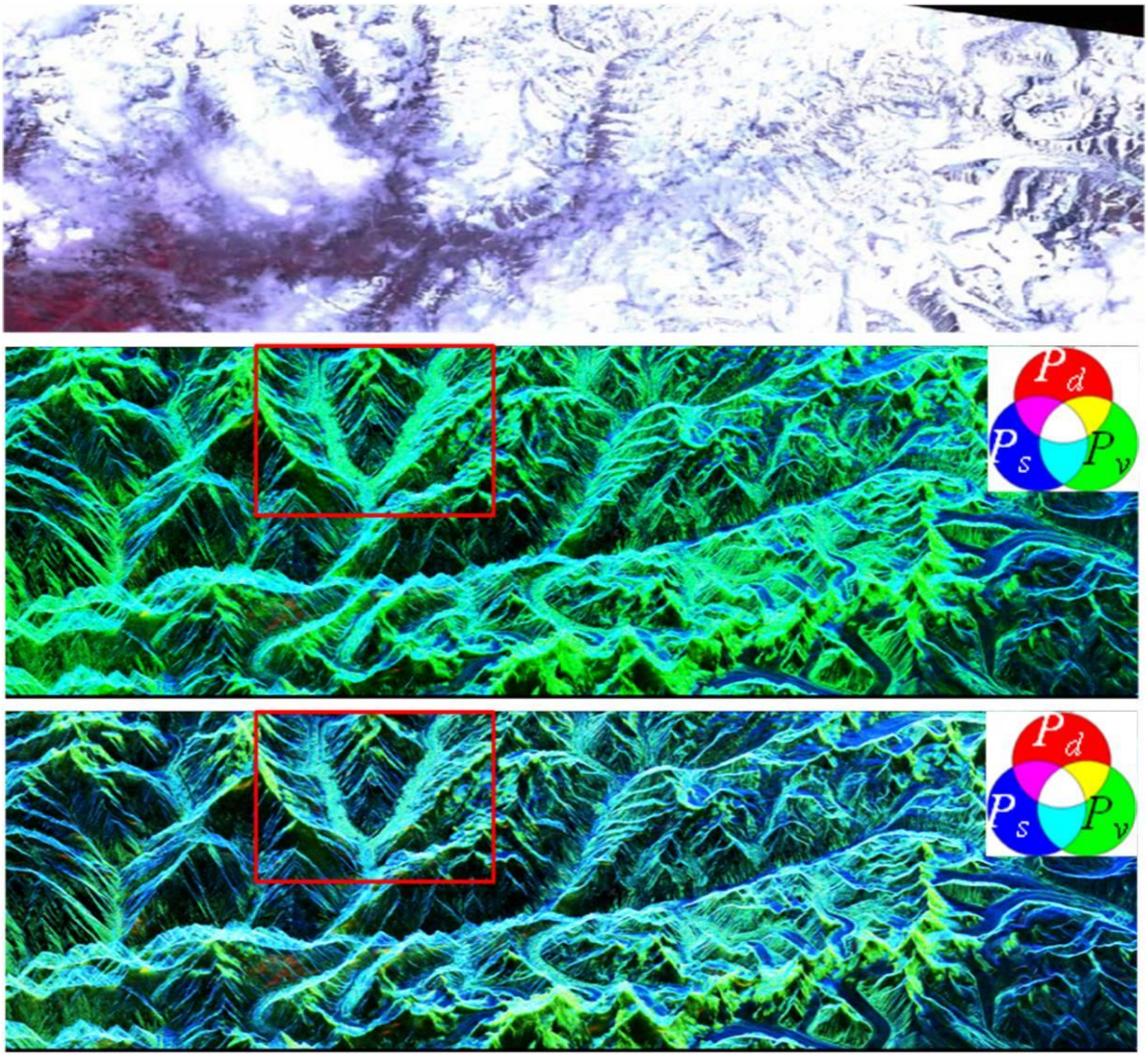

Fig.3.6. (**Top**) ALOS-AVNIR-2 image of May 6, 2007. Four-component scattering power decomposition FCC images: (**middle**) with original coherency matrix of May 12, 2007 PALSAR data; (**bottom**) with rotated coherency matrix of May 12, 2007 PALSAR data and enlarged views for red color rectangular boxed region on decomposition FCCs are shown in Fig. 3.7.

The differences are clearly seen between the original and modified approaches in Fig.3.7. Fig. 3.7 is an enlarged part of the red color-coded rectangular area in Fig. 3.6. Most of the changes can be visibly identified as double-bounce and surface scattering components of the four-component scattering power decomposition methods; and these components are clearly exposed in Fig. 3.7(b) and Fig. 3.7(d), with the aid of the rotated coherency matrix. It can be seen that more "Blue" appears in (b) and (d) as compared in (a) and (c). This indicates that the snow cover exhibiting "Blue" over the glacier area is enhanced by the modified method Y4R as compared to original method Y4O. Some of enhancement in "Blue" and "Red" are indicated by yellow circles number 1, 2 and 3 in Fig. 3.7(b) and correspond to yellow color-coded circles no. 1, 2 and 3 in Fig. 3.7 (a), respectively; and similarly yellow circle no. 1, 2 and 3 in Fig. 3.7(d) correspond to yellow circles no. 1, 2 and 3 in Fig. 3.7(c), respectively.

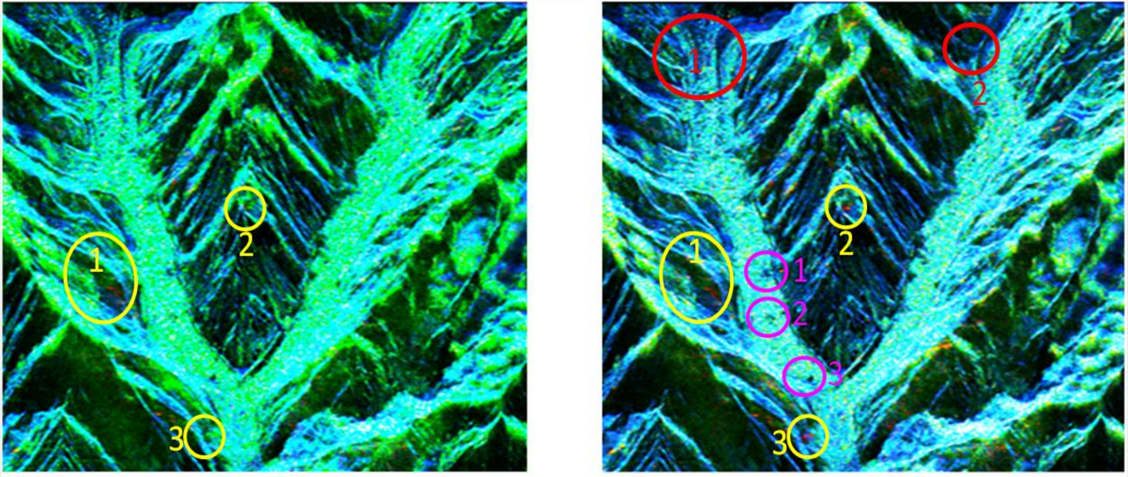

(a) Original **(12-05-07)** (b) After T_{33} rotation **(12-05-07)**

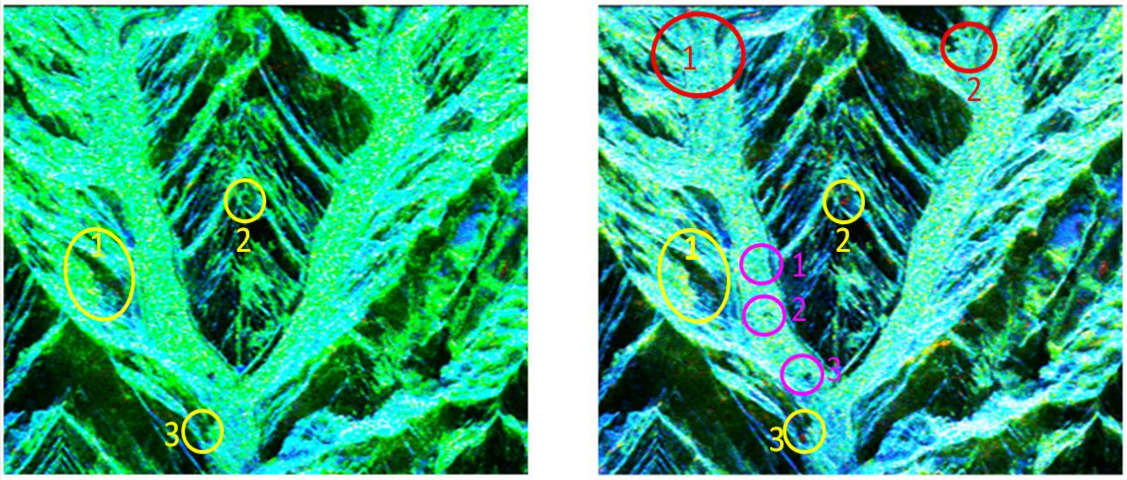

(c) Original **(12-11-07)** (d) After T_{33} rotation **(12-11-07)**

Fig. 3.7. Four-component scattering power decomposition FCC (P_d in "Red", P_v in "Green" and P_s in "Blue") images: (a) With original coherency matrix of May 12, 2007 PALSAR data; (b) with rotated coherency matrix of May 12, 2007 PALSAR data; (c) With original coherency matrix of November 12, 2007 PALSAR data; and (d) With rotated coherency matrix of November 12, 2007 PALSAR data.

Temporal changes can easily be seen in the November 12, 2007 image {just before starting snow fall in Himalayas, Fig. 3.7 (d); and the May 12, 2007 image in Himalayas is provided in Fig. 3.7 (b)}. Red circles no.1 and 2 in Fig. 3.7 (b) correspond to red circles no. 1 and 2 in Fig. 3.7 (d), clearly identifying the temporal changes in snow cover. Since P_s becomes the dominating scattering component in the decomposition scheme due to wet snow over the glacier in the May 12, 2007 image as compared to snow-free glacier in November 12, 2007 image, thus more "Blue" appears in red circles no.1 and 2 in Fig. 3.7 (b) as compared to red circles no. 1 and 2 in Fig. 3.7 (d). In magenta circle no. 1, moraine dammed lake disappeared in the November, 2007 image whereas lakes within circles no 2 and 3 changed their shape as compared to the May, 2007 image.

Moreover, the quantitative analysis of decomposed power distribution is shown in Fig. 3.8 for 12 May 2007 data of PALSAR data within the enlarged area. It is found that after rotation, P_s and P_d increase whereas P_v decreases, respectively.

The modified method Y4R gives very decisive information about the double-bounce features in the study area as compared to the original decomposition. The new application of this modified method Y4R will be useful to identify relatively permanent scatterer ensembles using time series data, which can be used for studying glacier movement.

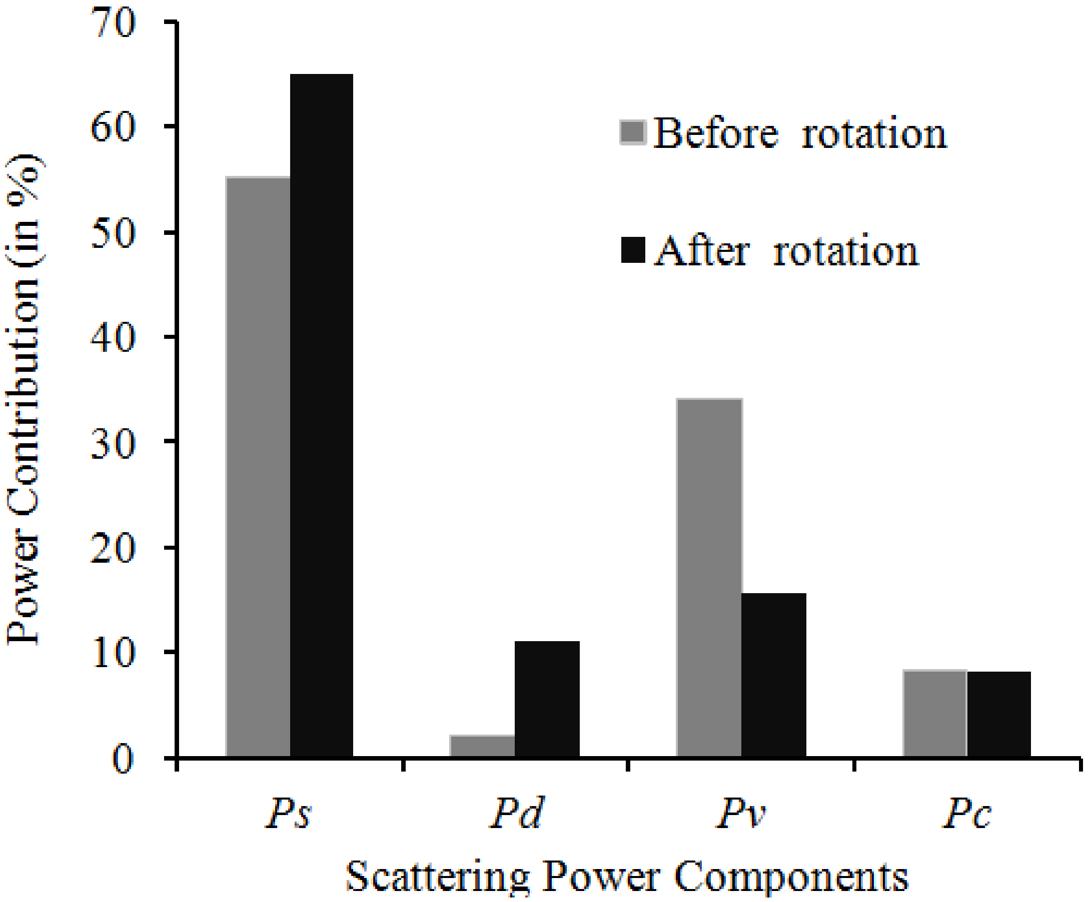

Fig. 3.8. Four-component scattering power decomposition based power distribution before and after rotation of coherency matrix for the red rectangular area (Fig.3.6) on 12 May 2007.

3.6 Summary and Conclusions

In this Chapter 3, fully polarimetric PALSAR data have been analyzed for high altitude glaciated terrain in Himalayan region based on the Y4R method for extracting information from different types of terrain features. It has been found that the Y4R method discriminates better terrain features like snow cover, dihedral (double-bounce) and glacier features as compared with un-rotated the Y4O method. Since rotation angles become noisy at steep slopes due to layover distortion in PALSAR images, a further extending of the Y4R method cannot help too much for correctly discriminating targets in steep sloped areas at single flight direction. In future work, both ascending and descending pass images need to be used for correctly discriminating the targets in steep sloped areas by implementing the presently discussed approach. The Y4R method will also be analyzed for the detection of changes in the glaciated terrain features during two temporal POL-SAR images. In addition, with the currently introduced novel beam-forming fully polarimetric POLSAR method at DLR (Krieger *et al.* 2008), the change of incidence angle over a wide range is made possible, and will strongly contribute to extending the currently discussed Y4R method – an important task for the near future to verify.

Chapter.4 Four-Component Scattering Power Decomposition with Extended Volume Scattering Model S4R

Scientific concepts are subject to change the better and deeper we comprehend nature

4.1 Abstract

In the three- or four-component decompositions, polarimetric scattering properties and corresponding physical scattering models play essential roles for power decomposition. This chapter proposes an improved four-component scattering power decomposition method that employs a suitable volume scattering model for single- or double-bounce scattering in the POL-SAR image analysis. The cross-polarized *HV* component is generated by both single-bounce object (such as vegetation) and double-bounce structures (such as oriented building blocks). It has been difficult to discriminate these two scatterer classes (vegetation against oriented buildings) in the decomposition images, since the *HV* component is assigned to the volume scattering due to vegetation only. We propose to extend the volume scattering model suited for two physical scattering models. It is shown that a vegetated area *versus* an oriented urban building area can well be discriminated when compared to those models resulting from implementation of the existing four-component scattering power decomposition formulations.

4.2 Introduction

The Y4O is an extension of the FDD, for the general scattering case with non-reflection symmetry condition. After decomposing the total power into four components, it has been found that the method Y4O has problems of overestimating the volume scattering in urban areas and orientated surface features with associated negative power occurrence in the processing caused by a large cross-polarization component (Yajima *et al.* 2008;Yamaguchi *et al.* 2011). In order for overcoming this shortcoming, Yamaguchi *et al.* (2011) proposed a rotation method of the coherency matrix for more accurate POL-SAR image decomposition and target classification. The four-component decomposition method with rotation of coherency matrix, labelled as Y4R, significantly improved the decomposition results by minimizing the cross-polarized (*HV*) components and in turn reducing the negative power occurrence in the surface scattering and the double-bounce scattering components. The Y4O and Y4R methods were described with an example in previous Chapters 2 and 3, respectively.

However, there still exists a problem of discrimination between vegetated areas and oriented buildings within the same volume scattering (green) area. This ambiguity is caused by not properly accounting for the *HV* component which requires very precise polarimetric antenna design techniques and therefore often neglected as an utter nuisance rather than being of vital importance in high resolution precise radar polarimetry. So far, the volume scattering power is evaluated by the *HV* component due to vegetation only in the existing methods (Freeman and Durden 1998; Lee and Ainsworth 2011; Yajima *et al.* 2008; Yamaguchi *et al.* 2005), and rather poor acquisition was considered sufficient. To resolve the discrimination ambiguity, we have to assign the *HV* component whether it is being generated by vegetation (single bounce object) or by edges of oriented buildings (double-bounce structures). In this chapter, we propose to use a new volume scattering model that accounts for the *HV* component caused by double-bounce structures versus vegetation scatter and to improve the Y4R (Yamaguchi *et al.* 2011) for additional more accurate classification, denoted as S4R.

4.3 Y4R

The rotated measured coherency matrix $\langle[T(\theta)]\rangle$ is expanded into four sub-matrices which correspond to surface scattering, double-bounce scattering, volume scattering, and helix scattering mechanisms (Yamaguchi *et al.* 2011). The expression of Y4R is shown in (3.8) of Chapter 3, Section 3.4. Other relevant details of the Y4R method are not repeated in here, we refer to Chapter 3. For volume scattering mechanisms, we confirm from the experimental evidence that $\text{Re}\{\langle S_{HH}S_{VV}^*\rangle\} > 0$ is corresponding to the surface scattering. Under the condition of $\text{Re}\{\langle S_{HH}S_{VV}^*\rangle\} > 0$, the *HV* component is assigned to a cloud of randomly oriented dipole scatterers such as vegetation (see Section 2.5 of Chapter 2 for volume scattering models for the dipole case). However, for the case of $\text{Re}\{\langle S_{HH}S_{VV}^*\rangle\} < 0$, a different alternate volume scattering expansion matrix need be used as shown in the next section.

4.4 Four-Component Scattering Power Decomposition with extended volume scattering model S4R

In this section, a new four-component scattering power decomposition method S4R is explained using a new volume scattering model.

4.4.1 New Expansion Matrix for Dihedral Scattering

The experimental evidence indicates that $\text{Re}\{\langle S_{HH}S_{VV}^*\rangle\} < 0$ corresponds to the double-bounce scattering case. This situation typically occurs for man-made objects with right angle structures such as building walls and roads, and river surfaces and bridges orthogonal to radar illumination. We call this kind of structure dihedral structures. When the directions of the main surface of buildings are oriented with respect to radar illumination, the *HV* component is generated and becomes a relatively large term in the acquired scattering matrix. We must consider this physical situation in more detail and must incorporate the *HV* component by the oriented dihedral structures for more accurate modeling.

Since the rotation of coherency matrix (Yamaguchi *et al.* 2011) minimizes the *HV* component, most of the orientations of dihedral structures are centred about zero degree with respect to the direction of radar illumination after the rotation (see (3.1) of Section 3.4 in Chapter 3). In order to derive a new expansion coherency matrix for the *HV* component, we implement ensemble averaging of dihedral corner reflectors using a probability density function $p(\theta)$ with its peak at zero degree, as shown in Fig. 4.1.

$$p(\theta) = \begin{cases} \frac{1}{2}\cos\theta & \text{for} -\frac{\pi}{2} < \theta < \frac{\pi}{2} \\ 0 & \text{else} \end{cases} \tag{4.1}$$

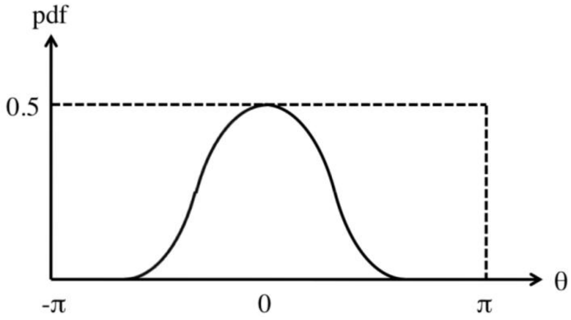

Fig.4.1. Probability density function

The theoretical ensemble matrix for a dihedral corner reflector can be derived from

$$\langle[T(\theta)]\rangle = \int_{-\pi/2}^{\pi/2} [T(\theta)]\ p(\theta)\ d\theta \tag{4.2}$$

yielding

$$\langle[T]\rangle_{\text{vol}}^{\text{dihedral}} = \frac{1}{15}\begin{bmatrix} 0 & 0 & 0 \\ 0 & 7 & 0 \\ 0 & 0 & 8 \end{bmatrix}. \tag{4.3}$$

This matrix was derived using (3.1) for dihedral in a similar way explained in Yamaguchi *et al.* (2005) and was set so that the *trace* becomes unity. We use this matrix as a new volume scattering expansion matrix that accounts for the *HV* component for dihedral structures.

4.4.2 Branch Condition

After the rotation of coherency matrix, we first discriminate the scattering mechanism using the sign of Re $\{\langle S_{HH}S_{VV}^{*}\rangle\}$. It is known from the experimental evidence that the double-bounce scattering by dihedrals cause the parameter Re $\{\langle S_{\text{HH}}S_{\text{VV}}^{*}\rangle\}$ to be negative. On the other hand, non-dihedral structures cause Re $\{\langle S_{\text{HH}}S_{\text{VV}}^{*}\rangle\} > 0$. These relations can be explained in more detail by rigorously using the covariance matrix formulation (Yamaguchi *et al.* 2005). By the expansion of the C_{13} component for randomly distributed dipoles (Yamaguchi *et al.* 2005), we can derive the pertinent relation as follows:

$$\text{Re}\,\{\, f_s\,\beta^{*} + f_d\ \alpha\} - \frac{7}{30}\ f_v - \frac{1}{4}\ f_c = \text{Re}\,\{\langle S_{\text{HH}}S_{\text{VV}}^{*}\rangle\} \tag{4.4}$$

This equation can be rearranged to

$$C_1 = 2\text{Re}\,\{\, f_s\,\beta^{*} + f_d\ \alpha\} = 2\text{Re}\,\{\langle S_{\text{HH}}S_{\text{VV}}^{*}\rangle\} + \frac{7}{15}\ f_v + \frac{1}{2}\ f_c \tag{4.5}$$

We have omitted the term $(7/15)f_v$ in the above equation (4.5) for the purpose of exaggerating double-bounce scattering in the oriented urban areas. The sign of (4.5) determines the dominant scattering mechanism, i.e., surface scattering versus double-bounce scattering. According to the sign of C_1, we assign the volume scattering (the *HV* component) to surface scattering (vegetation) or double-bounce scattering (oriented dihedral structure) according to the following condition:

$$C_1 = T_{11}(\theta) - T_{22}(\theta) + \frac{1}{2}\ f_c > 0 :\ \text{volume scattering by vegetation} \tag{4.6}$$

$$C_1 = T_{11}(\theta) - T_{22}(\theta) + \frac{1}{2}\ f_c \leq 0 :\ \text{volume scattering by dihedral.} \tag{4.7}$$

It should be noted that (4.6) and (4.7) are the first-stage criteria. It happens that (4.7) assigns the volume scattering as dihedral scattering when double-bounce generated by forest trunk and ground is too strong in a vegetated area. However, it is easy to recognize a vegetation scattering area in this case because the tree trunk and ground scattering (double-bounce) points appear randomly and sparsely in the surrounding area and the volume scattering dominants in the final decomposed forest image. To check the validity of the criteria, L-band Polarimetric and Interferometric SAR (Pi-SAR) data-take sets have been analyzed. These Pi-SAR data sets were acquired over Niigata University and the surrounding area: Fig. 4.2(a) shows the optical Google Earth image over the area; and Fig 4.2(b) represents the C_1 binary image of Pi-SAR data, corresponding to Fig. 4.2(a). We can clearly observe that $C_1>0$ in pine forest areas in the upper part of Fig.4.2 (a), and that $C_1\leq 0$ in orthogonal urban areas (middle left) to radar illumination direction. On the other hand, we see a mixture of $C_1>0$ and $C_1\leq 0$ in oriented urban area (right). This important finding result confirms the validity of these criteria, which will be applied to the development of a new decomposition method S4R.

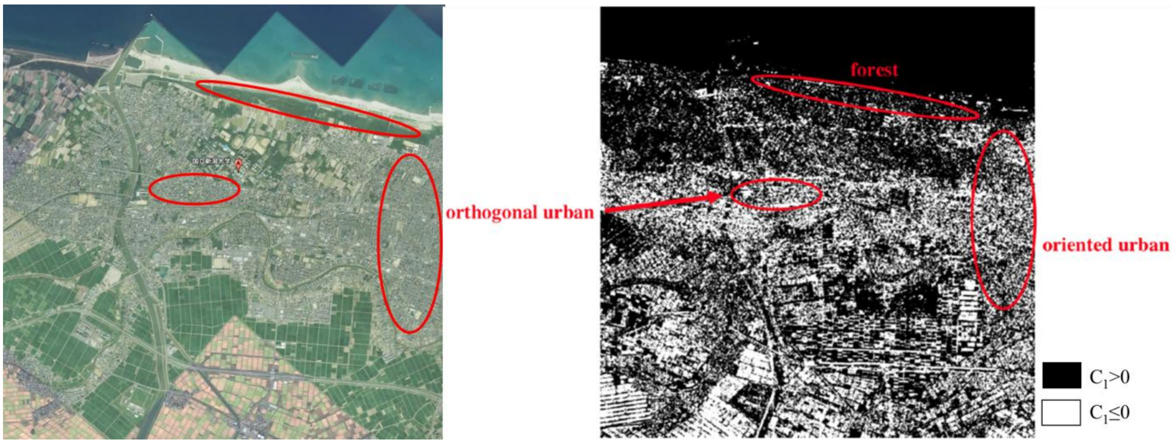

(a) (b)

Fig. 4.2. (a) Google Earth optical image. (b) C_1 binary image of Pi-SAR data over Niigata University and the srounding area derived by (4.6) and (4.7).

4.4.3 New four-component scattering power decomposition S4R

The new decomposition can be explained by (4.8) and by Fig. 4.3 by using the volume scattering component from vegetated and/or oriented dihedral structures.

$$\langle [T(\theta)]\rangle = f_s\langle[T]\rangle_{\text{surface}} + f_d\,\langle[T]\rangle_{\text{double}} + \begin{cases} f_v\,\langle[T]\rangle_{\text{vol}}^{\text{dipolel}}, & \text{for } C_1>0 \\ f_v\,\langle[T]\rangle_{\text{vol}}^{\text{dihedral}}, & \text{for } C_1\leq 0 \end{cases} + f_c\langle[T]\rangle_{\text{helix}} \tag{4.8}$$

where f_s, f_d, f_v and f_c are coefficients to be determined. $\langle[T]\rangle_{\text{surface}}$, $\langle[T]\rangle_{\text{double}}$ and $\langle[T]\rangle_{\text{helix}}$ are expansion matrices corresponding to surface, double-bounce, and helix scattering, respectively. $\langle[T]\rangle_{\text{vol}}^{\text{dihedral}}$ and $\langle[T]\rangle_{\text{vol}}^{\text{dipolel}}$ are the volume scattering matrices for oriented dihedral structure and wire (ensemble average of dipole), respectively.

The total power (TP) decomposes into surface scattering power P_s, double-bounce scattering power P_d, volume scattering power P_v, from dipole and/or oriented dihedral and helix (P_c), as shown in Fig.4.3.

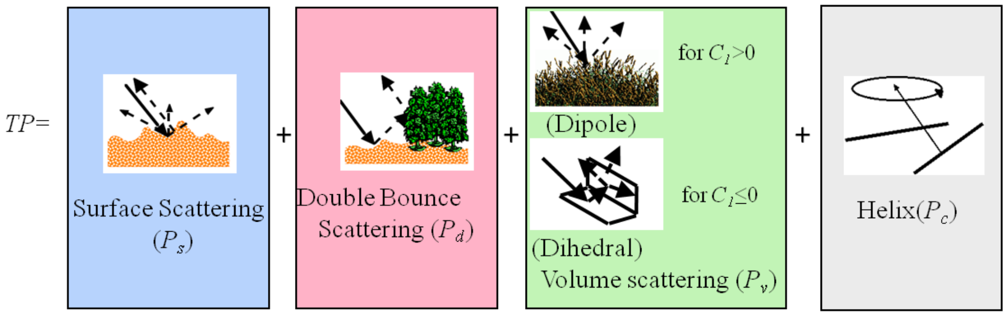

Fig. 4.3 New four-component scattering mechanism with rotation of coherency matrix

4.4.4 Decomposition Algorithm

The new decomposition algorithm is shown in Fig. 4.4. The first important step is the rotation of coherency matrix to minimize the *HV* component before the decomposition. It should be noted that (3.6) assumes arctan2 for obtaining the rotation angle in the computer algorithm. This rotation forces real part of T_{23} be zero, so that it ensures a reduction of the number of independent polarimetric parameters from nine to eight. Then, we check the sign of C_1 to assign the prevalent scattering mechanism. Once assigned to double-bounce scattering, we use a new expansion matrix (4.3) for volume scattering. Since most of the double-bounce structures are faced to radar illumination direction by implementation of the rotation of coherency matrix, the *HV* component derives from the dihedral structure.

On the other hand, if surface scattering is assigned, we use the same decomposition procedure as shown in previous Chapter 3 (Yamaguchi *et al.* 2011). Once the character of volume scattering power has been determined, it is possible to critically determine the dominant scattering mechanism within the volume scattering generated due dipoles at this stage. We check the second branch condition using (4.4) to confirm the scattering mechanism again.

$$2\mathrm{Re}\,\{\, f_s\,\beta^* + f_d\ \alpha\} = \ 2\ \mathrm{Re}\,\{\langle S_{HH}S_{VV}^*\rangle\} - 2\langle|S_{HH}|^2\rangle - P_c \tag{4.9}$$

This expression is equivalent to the following equation in terms of coherency matrix elements:

$$C_0 = \ T_{11}(\theta) - T_{22}(\theta) - \ T_{33}(\theta) + \ P_c \tag{4.10}$$

The sign of C_0 determines the dominant scattering mechanism precisely within the volume scattering

$C_0 > 0$: surface Scattering; $C_0 \leq 0$: double-bounce scattering (4.11)

All of these physical branch conditions are included in a flowchart of the decomposition algorithm in Fig.4.4.

4.5 Decomposition Results

Both Y4R (four-component decomposition with rotation of coherency matrix) and the proposed procedures of the new decomposition S4R methods have been applied to Pi-SAR images collected over Niigata University and environs. The volume scattering component due to Yamaguchi *et al.* (2011) and the proposed method are shown in Fig. 4.5. Using the proposed extended volume scattering model, significant reduction of volume scattering can be seen in dihedral structures (oriented urban and orthogonal urban areas) compared to the method developed in Yamaguchi *et al.* (2011). This fact serves for regulating the overestimation problem of the volume scattering in urban areas. On the other hand, the volume scattering remains almost the same in forested vegetation areas. Therefore, the proposed dihedral volume scattering model is expected to contribute toward improving the decomposition accuracy in volume scattering.

Fig. 4.6 shows the decomposition color-coded composite images by both the Y4R and the proposed new S4R methods for the sake of comparison. The differences are clearly seen between the images in Fig. 4.6(a) and (b). We can see more “Red” in Fig. 4.6(b), clearly more than in Fig. 4.6(a). This indicates that the dihedral structures is enhanced, while “Green” caused by volume scattering within dihedral structures are reduced. In order to examine these results quantitatively, the decomposition power profiles along a transect over sandy ground, forest and urban area [white line A in Figs. 4.6 and 4.7 (a)] are shown in Fig. 4.7 (b) and (c). The dashed lines in Fig. 4.7 (b) and (c) show the boundaries of sand, forest and urban areas. It is seen that the proposed method does not change the amount of volume scattering in sandy and forest areas as compared to the method Y4R (Yamaguchi *et al.* 2011). The presented new method S4R reduces the amount of volume scattering power in urban areas where many residential houses exist, as shown in the red circle in Fig. 4.7(b) and (c).

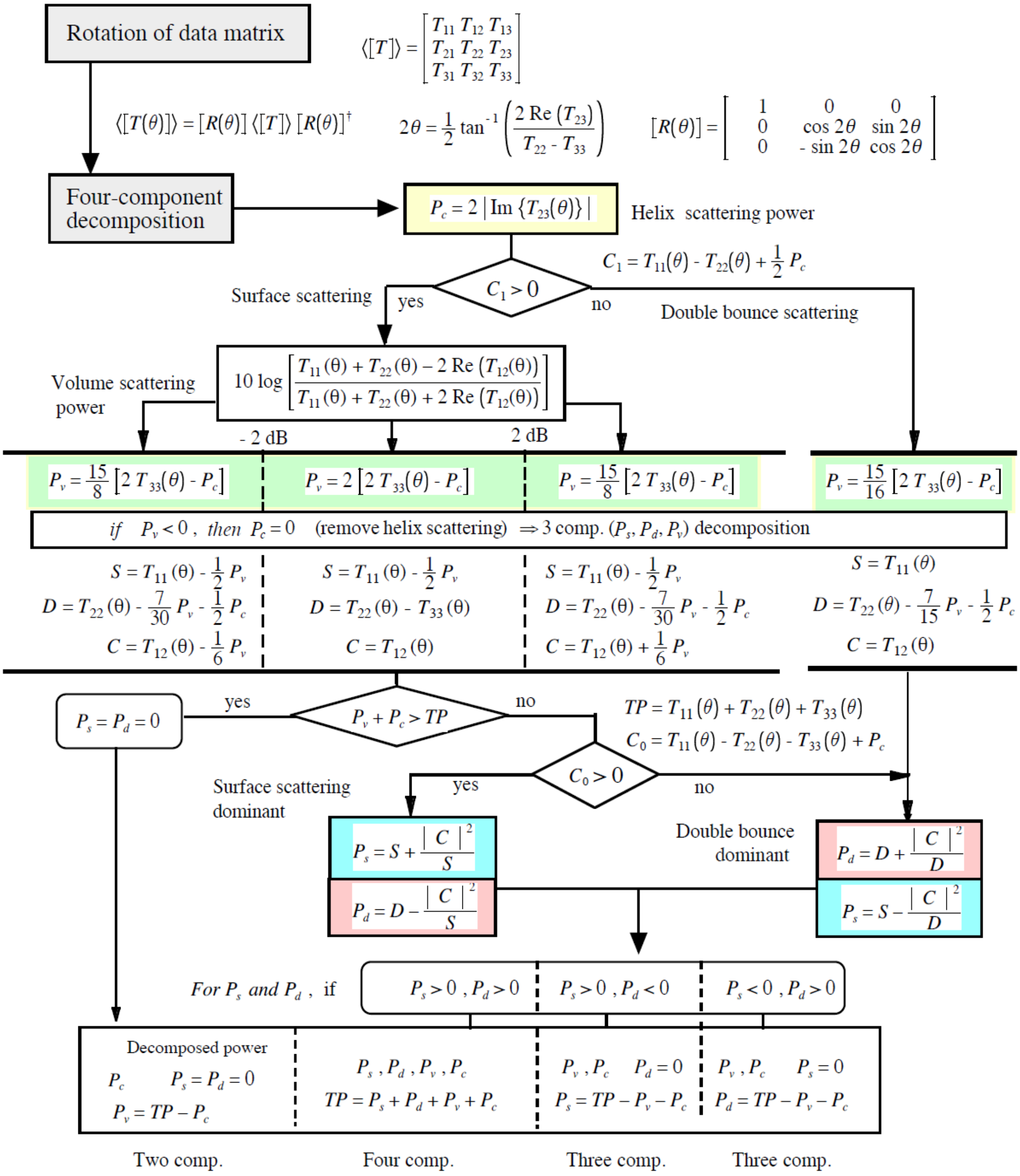

Fig. 4.4. Four-component decomposition with a rotation about the line of sight to set Re(T_{23})=0 rotation and the remaining *HV* contribution due to scattering from either a dihedral or a dipole distribution , denoted as S4R.

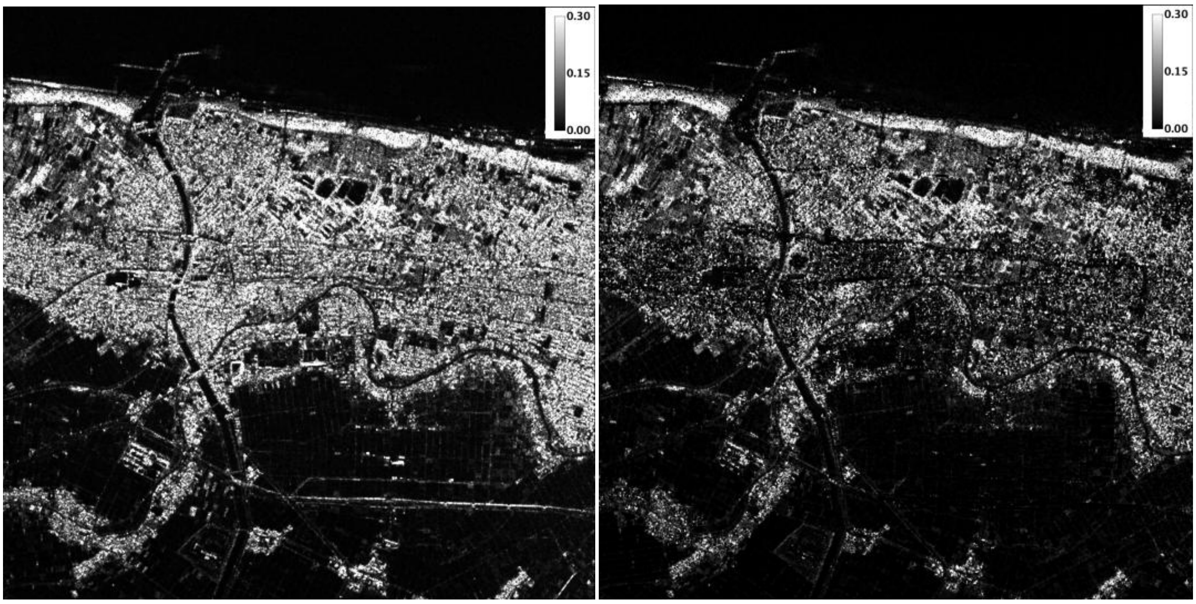

(a) (b)

Fig.4.5 (a) Volume scattering component derived from Y4R method. (b) Volume scattering component derived by the S4R method.

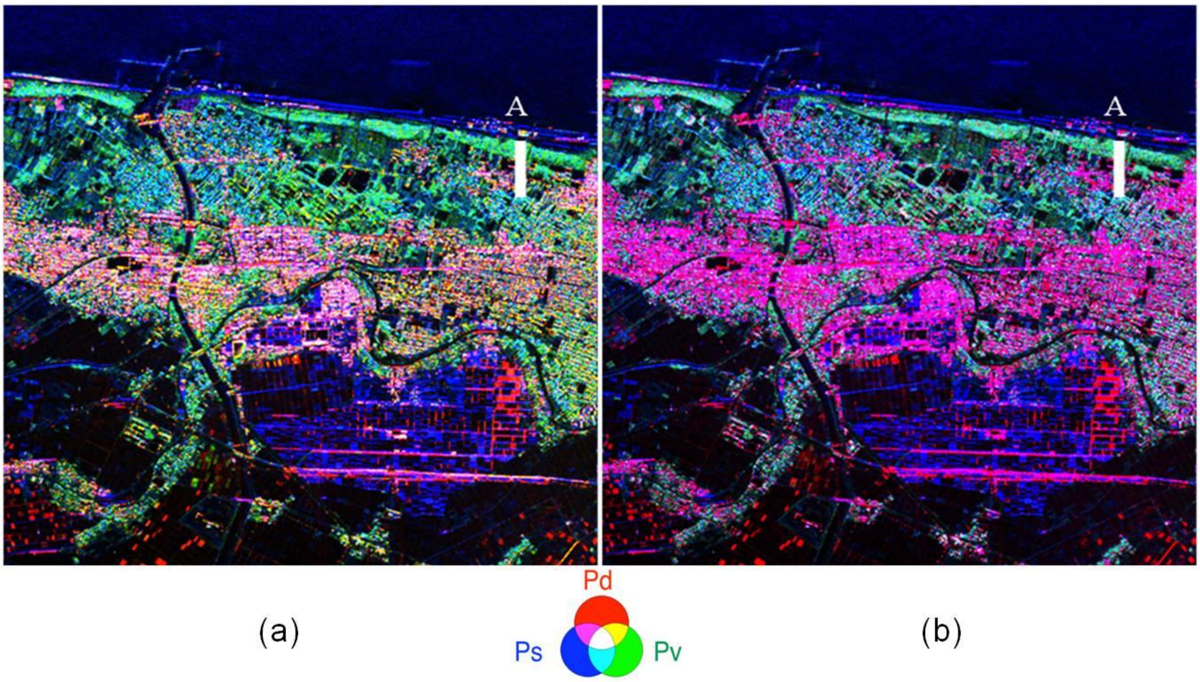

(a) (b)

Fig. 4.6 Color-coded decomposition image of the Niigata University area by L-band Pi-SAR polarimetric data. (a) By Y4R method. (b) By proposed S4R method.

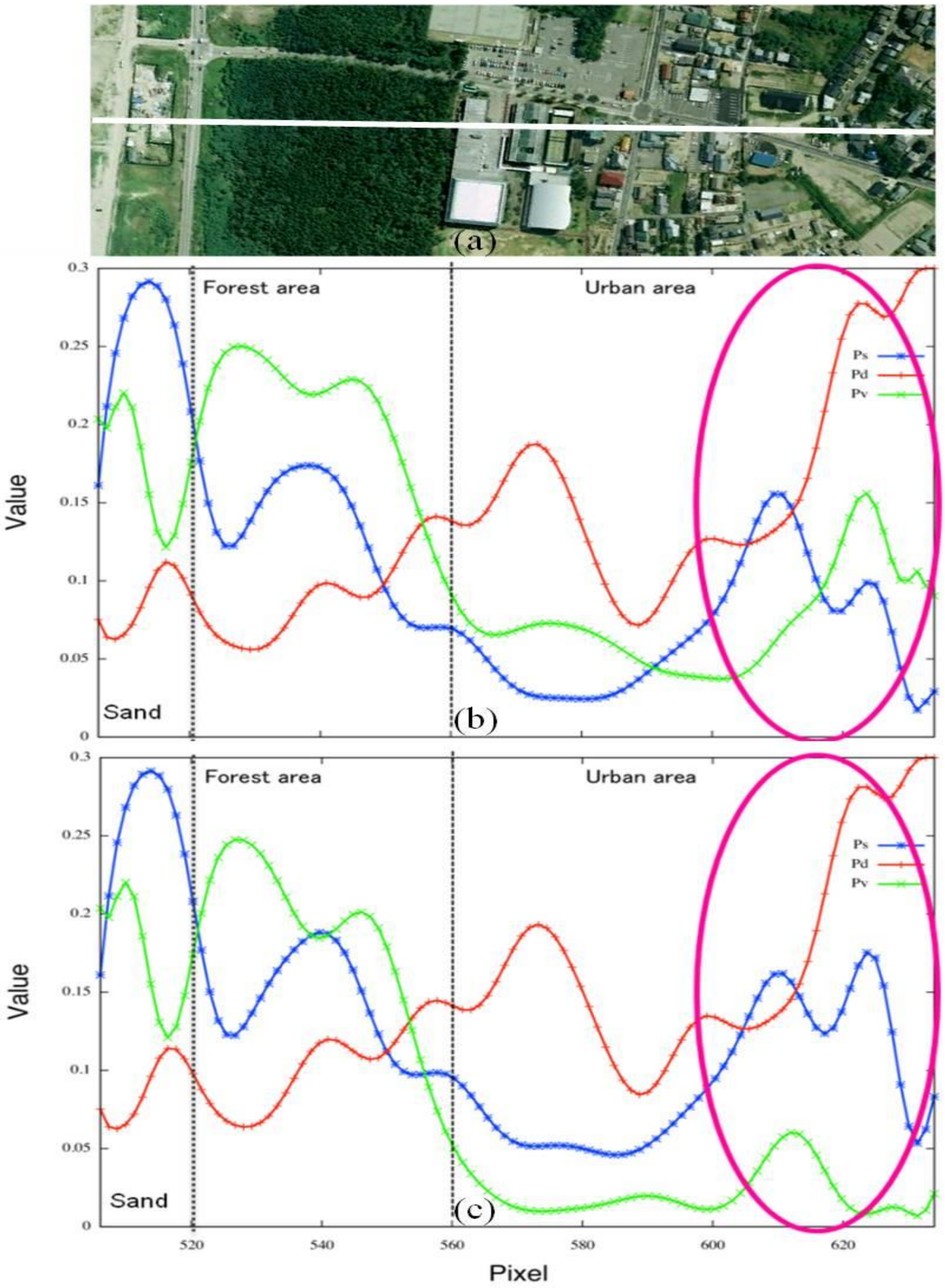

Fig.4.7. (a) Photo by Google Earth. (b) Profile of scattering components derived based on Y4R method. (c) Profile of scattering components derived based on proposed method S4R.

4.6 Summary and conclusions

In this Chapter 4, we have proposed a new volume scattering model that accounts for the *HV* component caused by double-bounce structures and is denoted as S4R. This decomposition method S4R better describes the *HV* component induced by rotated dihedral scattering and reduces the volume scattering power and enhances the double-bounce scattering power within man-made structures, leading to an improvement in the four-component scattering power decomposition. This new decomposition method accounts for six terms out of eight real independent polarimetric parameters for the most general scattering case with the aid of rotation of the coherency matrix. The decomposition results using S4R are in rather good agreement with Google Earth optical images.

Chapter 5 Hybrid Scattering Model-Based / Eigenvalue Decomposition with Extended Volume scattering Model S3H

Hybridization processes survive in nature

5.1 Abstract

In this Chapter 5, an advanced version of the hybrid Freeman/eigenvalue decomposition technique for land parameter extraction is presented, denoted as S3H, with an illustrative example of application. The motivation arises from decomposition problems in obtaining a meaningful volume scattering estimation, so that the technique can be used for both oriented objects and vegetation/forest areas. The idea is to improve the accuracy of the required parameter extraction. Two strategies are adopted to increase the applicability of a hybrid Freeman/eigenvalue technique: One is the unitary transformation of the coherency matrix; the other is to use an extended volume scattering model. The extension of the volume scattering model plays an essential role for the hybrid Freeman/eigenvalue decomposition technique. Since the volume scattering power is evaluated by assuming that the *HV* component is caused by vegetation only in the existing hybrid decomposition technique, an extended volume scattering power approach is utilized. It is shown that vegetation areas and oriented objects such as urban building areas are well discriminated by the proposed technique as compared to the existing hybrid decomposition technique F3H$_c$ (Cloude 2009).

5.2 Introduction

The model based schemes (Freeman and Durden 1998; Lee and Ainsworth 2011; Yajima *et al.* 2008; Yamaguchi *et al.* 2005; Yamaguchi *et al.* 2011) are well suited in that physical scattering models are used for classification and detection of typical scatterer ensembles. Using these schemes, interpretations are easy and straightforward; however, there is no guarantee of non-negative power occurrence. The solutions of the negative power problem were discussed by Yajima *et al.* (2008) and vanZyl *et al.* (2008). Specifically, vanZyl *et al.* (2008) proposed a non-negative eigenvalue decomposition (NNED) method to overcome negative power fatal deficiencies. Later, Arii *et al.* (2011) extended the method by vanZyl *et al.* (2008) to an adaptive NNED method. Thereupon, Cloude (2009) proposed a generalized hybrid Freeman/eigenvalue decomposition method for dealing with the negative power problems. The hybrid Freeman/eigenvalue decomposition is a mathematically and computationally very simple approach. The main idea of this approach is to use orthogonality to reduce the number of unknowns. In addition, the reformulation and computation of this approach enable a more transparent study of the effectiveness of a new scattering mechanism model.

On the other hand, the problem of overestimation of volume scattering power has been noticed when analyzing azimuthally sloped surfaces and oblique urban blocks or man-made structures whose main scattering centres are at an oblique direction with respect to radar illumination (see Chapter 3 and Chapter 4). The reason for this overestimation problem in the volume scattering power is that the polarization orientation changes from the azimuthally sloped surfaces and oriented urban blocks or man-made structures with respect to radar illumination (Lee and Ainsworth 2011; Lee *et al.* 2000; Lee *et al.* 2002; Xu and Jin 2005), thus producing a higher cross-polarization (*HV*) intensity (Yamaguchi *et al.* 2011). These effects in highly topographically irregular surface regions can be reduced with the help of polarization orientation compensation or minimization of the cross-polarized component (Lee and Ainsworth 2011; Lee *et al.* 2000; Lee *et al.* 2002; Xu and Jin 2005; Yamaguchi *et al.*

2011). A method of rotation of the coherency matrix for minimizing its T_{33} element has been adopted by Yamaguchi *et al.* (2011) to reduce the overestimation of the volume scattering component in oblique urban areas. In the previous Chapter 4, it was pointed out that the idea of minimization of the T_{33} element is not sufficient for discriminating vegetated areas from oblique urban areas since the volume scattering power is evaluated by the cross-polarization component caused by vegetation only as assumed intrinsically in the model-based decomposition methods (Freeman and Durden 1998; Yamaguchi *et al.* 2005) as well as in the hybrid decomposition method (Cloude 2009). As a result, the classification between vegetation and buildings becomes difficult (see Chapter 4). Therefore, we propose to use an extended volume scattering model suited for oriented urban buildings (i.e., an oriented dihedral model) to mitigate the overestimation problem. This proposed method shows the advancements in a three-component hybrid decomposition scheme (Cloude 2009) for resolving the discrimination ambiguity of oriented dihedral objects from vegetation, by implementing the extended volume scattering model (see Chapter 4) and the concept of rotation about the line of sight.

The brief description of the three-component hybrid decomposition F3H$_c$ scheme (Cloude 2009) is described in Section 5.3. The idea of rotation and unitary transformation of the coherency matrix is shown in Section 5.4. Section 5.5 provides the proposed scheme of three-component hybrid decomposition for improving the results. The results of the proposed S3H and existing hybrid decomposition F3H$_c$ schemes are compared and presented with illustrative examples in Section 5.6. Furthermore, remarks on the hybrid decompositions are also discussed in Section 5.6. Finally, in Section 5.7, the results of the new method are summarized.

5.3 Original Three-Component Hybrid Decomposition F3H$_c$

This section explains briefly the hybrid Freeman/eigenvalue decomposition method (Cloude 2009), denoted as F3H$_c$, implementing the coherency matrix $\langle[T]\rangle$ subject to the reflection symmetry condition. According to this hybrid scheme, $\langle[T]\rangle$ is expanded into three submatrices as

$$\langle[T]\rangle = \langle[T_S]\rangle + \langle[T_D]\rangle + \langle[T_V]\rangle$$

$$\langle[T]\rangle = \begin{bmatrix} T_{11} & T_{12} & T_{13} \\ T_{21} & T_{22} & T_{23} \\ T_{31} & T_{32} & T_{33} \end{bmatrix},$$

$$\langle[T_S]\rangle = m_s \begin{bmatrix} \cos^2\alpha_s & \sin\alpha_s \cos\alpha_s e^{j\phi_s} & 0 \\ \sin\alpha_s \cos\alpha_s e^{-j\phi_s} & \sin^2\alpha_s & 0 \\ 0 & 0 & 0 \end{bmatrix},$$

$$\langle[T_D]\rangle = m_d \begin{bmatrix} \cos^2\alpha_d & \sin\alpha_d \cos\alpha_d e^{j\phi_d} & 0 \\ \sin\alpha_d \cos\alpha_d e^{-j\phi_d} & \sin^2\alpha_d & 0 \\ 0 & 0 & 0 \end{bmatrix},$$

$$\langle[T_V]\rangle = m_v \begin{bmatrix} \frac{1}{2} & 0 & 0 \\ 0 & \frac{1}{4} & 0 \\ 0 & 0 & \frac{1}{4} \end{bmatrix} \tag{5.1}$$

In (5.1), $\langle[T_S]\rangle$, $\langle[T_D]\rangle$, and $\langle[T_V]\rangle$ are the surface scattering, double-bounce scattering and volume scattering matrices, respectively, and m_s, m_d, m_v are the corresponding, scattering power coefficients. $\alpha_s < \pi/4$ depends on the dielectric constant and angle of incidence, and $\alpha_d > \pi/4$ depends on the angle of incidence and the two dielectric constants of the surface and reflector. ϕ_s and ϕ_d are the scattering phase for surface scattering and double-bounce scattering, respectively**.** The key idea of orthogonality of the surface and dihedral component is applied in (5.1). The orthogonality condition can be expressed as

$$\alpha_d + \alpha_s = \frac{\pi}{2}; \text{ with } \phi_d - \phi_s = \pm\pi \tag{5.2}$$

Therefore, the orthogonality conditions reduce (α_d, α_s) to α, and (ϕ_d, ϕ_s) to ϕ in (5.1). Thus, (5.1) is rewritten as

$$\langle[T]\rangle = \begin{bmatrix} m_s\cos^2\alpha + m_d\sin^2\alpha & \cos\alpha\sin\alpha\, e^{j\phi}(m_d - m_s) & 0 \\ \cos\alpha\sin\alpha\, e^{-j\phi}(m_d - m_s) & m_d\cos^2\alpha + m_s\sin^2\alpha & 0 \\ 0 & 0 & 0 \end{bmatrix} + m_v \begin{bmatrix} \frac{1}{2} & 0 & 0 \\ 0 & \frac{1}{4} & 0 \\ 0 & 0 & \frac{1}{4} \end{bmatrix} \tag{5.3}$$

The scattering phase angle for dominant scattering mechanisms can then be decided (Cloude 2009) based on the criteria in

$$\phi = \begin{cases} \phi_s\,, \phi_d = 0 \ \ if \ \ \alpha < \pi/4 & \text{surface scattering} \\ \phi_d, \phi_s = 0 \ \ if \ \alpha > \pi/4 & \text{dihedral scattering.} \end{cases} \tag{5.4}$$

The volume scattering component is derived as

$$m_v = 4T_{33} \tag{5.5}$$

This model can be inverted by calculating m_s and m_d as eigenvalues of the rank-2 matrix $\langle[T_{SD}]\rangle$,

$$m_{d,s} = \frac{T_{11} + T_{22} - 3T_{33} \pm \sqrt{(T_{11} - T_{22} - T_{33})^2 + 4|T_{12}|^2}}{2} \tag{5.6}$$

5.4 Unitary Transformations of Coherency Matrix

In this section, two (real and complex) unitary transformations are explained. First, a real unitary transformation of coherency matrix ⟨[T]⟩ is introduced and is known as rotation of ⟨[T]⟩ about the line of sight by angle θ in the literature (Yamaguchi *et al.* 2011). The coherency matrix can be defined for the compensation of polarization orientation shifts as

$$\langle[T(\theta)]\rangle = \begin{bmatrix} 1 & 0 & 0 \\ 0 & \cos 2\theta & \sin 2\theta \\ 0 & -\sin 2\theta & \cos 2\theta \end{bmatrix} \langle[T]\rangle \begin{bmatrix} 1 & 0 & 0 \\ 0 & \cos 2\theta & -\sin 2\theta \\ 0 & \sin 2\theta & \cos 2\theta \end{bmatrix} \tag{5.7}$$

where the rotation angle θ was derived in terms of coherency elements by Yamaguchi *et al.* (2011). This rotation eliminates the real part of the element T_{23}. It is seen that T_{23} becomes purely imaginary. It can be noticed that, after orientation compensation, T_{23} is the best fit for the scattering helicity and roll-invariance (Lee and Ainsworth 2011).

The second unitary transformation is such that

$$\langle[T(\varphi)]\rangle = [U(\varphi)]\langle[T(\theta)]\rangle[U(\varphi)]^\dagger = \begin{bmatrix} T_{11}(\varphi) & T_{12}(\varphi) & T_{13}(\varphi) \\ T_{21}(\varphi) & T_{22}(\varphi) & 0 \\ T_{31}(\varphi) & 0 & T_{33}(\varphi) \end{bmatrix} \tag{5.8}$$

with the unitary transformation matrix

$$[U(\varphi)] = \begin{bmatrix} 1 & 0 & 0 \\ 0 & \cos 2\varphi & j\sin 2\varphi \\ 0 & j\sin 2\varphi & \cos 2\varphi \end{bmatrix} \text{ with } 2\varphi = \frac{1}{2}\, tan^{-1}\left(\frac{2\,\mathrm{Im}\,\{T_{23}(\theta)\}}{T_{22}(\theta) - T_{33}(\theta)}\right) \tag{5.9}$$

This second complex unitary transformation will be treated as unitary change of basis matrix.

5.5 Three-Component Hybrid Decomposition Method with Extended Volume Scattering Model

This section shows an improved methodology for the decomposition of FULL-POL-SAR data by using the real unitary transformation of the 3×3 coherency matrix (rotation of $\langle[T]\rangle$ about the line of sight by angle θ) and an extended volume scattering model (Sato *et al.* 2012). This modification gives accurate or similar results in comparison to Cloude (2009). We expand the measured and rotated coherency matrix $\langle[T(\theta)]\rangle$ under reflection symmetric scattering condition as,

$$\langle[T(\theta)]\rangle = \begin{bmatrix} m_s\cos^2\alpha + m_d\sin^2\alpha & \cos\alpha\sin\alpha\, e^{j\phi}(m_d - m_s) & 0 \\ \cos\alpha\sin\alpha\ e^{-j\phi}(m_d - m_s) & m_d\cos^2\alpha + m_s\sin^2\alpha & 0 \\ 0 & 0 & 0 \end{bmatrix} + m_v\begin{bmatrix} F_s & F_{sd} & 0 \\ F_{ds} & F_d & 0 \\ 0 & 0 & F_v \end{bmatrix} \tag{5.10}$$

It should be remembered that the second unitary transformation (5.8) has not been applied in (5.10). However, (5.8) can be applied in the decomposition scheme. Equation (5.8) does not change the properties of the volume scattering model as long as $\langle[T_V]\rangle$ is developed under the assumption of azimuthal symmetric scattering with equal second and third diagonal elements (Freeman and Durden 1998; Yamaguchi *et al.* 2005), e.g., see $\langle[T_V]\rangle$ in (5.1). Moreover, the second complex unitary transformation can be applied for accounting of the element T_{13} in the Y4R (see Chapter 3) and S4R (see Chapter 4) methods and guaranteeing the general applicability of the four-component scattering power decomposition method as will be discussed in Chapter 6.

The terms F_s, F_d, F_v , F_{sd} and F_{ds} are the elements of the volume scattering matrix. These elements of the volume scattering model are chosen, according to the generation of the cross-polarized *HV* term in Chapter 4 (Sato *et al.* 2012). For volume scattering caused by the *HV* component by vegetation (dipole) (Re $\{S_{HH}\, S^*_{VV}\} \geq 0$), one of the following distributions is adopted based on the magnitude balance of $|S_{HH}|^2$ and $|S_{VV}|^2$, i.e., 1) *uniform* distribution, 2) *cosine* distribution, or 3) *sin* distribution from the reference Yamaguchi *et al.* (2011). For volume scattering caused by oriented dihedral scatter (Re $\{S_{HH}\, S^*_{VV}\} < 0$), we use the following probability distribution $p(\theta)$ with its peak centred on zero degree (Sato *et al.* 2012)

$$p(\theta) = \begin{cases} \dfrac{1}{2}\cos\theta & \text{for} -\dfrac{\pi}{2} < \theta < \dfrac{\pi}{2} \\ 0 & \text{else} \end{cases} \tag{5.11}$$

When these distributions are applied to the ensemble average of dipole scatterers or dihedral (horizontal or vertical) corner reflectors, the F_s, F_d, F_v , F_{sd} and F_{ds} elements can be determined. For example, based on (5.11), the following elements are obtained (Sato *et al.* 2012)

$$F_s = 0\,; F_d = \frac{7}{15}\,;\; F_v = \frac{8}{15}\,;\; F_{sd} = F_{ds} = 0 \tag{5.12}$$

By using (5.10) and (5.12), m_v is determined as

$$m_v = \frac{15}{8} T_{33}(\theta) \tag{5.13}$$

The m_s and m_d can be calculated as eigenvalues of the rank-2 matrix $\langle [T_{SD}] \rangle$ as

$$m_{d,s} = \frac{T_{11}(\theta) + T_{22}(\theta) - (F_s + F_d)\, m_v}{2} \pm \frac{\sqrt{(T_{11}(\theta) - T_{22}(\theta) - (F_s - F_d) m_v)^2 + 4|(T_{12}(\theta) - F_{sd}\, m_v)|^2}}{2} \tag{5.14}$$

It should be emphasized that highly accurate acquisition of the *HV* component with strong suppression of the noise floor is here of paramount relevance and has been more or less totally overlooked in the past.

5.6 Results and Discussion of S3H derived from F3H$_c$

The original and proposed decomposition schemes are applied to TerraSAR-X quad-polarization image data sets of April 22, 2010 over Niigata, Japan, for verifying the correct implementation of the proposed scheme. For example, color-coded images over Niigata are shown in Fig. 5.1. The window size for the ensemble average in image processing was chosen as 12 in the range direction and 10 in the azimuth direction, which corresponds to 20 m × 20 m on the ground area. The results of the method derived in Cloude (2009) F3H$_c$ are compared with those of the proposed method S3H. Dynamic improvements of the decomposition results are shown in Fig. 5.1. It is seen that the discrimination between the forest areas and agricultural areas is difficult in Fig. 5.1(c), whereas these two areas can be easily identified in Fig. 5.1 (b) by implementing the real rotation concept on the coherency matrix only. Whereas volume scattering in between forest areas and agricultural areas is separable by using the real rotation of the coherency matrix, it was still difficult to discriminate agricultural areas from the oriented urban areas (Fig. 5.1 and Fig. 5.2) when based on the minimization of the T_{33} component only. This is because the *HV* component is assigned to the dipole scattering (volume scattering from vegetation) for generating Fig. 5.1(b) and (c). When the *HV* component is assigned to the dipole and dihedral scattering according to the extended volume scattering model in Fig. 5.1(a), in addition to the minimization of the T_{33} component, it is noticed that the double-bounce scattering power P_d (Red) is either enhanced or kept similar in the proposed scheme (three-component hybrid decomposition + real rotation about the line of sight + extension of the volume scattering model) as compared to implementing the original three-component hybrid decomposition with or without real rotation about the line of sight. This enhancement of Red in Fig. 5.1(a) as compared to Fig. 5.1(b) and 1(c) helps to resolve the discrimination ambiguity in between the man-made structures and vegetation areas. The close-up areas of the black rectangular box in Fig. 5.1 are shown in Fig. 5.2 to relate to the interesting observations of the double-bounce scattering and the volume scattering appraisal over the oriented urban areas. The improvements are clearly seen in the determination of the double-bounce scattering and the volume scattering by the proposed scheme over the oriented urban area and the intermittent and surrounding vegetated environments. The results are confirmed using Google optical images that are shown in Fig. 5.2(a). Fig. 5.2 (b) shows good discrimination in between dihedral and other scatterers as compared to Fig 5.2 (c) and (d). The green color of the oriented urban area is suppressed in Fig. 5.2(b) as compared to Fig. 5.2(c) and (d).Vegetation areas are displayed similarly in both images (Fig. 5.2(b) and 5.2(c)).

In general, the results of the new hybrid decomposition scheme are remarkable for the case of the reflection symmetric condition, but results over highly oriented urban areas are not satisfactory. Since the three-component hybrid method works under the reflection symmetry assumption, this assumption causes an overestimation problem in volume scattering power in highly oriented urban areas and for sloped terrain (Yamaguchi *et al.* 2011). However, an outstanding approach of Arii *et al.* (2011) accounts for all polarimetric measurements and becomes a generalized four-component hybrid-model-based decomposition scheme (ANNED) under the nonreflection symmetry condition. The decomposition by Arii *et al.* (2011) forces the third eigenvalue (known as remainder in their approach) of $\langle[T_{SD}]\rangle$ to be minimized. It may be possible that the remainder in Arii *et al.* (2011) can be further minimized by extracting the helix scattering power at the initial stage of the decomposition scheme when the coherency matrix $\langle[T_{SD}]\rangle$ holds for the nonreflection symmetry condition with existence of the helical scattering component (in highly oriented urban areas and for sloped terrain). Moreover, a generalized volume scattering model with nonreflection symmetry assumption was applied, while surface scattering and double-bounce scattering coherent models were considered under reflection symmetry (Arii *et al.* 2011). Our interest is to explore the consideration of the aforementioned issues in future work and to understand the effect of reflection symmetric depolarization (incoherent surface and double-bounce scattering models) on results after inclusion in the decomposition schemes. On other hand, by applying the second unitary transformation of the coherency matrix, it may be possible to use all seven elements of the unitarily transformed coherency matrix $\langle[T(\varphi)]\rangle$ without the reflection symmetry assumption in the linear fitting model-based four-component scattering powers decomposition method as

$$\langle[T(\varphi)]\rangle = m_s[U(\varphi)]\langle[T_s]\rangle[U(\varphi)]^\dagger + m_d[U(\varphi)]\langle[T_D]\rangle[U(\varphi)]^\dagger + m_v[U(\varphi)]\langle[T_V]\rangle[U(\varphi)]^\dagger + m_c[U(\varphi)]\begin{bmatrix}0 & 0 & 0\\ 0 & 1 & \pm j\\ 0 & \mp j & 1\end{bmatrix}[U(\varphi)]^\dagger \tag{5.15}$$

Furthermore, to understand the depolarization (in incoherent surface $\langle[T_s]\rangle$ and double-bounce $\langle[T_D]\rangle$ scattering models) effects on the decomposition behavior, the extended surface and double-bounce scattering models can be adopted in (5.15) from (Cloude 2009) and (Lee *et al.*

2011). In (5.15), the extended volume scattering model $\langle[T_V]\rangle$ can be used similar to that of (5.10).

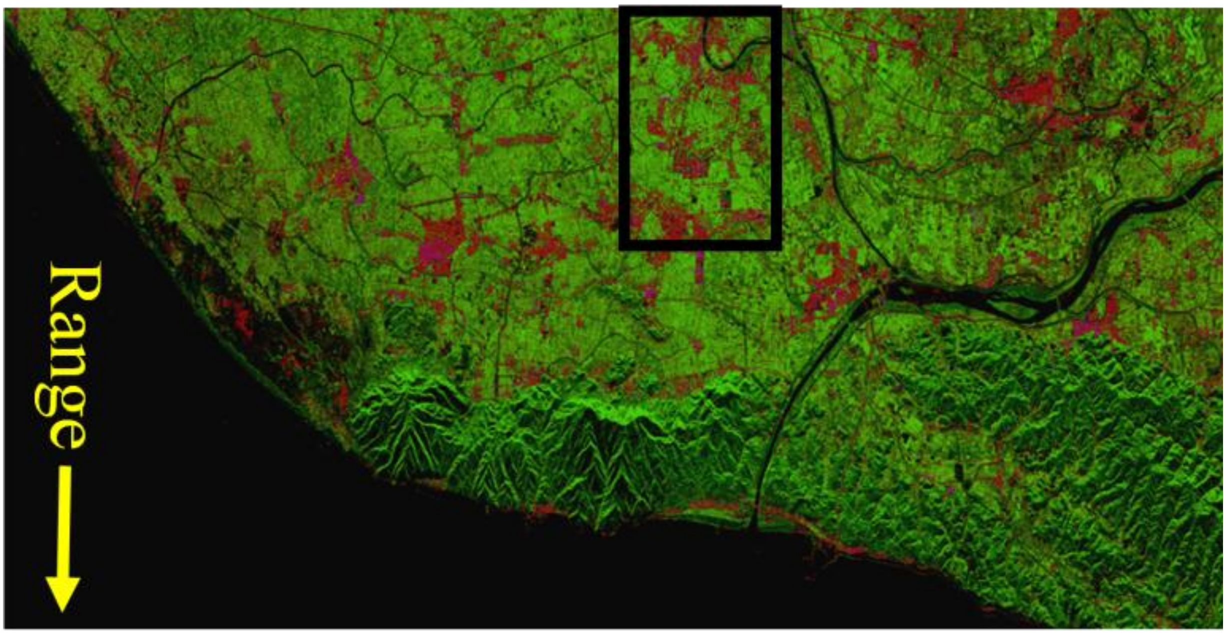

(a)

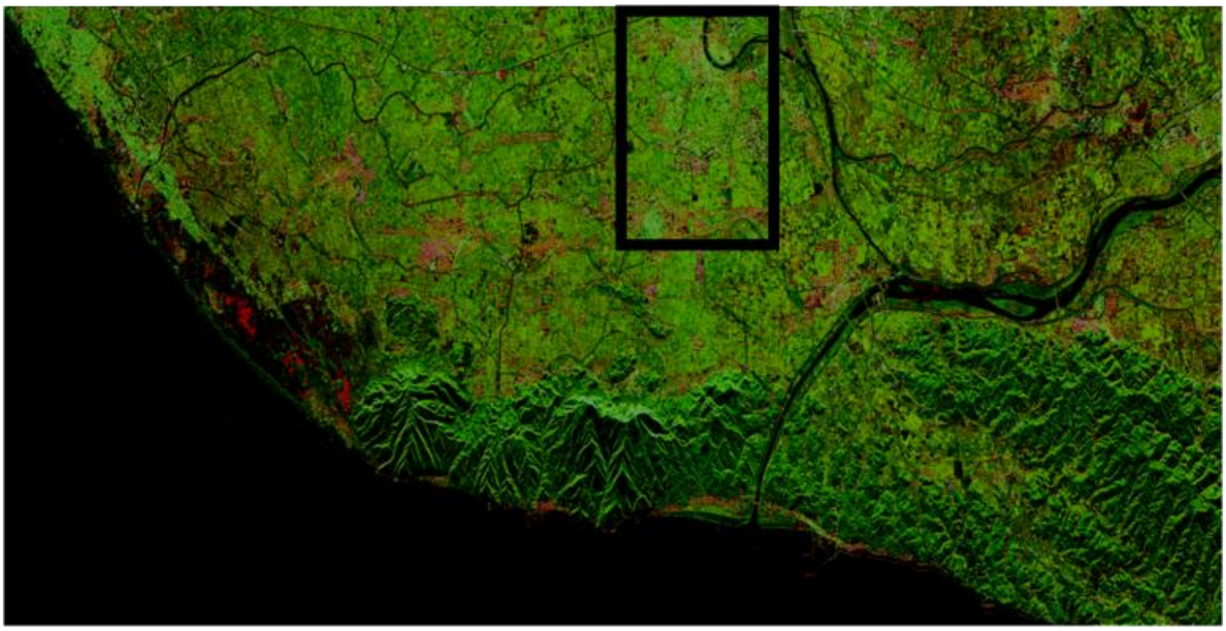

(b)

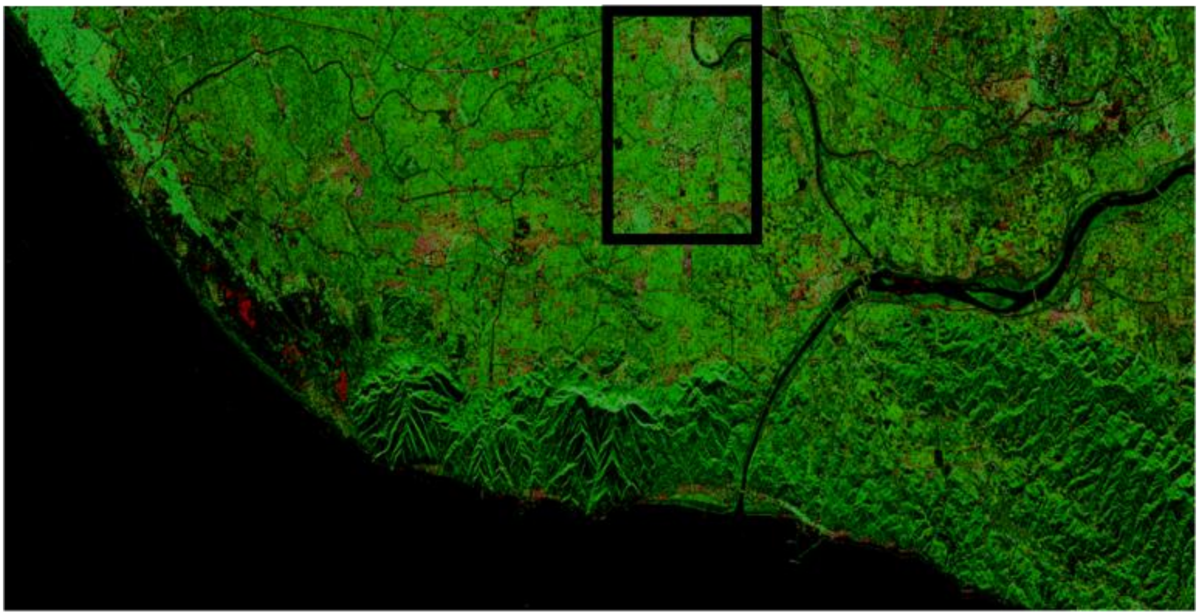

(c)

Fig. 5.1. Color-coded decomposition image with Red (m_d: double bounce), Green (m_v: volume scattering), and Blue (m_s: surface scattering). (a) New hybrid decomposition with rotation about the line of sight (real unitary transformation) and extended volume scattering model. (b) Original hybrid decomposition with rotation about the line of sight (real unitary transformation). (c) Original hybrid decomposition.

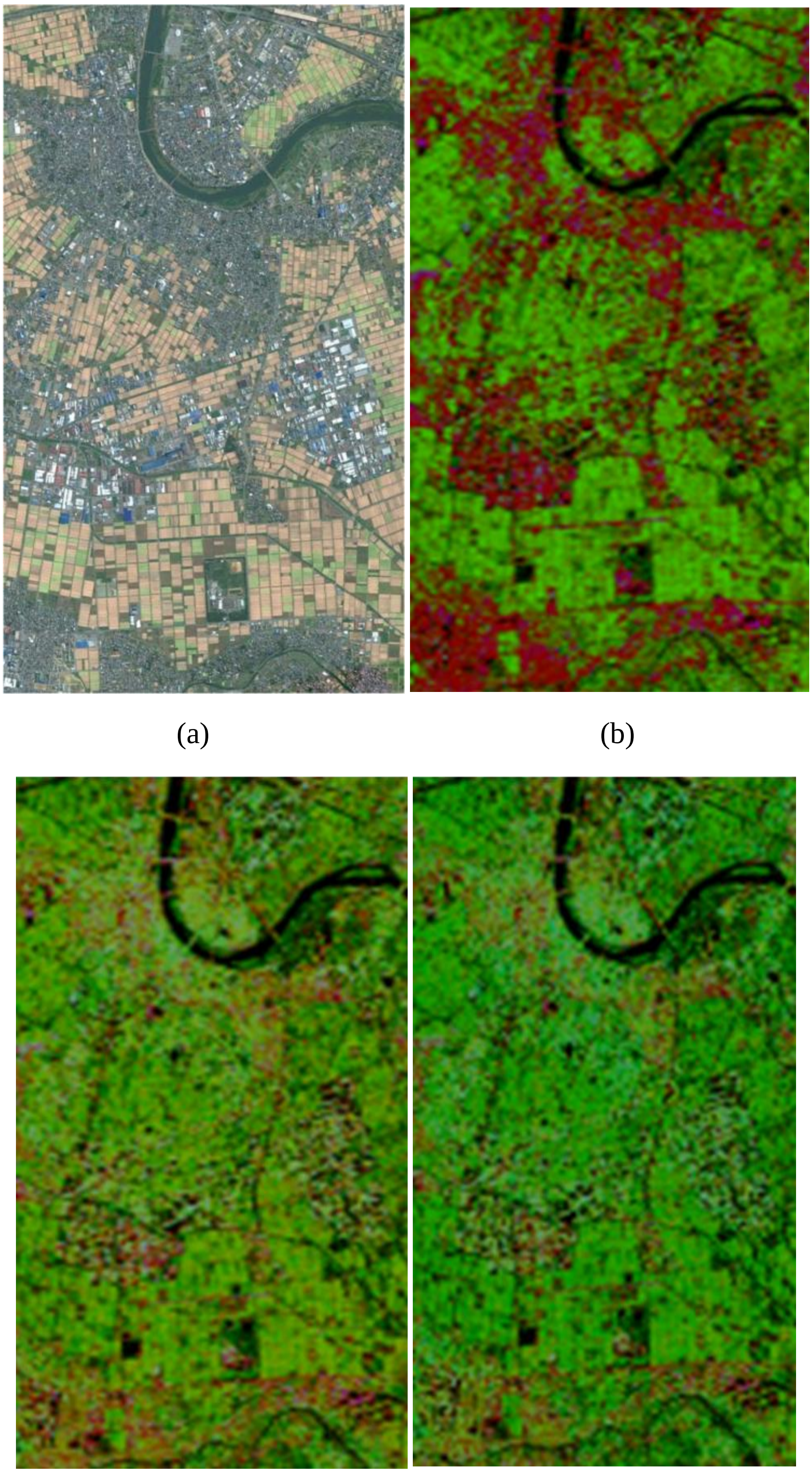

(a) (b)

(c) (d)

Fig. 5.2. Close-up areas of black box areas on Fig. 5.1, color-coded decomposition image with Red (m_d: double-bounce), Green (m_v: volume scattering), Blue (m_s: surface scattering). (a) Google Earth optical image. (b) New hybrid decomposition with rotation about the line of sight and extended volume scattering model. (c) Original hybrid decomposition with rotation about the line of sight. (d) Original hybrid decomposition.

5.7 Summary and Conclusions

An improved hybrid decomposition scheme S3H has been presented in this chapter. The resultant decomposition image is good as compared to that in Cloude (2009) F3H$_c$. However, the overall results of the improved hybrid decomposition scheme are good enough subject to relying on the reflection symmetric condition, but the results over highly oriented inclined regions are not reasonable and are mixed with contributions from vegetation areas. In addition, an alternative procedure has been proposed to account for the reflection symmetric depolarization and all polarimetric information in decomposition. In the near future, the effects of reflection symmetric depolarization and accounting for all polarimetric information in the decomposition schemes will be analyzed in more detail.

Chapter 6 General Four-Component Scattering Power Decomposition with Unitary Transformation of Coherency Matrix G4U

Science is simple and nature extremely complex; the complex nature becomes the simple science, once discovering it

6.1. Abstract

This Chapter 6 presents a new general four-component scattering power decomposition method G4U by implementing a double-set of unitary transformations for the polarimetric coherency matrix. There exist nine real independent observation parameters in the 3 x 3 coherency matrix with respect to the second order statistics of polarimetric information. The proposed method accounts for all observation parameters in the new scheme. It is known that the existing four-component decomposition method S4R reduces the number of observation parameters from nine to eight by rotation of the coherency matrix, and that it accounts for six parameters out of eight, leaving 2 parameters (i.e., real and imaginary parts of T_{13} component) unaccounted for. By implementing an additional special unitary transformation to this rotated coherency matrix formulations of Y4R and S4R, it became possible to reduce the number of independent parameters from eight to seven. After the unitary transformation, the new four-component decomposition is carried out that accounts for all parameters in the coherency matrix including the remaining T_{13} component. Therefore, the proposed method G4U makes use of full utilization of the polarimetric coherency phase information provided by FULL-POL-SAR in the expanded alternate decomposition formulation.

The decomposition also employs an extended volume scattering model, which discriminates the volume scattering between dipole and dihedral scattering structures caused by the cross-polarized *HV* component. It is found that the new method enhances the double-bounce scattering contributions over the urban areas compared with those of the existing four-component decomposition, resulting from the full utilization of polarimetric coherency phase information, which requires highly improved acquisitions of the cross-polarized *HV* component above the strongly suppressed noise floor.

6.2. Introduction

Scattering power decompositions have been a research topic in radar polarimetry for the analysis of FULL-POL-SAR data image data for the past two decades (Arii *et al.* 2011; Cloude 2009; Freeman and Durden 1998; Lee and Pottier 2009; Lee and Ainsworth 2011; Touzi 2007; vanZyl and Kim 2010; Yamaguchi 2007; Yamaguchi *et al.* 2005; Yamaguchi *et al.* 2006; Yajima *et al.* 2008; Yamaguchi *et al.* 2011). There exist nine real independent polarimetric parameters in the 3 x 3 coherency or covariance matrices. Physical model-based scattering power decomposition tries to account for these polarimetric parameters as much as possible in the decomposition. The original three-component decomposition was proposed by Freeman and Durden (1998) under the reflection symmetry condition that the cross correlation between the co- and cross-polarized scattering elements is close to zero for natural distributed objects resulted from findings based on relatively poor POL-SAR scattering matrix measurements with the cross- polarized *HV* component disappearing in the noise floor and being neglected. This method accounts for five terms out of nine independent parameters. In order to accommodate the decomposition scheme for more general scattering cases encountered in urban areas or by more complicated geometric scattering structures, Yamaguchi *et al.* (2005) have added a helix scattering term and proposed the four-component decomposition. This helix power is generated by the imaginary part of $T_{23} = \left\langle \left(S_{HH} - S_{VV} \right) S_{HV}^{*} \right\rangle$ in the coherency matrix, and the related method accounts for six parameters out of nine, leaving three unaccounted for. Then, by using the rotation of coherency matrix, Lee and Ainsworth (2011) and Yamaguchi *et al.* (2011) reduced the number of polarization parameters from nine to eight. These methods yielded better decomposition results by accounting for six parameters out of eight (Yamaguchi *et al.* 2011). The unaccounted parameters are the real and imaginary parts of $T_{13} = \left\langle (S_{HH} + S_{VV})\, S_{HV}^{*} \right\rangle$ in the coherency matrix. They still remain unaccounted in any of the known physical scattering model-based decomposition methods (Freeman and Durden 1998; Lee and Ainsworth 2011; Yamaguchi *et al.* 2005; Yamaguchi *et al.* 2011).

In this Chapter 6, a new general four-component decomposition method G4U is proposed using a special unitary transformation to the rotated coherency matrix, which has been used in the existing four-component decomposition (Yamaguchi *et al.* 2011) Y4R, see Chapter 3. Since unitary transformations do not change any information included in the coherency matrix, the rotated coherency matrix is transformed by a special unitary transformation to eliminate the T_{23} element. The new features are the reduction in the number of observed polarization parameters from eight to seven, and accounting for the remaining T_{13} element. This new four-component decomposition finally accounts for seven terms out of seven polarimetric parameters. It is shown that this method yields accurate and/or similar decomposition images compared with those by the existing four-component decomposition (Yamaguchi *et al.* 2011; Sato *et al.* 2012).

In Section 6.3, a basic principle for reduction of polarization parameters is explained by implementing the unitary transformation for the coherency matrix. Based on the unitary transformation of the rotated coherency matrix, a new four-component scattering power decomposition scheme is carried out in Section 6.4. At this decomposition stage, all elements of the coherency matrix are utilized to derive four-component scattering powers, i.e., surface, double-bounce, volume, and helix scattering power values. An extended volume scattering model is also incorporated to discriminate against volume scattering between dipole and dihedral scattering structures caused by the cross-polarized *HV* component. Section 6.5 shows some decomposition results in comparison with the existing four-component scattering power decomposition Y4R and S4R. The summary and conclusion is given in Section 6.6.

6.3 Basic Principle for Double Unitary Transformation

By acquiring the scattering matrix data sets, the corresponding coherency matrix can be recovered, which retains the second order statistics of polarimetric information. There are nine independent and real-valued polarization parameters included in the general form of the coherency matrix (6.1).

$$\langle [T] \rangle = \begin{bmatrix} T_{11} & T_{12} & T_{13} \\ T_{21} & T_{22} & T_{23} \\ T_{31} & T_{32} & T_{33} \end{bmatrix} \tag{6.1}$$

Unitary transformation preserves all information contained in the 3 x 3 positive definite coherency matrices without loss of generality. This guarantees that observed polarimetric information remains in the coherency matrix after unitary transformation. Using this mathematical property, it is possible to transform the measured coherency matrix (6.1) to a new one with $T_{23} = 0$ as

$$\langle[T']\rangle = \begin{bmatrix} T'_{11} & T'_{12} & T'_{13} \\ T'_{21} & T'_{22} & 0 \\ T'_{31} & 0 & T'_{33} \end{bmatrix} \qquad . \tag{6.2}$$

If the T_{23} element is eliminated, the number of independent information in the coherency matrix becomes seven, for which the new scattering power decomposition is carried out. The reason why we choose T_{23} element is that the helix scattering is directly related to this term (more details are given in the Annexure A). In order to achieve T_{23} = 0, the unitary transformation is implemented twice.

The first one is the rotation of about the line of sight (Yamaguchi *et al.* 2011)

$$\langle[T(\theta)]\rangle = [R(\theta)]\langle[T]\rangle[R(\theta)]^{\dagger} \tag{6.3}$$

with a unitary rotation matrix,

$$[R(\theta)] = \begin{bmatrix} 1 & 0 & 0 \\ 0 & \cos 2\theta & \sin 2\theta \\ 0 & -\sin 2\theta & \cos 2\theta \end{bmatrix} \tag{6.4}$$

The angle θ is chosen as to minimize the T_{33} element (Yamaguchi *et al.* 2011)

$$2\theta = \frac{1}{2}\, tan^{-1}\left(\frac{2\ \mathrm{Re}\ \{T_{23}\}}{T_{22} - T_{33}}\right) \tag{6.5}$$

After this rotation, the T_{23} element becomes purely imaginary,

$$T_{23}(\theta) = j\ \mathrm{Im}\{T_{23}\}. \tag{6.6}$$

Then, the second unitary transformation is employed such that

$$\langle[T(\varphi)]\rangle = [U(\varphi)]\langle[T(\theta)]\rangle[U(\varphi)]^{\dagger} \tag{6.7}$$

with a special unitary transform matrix

$$[U(\varphi)] = \begin{bmatrix} 1 & 0 & 0 \\ 0 & \cos 2\varphi & j\sin 2\varphi \\ 0 & j\sin 2\varphi & \cos 2\varphi \end{bmatrix} \tag{6.8}$$

The angle φ is derived so as to minimize the T_{33} element in a way similar to θ (see Chapter 3)

$$2\varphi = \frac{1}{2}\, tan^{-1}\left(\frac{2\ \mathrm{Im}\ \{T_{23}(\theta)\}}{T_{22}(\theta) - T_{33}(\theta)}\right) \tag{6.7}$$

This unitary transformation yields the coherency matrix element as

$$T_{11}(\varphi) = T_{11}(\theta) = T_{11}$$

$$T_{12}(\varphi) = T^{*}_{21}(\varphi) = T_{12}(\theta)\cos 2\varphi - j\ T_{12}(\theta)\sin 2\varphi$$

$$T_{13}(\varphi) = T^{*}_{31}(\varphi) = T_{13}(\theta)\cos 2\varphi - j\ T_{12}(\theta)\sin 2\varphi$$

$$T_{22}(\varphi) = T_{22}(\theta)\cos^{2} 2\varphi + T_{33}(\theta)\sin^{2} 2\varphi + \mathrm{Im}\ \{T_{23}(\theta)\}\sin 4\,\varphi$$

$$T_{23}(\varphi) = T^{*}_{32}(\varphi) = \mathrm{Re}\ \{T_{23}(\theta)\}$$

$$T_{33}(\varphi) = T_{33}(\theta)\cos^2 2\varphi + T_{22}(\theta)\sin^2 2\varphi - \text{Im}\{T_{23}(\theta)\}\sin 4\varphi. \qquad (6.10)$$

This second unitary transformation forces the T_{23} element to be zero using (6.10) and (6.6).

$$T_{23}(\varphi) = \text{Re}\{T_{23}(\theta)\} = \text{Re}\{j\,\text{Im}\{T_{23}\}\} = 0. \qquad (6.11)$$

Hence, the T_{23} element is completely eliminated as shown in (6.11). Therefore, the number of independent polarization parameters from nine to seven can be theoretically reduced by rotating the unitary transformation matrix twice, as shown in (6.2). This means that the elements of $\langle[T']\rangle$ in (6.2) are equal to the elements of $\langle[T(\varphi)]\rangle$ in (6.7), i.e.,

$$\langle[T']\rangle = \langle[T(\varphi)]\rangle. \qquad (6.12)$$

It should be noted that the T_{13} element still remains as a complex number, which has not been incorporated in any physical model-based decomposition.

6.4 New Four-Component Scattering Power Decomposition

In this section, a new four-component scattering power decomposition is presented using (6.7). The four-component power values represent surface scattering power P_s, double-bounce scattering power P_d, volume scattering power P_v, and helix scattering power P_c. Illustrative examples for these power values are shown in Fig. 6.1, which are well known from the pertinent literature (Freeman and Durden 1998; Lee and Ainsworth 2011; Yamaguchi *et al.* 2005; Yamaguchi *et al.* 2011).

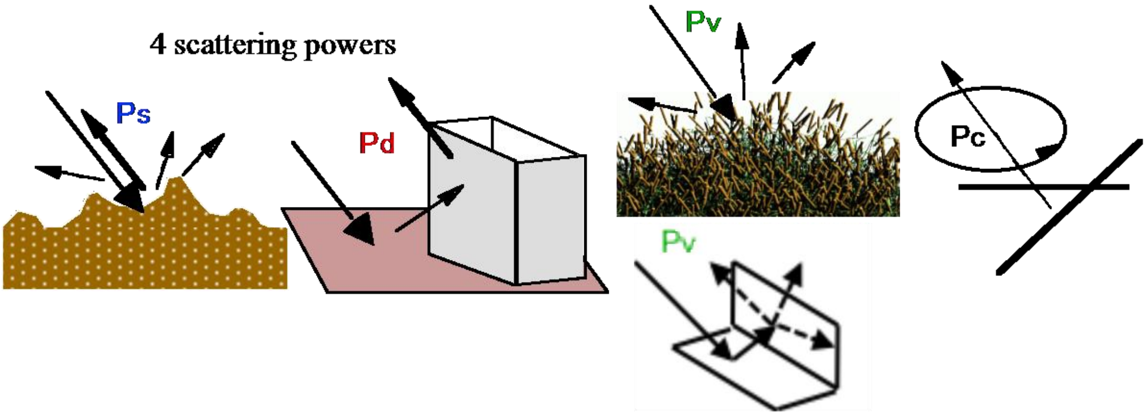

Fig. 6.1 Illustrative examples of four-component scattering power values: surface scattering power P_s, double-bounce scattering power P_d, volume scattering power P_v, and helix scattering power P_c.

The starting point is the four-component decomposition after the rotation (6.4), expressed as

$$\langle[T(\theta)]\rangle = f_s\langle[T]\rangle_{\text{surface}} + f_d\,\langle[T]\rangle_{\text{double}} + f_v\,\langle[T]\rangle_{\text{vol}} + f_c\langle[T]\rangle_{\text{helix}} \qquad (6.13)$$

where f_s, f_d, f_v and f_c are expansion coefficients to be determined, and the four sub-matrices represent physical scattering models in the form of coherency matrix description (Yamaguchi *et al.* 2011; Sato *et al.* 2012). The details are given in Chapter 2 and Chapter 4. In this expression, six terms out of eight parameters are accounted for, for which the unaccounted two terms are real and imaginary parts of T_{13}. Now we transform (6.13) using unitary transformation (6.7) so that the T_{13} element can be accounted for. The model expansion can be transformed from the rotated basis to the new unitary basis such that

$$\begin{aligned}\langle[T']\rangle &= \langle[T(\varphi)]\rangle = [U(\varphi)]\langle[T(\theta)]\rangle[U(\varphi)]^{\dagger} \\ &= [U(\varphi)]\left(f_s\langle[T]\rangle_{\text{surface}} + f_d\langle[T]\rangle_{\text{double}} + f_v\langle[T]\rangle_{\text{vol}} + f_c\langle[T]\rangle_{\text{helix}} \right)[U(\varphi)]^{\dagger} \\ &= f_s\langle[T(\varphi)]\rangle_{\text{surface}} + f_d\langle[T(\varphi)]\rangle_{\text{double}} + f_v\langle[T(\varphi)]\rangle_{\text{vol}} + f_c\langle[T(\varphi)]\rangle_{\text{helix}}\,. \quad (6.14)\end{aligned}$$

The expansion matrices on the right hand side of (6.14) after unitary transformation become as derived in detail next.

6.4.1 Theoretical expansion matrices for scattering models

The expansion matrix for surface scattering is expressed as

$$\langle[T(\varphi)]\rangle_{\text{surface}} = [U(\varphi)]\langle[T]\rangle_{\text{surface}}[U(\varphi)]^{\dagger}$$

$$= [U(\varphi)]\begin{bmatrix} 1 & \beta^* & 0 \\ \beta & |\beta|^2 & 0 \\ 0 & 0 & 0 \end{bmatrix}[U(\varphi)]^{\dagger} = \begin{bmatrix} 1 & \beta^*\cos 2\varphi & -j\,\beta^*\sin 2\varphi \\ \beta\,\cos 2\varphi & |\beta|^2\,\cos^2 2\varphi & -j|\beta|^2\,\dfrac{\sin 4\varphi}{2} \\ j\,\beta\sin 2\varphi & j|\beta|^2\,\dfrac{\sin 4\varphi}{2} & |\beta|^2\,\sin^2 2\varphi \end{bmatrix}. \quad (6.15)$$

The double-bounce scattering model is defined as

$$\langle[T(\varphi)]\rangle_{\text{double}} = [U(\varphi)]\langle[T]\rangle_{\text{double}}[U(\varphi)]^{\dagger}$$

$$= [U(\varphi)]\begin{bmatrix} |\alpha|^2 & \alpha & 0 \\ \alpha^* & 1 & 0 \\ 0 & 0 & 0 \end{bmatrix}[U(\varphi)]^{\dagger} = \begin{bmatrix} |\alpha|^2 & \alpha\cos 2\varphi & -j\,\alpha\sin 2\varphi \\ \alpha^*\,\cos 2\varphi & \cos^2 2\varphi & -j\,\dfrac{\sin 4\varphi}{2} \\ j\,\alpha^*\sin 2\varphi & j\,\dfrac{\sin 4\varphi}{2} & \sin^2 2\varphi \end{bmatrix}. \quad (6.16)$$

The helix scattering model is written as

$$\langle[T(\varphi)]\rangle_{\text{helix}} = [U(\varphi)]\langle[T]\rangle_{\text{helix}}[U(\varphi)]^{\dagger}$$

$$= [U(\varphi)]\frac{1}{2}\begin{bmatrix} 0 & 0 & 0 \\ 0 & 1 & \pm j \\ 0 & \mp j & 1 \end{bmatrix}[U(\varphi)]^{\dagger} = \frac{1}{2}\begin{bmatrix} 0 & 0 & 0 \\ 0 & 1 \pm \sin 4\varphi & \pm j\,\cos 4\varphi \\ 0 & \mp j\,\cos 4\varphi & 1 \mp \sin 4\varphi \end{bmatrix}. \quad (6.17)$$

6.4.2 Four-component Decomposition Depending on the Volume Scattering Model

Since there are four scattering models (as explained in Chapter 4) for volume scattering, according to the generation of the cross-polarized *HV* term, the decomposition scheme is applied accordingly. For volume scattering caused by the *HV* component by vegetation, one of the following distributions is chosen based on the magnitude balance of $\langle|S_{HH}|^2\rangle$ and $\langle|S_{VV}|^2\rangle$ (Yamaguchi *et al.* 2005), i.e., 1) *uniform* distribution, 2) *cosine* distribution, or 3) *sin* distribution.

1) Uniform distribution: $p(\theta) = \dfrac{1}{2\pi}$

$$\langle [T(\varphi)] \rangle_{\mathrm{vol}} = [U(\varphi)] \frac{1}{4} \begin{bmatrix} 2 & 0 & 0 \\ 0 & 1 & 0 \\ 0 & 0 & 1 \end{bmatrix} [U(\varphi)]^{\dagger} = \frac{1}{4} \begin{bmatrix} 2 & 0 & 0 \\ 0 & 1 & 0 \\ 0 & 0 & 1 \end{bmatrix} \tag{6.18}$$

The element relations after the unitary transformation (6.14) are expanded. The expansion of (6.14) leads to the following relations,

$$\begin{aligned}
T'_{11} &= f_s + f_d\, |\alpha|^2 + \tfrac{1}{2}\, f_v \\
T'_{22} &= (\, f_s\, |\beta|^2 + f_d\,) \cos^2 2\varphi + \frac{1}{4}\, f_v + \frac{1}{2}\, f_c\, (1 \pm \sin 4\varphi) \\
T'_{22} &= (\, f_s\, |\beta|^2 + f_d\,) \sin^2 2\varphi + \frac{1}{4}\, f_v + \frac{1}{2}\, f_c\, (1 \mp \sin 4\varphi) \\
T'_{12} &= (\, f_s\, \beta^* + f_d\, \alpha) \cos 2\varphi \\
T'_{13} &= -j(\, f_s\, \beta^* + f_d\, \alpha) \sin 2\varphi \\
T'_{23} &= -(\, f_s\, |\beta|^2 + f_d\,) \sin 4\varphi \ \pm f_c\ \cos 4\varphi = 0
\end{aligned} \tag{6.19}$$

Arrangement of the element relations provides 5 equations with 6 unknowns (i.e., α, β, f_s, f_d, f_v, and f_c).

$$T'_{11} = f_s + f_d\, |\alpha|^2 + \frac{1}{2}\, f_v \tag{6.20}$$

$$T'_{22} + T'_{33} = \ f_s\, |\beta|^2 + f_d + \frac{1}{2}\, f_v + f_c \tag{6.21}$$

$$T'_{22} - T'_{33} = (\, f_s\, |\beta|^2 + f_d) \cos 4\varphi \pm f_c \sin 4\varphi \tag{6.22}$$

$$T'_{12} + \ T'_{13} = (\, f_s\, \beta^* + f_d\, \alpha)\, (\cos 2\varphi - \ j \sin 2\varphi) = (\, f_s\, \beta^* + f_d\, \alpha)\, e^{-j2\varphi} \tag{6.23}$$

$$(\, f_s\, |\beta|^2 + f_d\,) \sin 4\varphi = \pm f_c\ \cos 4\varphi \tag{6.24}$$

From (6.24) and (6.22) together with (6.10) and (6.21), f_c and f_v can be derived

$$f_c = P_c = |(T'_{22} - T'_{33}) \sin 4\varphi| = 2\ \ |\mathrm{Im}\{T_{23}(\theta)\}| = \ 2\ \ |\mathrm{Im}\{T_{23}\}| \tag{6.25}$$

$$f_v = P_v = 2[(T'_{22} - T'_{33}) - \ (T'_{22} - T'_{33}) \cos 4\varphi - f_c] = 2\ [2\, T_{33}(\theta) - f_c] \tag{6.26}$$

Once f_c and f_v are determined, we have a set of three equations with four unknowns (i.e., α, β, f_s, and f_d)

$$\begin{cases} f_s + f_d\, |\alpha|^2 = S \\ f_s\, |\beta|^2 + f_d = D \\ f_s\, \beta^* + f_d\, \alpha = C \end{cases} \tag{6.27}$$

where

$$\begin{cases} S = T'_{11} - \frac{1}{2} f_v \\ D = T'_{22} + T'_{33} - \frac{1}{2} f_v - f_c \\ C = (T'_{12} + T'_{13}) e^{j2\varphi} \end{cases} \qquad (6.28a)$$

(6.28a) can be written using (6.10) as

$$\begin{cases} S = T_{11}(\theta) - \frac{1}{2} P_v \\ D = T_{22}(\theta) + T_{33}(\theta) - \frac{1}{2} P_v - P_c \\ C = T_{12}(\theta) + T_{13}(\theta) \end{cases} \qquad (6.28b)$$

or

$$\begin{cases} S = T_{11} - \frac{1}{2} P_v \\ D = TP - P_v - P_c - S \\ C = T_{12}(\theta) + T_{13}(\theta) \end{cases} \qquad (6.28c)$$

where *TP* denotes total power.

2) Cosine distribution: $p(\theta) = \frac{1}{2} \cos\theta$

$$\langle [T(\varphi)] \rangle_{\text{vol}} = [U(\varphi)] \frac{1}{30} \begin{bmatrix} 15 & -5 & 0 \\ -5 & 7 & 0 \\ 0 & 0 & 8 \end{bmatrix} [U(\varphi)]^\dagger$$

$$= \frac{1}{30} \begin{bmatrix} 15 & -5\cos 2\varphi & j\,5\sin 2\varphi \\ -5\cos 2\varphi & 7 + \sin^2 2\varphi & j\frac{\sin 4\varphi}{2} \\ -j5\sin 2\varphi & -j\frac{\sin 4\varphi}{2} & 7 + \cos^2 2\varphi \end{bmatrix} \qquad (6.29$$

The expression (6.14) is expanded in the same way as in 1) uniform distribution. After the expansion and rearrangement, a similar set of three equations with four unknowns can be obtained.

$$\begin{cases} f_s + f_d\,|\alpha|^2 = S \\ f_s\,|\beta|^2 + f_d = D \\ f_s\,\beta^* + f_d\,\alpha = C \end{cases} \qquad (6.30)$$

where

$$\begin{cases} S = T_{11} - \frac{1}{2} P_v \\ D = TP - P_v - P_c - S \\ C = T_{12}(\theta) + T_{13}(\theta) + \frac{1}{6} P_v \end{cases} \qquad (6.31)$$

$$\begin{cases} \quad f_c = P_c = \; 2 \;\, |\mathrm{Im}\{T_{23}\}| \\ f_v = P_v = 2\,[2\, T_{33}(\theta) - f_c]\,. \end{cases} \tag{6.32}$$

3) Sin distribution: $p(\theta) = \frac{1}{2}\sin\theta$

$$\langle [T(\varphi)] \rangle_{\mathrm{vol}} = [U(\varphi)]\,\frac{1}{30}\begin{bmatrix} 15 & 5 & 0 \\ 5 & 7 & 0 \\ 0 & 0 & 8 \end{bmatrix}[U(\varphi)]^{\dagger}$$

$$= \frac{1}{30}\begin{bmatrix} 15 & 5\cos 2\,\varphi & -j\,5\sin 2\,\varphi \\ 5\cos 2\,\varphi & 7+\sin^2 2\varphi & j\,\dfrac{\sin 4\,\varphi}{2} \\ j5\sin 2\varphi & -j\,\dfrac{\sin 4\,\varphi}{2} & 7+\cos^2 2\varphi \end{bmatrix} \tag{6.33}$$

After a similar expansion of (6.14) and rearrangement, it can be obtained a similar set of three equations with four unknowns.

$$\begin{cases} f_s + f_d\,|\alpha|^2 = S \\ f_s\,|\beta|^2 + f_d = D \\ f_s\,\beta^* + f_d\,\alpha = C \end{cases} \tag{6.34}$$

where

$$\begin{cases} S = T_{11} - \dfrac{1}{2}\,P_v \\ D = TP - \;P_v\; - P_c - S \\ C = T_{12}(\theta) + T_{13}(\theta) - \dfrac{1}{6}\;\,P_v \end{cases} \tag{6.35}$$

$$\begin{cases} \quad f_c = P_c = \; 2 \;\, |\mathrm{Im}\{T_{23}\}| \\ f_v = P_v = 2\,[2\, T_{33}(\theta) - f_c]\,. \end{cases} \tag{6.36}$$

4) For volume scattering caused by oriented dihedral scatter:

The following matrix is used:

$$\langle [T(\varphi)] \rangle_{\mathrm{vol}} = [U(\varphi)]\,\frac{1}{15}\begin{bmatrix} 0 & 0 & 0 \\ 0 & 7 & 0 \\ 0 & 0 & 8 \end{bmatrix}[U(\varphi)]^{\dagger}$$

$$= \frac{1}{15}\begin{bmatrix} 0 & 0 & 0 \\ 0 & 7+\sin^2 2\varphi & j\,\dfrac{\sin 4\,\varphi}{2} \\ 0 & -j\,\dfrac{\sin 4\,\varphi}{2} & 7+\cos^2 2\varphi \end{bmatrix} \tag{6.37}$$

After the expansion (6.14) and rearrangement, a set of three equations with four unknowns can be obtained.

$$\begin{cases} f_s + f_d\,|\alpha|^2 = S \\ f_s\,|\beta|^2 + f_d = D \\ f_s\,\beta^* + f_d\,\alpha = C \end{cases} \tag{6.38}$$

where

$$\begin{cases} S = T_{11} \\ D = TP - P_v - P_c - S \\ C = T_{12}(\theta) + T_{13}(\theta) \end{cases} \tag{6.39}$$

$$\begin{cases} f_c = P_c = 2\ |\mathrm{Im}\{T_{23}\}| \\ f_v = P_v = \dfrac{15}{16}\ [2\,T_{33}(\theta) - f_c] \end{cases} \tag{6.40}$$

6.4.3 Procedure to Solve 3 Equations with 4 Unknowns

The same set of three equations with 4 unknowns is obtained in (6.27), (6.30), and (6.34), respectively. In order to solve these equations, the same assumption as described in Chapter 2 is used to eliminate one of the unknowns (Freeman and Durden 1998; Lee and Ainsworth 2011; Yamaguchi *et al.* 2005; Yamaguchi *et al.* 2011). Since the volume scattering coefficient f_v and the helix scattering coefficient f_c are obtained, the remaining dominant scattering mechanism (surface scattering or double-bounce scattering) can be checked. The dominant scattering can be discriminated by the expansion of the C_{13} component for randomly distributed dipoles in the covariance matrix formulation (Yamaguchi *et al.* 2005)

$$\mathrm{Re}\,\{\, f_s\,\beta^* + f_d\ \alpha\} + \frac{1}{8}\, f_v - \frac{1}{4}\ f_c = \mathrm{Re}\,\{\langle S_{\mathrm{HH}} S_{\mathrm{VV}}^* \rangle\} \tag{6.41}$$

This equation can be rearranged to

$$\begin{aligned} C_0 &= 2\mathrm{Re}\,\{\, f_s\,\beta^* + f_d\ \alpha\} \\ &= 2\mathrm{Re}\,\{\langle S_{\mathrm{HH}} S_{\mathrm{VV}}^* \rangle\} - \frac{1}{4}\, f_v + \frac{1}{2}\ f_c \\ &= T_{11}(\theta) - T_{22}(\theta) - T_{33}(\theta) + P_c \\ &= 2T_{11} - TP + P_c\,. \end{aligned} \tag{6.42}$$

The sign of C_0 determines the dominant scattering mechanism, i.e., surface *versus* double-bounce scattering.

If $C_0 > 0$, it can be assumed that the surface scattering is dominant. Since the double-bounce scattering magnitude is negligible in this case, it can be assumed $|\alpha| \ll 1$ and fixed $\alpha = 0$. This condition leads to

$$f_s = S, \qquad \beta^* = \frac{C}{S}, \quad f_d = D - \frac{|C|^2}{S}\,. \tag{6.43}$$

If $C_0 \leq 0$, it can be assumed that the double-bounce scattering is dominant. Since the surface scattering magnitude is negligible in this case, it can be assumed $|\beta| \ll 1$ and putted $\beta^* = 0$. This condition leads to

$$f_d = D, \qquad \alpha = \frac{C}{D}, \quad f_s = S - \frac{|C|^2}{D}\,. \tag{6.44}$$

Once these coefficients are determined, the scattering powers can be derived from

$$P_s = f_s\,(1 + |\beta|^2) \tag{6.45}$$

$$P_d = f_d\,(1 + |\alpha|^2) \tag{6.46}$$

$$P_c = f_c \tag{6.47}$$

$$P_v = f_v \tag{6.48}$$

The equation (6.38) is solved with assumptions that double-bounce scattering is dominant so that the solution of (6.38) will be similar to the one of (6.44).

6.4.4 Decomposition Algorithm Implementation

The procedures in Sections 6.3 and 6.4 are summarized for implementation to POL-SAR image analysis directly. The corresponding flow-chart of the new four-component scattering power decomposition algorithm is shown in Fig.6.2. In the first stage before the decomposition, the measured coherency matrix is rotated about the line of sight (Yamaguchi *et al.* 2011), and then a unitary transformation is applied on the rotated coherency matrix to force $T_{23} = 0$ for various scattering model expressions. It should be noted that $\arctan 2$ should be used for obtaining (6.6) and (6.9) in the computer algorithm. The number of independent parameters in the coherency matrix is reduced from eight to seven by the unitary transformation. The decomposition starts by retrieving the helix scattering power at this stage. Then, the sign of a branch condition C_1 is checked for assigning the *HV* component, which ought to be recovered as precisely as ever possible and be acquired well above the noise floor. The condition is specifically developed for retrieving the *HV* component by dihedral scattering only in a similar way to (6.41) with (6.40),

$$\mathrm{Re}\,\{ f_s\,\beta^* + f_d\,\alpha\} - \frac{7}{30}\,f_v - \frac{1}{4}\,f_c = \mathrm{Re}\,\{\langle S_{\mathrm{HH}} S_{\mathrm{VV}}^*\rangle\} \tag{6.49}$$

$$\begin{aligned} C_1 &= 2\mathrm{Re}\,\{ f_s\,\beta^* + f_d\,\alpha\} \\ &= 2\mathrm{Re}\,\{\langle S_{\mathrm{HH}} S_{\mathrm{VV}}^*\rangle\} + \frac{7}{15}\,P_v + \frac{1}{2}\,P_c \\ &= T_{11}(\theta) - T_{22}(\theta) + \frac{7}{8}T_{33}(\theta) + \frac{1}{16}P_c \end{aligned} \tag{6.50}$$

Once assigned to the double-bounce scattering ($C_1 \le 0$), the dihedral expansion matrix (6.37) is used for the volume scattering. On other hand, if the surface scattering is assigned ($C_1 > 0$), one of the expansion matrices, i.e., (6.18), (6.29), or (6.33), is used for the volume scattering based on the magnitude balance of $\langle |S_{HH}|^2\rangle$ and $\langle |S_{VV}|^2\rangle$. After determination of the volume scattering power, it is possible to determine the dominant scattering mechanism (surface *versus* double-bounce) within the volume scattering by dipole scattering. Then, four scattering powers are obtained using C_0 in (6.42). This new decomposition accounts for inclusion of all the elements of the coherency matrix.

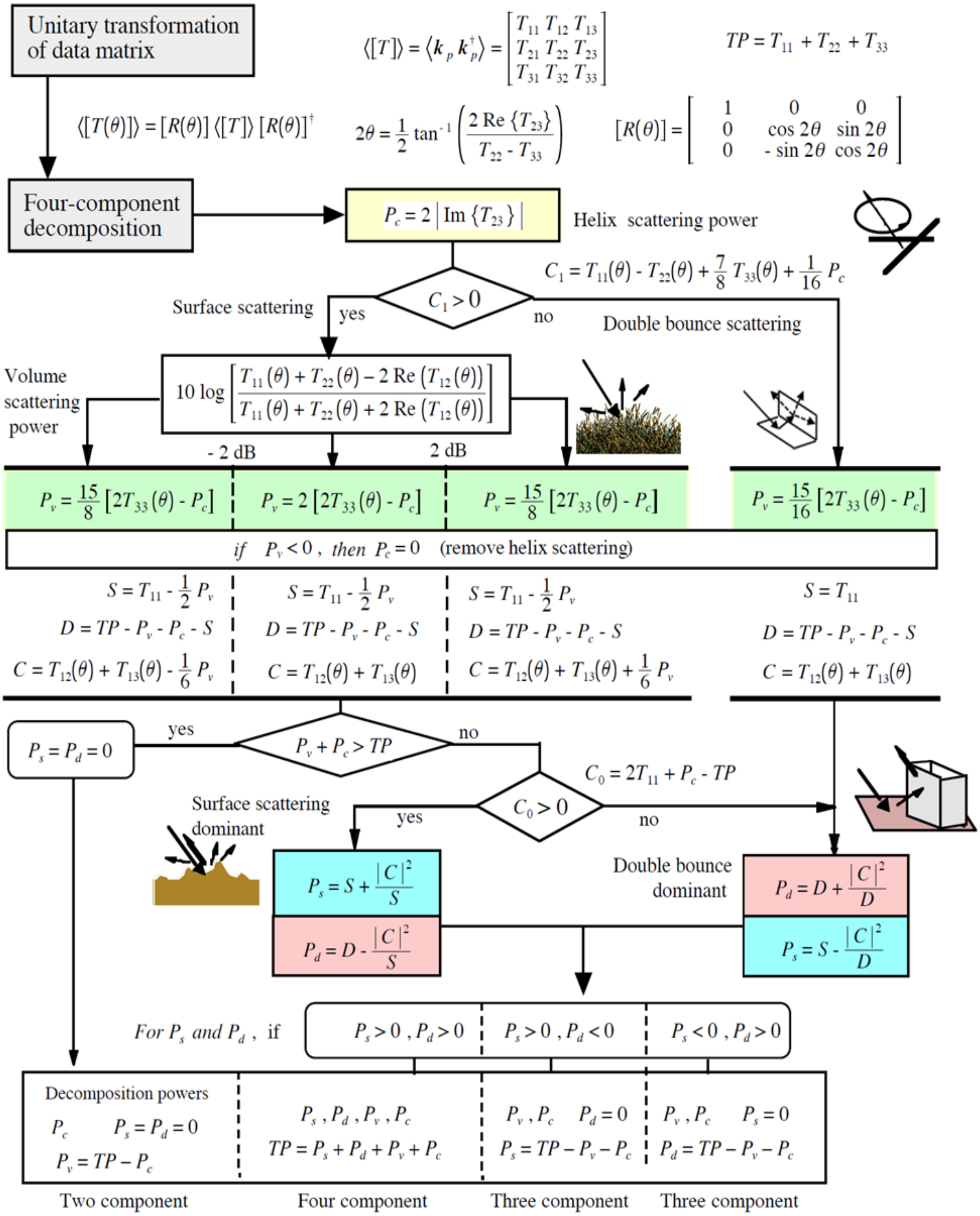

Fig. 6.2. Flow-chart of new four-component scattering power decomposition G4U. All calculations can be executed from the elements of coherency matrix.

6.5 Decomposition Results and Discussion

In order to compare the results by this advanced method, two existing methods Yamaguchi *et al.* (2011) Y4R and Sato *et al.* (2012) S4R are examined for scattering power decomposition.

Y4R: Four-component decomposition with rotation of coherency matrix (Yamaguchi *et al.* 2011), which makes Re$\{T_{23}\}$=0. This method minimizes the cross-polarized (T_{33}) scattering power generated by dipole scattering.

S4R: Four-component decomposition with rotation of coherency matrix (Sato *et al.* 2012), which makes Re$\{T_{23}\}$=0. This method minimizes the cross-polarized (T_{33}) scattering power generated by dipole scattering plus dihedral scattering. One modification is made before applying to FULL-POL-SAR data as compared to Sato *et al.* (2012). This modification is made in branch condition C_1 for selecting the dihedral volume scattering model. The modified C_1 is the same as proposed one in previous Section 6.4, whereas C_1 in Chapter 4 is T_{11} (θ) – T_{22} (θ) – (1/2) P_c (Sato *et al.* 2012). The modified C_1 is employed only for the purpose of retrieving dihedral scattering and of preserving volume scattering power in vegetation areas.

G4U: General four-component decomposition (the present method), which makes T_{23}=0 by unitary transformation of $\langle[T(\theta)]\rangle$. This method also minimizes the cross-polarized (T_{33}) scattering power generated by dipole plus dihedral scattering (Singh *et al.* 2013b).

These decomposition schemes are applied to many ALOS-PALSAR quad-polarization single-look complex level 1.1 images for verifying the correct implementation of this scheme. For example, color-coded images over heterogeneous areas in San Francisco images are displayed in Fig. 6.3 using ALOS-PALSAR quad-polarization data sets (Scene ID: ALPSRP276160750, acquired on April 1, 2011). The resolution is 30 m in the range and 5 m in the azimuth directions, respectively. The window size for the ensemble average in image processing was chosen as 2 in the range direction and 12 in the azimuth direction, which corresponds to 60 m × 60 m on the ground area. Results of the method derived in Y4R and S4R are compared with the proposed G4U method. It is seen that double-bounce scattering power P_d (red) is either enhanced or kept similar in Fig. 6.3(a) compared with Figs. 6.3(b) and 6.3(c) over the urban areas and man-made structures. It is also noticed that surface scattering power P_s (blue) is either enhanced or kept similar by the G4U, as compared to the S4R and the Y4R over the vegetated areas and sloped-surface areas.

The close-up view of white rectangular areas in Fig. 6.3 is shown in Fig. 6.4. The interesting observation relates to the 40^0 oriented urban areas in patch A in Fig. 6.4. The red color of the oriented urban area is enhanced in Fig. 6.4(a) as compared with 6.4(b) and 6.4(c). This enhancement of red serves to recognize man-made structures from vegetation areas more easily. This is because the unitary-transformation-based method is accounting for all elements of the coherency matrix.

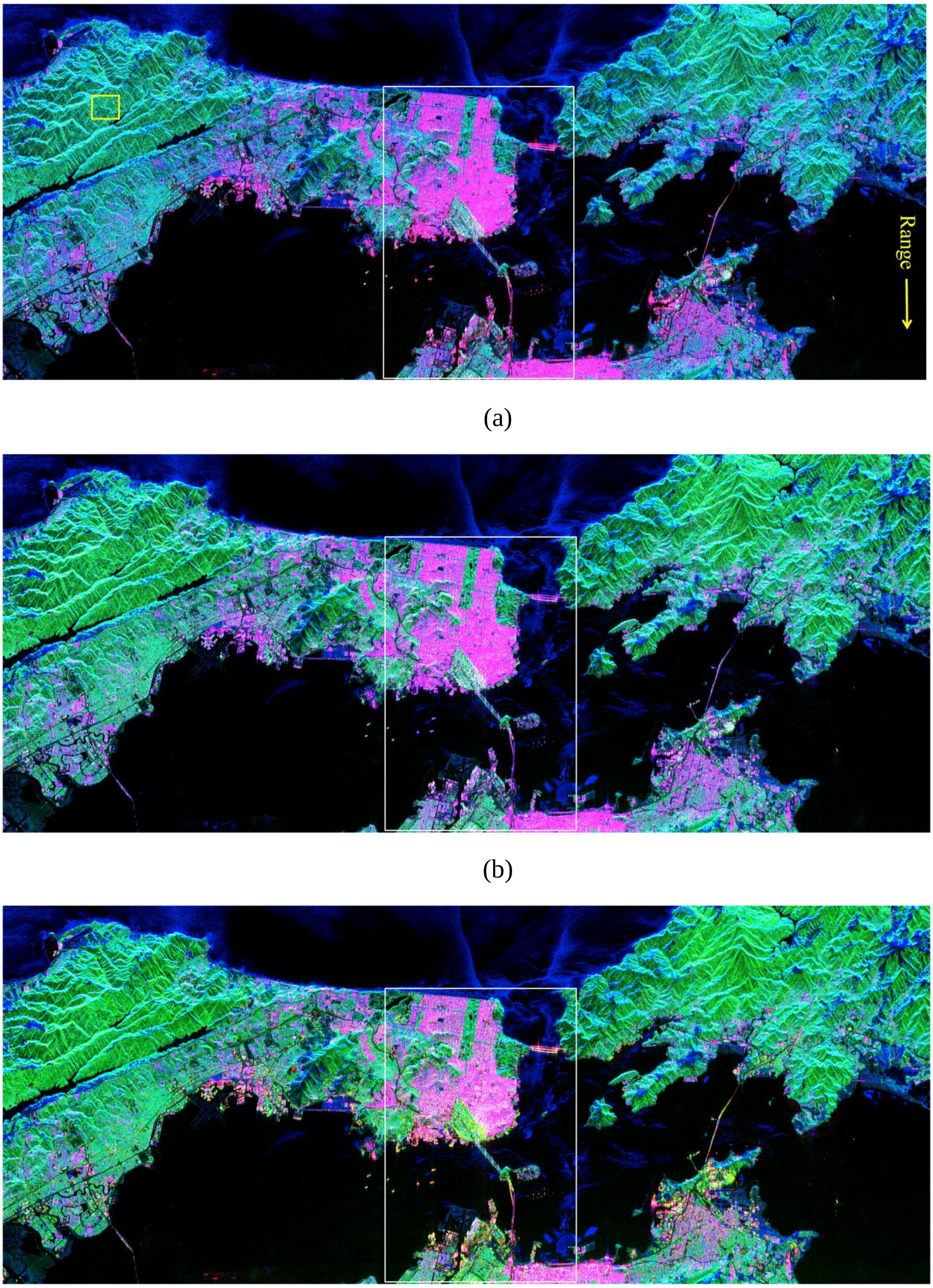

(a)

(b)

(c)

Fig.6.3. Color-coded scattering power decomposition with red (double-bounce), green (volume scattering), and blue (surface scattering): (a) G4U: new four-component decomposition with a unitary transform coherency matrix and $T_{23} = 0$ for which *HV* component is assigned to dihedral and dipole scattering; (b) S4R: four-component decomposition with $\mathrm{Re}\{T_{23}\} = 0$ rotation for which the *HV* component is assigned to dihedral

and dipole scattering; (c) Y4R: four-component decomposition with Re(T_{23}) = 0 rotation for which the *HV* component is assigned only to dipole scattering.

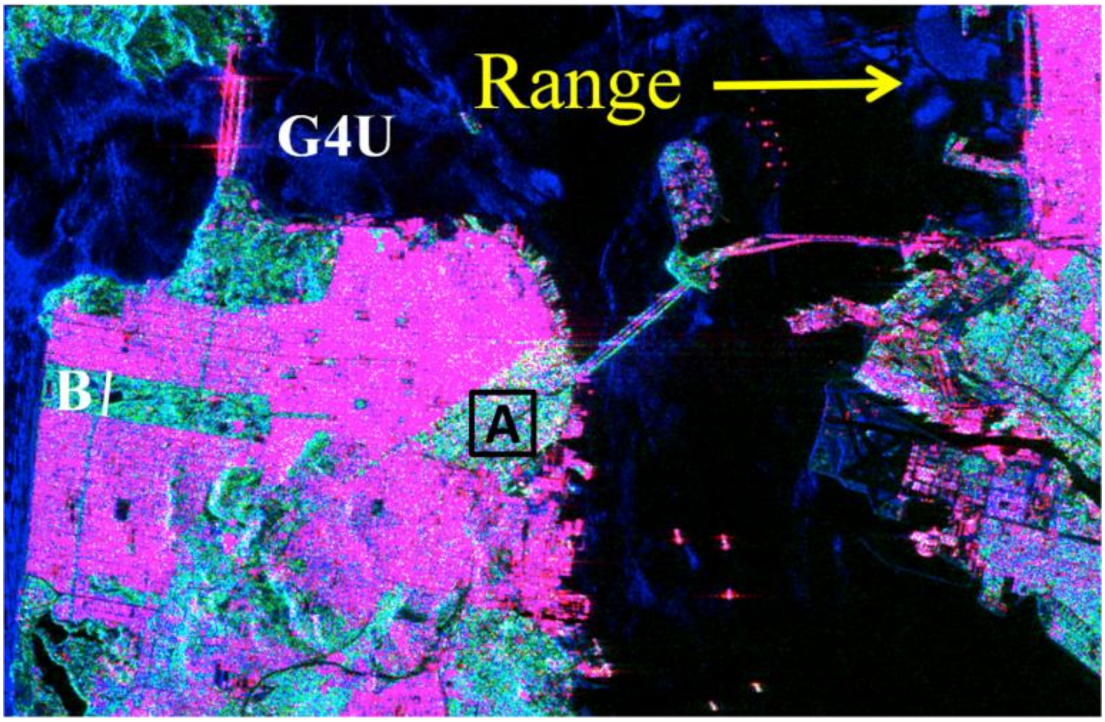

(a)

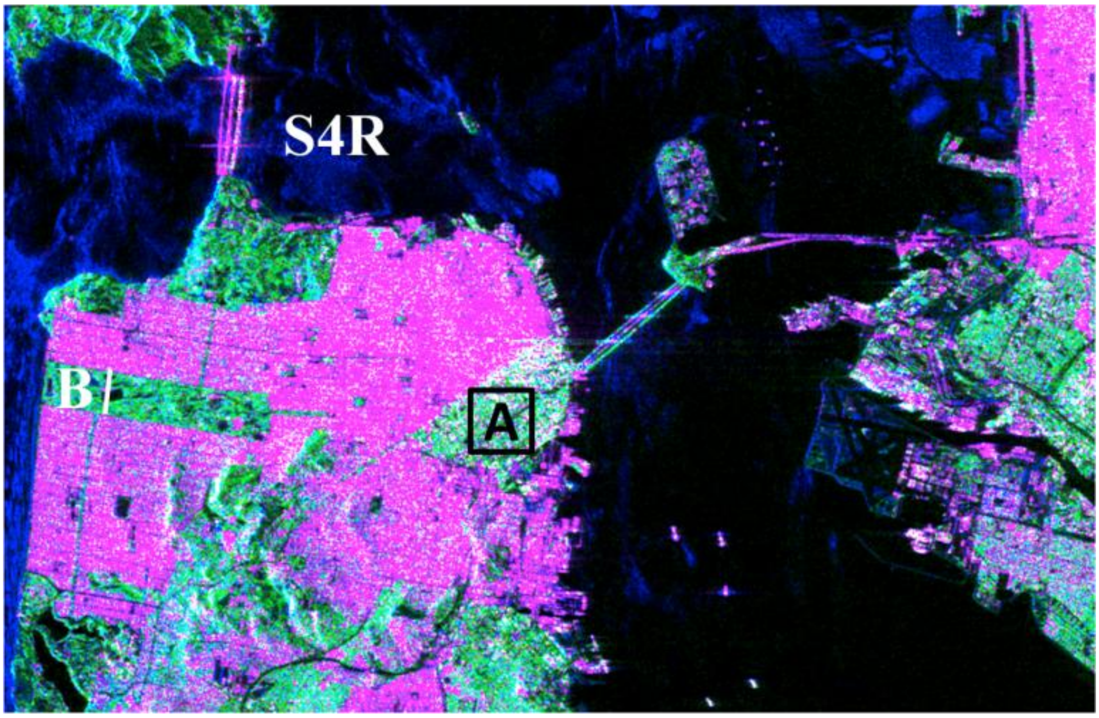

(b)

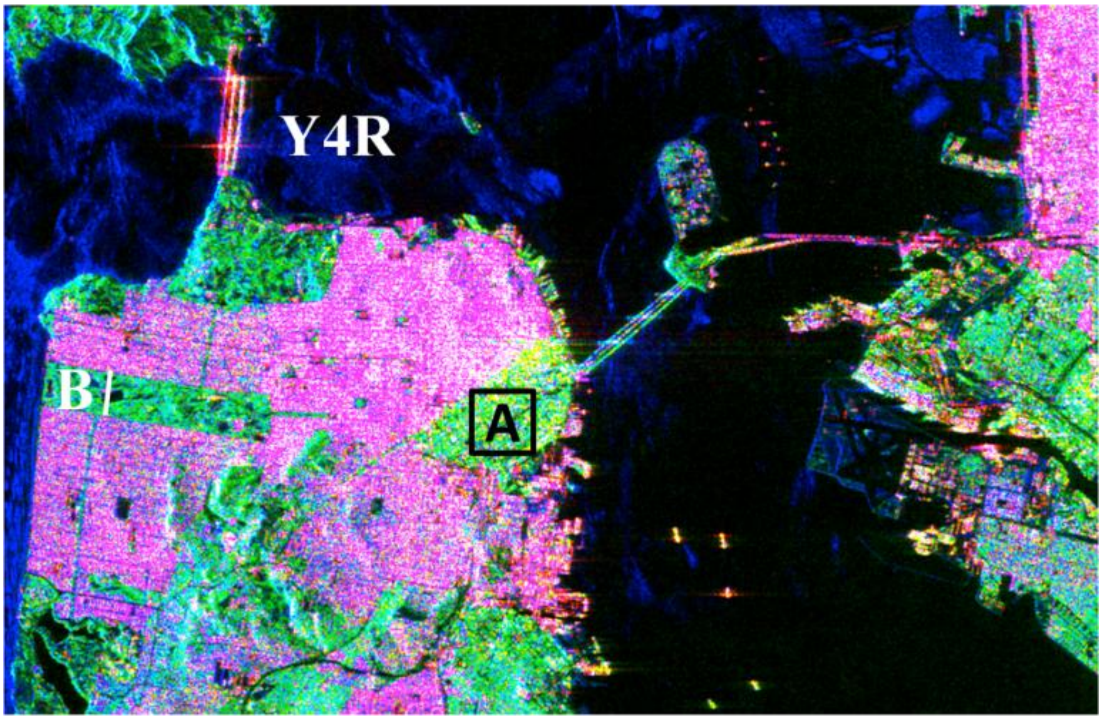

(c)

Fig. 6.4. Close-up view of white rectangular images in Fig.6.3: (a) G4U, new four-component decomposition with a unitary transformed coherency matrix; (b) S4R, four-component decomposition with Re$\{T_{23}\} = 0$ rotation for which the *HV* component is assigned to dihedral and dipole scattering; and (c) Y4R, Four-component decomposition with Re$(T_{23}) = 0$ rotation.

The decomposition power contributions of highly oriented dense urban areas in the San Francisco image are also shown in Table 6.1, for patch A (see the black line box in Fig. 6.4) in San Francisco images in Fig. 6.4, for a quantitative comparison of the existing four-component schemes *versus* the proposed four-component scheme. It can be seen that the volume scattering components of the G4U and S4R methods are decreased and the surface scattering components of the methods G4U and S4R are increased, as compared with those of the Y4R method. The double-bounce scattering component of the present method G4U is increased, as compared with those of the Y4R and S4R methods. The helix power remains invariant, which implies that the proposed method works well in highly oriented urban areas as compared to the existing improved extension of the three-component method in Y4R and S4R. In addition, the total power differences between the measured data and the decomposition results over the oriented urban areas for patch A are listed in Table 6.1. Although they are very small (less than 0.2%), the order of the relative errors is G4U < Y4R < S4R.

The decomposition power contribution of vegetation areas in the San Francisco image are also shown in Table 6.2, for the yellow line box in Fig. 6.3, for a quantitative comparison of the existing four-component schemes *versus* the proposed four-component scheme. It has been observed that the volume scattering components of the proposed methods are preserved and the surface scattering components of the present methods are increased, as compared with those of the Y4R and S4R methods. The double-bounce scattering components of present methods are decreased, as compared with those of the Y4R and S4R methods.

To further examine the volume scattering result of the newly proposed G4U method, the decomposition power profiles along a transect B in Fig. 6.4 (or white line in Fig. 6.5) over the forest, over the POLO ground and the orthogonally oriented urban areas, respectively, are shown in Fig. 6.5. It was found that the proposed G4U method preserves the amount of volume scattering in vegetated and for POLO ground areas similar to the Y4R and the S4R. Furthermore, statistics of whole image pixels processed by using the four volume scattering models are given in Table 6.3.

Table 6.1. Decomposition mean power statistics over the oriented urban area for patch a (see the black line box in Fig. 6.4) in San Francisco images in Fig. 6.4

Methods	P_s	P_d	P_v	P_c	*TP* from results	*TP* from data
S4R	0.415	0.444	0.432	0.117	1.408	1.405
G4U	0.406	0.450	0.432	0.117	1.405	1.405
Y4R	0.385	0.435	0.467	0.117	1.404	1.405

Table 6.2. Decomposition mean power statistics over the vegetation area for the yellow line box in Fig.6.3

Methods	P_s	P_d	P_v	P_c	*TP* from results	*TP* from data
S4R	0.089	0.045	0.26	0.029	0.423	0.423
G4U	0.091	0.043	0.26	0.029	0.423	0.423
Y4R	0.089	0.045	0.26	0.029	0.423	0.423

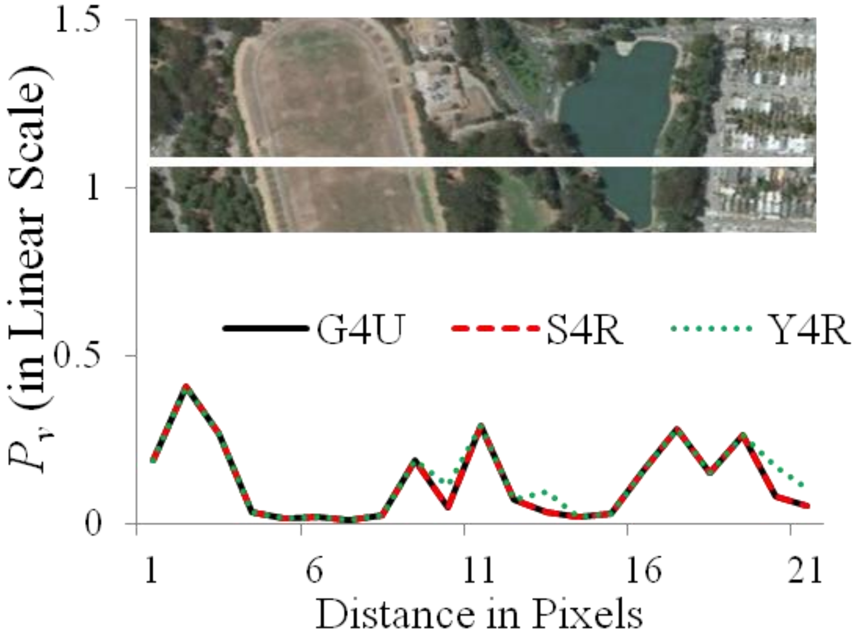

Fig. 6.5. Decomposition scattering power P_v profile along white line (same as white line B in Fig.6.4) for various targets scattering ensembles.

Table 6.3 Processed pixel statistics of P_v by using the four volume scattering models and by the power constrain

Models	Pixels processed by	Sin	Cos	Uniform	Oriented dihedral
Y4R	Model	283473	44605	623437	-
	Power Constrain	2601	269	4079	
S4R/G4U	Model	245513	42442	590470	77422
	Power Constrain	835	76	2012	0

The Proposed G4U method is also applied to a fine-beam-mode (FQ9) quad-polarization Radarsat-2 image (acquired on April 9, 2008) over San Francisco with multilook factors 6 in the range direction and 12 in the azimuth direction. A color-coded image of proposed G4U method results with Radarsat-2 data sets is shown in Fig. 6.6. A comparison of decomposition results with C- band and L-band POL-SAR data has been investigated for vegetation (volume scattering dominant features), urban (double-bounce scattering dominant areas) and airport runway (surface scattering dominant) areas. The statistics of the scattering power contribution shifting from volume scattering (see the golden color box in Fig.6.6) at C-band to surface and double-bounce scattering in L-band in vegetated areas are shown in Table 6.4. Moreover, similar statistics for the change of single bounce (in airport runway areas, see the white box in Fig.6.6) and double-bounce (orthogonal urban areas, see the black box in Fig.6.6) at C-band to other scattering classes at L-band are shown in Table 6.4.

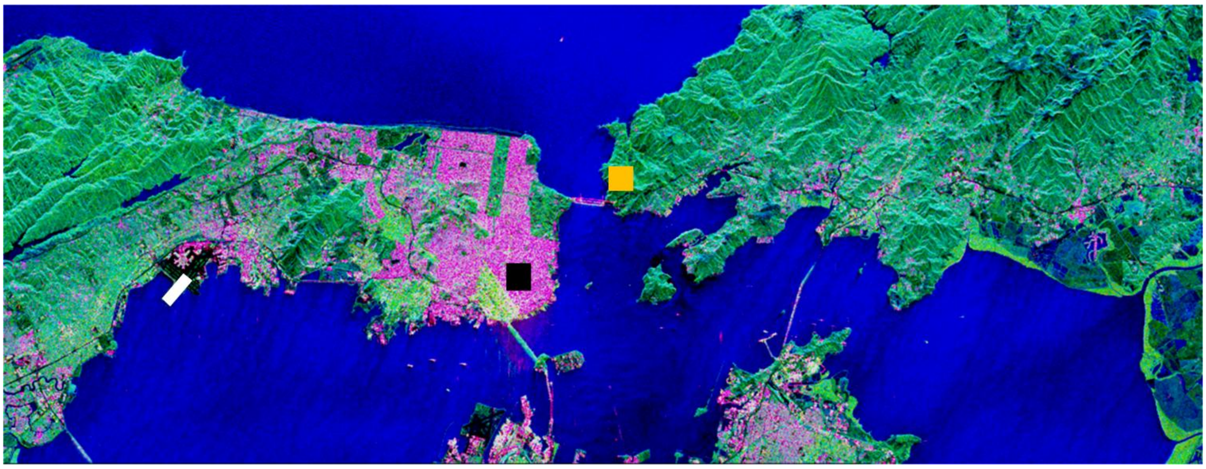

Fig. 6.6. A color-coded image of proposed G4U method results with Radarsat-2 data sets. {*RADARSAT-2 Data and Products MacDonald, Dettwiler and Assocates Ltd., 2008 - All Rights Reserved*}.

Due to longer wavelength of L-band compared with that of C-band and nearly 5.5^0 lower incident angle of the acquired PLASAR scene (23.5^0) than the angle of incidence of the acquired Radarsat-2 scene (29^0), the L-band PLASAR scene reflects surface and double-bounce scattering more than the C-band Radarsat-2 scene in vegetation areas. Moreover, it can be seen that the double-bounce contribution is reduced by 14.9% at L-band PALSAR data as compared with C-band Radarsat-2 data. The surface scattering dominant areas show slightly higher contribution at L-band than C-band POL-SAR data.

Table 6.4. Surface (P_s), double-bounce (P_d) and volume (P_v) scattering power component contribution statistics of proposed G4U method for the C-band and L-band over the vegetated areas (see the golden color box in Fig.6.6), urban areas (see the black box in Fig.6.6), and airport runway areas (see the white box in Fig.6.6)

Area/Feature	POLSAR Data	P_s (%)	P_d (%)	P_v (%)	*Dominant Scattering*
Golden Color Box /Vegetation Areas	Radarsat-2	31.1	4.8	59.7	Volume
	PALSAR	35.2	8.2	50.9	
Black Box /Urban Areas	Radarsat-2	30.6	62.7	5.6	Double-bounce
	PALSAR	47.2	47.8	1.8	
White Box/Airport Runway Areas	Radarsat-2	45.9	12.4	37.9	Surface
	PALSAR	47.4	10.2	37.8	

6.6 Summary and Conclusions

A new four-component scattering power decomposition scheme is presented in this scheme, denoted as G4U, was presented in this Chapter 6. The element T_{23} of the measured rotated coherency matrix is completely eliminated by implementing of double unitary transformations. This four-component decomposition accounts for seven parameters out of seven independent polarimetric parameters included in the coherency matrix. Therefore, this method uses full polarimetric coherency phase information in the decomposition. The double-bounce component is enhanced over the urban areas. It was shown that this method yields accurate and/or similar decomposition images compared with those by the existing four-component decomposition Y4R and S4R resulting from the full utilization of polarimetric information, which requires highly improved acquisitions of the cross-polarized *HV* component above a strongly suppressed noise floor as proposed in Touzi (2007) and advocated for three decades by W.-M. Boerner (Boerner 1981; Boerner *et al.* 1981).

Chapter 7 Monitoring of the March 11, 2011, Off-Tohoku 9.0 Earthquake with Super-Tsunami Disaster by Implementing Fully Polarimetric High Resolution POL-SAR Decomposition G4U Techniques

Prediction of nature is crucial

1.1 Abstract

This Chapter 7 reflects the POL-SAR data utilization for near-real-time earthquake and/or tsunami damage assessment in urban areas. In order to show the potential of the fully polarimetric high resolution POL-SAR image data sets, a four-component scattering power decomposition scheme has been developed and applied to monitor near-real-time earthquake and tsunami disaster damages. The test site for natural disaster damages has been selected: parts of the coastal area affected by the March 11, 2011, 9.0 magnitude earthquake that struck off Japan's north-eastern coast and triggered a super-tsunami. The color-coded images of the newly developed G4U scattering power decomposition method provide a simple and straightforward tool for interpreting the changes over the earthquake/tsunami affected urban areas and man-made infrastructures. This method also applies well for other types of natural (typhoon or tornado) and manmade disaster assessment applications. It is found that the double-bounce scattering power is the most promising of the input parameters to detect automated disaster affected urban areas at pixel level. It is also observed that the very-high-resolution, FULL-POL-SAR images are required for superior urban area monitoring over the oriented urban blocks with respect to the illumination of radar.

7.2 Introduction

In recent decades, earthquake and tsunami hazards have frequently occurred causing significant loss of life and devastating damage to property and infrastructure (Yamazaki 2007). It is quite difficult to obtain an immediate response of large-scale earthquakes and tsunami disaster areas by ground survey-based methods (Brunner *et al.* 2010). The ground survey method is accurate but highly time consuming and manpower extensive, which causes delays in assessment responses to rescue teams. Since these kinds of natural disasters will continue to occur, observations by airborne, high-altitude unmanned vehicle or space-borne high-resolution sensor techniques are needed to shorten the time lag of ground-survey-based damage assessment at large scales (Matsuoka and Koshimura 2010) in order to properly and swiftly provide localized destruction assessments to rescue agencies regarding earthquake/tsunami affected areas for rescue operations. Since microwave radar remote sensing is a suitable tool for monitoring the near-real-time earthquake and tsunami damage at large scales, at any time of day or night and independent of meteorological conditions, its implementation becomes of vital relevance to governmental and other agencies for initiating swift and well-orchestrated rescue operations. Hitherto, several methods are available to monitor earthquake and tsunami damages by using multispectral and monochromatic optical images as well as mono/dual-polarization SAR images (Chini *et al.* 2009; Matsuoka and Yamazaki 2004; Yonezawa and Takeuchi 2001). High-resolution multispectral optical images enable direct visual interpretation of the damages and are rather straightforward and simple to interpret by users. However, optical remote sensing fails under cloudy, foggy and hazy as well as severe rainy conditions for monitoring near-real-time damage. Single wavelength SAR images obtained from fixed single- and/or dual-polarization sensors are independent of meteorological conditions, but are difficult to interpret and require tedious computational analyses for at most incomplete assessments only.

The aim of this chapter is to generate pertinent information from high-resolution POL-SAR images for identifying directly the differences on damages between pre- and post-tsunami conditions of the affected regions. However, single observations using conventional SAR images make it difficult to generate desirable images ready for direct visual interpretation. In case we are given multiwavelength mono/dual-polarization SAR image data sets, it could possibly be done similar to cloud-free multi/hyperspectral optical imaging methods. Current space-borne SAR systems collect multiple polarization data (dual-polarization or quad-polarization) at a single frequency, either X-, C- or L-band. We take the advantage of the excellent quad-polarization data sets acquired with the Japanese ALOS-PALSAR imaging system using its high-resolution FULL-POL-SAR mode at L-Band to produce color-coded images for monitoring earthquake and tsunami damage along the Miyagi coast affected by the March 11, 2011, tsunami. Furthermore, very-high-resolution (VHR) TerraSAR-X (X-band) and DLR F-SAR (S-band) quad polarization images were processed to prove the effect of VHR for extracting detailed information from the urban areas.

This Chapter 7 is organized as follows: In Section 7.3 we describe the test sites and features of data sets that we have used in this study and give a brief explanation of the methods that were involved in analyzing of POL-SAR data; Section 7.4 presents the results; Section 7.5 concludes this chapter.

7.3 Test Sites, Data Used and Methods

This section discusses test sites for monitoring the chosen disaster area using fully polarimetric high-resolution SAR data acquired with ALOS-PALSAR and for the requirements of VHR FULL-POL-SAR images for recovering improved information over the selected urban areas of the affected region. This section also briefly explains the inherent applicability of the recently updated four-component scattering decomposition scheme G4U.

7.3.1 Test Site and Data Sets for Disaster Monitoring in the Urban Area

The parts of the coastal areas within the Miyagi Prefecture of central Eastern Honshu, affected most severely by the March 11, 2011 magnitude, 9.0 Honshu, Japan earthquakes (38.322 N, 142.369 E, depth 32 km) that struck off Japan’s north-eastern coast and triggered a historical super-tsunami (Fig. 7.1), have been selected. This super-tsunami, caused by the most powerful known earthquake to have hit Japan during the last three centuries and one of the five most powerful earthquakes in the world in recent times, reached more than 7.6 m height in Ishinomaki, part of the Miyagi Prefecture, and up to maximum height 40.5 m was noticed in Miyako in Iwate Prefecture. A Japanese National Police Agency report (NPA 2012) on September 10, 2012 confirmed 15,870 deaths, 6,114 injured and 2,814 people missing across twenty prefectures of Japan. Out of these numbers, 9527 deaths, 4140 injured and 1,394 people missing are reported within Miyagi prefecture. Moreover, the earthquake and tsunami caused extensive and severe structural damage in north-eastern Japan, including heavy damage to buildings, roads, and railways as well as fires in many areas, and a dam collapses far into the western inland from the Eastern Pacific coast including Sendai, the historical capital of Miyagi Prefecture and the Tohoku District of North-eastern Honshu. According to a National Police Agency of Japan report of September 10, 2012, more than 237,030 buildings have collapsed and 224,225 were partially damaged by the earthquake/tsunami in Miyagi prefecture (NPA 2012). The information about the collapsed buildings and tsunami covered areas over the off-Tohoku region by tsunami disaster was also mapped by the Association of Japanese Geographers, and Geospatial Information, Authority of Japan (GSI 2011) by ground-survey methods completed only four months after the disaster had set in.

In order to examine the capability of quad-polarization SAR image data sets for monitoring damages, we used the ALOS-PALSAR fully polarimetric, single-look complex (SLC), level 1.1(ascending orbit) images at L-Band acquired over study areas before (April 02, 2009 and November 21, 2010) and after the earthquake/tsunami (April 8, 2011) has struck (Table 7.1).

During the April 2009 acquisition, most of the agricultural areas were prepared for rice transplantation. In the November, 2010 image, agricultural fields were harvested and paddy fields were bare. After the disaster acquisition in April, 2011, the agricultural fields had been inundated and were affected by tsunami’s inward and outward flow of debris and sludge. The affected areas due to the earthquake/tsunami disaster were confirmed by using the ground-truth information provided by the Association of Japanese Geographers, and Geospatial Information, Authority of Japan (GSI 2011), which is illustrated in Fig. 7.2. Specifically, four patches (A-D) were selected for exploring the changes in the study area by earthquake/tsunami disaster. Patch A is selected over a vegetated area, patch B is taken in the agricultural area, patch C is chosen in the urban areas of Ishinomaki city, and patch D is selected over the Onagawa urban region/Onagawa Bay. The changes over the patch A occurred mainly due to the damages of uprooted trees and deposition of mud/sludge by tsunami flow forces. The changes over patch B are due to the deposition of collapsed and washed out building debris and water cover over the bare agriculture field area by tsunami flow. The changes over patches C and D occurred by the washout and damages of building blocks after the earthquake/tsunami disaster. The changes in these patches (A-D) were also cross checked with before (April 04, 2010 and June 26, 2010) and after (April 06, 2011) disaster ultrahigh-resolution Google earth optical images.

Table 7.1. Characteristics of the quad polarization space-borne ALOS-PALSAR SLC data sets and TerraSAR-X SSC data and an airborne F-SAR SLC quad polarization data

Date	Sensor	Frequency (GHz)	Off-nadir angle $(^{0})$	Resolution (m)	Region	Main purpose to use data sets
20090402	PALSAR	1.27	21.5	30	Ishinomaki	To monitor temporal and post disaster effects in the urban areas
20101121	PALSAR	1.27	21.5	30	Ishinomaki	
20110408	PALSAR	1.27	21.5	30	Ishinomaki	
20100304	PALSAR	1.27	21.5	30	Niigata	To show the strength and efficacy of VHR in the urban area
20100422	TerraSAR-X	9.6	36.7	2	Niigata	
20100608	DLR F-SAR	3.25	37.0	0.5	Kaufbeuren Germany	

7.3.2 Test Sites and Data Sets for Proving the Requirement of VHR POL-SAR Images Over the Urban Area

Due to non-availability of either airborne or satellite VHR FULL-POL-SAR images before and after the earthquake/tsunami disaster over the Ishinomaki, Miyagi Prefecture industrial harbour region, three more data sets were acquired to show the disaster imaging capabilities of the VHR FULL-POL-SAR images over the highly oriented urban areas in other parts of the World. Out of these three images, two images [one image from high-resolution fully polarimetric ALOS-PALSAR products during the descending orbits in the form of SLC, level

1.1 products, and a second image from the experimental mode for VHR fully polarimetric TerraSAR-X products during the descending orbits in the form of a single-look slant range complex (SSC) product] were acquired by space-borne POL-SAR sensor over the Niigata city, Japan (see Table 7.1) and another one VHR POL-SAR SLC image was acquired from the DLR F-SAR S-band system over the Kaufbeuren, Germany. Although, these data sets are acquired over different regions, these data sets can serve well the purpose of showing the improvements to be found by using VHR POL-SAR image.

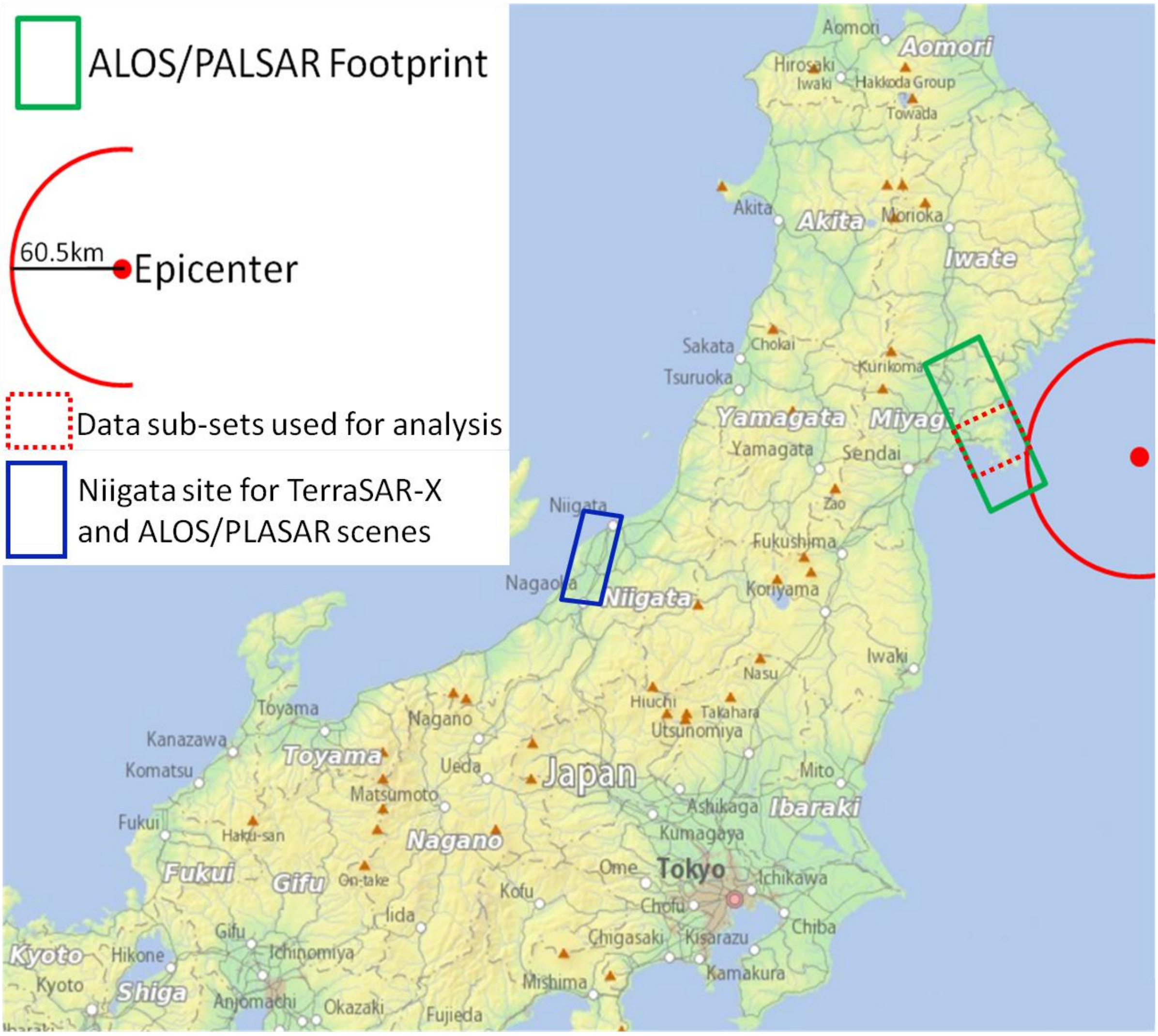

Fig.7.1. Location map of selected disaster-affected site near Ishinomaki, Miyagi Prefecture and of a selected test site over Niigata for proving the requirement of VHR FULL-POL-SAR image to get better information over the urban area.

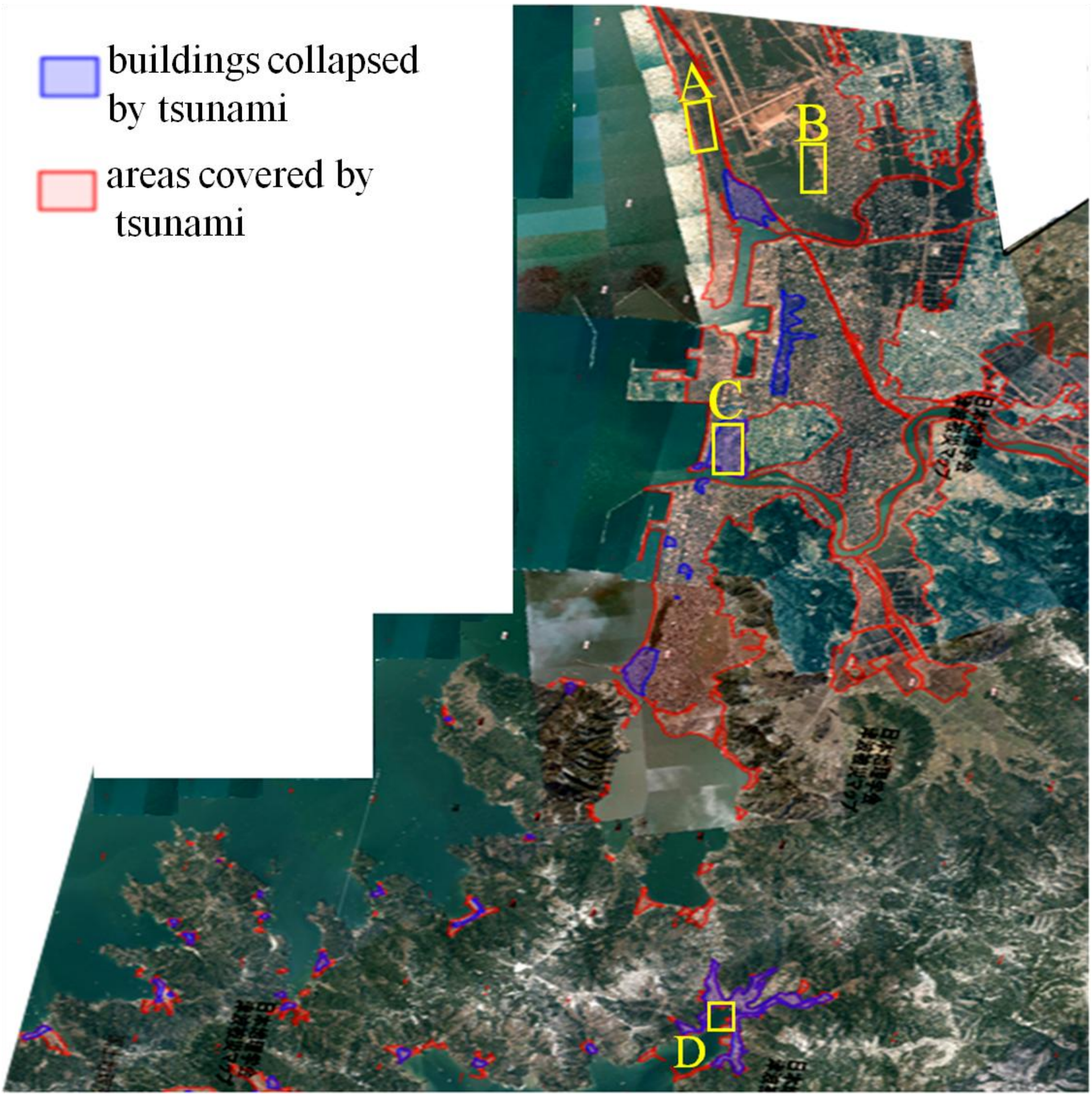

Fig. 7.2. The ground truth data. Patch A shows the vegetation area on relatively flat surface area; patch B represents the agricultural area over a relatively flat ground; patch C illustrate urban areas of Ishinomaki city; and patch D demonstrates the Onagawa urban region/Onagawa Bay.

7.3.3 Methods: Utilization of FULL-POL-SAR-Model-Based Decomposition G4U

For this investigation, all POL-SAR data are acquired from the monostatic POL-SAR sensor configuration. In this case, the scattering matrix carries useful information by five independent quantifies (three amplitudes and two phase differences) (Cloude 2009; Lee and Pottier 2009; Mott 2007, Yamaguchi 2007). Various methods have been proposed in the last century to decompose the scattering matrix (Boerner *et al.* 1998; Touzi *et al.* 2004) for characterizing the point targets. On the other hand, the complete scattering information in the form of second-order statistics like coherency or covariance matrix is required to characterize the distributed targets (Boerner *et al.* 1998; Cloude 2009; Freeman and Durden 1998; Touzi 2007; vanZyl and Kim 2010; Yamaguchi *et al.* 2005). There exist nine independent polarization parameters in the coherency matrix $\langle[T]\rangle$ as the second-order statistics (Lee and Ainsworth 2011, Sato *et al.* 2012; Singh *et al.* 2013b; Singh *et al.* 2013c; Yamaguchi *et al.* 2011). The coherency matrix $\langle[T]\rangle$ is defined in (2.5) of Section 2.5 in Chapter 2.

We have used the general four-component scattering power decomposition method (G4U) (Singh *et al.* 2013b) to examine the disaster area. This decomposition scheme describes the total scattering power into surface scattering power P_s, double-bounce scattering power P_d, volume scattering power P_v, from dipole and/or oriented dihedral and helix P_c, as shown in Chapter 6 in details. This general four-component scattering power decomposition scheme (Singh *et al.* 2013b) also includes the complete fully polarimetric phase information and the extended volume scattering model for oriented dihedral structures (which are mostly prevalent in urban areas (see previous Chapter 6) to estimate the appropriate volume scattering power as compared to the three-component decomposition (Freeman and Durden 1998)).

The physical understanding of polarimetric four-component scattering mechanisms is briefly explained as follows:

1) *Surface scattering*: the scattering which takes place only on the border surface between two different but homogeneous media, from one of which a radar pulse is incident on to the other (Rice 1951). The surface scattering mechanism is mainly caused by rough surfaces such as bare soil, water surface, sea surfaces, agricultural fields, etc. (Beckmann and Spizzichino 1963; Freeman and Durden 1998; Fung *et al.* 1992; Rice 1951; Ulaby *et al.* 1986; vanZyl 1989; Yajima *et al.* 2008;Yamaguchi *et al.* 2005). In this case, the phase difference of co-polarized components *HH-VV* is closer to zero (vanZyl and Kim 2010); however, the *HH* and *VV* magnitudes may differ. Scattering of POL-SAR on the ground surface increases according to the increase of relative dielectric constant, and the behavior of scattering depends on the surface roughness and the orientation of the surface (Cloude 2009; Peake and Oliver 1971; Hajnsek 2001; Hajnsek *et al.* 2003).

2) *Double-bounce scattering:* This type of scattering comes from two surfaces at right angle, for example, one flat on the ground (horizontal), and the other upright (vertical) such as road surfaces and building walls, river surfaces and bridge structures, etc. (Cloude 2009; Freeman and Durden 1998; Yamaguchi *et al.* 2005). The radar return signal hits both surfaces, one after the other, and the total angle of radar reflection is π, in the backscatter direction. This double-bounce scattering phenomenon generates the compound scattering matrix from two surfaces, and the most important consequence of this compound matrix is that the co-polarized components *HH* and *VV* are out of phase (Cloude 2009; vanZyl 1989;vanZyl and kim 2010). Typically, urban areas show double-bounce scattering dominance due to the wall-

ground or ground-wall interactions of the radar signal. Double-bounce scattering can also occur frequently in nature, whenever there are upright vegetation stems (stalks, trunks) and relatively smooth (and flat) surface underneath. Examples are flooded forests, and parallel (to the azimuth direction of radar) rows of rice fields, corn fields, etc..

3) *Volume scattering:* Volume scattering can be observed if a SAR beam penetrates into a medium (Ulaby *et al.* 1986). Scattering from trees or branches, crops, subsurface, oriented buildings from the line of sight of radar, etc. (Freeman and Durden 1998; Lee and Ainsworth 2011; Nghiem *et al.* 1992; Yamaguchi *et al.* 2005; Yamaguchi *et al.* 2011) are examples of volume scattering. When the radar beam interacts with the vegetation, the random scattering process (random volume scattering over the ground) will be generated.

4) Helix scattering: The helix scattering power is essentially the same as the circular polarization power. The circular polarization can be generated from a source of horizontally polarized component plus vertically polarized component being 90^0 out of phase. For example, orthogonal wires with 1/8 wavelength separation structures reflects circular polarization (Kitayama *et al.* 2001). These sources can be seen in urban areas, i.e., in man-made structures such as facets of buildings or urban area with lots of wire structures placed in orthogonal directions depending on frequency (Lee and Ainsworth 2011; Sato *et al.* 2012; Singh *et al.* 2013b; Yamaguchi *et al.* 2005; Yamaguchi *et al.* 2006; Yajima *et al.* 2008; Yamaguchi *et al.* 2011). Similar helical scattering effects also exist in nature often manifested by left versus right circular polarization sensitivity changes. In case, the sources of the helix scattering increase over the surface, the scattering helicity will increase.

Since the G4U in Chapter 6 (Singh *et al.* 2013b) is an improved version of Y4R (Yamaguchi *et al.* 2011) and S4R (Sato *et al.* 2012), fully polarimetric high-resolution ALOS-PALSAR data sets as well as VHR data of space-borne fully polarimetric TerraSAR-X and the fully polarimetric DLR F-SAR data sets have been analyzed based on the this recently updated version of the decomposition scheme. Decomposition color composite images of PALSAR data sets were generated with multilook factors twelve times in azimuth direction and two times in range direction. The color composite image of TerraSAR-X data with decomposition was made with multilook factors ten times in azimuth direction and twelve times in range direction, and the multilook window size for the DLR F-SAR data to produce the color composite images was chosen as ten in the range direction and ten in the azimuth direction.

After the decomposition of ALOS-PALSAR data over the earthquake/tsunami disaster site, the four scattering components, namely the surface scattering (P_s), the double-bounce scattering (P_d), the volume scattering (P_v), and the helix scattering (P_c), components were normalized by the *Total Power* (*TP*) for further analysis. The normalized scattering components are defined as

$$p_s = \frac{P_s}{TP};\ p_d = \frac{P_d}{TP};\ p_v = \frac{P_v}{TP};\ p_c = \frac{P_c}{TP} \tag{7.1}$$

where p_s , p_d, p_v, and p_c are the normalized scattering powers corresponding to surface , double-bounce , volume, and helix scattering, respectively, and

$$TP = P_s + P_d + P_v + P_c \quad . \tag{7.2}$$

The mean filter with 3×3 window size is applied on these normalized scattering power component images before analyzing the images in more detail.

7.4 Results and Discussion

7.4.1 Interpretation of RGB Color-Coded Images

Three (two pre-disaster and one post-disaster) images, corresponding to the same region of recovered fully polarimetric PALSAR images for the pre- *versus* post-disaster are processed by implementing the recently developed general four-component scattering power decomposition (G4U) scheme (Singh *et al*. 2013b). These decomposition RGB color-coded images of 20090402, 20101121, and 20110408 are presented in Fig. 7.3 (a), Fig. 7.3 (b) and Fig. 7.3 (c), respectively. Fig. 7.4 and Fig. 7.5, show the enlarged parts of the pre- *versus* post-tsunami G4U color-coded images for examining the tsunami damages for patch A (vegetated area), patch B (agricultural area), patch C (urban region), and patch D (urban region/Onagawa Bay) [see Fig. 7.2], respectively for which color-coding RGB was chosen according to the established conventions (Yamaguchi *et al*. 2011).

Moreover, when a tsunami impacts the vegetated fields (see patch A, Fig.7.4), the random scattering process (random volume scattering over the ground) is reduced due to the deposition of mud soil and the wiped out vegetated areas. This phenomenon decreases the depolarization phenomena over the vegetation areas, thus surface scattering increases and volume scattering mechanism reduces. The increment in double-bounce scattering mechanism can also be expected due to the exposed stems over the ground and deposited dihedral structures caused by the tsunami in the vegetated/forested areas. In contrast, the amount and direction of surface scattering depends on the relative permittivity, the surface roughness, and the orientation of the surface (Cloude 2009; Peake and Oliver 1971). The deposition of urban areas debris by tsunami flow on Bragg surfaces like bare surface, agricultural fields and/or floating debris on water surface increases the surface roughness of the Bragg surface, for example, patch B in Fig. 7.4. Since surface scattering provides a diversity of polarization responses, varying with an angle of incidence, dielectric constant, and surface roughness/slope, the roughness leads to depolarization of surface scattering (Cloude 2009; Hajnsek 2001). This cause reduces the surface scattering and mixes with random scattering processes in those areas, where debris was deposited by tsunami flow. Surface scattering increases over damaged and wiped out man-made structures (see patches C and D, Fig. 7.5).

Since man-made structures such as building and bridges orthogonal to radar illumination are categorized into double-bounce scatterer types in the G4U scheme, the double-bounce (P_d) scattering component in urban area is caused by right angle scattering between building-block-walls and road surfaces. Volume scattering (P_v) and surface scattering (P_s) components are small for orthogonally illuminated man-made structures. However, damaged or collapsed urban blocks or man-made structures, resulting from the earthquake/tsunami impact that do not appear to be orthogonal to radar direction and having their corresponding main scattering centre in an oblique direction with respect to radar illumination, generate no double-bounce type effect in the G4U images after the tsunami struck. Due to multiple scattering, these red areas (pre-tsunami image) turn into green (volume scattering) in post-tsunami images. In cases for which buildings are washed out and/or eliminated by the tsunami, those areas appear as blue surface scattering types of the G4U scheme in the post-tsunami images (see patches C and D in Fig.7.5). These effects in post-tsunami images as compared to pre-tsunami images are providing a simple straightforward tool for interpreting collapsed buildings in tsunami affected areas. These observations are matched with ground-truth data provided by the Association of Japanese Geographers, and Geospatial Information, Authority of Japan (GSI 2011), and the obtained comparisons are very convincing.

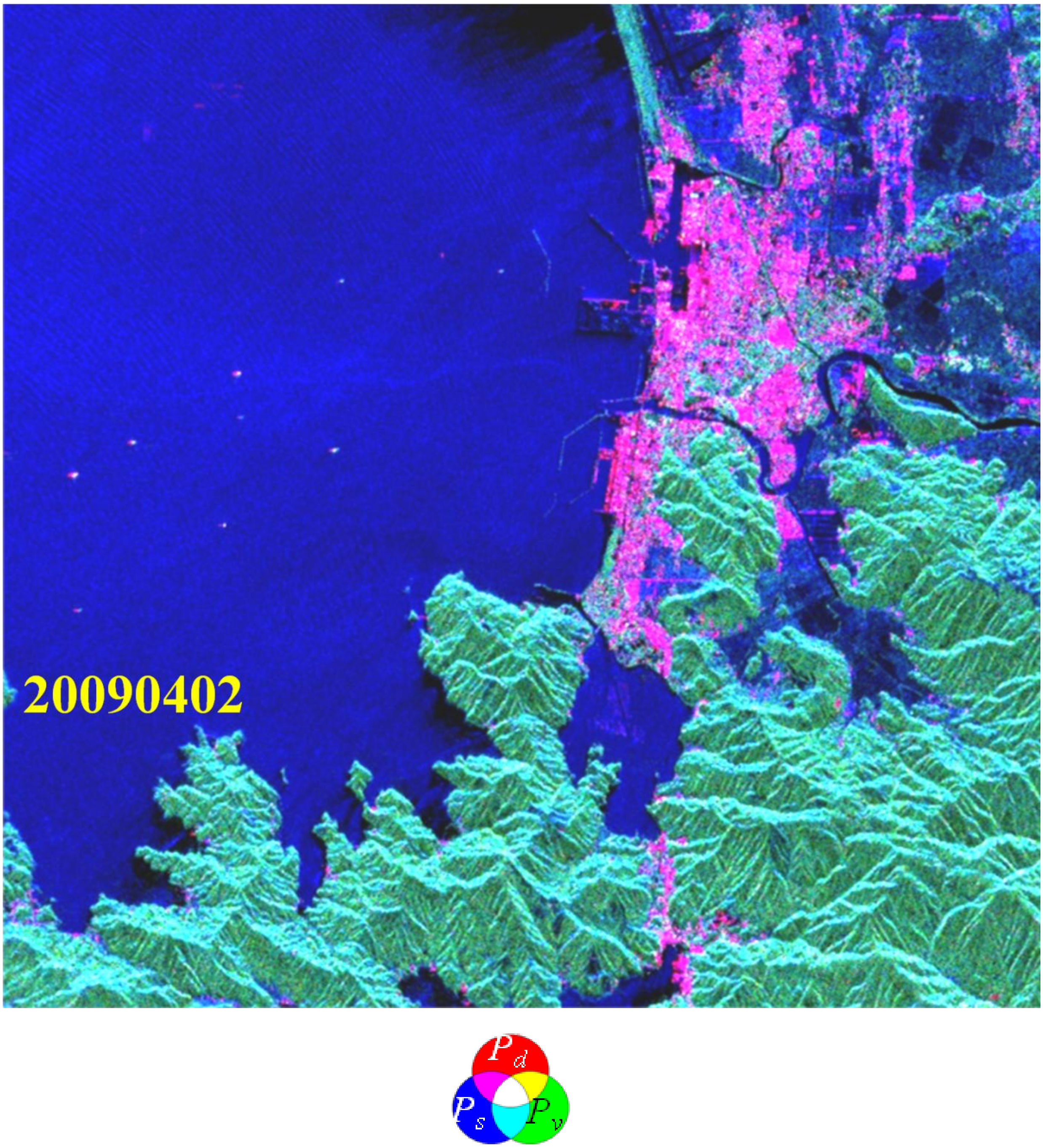

(a)

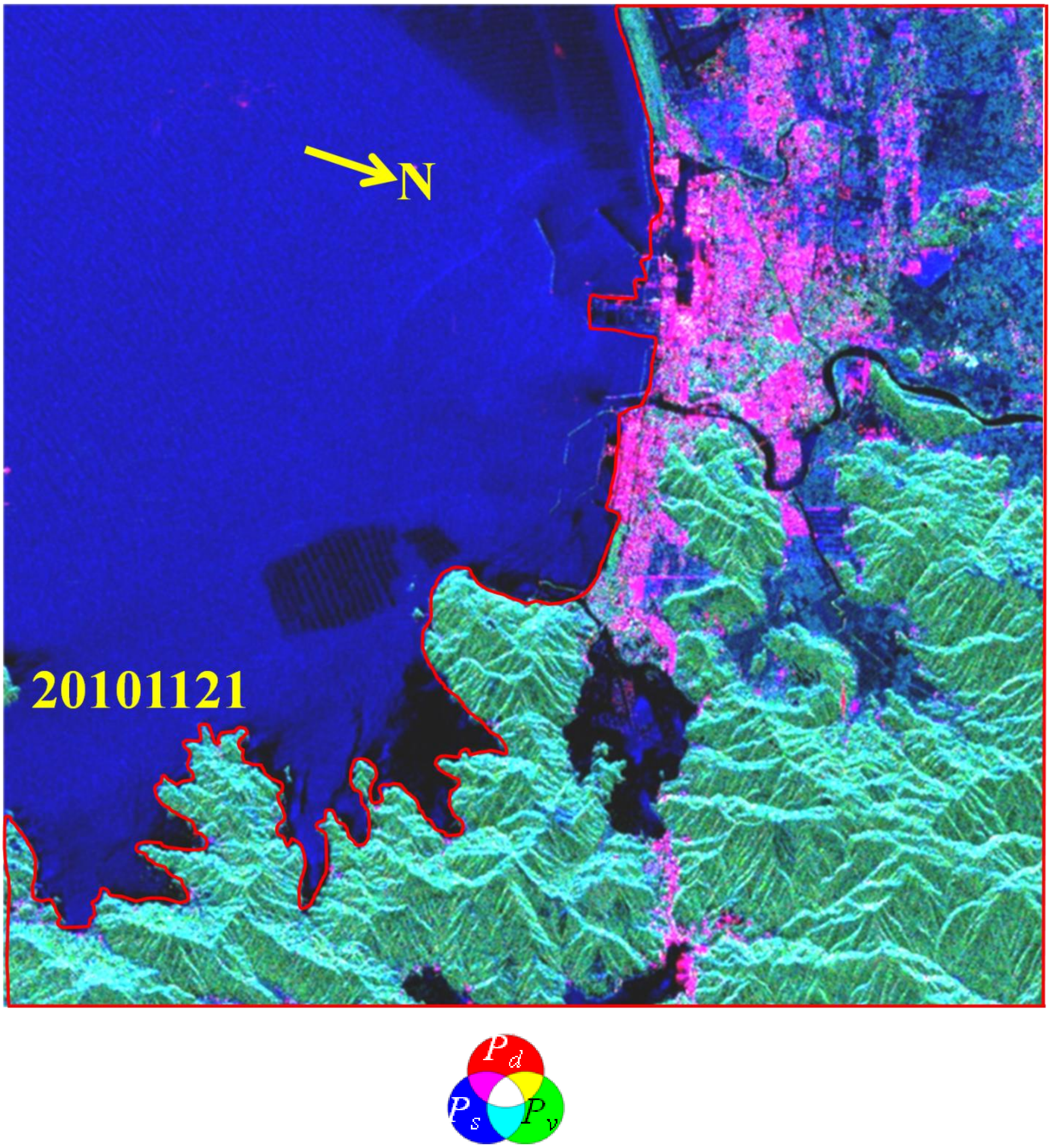

(b)

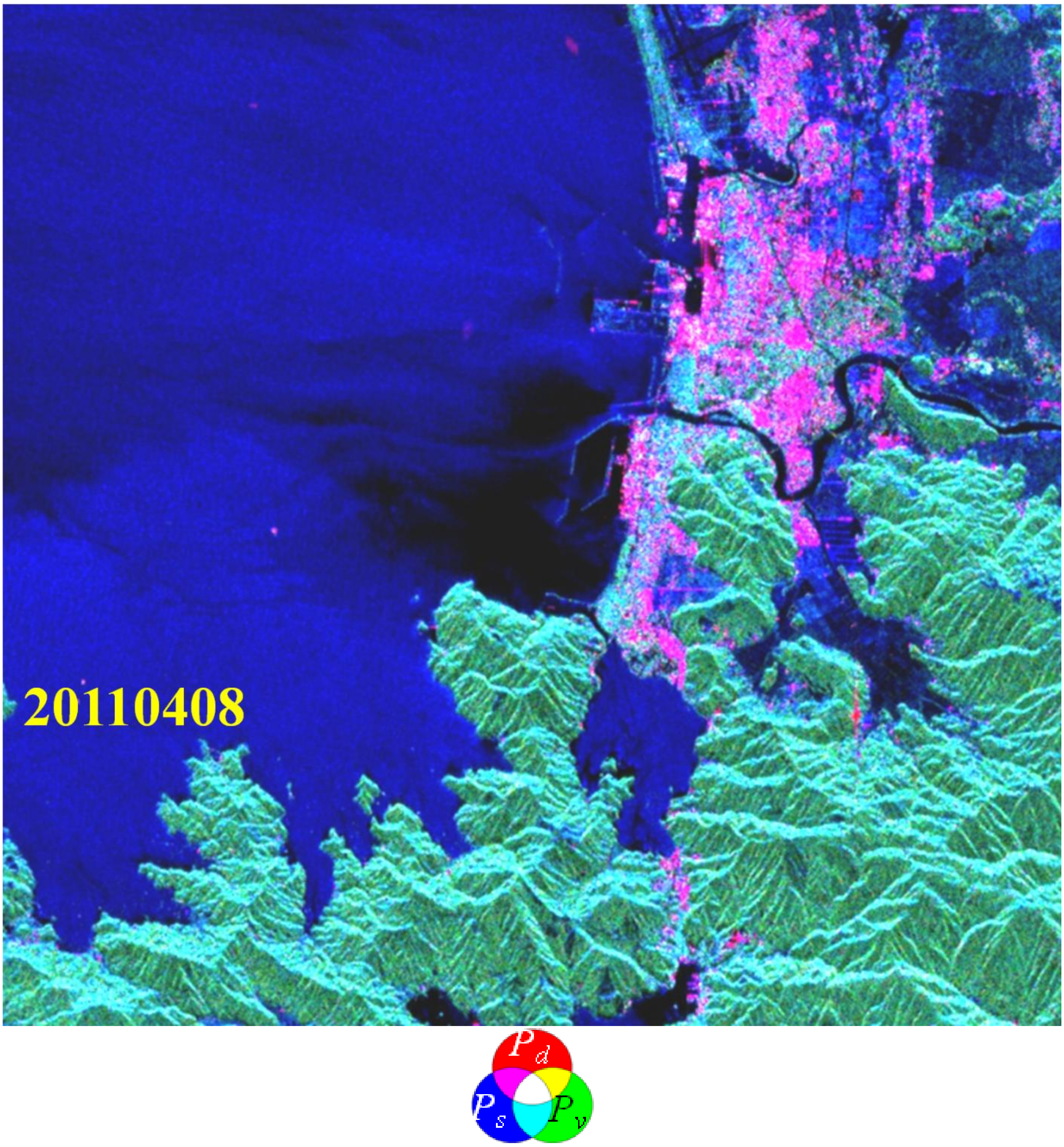

(c)

Fig. 7.3. (a) and (b) Pre-earthquake and (c) post-earthquake/tsunami G4U images for PALSAR data (For all images, the flight direction of ALSO-PALSAR is from left to right and PALSAR illumination direction is from top to bottom.)

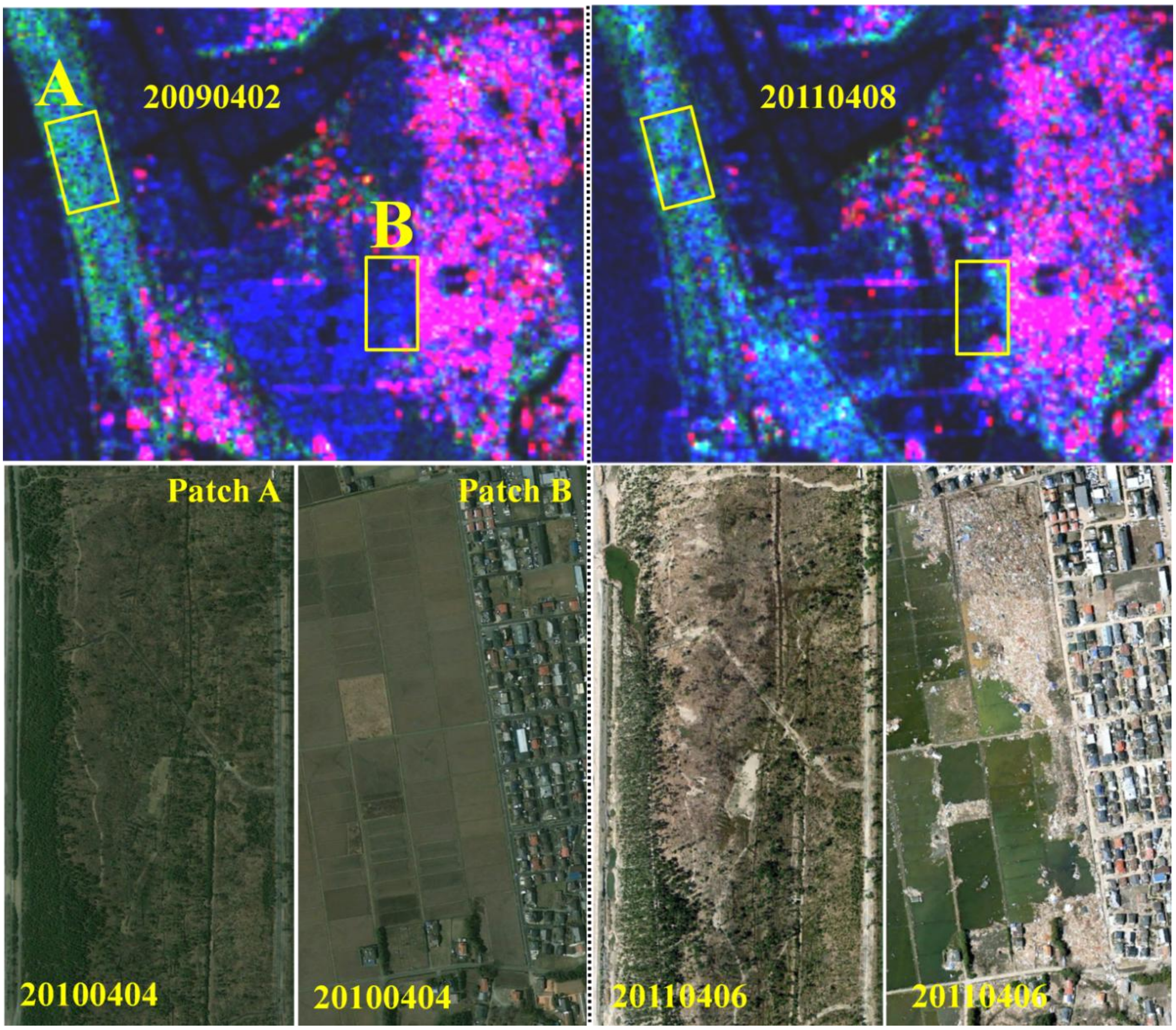

Fig. 7.4. Enlarged view of patch A (vegetation area) and patch B (agricultural areas) in Fig.7.2. **Left side from black dashed line:** pre earthquake/tsunami disaster images. **Right side from black dashed line:** post-earthquake/tsunami images. **Top row:** G4U images for patch A and patch B and surrounding areas. **Bottom row:** Google optical images for patch A and patch B. Volume scattering (green) over Patch A is decreased in the post-disaster G4U images due to damage of forest areas as compared to pre-disaster G4U images and surface scattering (blue) is increased. Surface scattering (blue) over patch B is reduced in the post-disaster G4U images due to the deposition of buildings debris in the agricultural areas as compared to pre-disaster G4U images, and volume scattering (green) is increased.

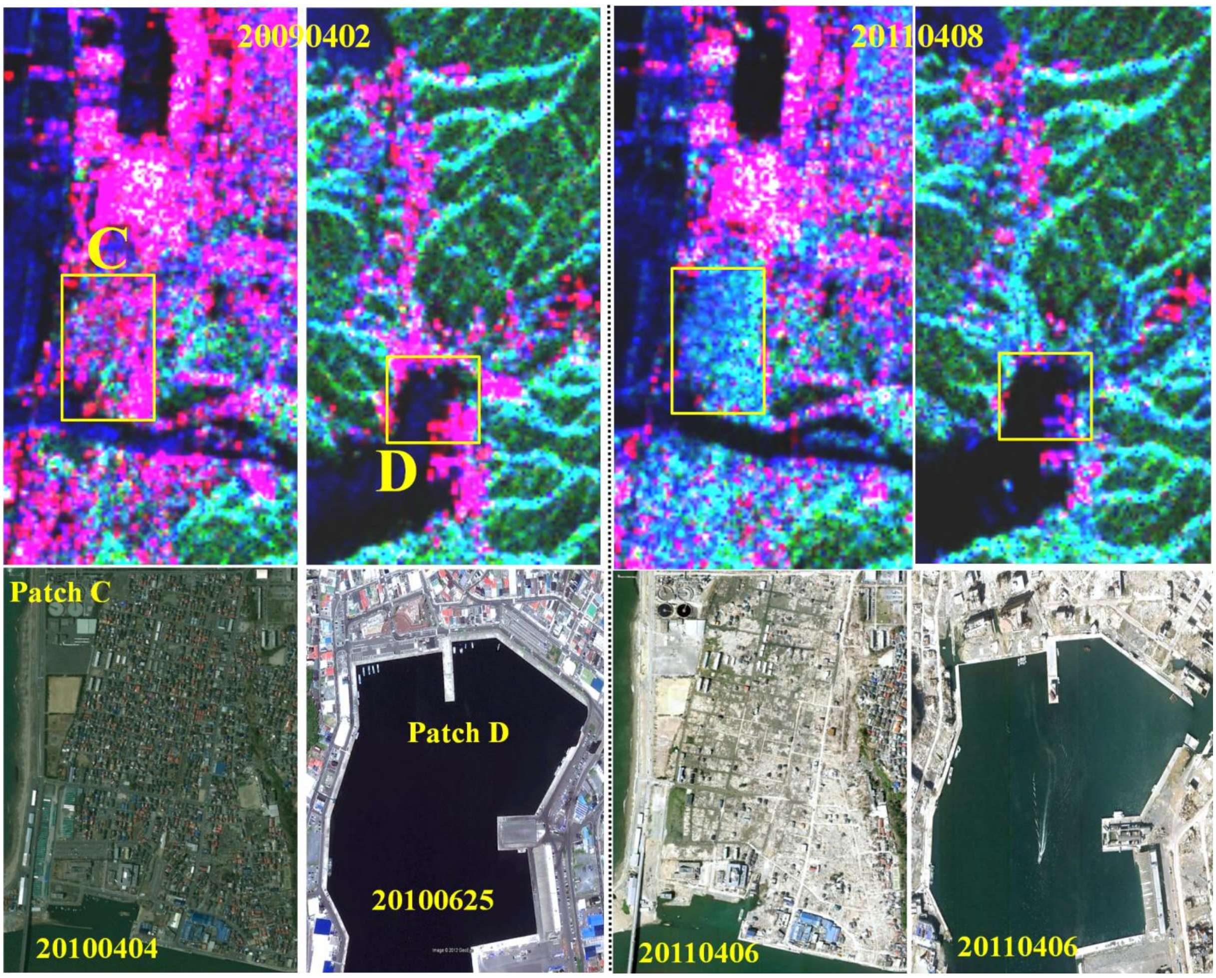

Fig. 7.5. Enlarged view of patch C (urban region) and patch D (urban region/ Onagawa bay) in Fig.7.2. **Left side from black dashed line:** pre-earthquake/tsunami disaster images. **Right side from black dashed line:** post-earthquake/tsunami images. **Top row:** G4U images for patch C and patch D and surrounding areas. **Bottom row:** Google optical images for patch C and patch D. Double-bounce scattering (red) over Patch C and patch D is decreased in the post-disaster G4U images due to the damage of buildings as compared to pre-disaster G4U images, and surface scattering (blue) and volume scattering (green) are increased.

7.4.2 Change Analysis

It was shown in the previous subsection that POL-SAR data with G4U provided effective visual interpretation to identify the damaged areas resulting from the earthquake/tsunami disaster without difficulties from the temporal changes and seasonal changes. For the accurate and the automated change detection in urban areas for registering damages caused by earthquake/tsunami disasters, it is implicit that we first need to identify the input parameters to recognize the automated changes properly. If the strategy of input parameter selection of the G4U is done properly, then this identification helps to estimate the damaged areas in the urban regions. Therefore, there is need to understand and recognize the discriminating and overlapping behaviour in between the temporal changes and disaster effects (pre- and post-disaster changes) on the decomposition parameters (p_s, p_v, p_d and p_c) over vegetated areas, agricultural areas, and urban areas. For example, the temporal changes (in between the 20090402 and the 20101121) and the post disaster-changes [in between the pre-earthquake/tsunami (20090402) and the post-earthquake/tsunami (20110408)] in the value of the parameters p_s, p_v, p_d and p_c over patch A (vegetated area, Fig.7.4), patch B (agricultural area/ wiped out buildings debris deposited area, Fig. 7.5), and patch C (urban region, Fig.7.5) are analyzed in Fig. 7.6, Fig. 7.7 and Fig. 7.8, respectively. Table 7.2 shows the quantitative statistics of Figs 7.6, 7.7 and 7.8. The temporal difference values and the difference values after the disaster in parameters p_s, p_v, p_d, and p_c vary within the certain ranges as shown in Fig. 7.6, Fig. 7.7 and Fig. 7.8, and Table 7.2. It is found that the mean, mode and median statistics of change are larger in post-disaster changes than the temporal change and overall changes after the disaster can be separated from temporal changes based on mean, mode, and median. The mean statistics including ± standard deviation of the pixel distributions over all patches were analysed, and we observed that parameter p_v correlated with the estimated vegetation damage, the four parameters (p_s, p_v, p_d, and p_c) correlated with damage and debris deposition monitoring over the agricultural areas, and parameters p_s, p_v, and p_d corresponded with the damage assessment in urban areas. But most of individual pixel difference values of temporal and post-disaster changes overlapped, except the individual pixel difference values in p_s over patch B and p_d over patch C. Moreover, the factors for temporal and post-disaster changes are explained in detail next.

The surface component in the vegetation area (Patch A) is particularly relevant to the radar return from a ground surface underneath the vegetation canopy (Freeman and Durden 1998). The surface component occurs when the radar beam reaches directly to the ground through gaps in the canopy, or there is penetration of the canopy. Double-bounce components in the vegetation area appear due to ground-trunk interactions. In both surface and double-bounce scattering processes, the factors such as surface roughness, soil moisture, surface slope, and understory vegetation layer have an important influence on radar beam interaction with ground (Ulaby *et al.* 1986; Leckie and Ranson 1998). The volume scattering component is relevant to the radar return from vegetation canopies due to gradual changes in dielectric constant and inhomogeneities within the canopy structure (Zoughi et al.1986; Durden *et al.* 1989; Durden *et al.* 1990). Leaves, branches, and trunks of the vegetation canopy behave as attenuators (Chauhan and Lang 1989). The radar beam penetration depends on the density, moisture contents and structure of the vegetation canopy, and on the presence of gaps within the canopy. If the changes are underneath the canopy, in the dielectric constant of the ground and vegetation, then these changes influence the radar return. Although the changes in underneath forest canopy roughness during temporal observation are not significant without natural or anthropogenic disaster activities, the dielectric constant (moisture content) can vary quickly for both ground and vegetation (Dobson *et al.* 1991). Apart from these parameters, size, shape, and orientation of the surface or canopy elements also affect the scattering components. During the maturation stage of vegetation growth, temporal variations of parameters p_s, p_v, and p_d over the vegetation area are expected with changes either in the vegetative seasonal cycle or in the ground parameters (Ulaby *et al.* 1986; Dobson *et al.* 1991). Overall, the temporal changes are somewhat barely distinguishable (see Fig.7.3 and Fig.7.6, and Table 7.2 for patch A) but after the tsunami disaster, the trends in change are understandable (see Fig.7.4 and Fig. 7.6). Since vegetation/trees were damaged by the tsunami disaster, the volume scattering decreases due to the reduction in the major sources of depolarization in scattering processes. The surface and the double-bounce scattering increase over the damaged vegetated areas due to loss in standing tree density, gaps between crowns, and damaged understory vegetation.

Scattering processes over a flat bare-soil surface in the agricultural field areas are affected by two attributes: 1) surface roughness; and 2) the dielectric constant of the soil medium. Due to the dynamic nature of these factors by natural or anthropogenic processes over agricultural areas, soil moisture and soil surface roughness are variables in space and time. The temporal changes in the bare agricultural field areas are anticipated due to different soil moisture and roughness conditions in April, 2009 and November, 2010. However, the changes after the earthquake/tsunami in the agricultural field areas are envisaged due to the deposition of debris and inundation in agriculture field areas since images are used from the similar field conditions at the beginning of the month April (bare field condition). The changes after the tsunami are also confirmed due the deposition of buildings debris by using high-resolution Google Earth images [see Fig. 7.4 and Fig.7.7, and Table 7.2 for patch B]. The deposition of debris over the bare agricultural fields increases the roughness; this cause generates depolarization in surface scattering. As resultant, surface scattering is decreased and volume and double-bounce scattering are greater than before the disaster condition over the debris covered areas in agricultural fields.

Temporal changes in p_s, p_v, and p_d over the urban areas are not observed to be significant because of permanent man-made structure dominance [see Fig.7.5 and Fig. 7.8, and Table 7.2 for patch C]. However, changes in p_s, p_v, and p_d, over the urban areas are noticeable after the earthquake/tsunami disaster event due to the changes in POL-SAR scattering mechanism interactions with the damaged urban block and/or washed out urban block areas as compared to the pre-disaster scattering behaviour over the urban areas [Fig. 7.5 and Fig. 7.8 for patch C]. After the disaster, the double-bounce scattering reduces due to the damage of the ground-wall and/or wall-ground interaction because the radar signal is scattered in different direction as compared to before the disaster. These ground-wall and wall-ground interfaces over the urban areas are destroyed and/or washed out and/or reduced to debris due to the earthquake/tsunami disaster. Surface scattering becomes dominant after the disaster in those areas where the buildings are washed out by the force of the tsunami flow, leaving the ground exposed. Volume scattering becomes dominant after the disaster in those areas where buildings are oriented from the orthogonal direction with respect to the radar illumination by the force of the tsunami flow. Therefore, the values of the p_s and the p_v are increased with the earthquake and tsunami hazard compared to pre-disaster conditions over the urban areas.

When the sources of helix scattering in urban areas are damaged or changed, then the scattering helicity decreases/changes in the urban areas. However, in most POL-SAR measurements over vegetated areas (volume scattering dominant areas) and sea water or bare flat surfaces (Bragg surface), the reflection symmetry condition holds; but for POL-SAR measurements over the double-bounce scattering dominant areas (urban areas), the reflection symmetry condition does not hold (Yamaguchi *et al.* 2011; Singh *et al.* 2013c). So there is no remarkable advantage to use the value of the parameter p_c over the vegetation area but when the wiped out buildings and debris were deposited in the agricultural areas by the tsunami, it is found that the value of the parameter p_c increases in agricultural area due to the loss of the reflection symmetry condition. On other hand, the value of parameter p_c decreases in damaged urban areas.

Furthermore, the changes for the red line boundary areas in Fig. 7.3(b) for the value of p_s, p_v, and p_d parameters [in between the pre- earthquake/tsunami (20090402) and post-earthquake/tsunami (20110408)] are categorized in Figs. 7.9(a), 7.9(b) and 7.9(c), respectively. The value of the p_s increases 0.1 to 0.3 in distorted ocean-shore vegetation areas and agricultural areas while the value of p_v of those areas decreases. A decrement of more than 0.1 in the value of the p_s is also noticed in those areas containing wiped out buildings and debris deposited by tsunami flow (e.g., patch B) and the washed out buildings debris floating in bay areas, e.g., in the water areas of patch D. Moreover, it was observed that the value of the parameter p_v decreases by more than 0.1 in the damaged vegetated area by the tsunami impact, nevertheless temporal/seasonal changes in land cover (which is not affected by the tsunami) overlap with tsunami affected areas. The value of p_d over the collapsed or wiped out buildings is decreased while that of distorted vegetation areas along the ocean-shore is increased up to 0.1 as compared to pre-disaster conditions. The value of p_d over the vegetation and the agricultural areas is found to be ±0.1 and also mixed with the non-tsunami-covered areas. The value of parameter p_d increases from 0.1 to 0.3 for locations where the wiped out buildings were deposited in the agricultural areas and/or floated in bay areas.

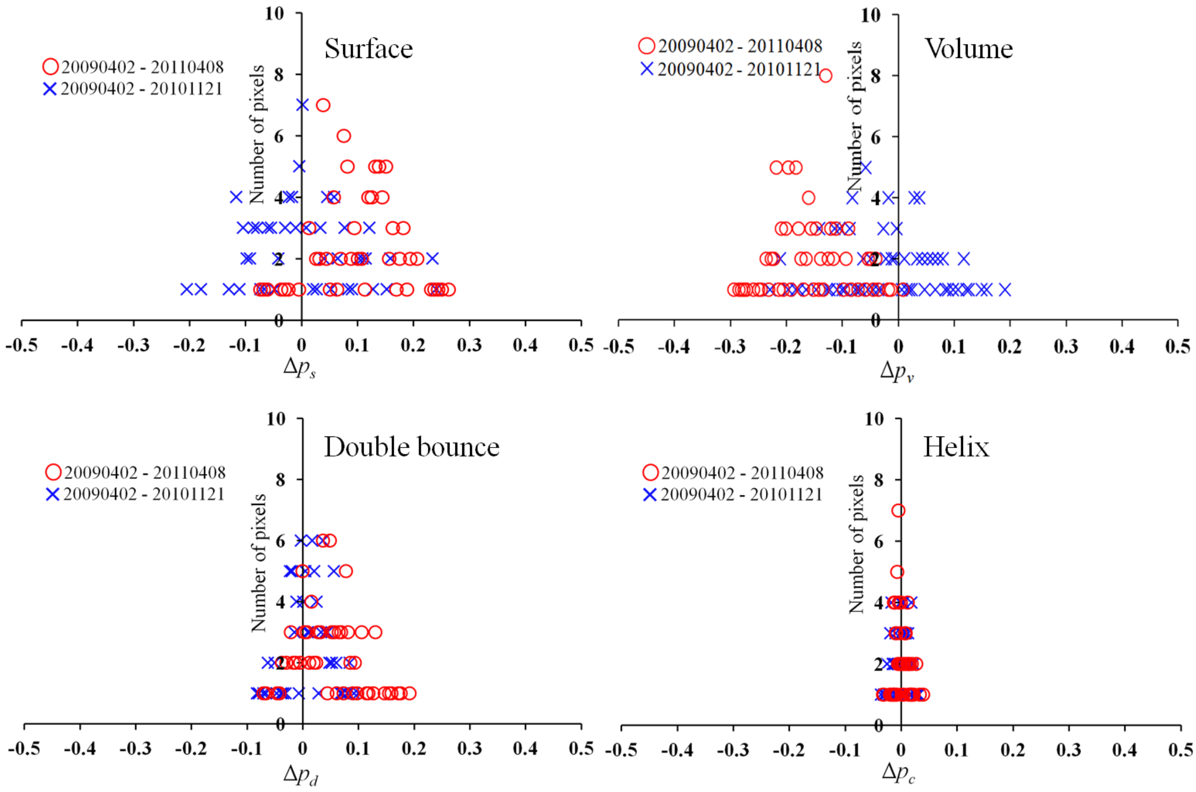

Fig. 7.6. Differences in pixel values for the Δp_s (normalized surface scattering components difference), Δp_v (normalized volume scattering components difference), Δp_d (normalized double-bounce scattering components difference), and Δp_c (normalized helix scattering components difference) over vegetation, which are drawn by using patch A (see Fig. 7.4) [○ denotes the difference in between pre-earthquake/tsunami (20090402) and post-earthquake/tsunami (20110408) decomposition parameters; and × denotes temporal difference [before (20090402) –after (20101121)] of the decomposition parameters].

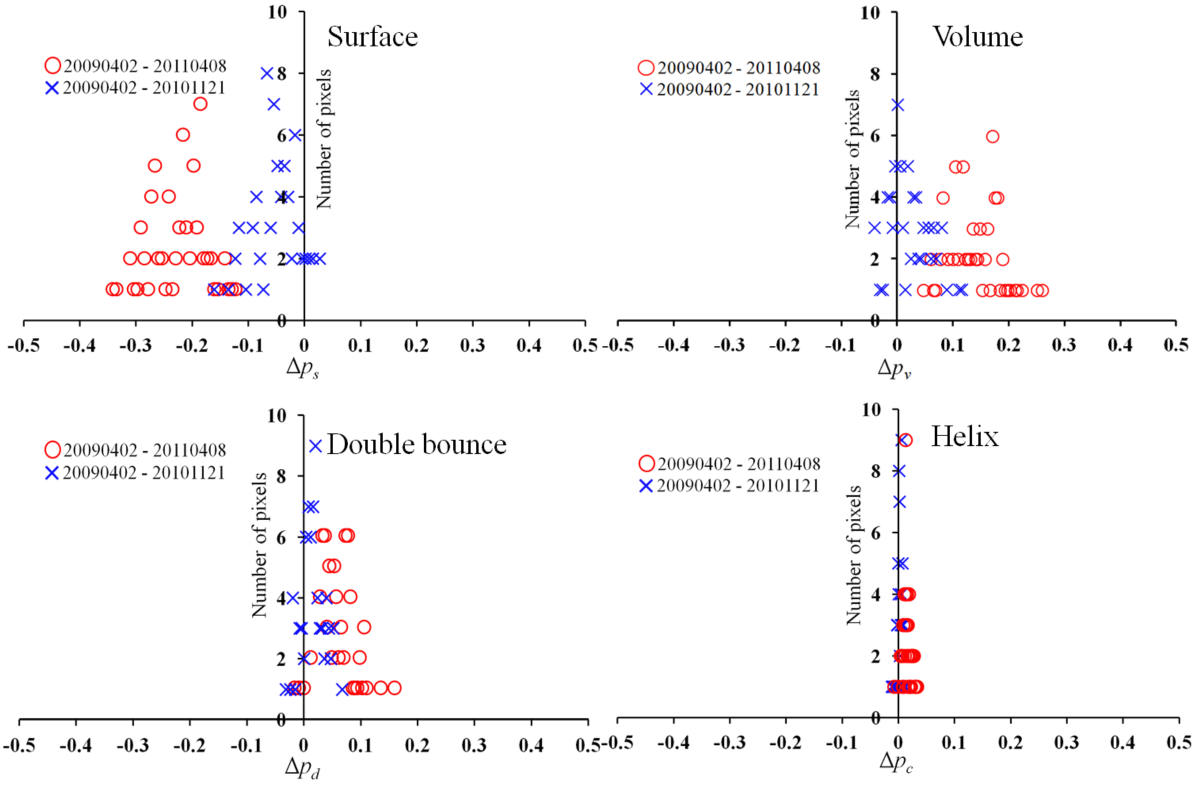

Fig. 7.7. Differences in pixel values for Δp_s, Δp_v, Δp_d, and Δp_c over agricultural area/ debris on the agricultural area; these plots are plotted by using patch B (see Fig. 7.4) [○ denotes the difference in between pre-earthquake/tsunami (20090402) and post-earthquake/tsunami (20110408) decomposition parameters; and × denotes temporal difference [before (20090402) –after (20101121)] of the decomposition parameters].

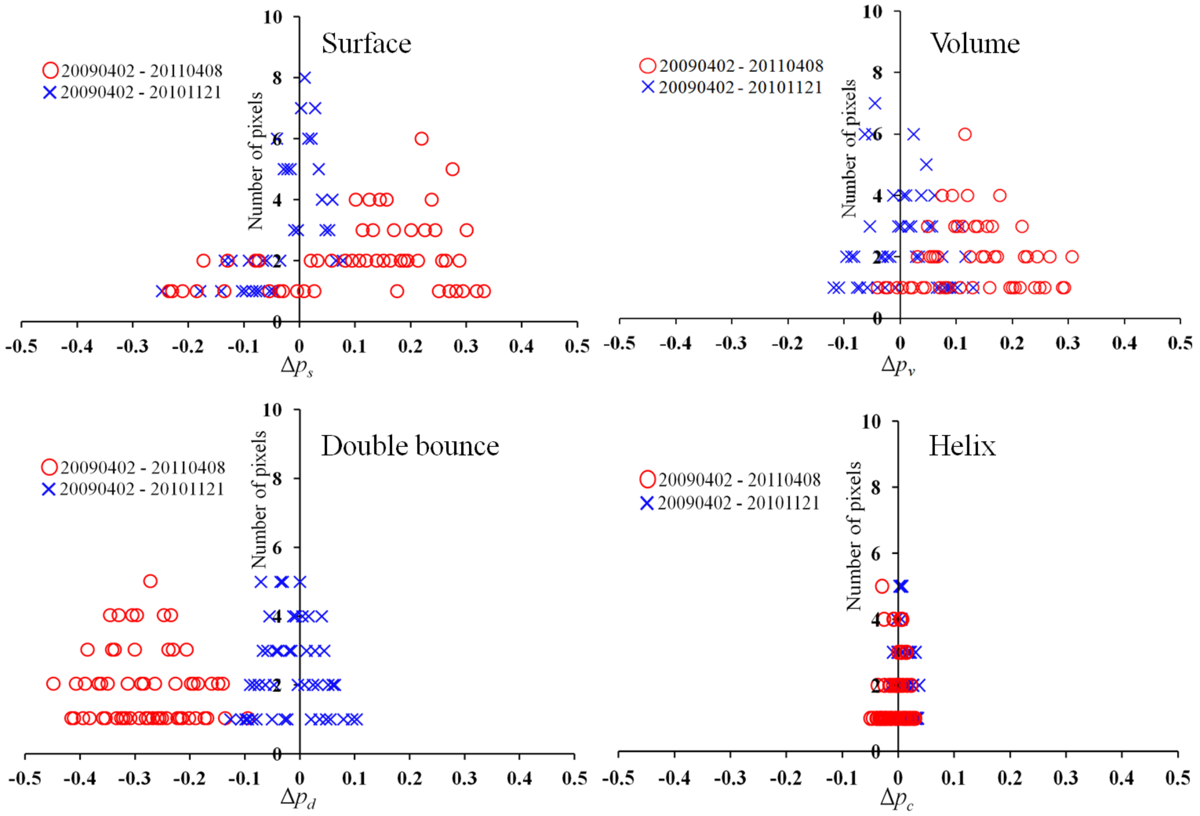

Fig. 7.8. Differences in pixel values for the Δp_s , Δp_v , Δp_d , and Δp_c over urban area; these plots are drawn by using patch C (Fig. 7.5) [○ denotes the difference in between pre-earthquake/tsunami (20090402) and post-earthquake/tsunami (20110408) decomposition parameters, and also × denotes temporal difference [before (20090402) –after (20101121)] of the decomposition parameters].

Table 7.2. Statistics of the difference values of pixels for patches A, B, and C [○ denotes the difference in between pre-earthquake/tsunami (20090402) and post-earthquake/tsunami (20110408) decomposition parameters, and × denotes temporal difference [before (20090402) –after (20101121)] of the decomposition parameters]

	Scattering component		Min.	Max.	Mean	Median	Mode	Std. Dev.	Number of pixels
Patch A	Δp_s	○	-0.073	0.263	0.107	0.107	0.038	0.070	100
		×	-0.204	0.240	0.007	-0.004	0.002	0.087	
	Δp_v	○	-0.299	0.008	-0.154	-0.160	-0.129	0.066	
		×	-0.229	0.189	-0.022	-0.022	-0.058	0.088	
	Δp_d	○	-0.067	0.192	0.047	0.036	0.036	0.054	
		×	-0.083	0.099	0.013	0.012	0.012	0.038	
	Δp_c	○	-0.032	0.038	-0.000	0.000	-0.018	0.015	
		×	-0.036	0.030	0.001	-0.001	-0.005	0.013	
Patch B	Δp_s	○	-0.341	-0.123	-0.222	-0.216	-0.185	0.050	75
		×	-0.160	0.027	-0.046	-0.048	-0.066	0.039	
	Δp_v	○	0.048	0.262	0.145	0.142	0.173	0.046	
		×	-0.040	0.116	0.024	0.019	0.001	0.035	
	Δp_d	○	-0.017	0.158	0.061	0.056	0.032	0.031	
		×	-0.031	0.068	0.019	0.016	0.020	0.020	
	Δp_c	○	-0.008	0.033	0.016	0.014	0.012	0.008	
		×	-0.012	0.020	0.004	0.003	0.005	0.005	
Patch C	Δp_s	○	-0.235	0.331	0.136	0.157	0.219	0.132	112
		×	-0.248	0.140	-0.001	0.008	0.062	0.002	
	Δp_v	○	-0.040	0.355	0.150	0.128	0.115	0.093	
		×	-0.118	0.130	0.005	0.005	-0.045	0.056	
	Δp_d	○	-0.445	-0.095	-0.280	-0.288	-0.272	0.075	
		×	-0.126	0.175	-0.012	-0.015	-0.070	0.050	
	Δp_c	○	-0.050	0.030	-0.006	-0.003	-0.028	0.018	
		×	-0.270	0.036	0.007	0.005	0.001	0.014	

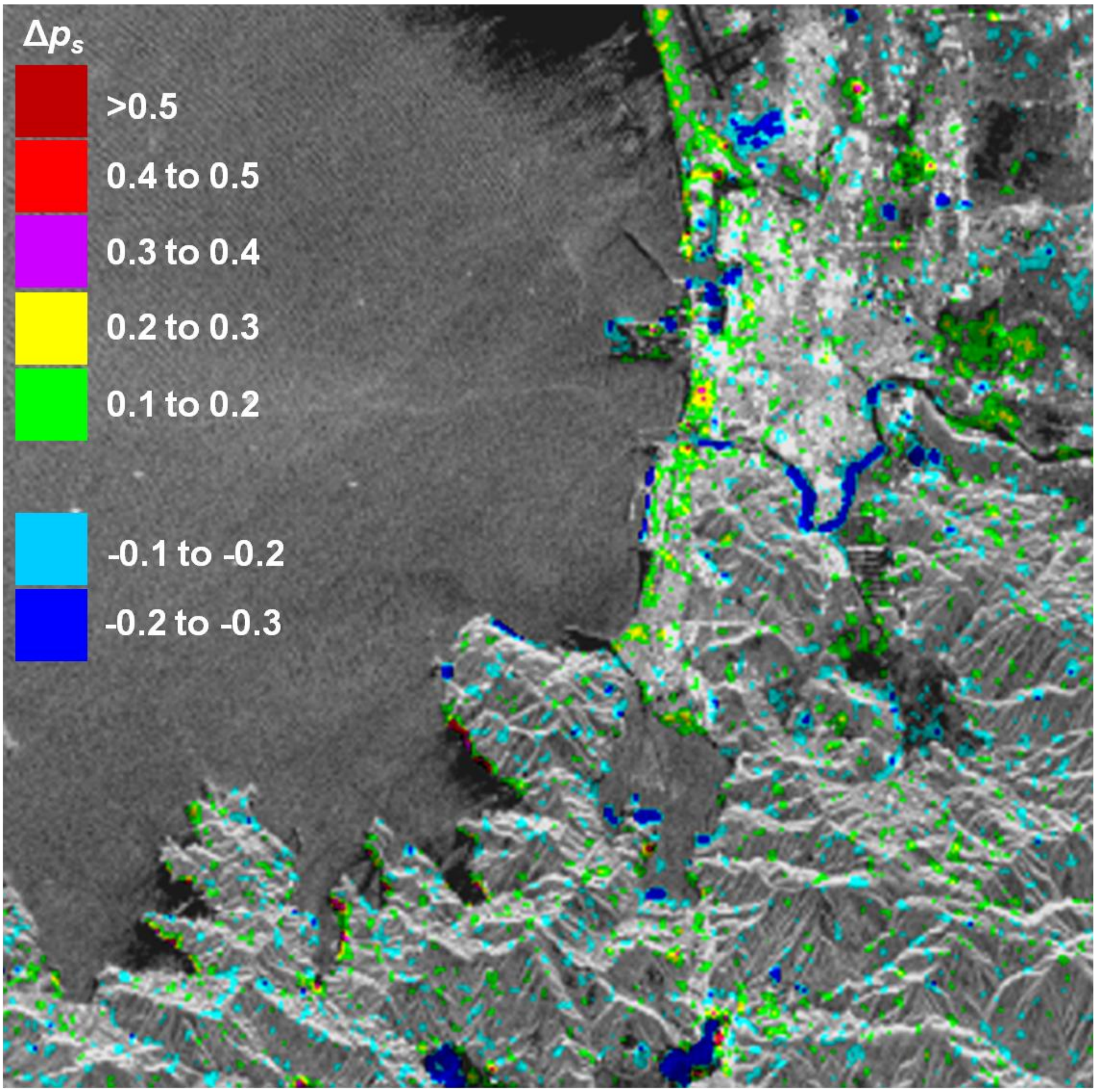

(a)

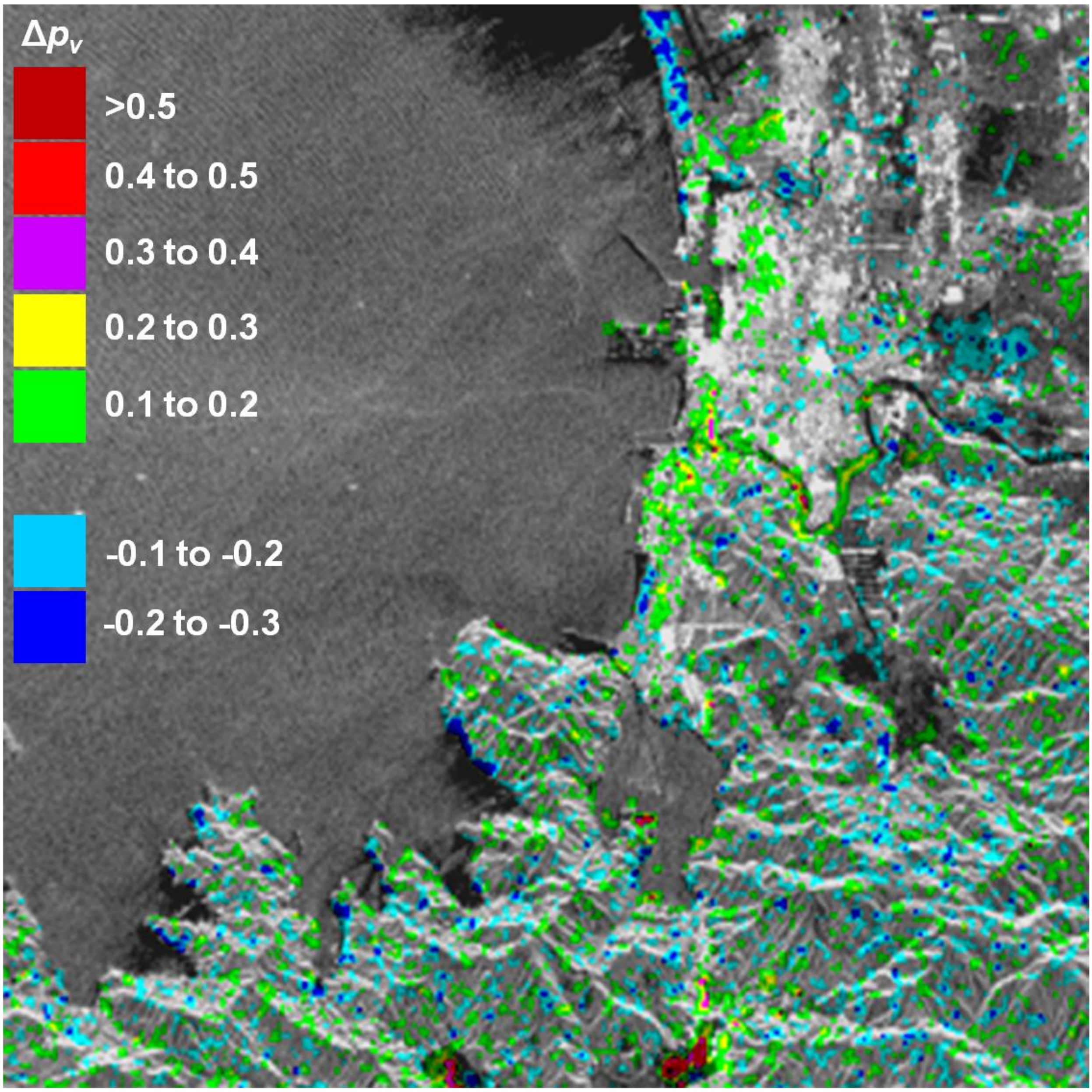

(b)

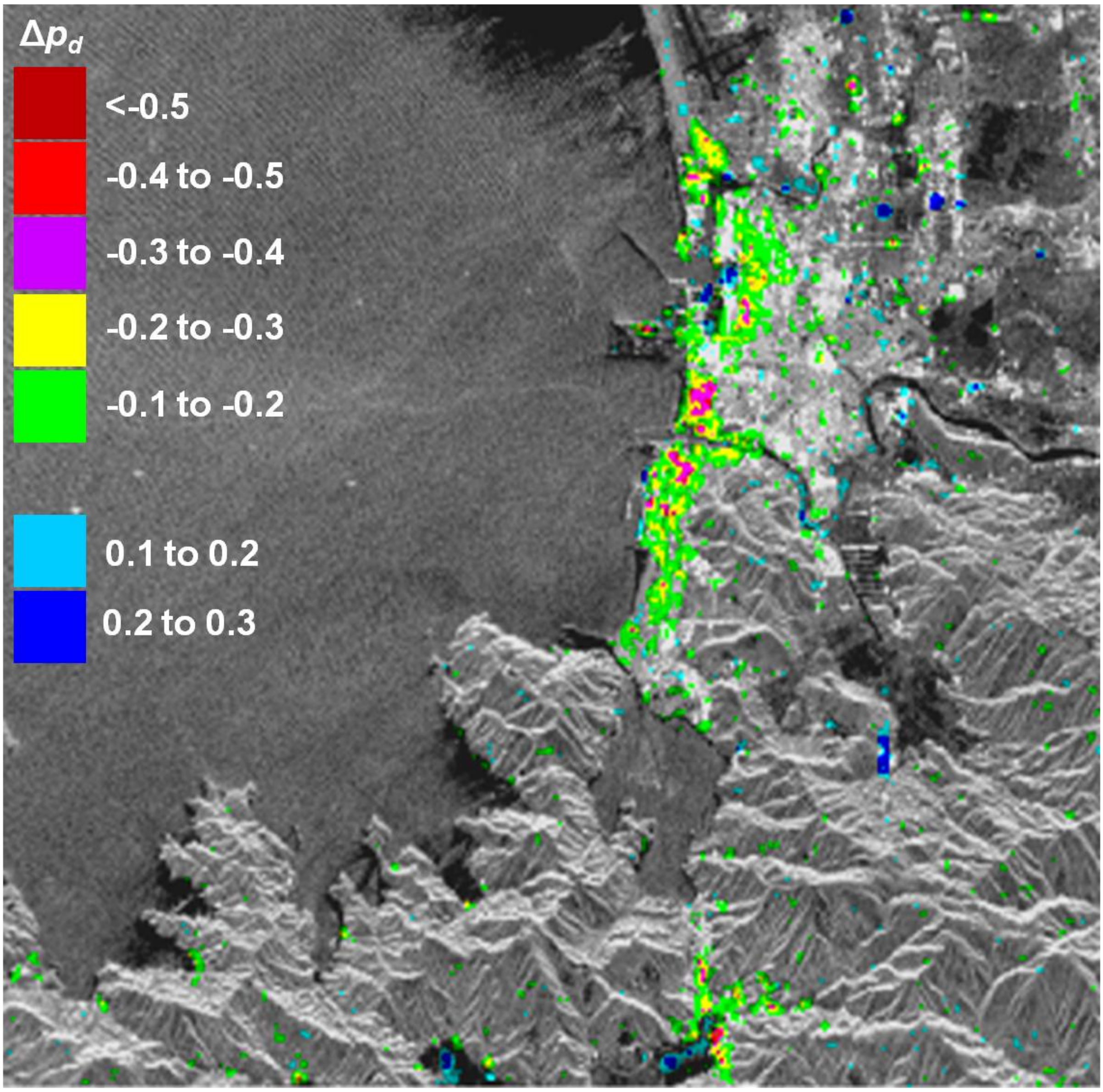

(c)

Fig. 7.9. Difference images in between pre-earthquake/tsunami (20090402) and post-earthquake/tsunami (20110408) behaviour of decomposition parameters. (a) Δp_s , (b) Δp_v , and (c) Δp_d are superimposed on *TP* image of 20090402.

As comparisons of the G4U RGB in Fig.7.3 and the pixel distribution plots in Fig.7.8 show, the dominating double-bounce scattering contribution (red color in Fig. 7.3) in between 20090402 and 20101121 is not significantly changed, and the difference value only slightly changes within the range ±0.1. This slight temporal change ±0.1 in p_d is because of the seasonal change that could be sustained in minor natural scattering behaviour, e.g., tree or vegetation (Dobson *et al.* 1991), which are mixed with urban blocks in resolution cells. The change of season affects the moisture content of vegetation and soil, which in turn influences the intensity of radar backscatter and settlement detectability. This cause forces fluctuations in the difference value of p_d but this change in p_d is small as compared to changes after the earthquake/tsunami. Moreover, a few spots show temporal changes of more than 0.1 in p_d over the car parking areas, small agricultural land in urban areas, and building close to agricultural areas; the effect of the agricultural land on settlement detectability implies variability with the climatic season. Otherwise, changes of more than 0.1 in p_d over urban blocks and other areas containing man-made structures are less sensitive to temporal changes (Fig.7.10). However, the same season's images are utilized to minimize effect of the seasonal cycle changes in the urban area.

Furthermore, it is well illustrated in the pertinent literature (Arii *et al.* 2011; Cloude 2009; Cloude and Pottier 1997; Freeman and Durden 1998; Krogager1990; Lee and Pottier 2009; Lee and Ainsworth 2011; Singh *et al.* 2013b; Singh *et al.* 2013c; Touzi 2007; vanZyl *et al.* 2008; vanZyl and Kim 2010;Yamaguchi 2007; Yamaguchi *et al.* 2005; Yamaguchi *et al.* 2006;Yajima *et al.* 2008;Yamaguchi *et al.* 2011) that the double-bounce scattering over the urban area becomes dominant because of the ground-wall interface or the wall–ground interface and other man-made structures. Building blocks in the urban areas can be treated as relatively coherent scatterers (Mott 2007), which do not change with time unless natural and/or anthropogenic disaster occurs. When these wall-ground and ground-wall interfaces are damaged by the earthquake/tsunami disaster, the reduction in the amount of the double-bounce scattering power is noticed. Since the difference of the p_d value in between pre- and post-disaster is very sensitive in man-made structures, parameter p_d is useful to analyze the influence of earthquake and tsunami before and after the natural hazard event. Further, these changes in parameter p_d are related to the urban areas affected by the earthquake and tsunami. For example, the difference of the p_d value in between pre- and post-disaster is categorized over the Ishinomaki city and surrounding areas, and it is observed that green color (from -0.1 to -0.2) coded areas in Fig. 7.11 appear in urban areas for partly damaged buildings and/or man-made structures, whereas yellow (from -0.2 to -0.3), magenta (from -0.3 to -0.4), red (from -0.4 to -0.5) and brown (< -0.5) colors in Fig. 7.11 represent the severely damaged urban areas and/or areas with completely wiped out buildings by earthquake/tsunami impact.

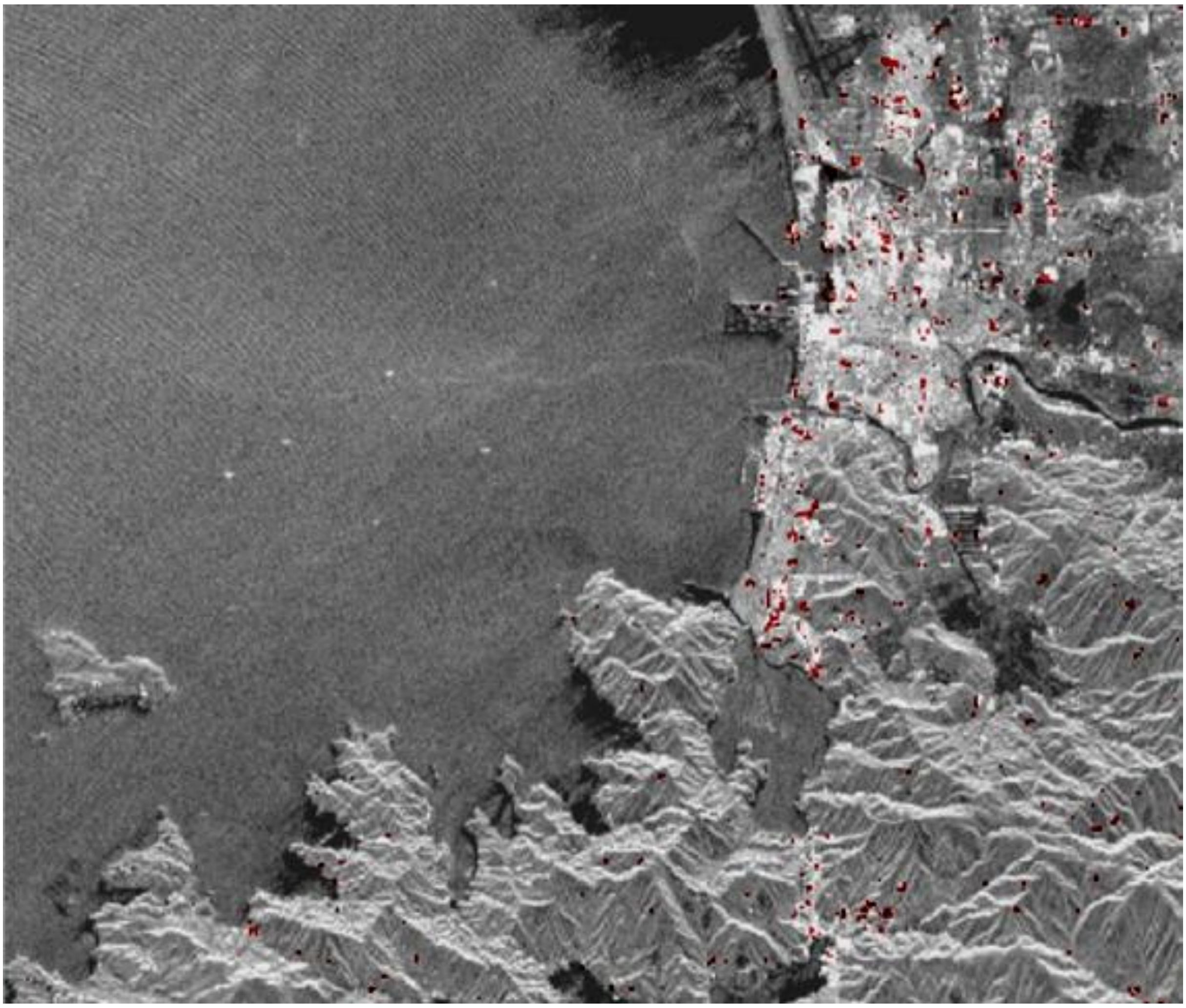

Fig. 7.10. The masked temporal difference (in between the 20090402 and 20101121) of the decomposition parameter Δp_d image is superimposed on the *TP* image of 20090402 (brown color denotes the difference < -0.1).

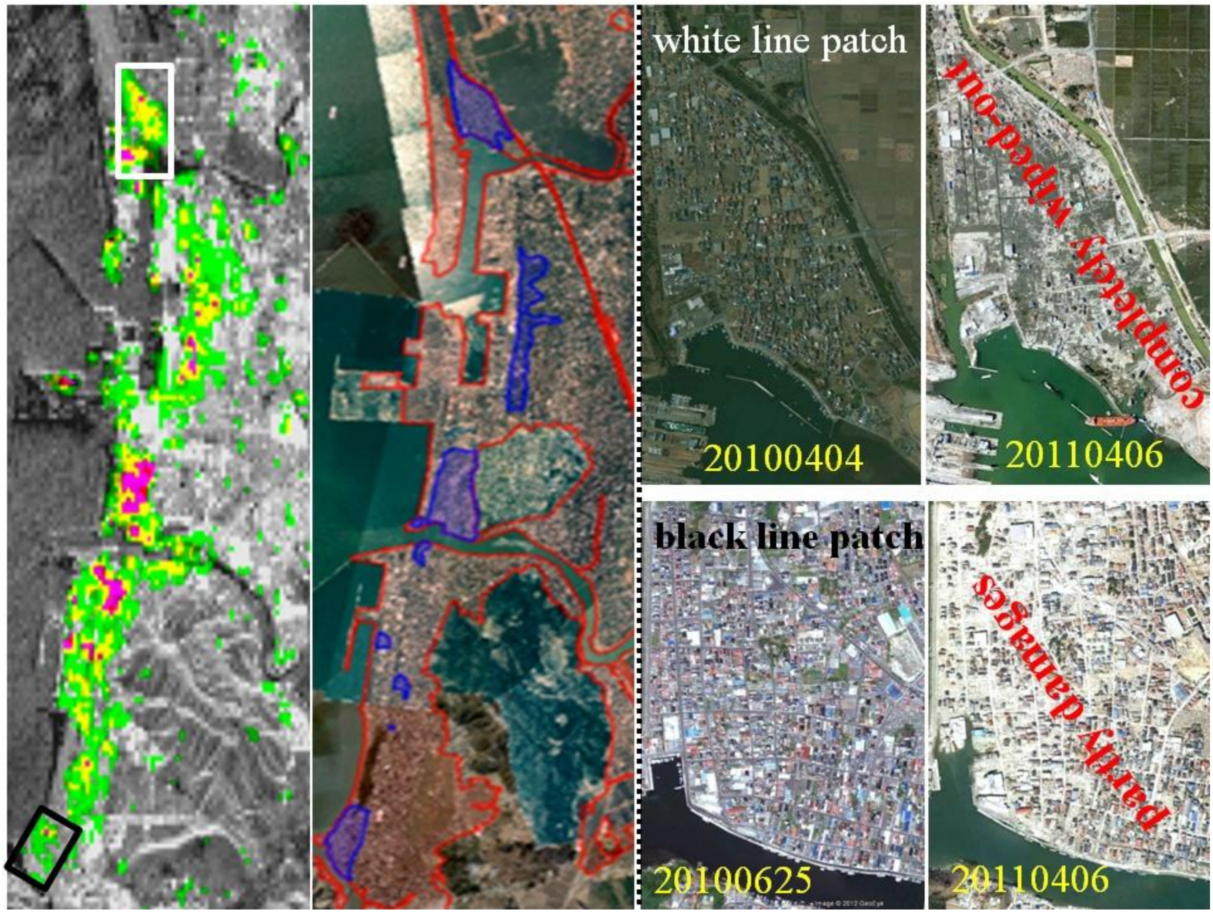

Fig. 7.11. **Left:** the masked temporal difference (in between the 20090402 and 20101121) of decomposition parameter Δp_d image is superimposed on *TP* image of 20090402 (green color represents partly damages in urban areas, and yellow, magenta, red and brown color denote the completely wiped out urban areas). **Second image from left:** ground-truth information (blue color areas show damages in urban areas and red color represents tsunami covered areas).**Right side from the black dashed line:** Google optical pre- and post-earthquake/tsunami images; the upper optical images for white line patch in the left-side image and the lower optical images for black line patch in the left-side image, respectively.

7.4.3 VHR SAR Color-Coded Images

The high-resolution quad-polarization PALSAR images showed their capability in the detection and analysis of urban areas. In addition, VHR quad-polarization SAR sensors permit to extract information from VHR SAR images about the man-made and natural features individually. Unfortunately, we do not have polarimetric VHR image data sets over the Off-Tohoku Tsunami/earthquake coastal areas; but we have VHR FULL-POL-SAR image data access the other parts of the globe. These data sets cover various features such as urban areas, vegetation, water areas, etc. This section shows that VHR SAR images (TerraSAR-X images) provide better decomposition images over highly oriented man-made features and urban areas as compared to standard resolution images (e.g., PALSAR images). Therefore, polarimetric VHR imagery should provide more accurate damage assessments of natural occurring and anthropogenic hazards in dense urban areas. For example, the high-resolution ALOS-PALSAR and VHR TerraSAR-X quad-polarization data sets were used over Niigata, Japan, for comparing the effect of resolution with the G4U scheme (Singh *et al.* 2013b). High-resolution ALOS-PALSAR quad-polarization data were acquired on March 04, 2010, with

21.5^0 off-nadir angle and VHR TerraSAR-X quad-polarization data were acquired on April 22, 2010 with 36.7^0 off-nadir angle. For TerraSAR-X data sets, the window size for the ensemble average in image processing was chosen as twelve in the range direction and ten in the azimuth direction. The G4U color-coded images of ALOS-PALSAR and TerraSAR-X over the Niigata are displayed in Fig. 7.12 and Fig 7.13. The VHR (2m ground range resolution) quad-polarization TerraSAR-X data with the G4U method clearly envisages urban areas compared to high-resolution (30 m ground range resolution) ALOS-PALSAR data. Additionally, a representative VHR DLR F-SAR S-band image of June 08, 2010, over the chosen region of Kaufbeuren, Germany, is shown in Fig. 7.14 with the G4U method; the VHR resolution (0.5 m) provides the information on individual buildings and single trees. The DLR F-SAR images were averaged by factor ten both in the range direction and the azimuth direction before generating the G4U color-coded image. The comparison of the Pauli and G4U RGB in Fig. 7.15 showed that objects discriminations are visible in the G4U RGB much more clearly. Moreover, it becomes apparent that using VHR quad-polarization SAR images and implementing the G4U method improves rather considerably the discrimination of the land-use/land-cover objects from one another.

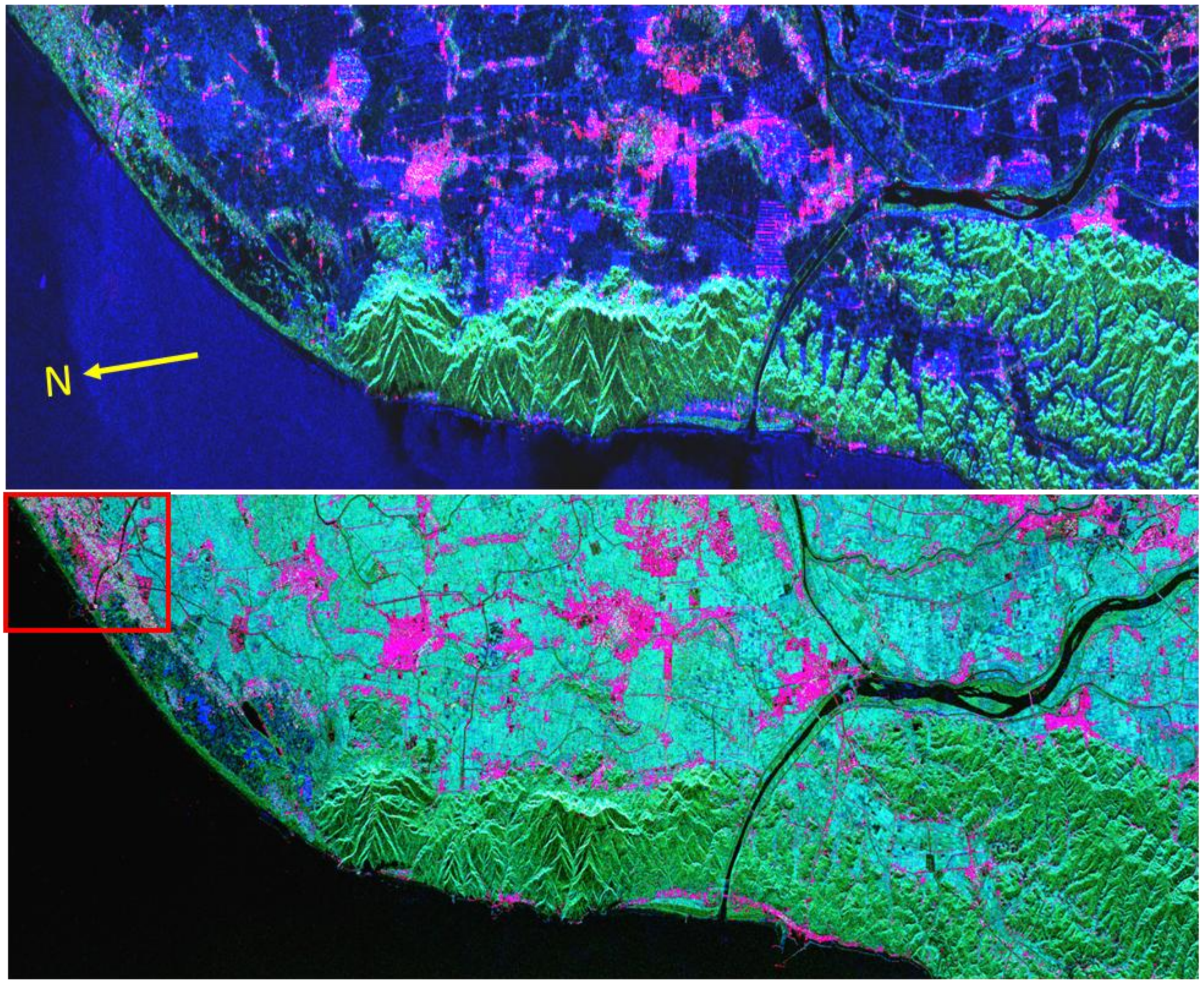

Fig.7.12. The G4U color-coded images with surface scattering (blue), volume scattering (green), and double-bounce scattering (red) over the Niigata, Japan. (**Top**) ALOS-PALSAR data of March 03, 2010.(**Bottom**) TerraSAR-X data of April 22, 2010.

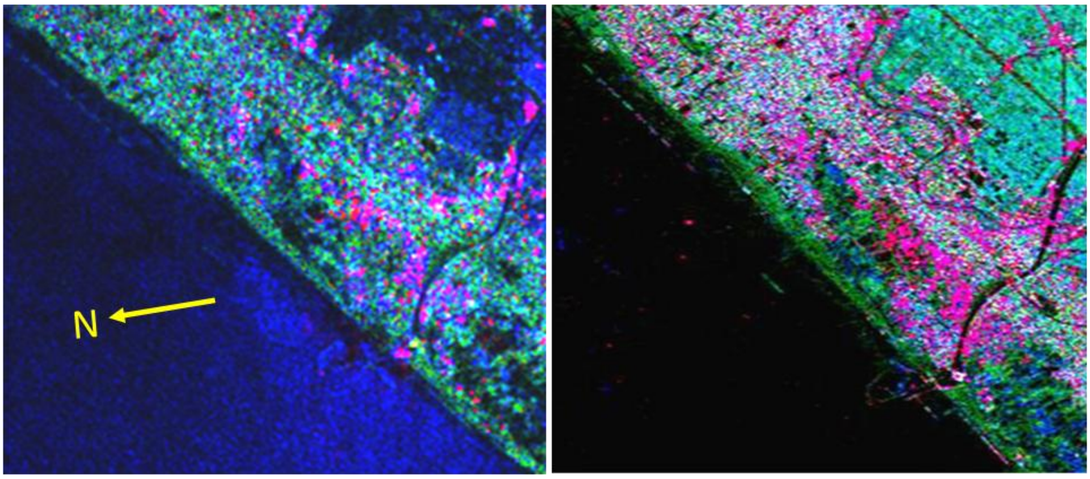

Fig.7.13. Close-up of the G4U color-coded images with surface scattering (blue), volume scattering (green), and double-bounce scattering (red) over the Niigata, Japan, for red rectangular areas in Fig. 7.12. (**Left**) ALOS-PALSAR. (**Right**) TerraSAR-X.

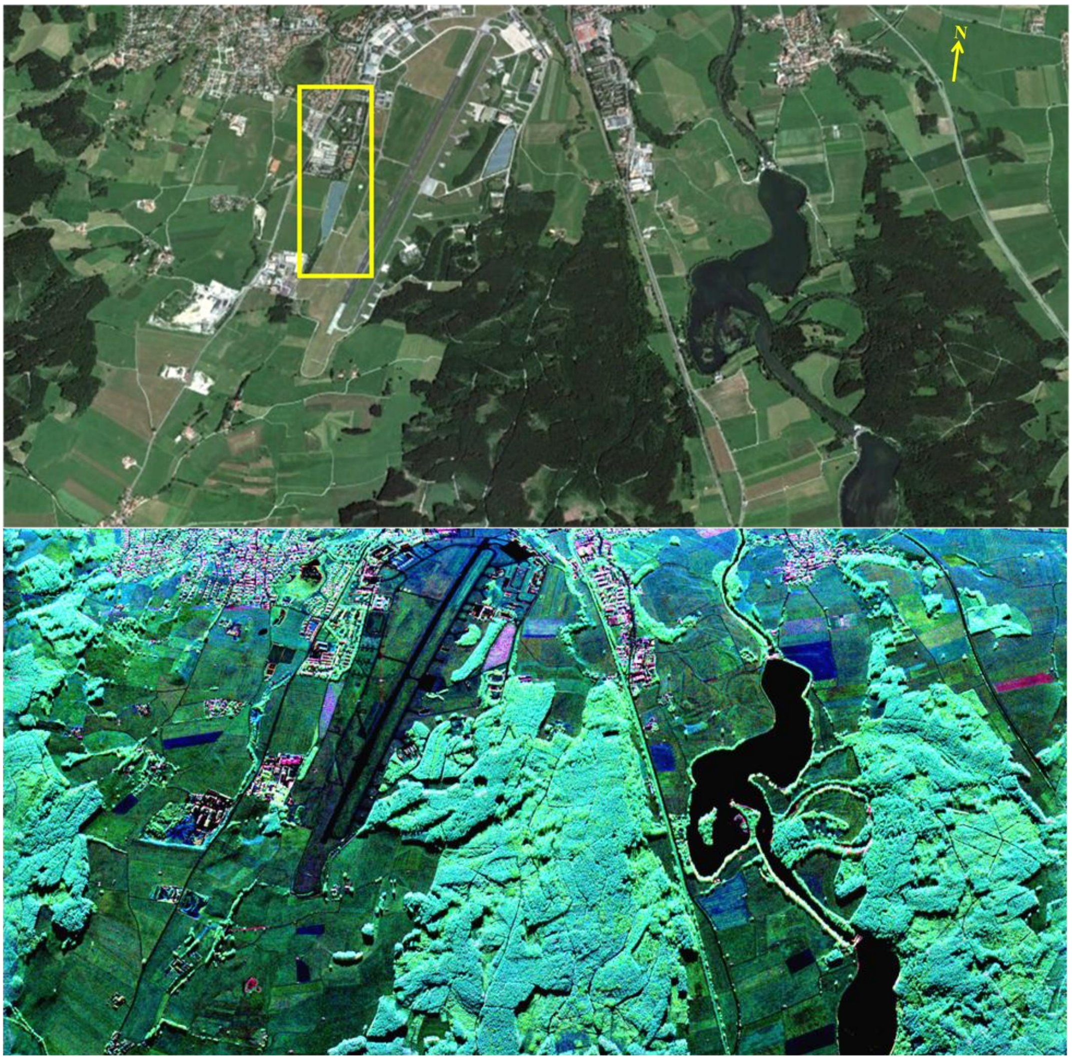

Fig.7.14. (**Top**) Google optical image of July 16, 2010. (**Bottom**) The G4U color-coded image for DLR F-SAR S-band data of the June 08, 2010 with surface scattering (blue), volume scattering (green), and double-bounce scattering (red) over the Kaufbeuren, Germany.

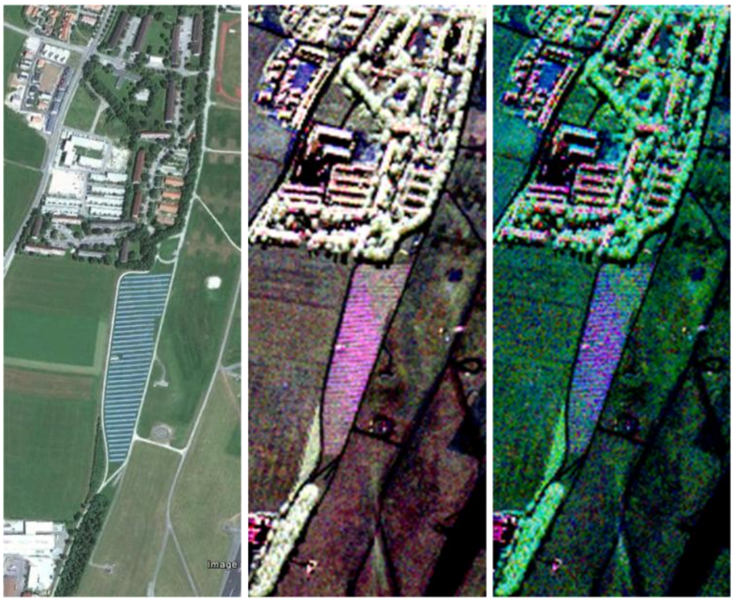

Fig.7.15. Close-up area of the yellow line box in Fig.7.14. (**Left**) Google optical image of July 16, 2010.(**Center**) Pauli RGB HH-VV (red), 2HV (green), HH+VV (blue) image.(**Right**) the G4U color-coded image for DLR F-SAR S-band data of June 08, 2010, with surface scattering (blue), volume scattering (green), and double-bounce scattering (red) over the Kaufbeuren, Germany.

7.5. Summary and Conclusions

Fully polarimetric high-resolution L-Band image data sets with the implementation of the G4U scheme provide a straightforward simple tool for interpreting as well as identifying collapsed buildings caused by earthquake/ tsunami disasters. This result holds equally well for typhoon or tornado and other man-made disaster assessments. Furthermore, the basic behaviours of scattering parameters p_s , p_v, and p_d are observed as follows. 1) Generally, surface scattering is increased in tsunami affected areas (vegetation damaged area and wiped out/collapsed urban block areas), but it can be decreased in the areas of the deposition of wiped out buildings by the retreating tsunami and for the floating buildings in bay areas; 2) Volume scattering is decreased in tsunami affected or damaged vegetation areas and increased in damaged or collapsed, deposited and/or floating (on bays water surface) urban blocks or man-made structures by the earthquake/tsunami; 3) Double-bounce scattering is decreased in earthquake/tsunami collapsed or damaged urban areas and increased in areas with deposited (in agricultural field or other type scattering dominated areas) or floating (on bays water surface) wiped out urban blocks or man-made structures, mainly caused by the retreating tsunami.

Here, we need to emphasize that, based on reproducible multiband F-SAR experiments carried out at DLR (Reigber *et al.* 2011), the S-Band FULL-POL-SAR image data sets will be superior to L-band, because at S-Band higher resolution and still high polarimetric sensitivity can be achieved which for L-Band does not yield such high resolution although polarimetric sensitivity is high. The C-Band polarimetric sensitivity is inferior to S-Band and the resolution is not remarkably increased. Furthermore, currently, the S-Band operational bandwidth is still relatively larger for satellite implementation of fully polarimetric VHR POL-SAR sensors. Therefore, we are looking forward to toward the addition of high-resolution fully polarimetric S-Band POL-SAR satellite sensors for improved VHR POL-SAR natural and also anthropogenic *in situ* disaster damage assessments.

Chapter 8 Generalized FULL-POL-SAR Decomposition Scheme over Wet Snow Areas

Forward evolution is invertible when an unknown is to be determined

8.1 Abstract

Wet snowpack is very critical to forecasting of snow melt runoff and avalanche activity in snow-covered mountainous areas. This chapter presents the generalized fully polarimetric synthetic aperture radar (FULL-POL-SAR) decomposition scheme over a wet snow area. This decomposition accounts for all independent parameters of the coherency matrix. In the proposed decomposition scheme, a generalized spheroidal (ellipsoid) shape is considered for volume scattering model derivation. Furthermore, the generalized Cloude volume and the Freeman surface parameters have been derived for wet snow areas, which account for all independent relative polarimetric phase parameters of the coherency matrix. The generalized volume parameter is bounded in value by the dielectric constant to lie within certain limits. When prior information of the dielectric constant is not available, an adaptive volume parameter value can be employed. These generalized volume and surface parameters will be useful for the development of a snow dielectric constant retrieval inversion algorithm with one unknown parameter, i.e. the dielectric constant of snowpack.

8.2 Introduction

The development of simple theoretical inversion techniques with least unknown parameters for retrieving snowpack parameters (e.g. wetness) is important in fully polarimetric synthetic aperture radar (FULL-POL-SAR) research. Over the past few years, several case studies have been reported using active microwave remote sensing systems for the detection of the snow condition (Mätzler and Schanda 1984; Stiles and Ulaby 1980; Ulaby and Stiles 1980 ; Ulaby and Stiles 1981), snow extent (Nagler and Rott 2000; Rott and Nagler 1992; Shi and Dozier 1997; Shi *et al.* 1994), microwave backscattering response from dry and wet snow (Rott *et al.* 1992; Shi *et al.*1993), snow water equivalent (Rott *et al.* 2010; Shi and Dozier 2000), and snow wetness (Shi and Dozier 2000; Singh and Venkataraman 2010). It has been found that the backscattering coefficient image of radar is extremely useful for the quantitative estimation of snow wetness (Shi and Dozier 1995; Singh and Venkataraman 2010). The relationship between the backscattering coefficient and snow wetness depends on sensor parameters (frequency, polarization, and viewing geometry) and snow parameters (density, liquid water content, particle size and shape of ice and water inclusion and surface roughness) but the actual relationship between radar measurements and snow wetness depends on which scattering component is the dominant scattering source (e.g. surface or volume scattering) (Shi and Dozier 1995). Thus, it is essential to determine dominant and accurate scattering mechanisms for developing an effective snow wetness retrieval algorithm. FULL-POL-SAR measurements allow a discrimination of different types of scattering mechanisms from the snowpack and other land-covered areas by using various novel polarimetric target decomposition methods (Arii *et al.* 2011; Lee and Ainsworth 2011; Singh *et al.* 2013b; Yamaguchi *et al.* 2011). Since there is a need to explore the FULL-POL-SAR interactions with Himalayan snowpack and a methodology for retrieval of snow parameters, the main aim of this investigation is to develop a generalized decomposition scheme of FULL-POL-SAR data, incorporating the knowledge of polarimetric microwave interactions with snow and other associate objects in the Indian Himalayan regions. A generalized spheroidal shape of snow particle is assumed to express volume scattering model in the proposed decomposition scheme for wet snowpack in mountainous area because the particle shapes in wet snowpack become rounded (Singh 2010). Moreover, two generalized scattering parameter (volume and surface) methods have been proposed over wet snow-covered areas, which are invertible in the dielectric constant of snowpack.

8.3 Decomposition Algorithm Development

The generalized four-component decomposition scheme with unitary transformation (G4U) is developed in Chapter 6 (Singh *et al.* 2013b) for retrieving the scattering powers,

$$\begin{aligned}\langle[T(\varphi)]\rangle = [U(\varphi)]\langle[T(\theta)]\rangle[U(\varphi)]^{\dagger} &= \begin{bmatrix} T'_{11} & T'_{12} & T'_{13} \\ T'_{21} & T'_{22} & 0 \\ T'_{31} & 0 & T'_{33} \end{bmatrix} \\ &= f_s[U(\varphi)]\langle[T]\rangle_{surface}[U(\varphi)]^{\dagger} + f_d[U(\varphi)]\langle[T]\rangle_{double}[U(\varphi)]^{\dagger} + f_v[U(\varphi)]\langle[T]\rangle_{vol}[U(\varphi)]^{\dagger} \\ &\quad + f_c[U(\varphi)]\langle[T]\rangle_{helix}[U(\varphi)]^{\dagger} \qquad (8.1)\end{aligned}$$

with the unitary transform matrix,

$$[U(\varphi)] = \begin{bmatrix} 1 & 0 & 0 \\ 0 & \cos 2\varphi & j\sin 2\varphi \\ 0 & j\sin 2\varphi & \cos 2\varphi \end{bmatrix} \text{ with } 2\varphi = \frac{1}{2}\, tan^{-1}\left(\frac{2\,\mathrm{Im}\,\{T_{23}(\theta)\}}{T_{22}(\theta) - T_{33}(\theta)}\right) \qquad (8.2)$$

where † denotes complex conjugation and transposition, and the unitary transform matrix U (φ) and φ are introduced in Chapter 6 ; $\langle[T(\theta)]\rangle$ denotes the measured coherency matrix after orientation compensation (Lee and Ainsworth 2011; Yamaguchi *et al.* 2011); f_s, f_d, f_v and f_c are coefficients to be determined; $\langle[T]\rangle_{surface}$, $\langle[T]\rangle_{double}$, $\langle[T]\rangle_{vol}$ and $\langle[T]\rangle_{helix}$ are expansion matrices corresponding to the surface, double-bounce, volume, and helix scattering, respectively (Yamaguchi *et al.* 2006).

G4U is applied to fully polarimetric L-band ALOS-PALSAR polarimetric measurements for the development of an improved decomposition strategy over wet snow-covered areas for snow wetness retrieval. The polarimetric data set over the Gangotri glacier region was acquired with L-band PALSAR quad polarization mode at 23.1^0 of incident angle on June 06, 2010 at local time 10:37 PM. The land cover includes snow, debris covered glacier domains, and rocks, etc. (Fig.8.1). ALOS-AVNIR data (May 25, 2010) sets are used to interpret the behaviour of the glacier area although acquired at a different day (local time 11:02 AM). The comparison of visual interpretation can be done for decomposed images with the cloud free AVNIR-2 image in Fig.8.1. G4U shows good capability for delineation the snow line (the lower altitudinal boundary of a snow-covered area) with the L-band POL-SAR data over the glaciated terrain of the Indian Himalayan region. The double-bounce scattering term is small over snow-covered terrain. It should be emphasized that highly accurate acquisition of the *HV* component with strong suppression of the noise floor is here of paramount relevance (Touzi 2007).

8.3.1 Backscattering from snow-covered terrain

Microwave interaction with snow depends on dielectric and geometric properties of the object. Sensor properties also influence the target response to the incident wave. In general, the backscattering coefficient of snow-covered terrain consists of contributions resulting from (Ulaby *et al.* 1986): 1) backscattering from the snow-air interface; 2) volume scattering from the snow layer; and 3) backscattering from the underlying ground surface. When snow becomes wet, important backscattering contributions result from volume and snow-surface scattering contribution (Shi and Dozier 1995).

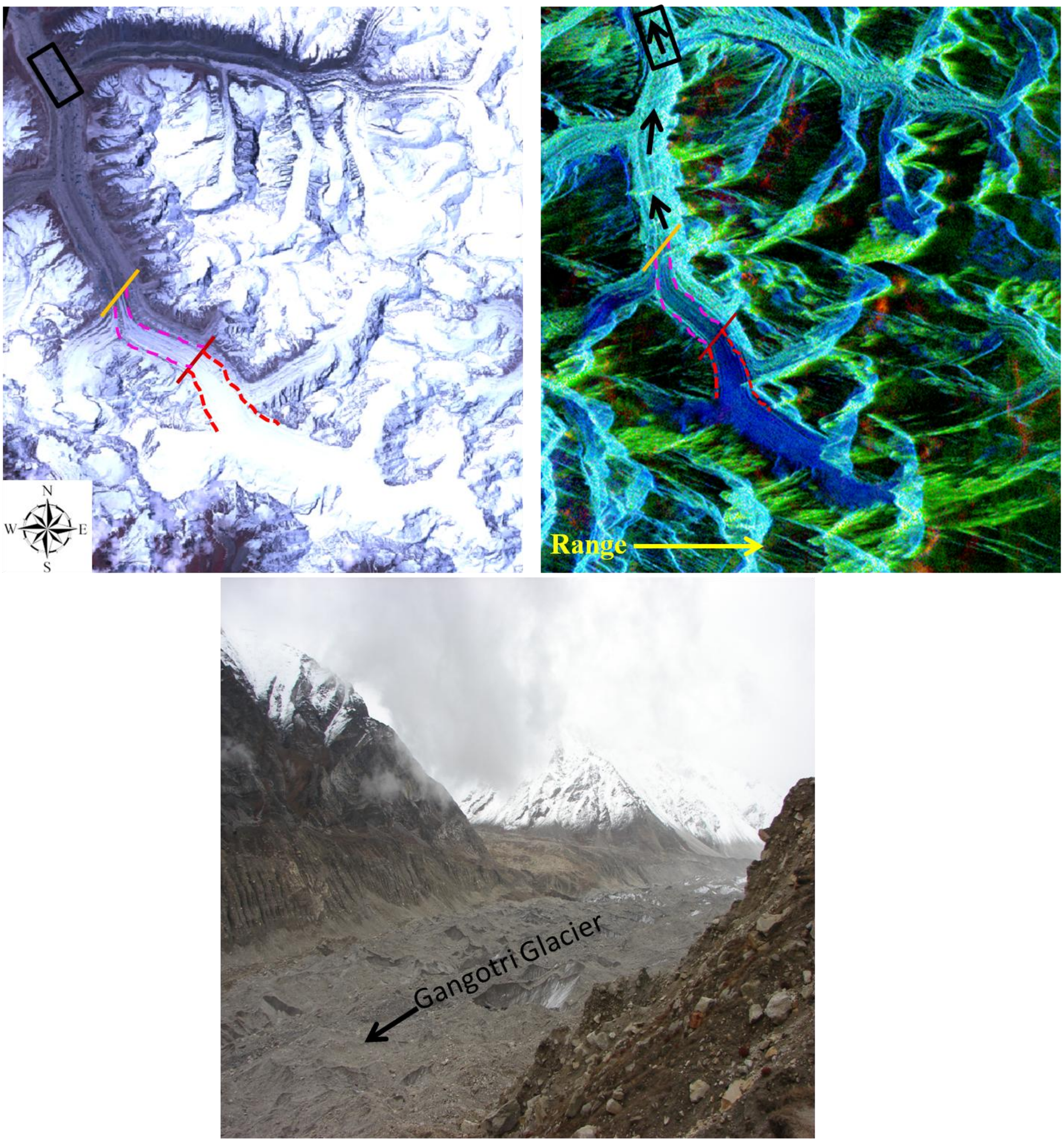

Fig.8.1 **Top row**: (**left**) ALOS-AVNIR-2 FCC image of 25-05-2010 over the Gangotri glacier (**right**) G4U: general four-component scattering decomposition FCC with 12 × 2 multi-look (azimuth × range) factors of 06-06-2010 over the Gangotri glacier (Red: double-bounce scattering, Green: volume scattering, Blue: surface scattering). (**Bottom**) Field photo of the black rectangular area in top row images. The magenta dashed lines cover the transition zone in between snow accumulated area behind the red line (across the glacier) and the ablation area below the golden line. Black arrows indicate the flow direction of the glacier.

8.3.2. Volume scattering model for wet snow

A snow layer is composed of scattering elements –ice particle and water inclusion –with different sizes, shapes and orientations. Volume scattering matrix for single particle is defined based on the first order backscattering coefficient derivation (Fung 1994) as

$$[\boldsymbol{S}_{vol}] = \begin{bmatrix} S_{HH}^{vol} & 0 \\ 0 & S_{VV}^{vol} \end{bmatrix} = S_{HH}^{vol} \begin{bmatrix} 1 & 0 \\ 0 & A_P \end{bmatrix} \qquad (8.3)$$

where

$$\left|S_{HH}^{vol}\right|^2 \approx \frac{1}{4\pi}\,\sigma^0_{HH,vol} = |\gamma_{HH}|^2 . f(\theta_i, \theta_r, \omega, \tau, P_{HH}) \tag{8.4}$$

$$\left|S_{VV}^{vol}\right|^2 \approx \frac{1}{4\pi}\,\sigma^0_{VV,vol} = |\gamma_{VV}|^2 . f(\theta_i, \theta_r, \omega, \tau, P_{VV}) \tag{8.5}$$

$$A_P = \frac{\gamma_{VV}}{\gamma_{HH}}\,. \tag{8.6}$$

ω is snow volume scattering albedo($\omega = K_s/K_e$); K_s is a scattering coefficient ($K_s = K_e - K_a$); K_e is the extinction coefficient ; K_a is the absorption coefficient ($K_a = 2\boldsymbol{k}$ ($|\mathrm{Im}\sqrt{\varepsilon_s}|$)); $\boldsymbol{k}$ is wave number ; ε_s is the media relative dielectric constant; τ is the optical depth ($\tau = K_e d$); d is snow depth; P_{HH} is a Rayleigh phase function for *HH*-Polarization ; P_{VV} is the Rayleigh phase function for *VV*-Polarization; θ_i and θ_r are the local incident and refractive angles, respectively. Since the scatterers are small compared to the wavelength, the Rayleigh phase function $P = P_{VV} = P_{HH} = 1.5$ (Floricioiu and Rott 2001; Fung 1994).

The right hand side of (8.3) shows that the scattering matrix [$\boldsymbol{S}_{vol}$] is similar to that given in Cloude (2009) for the spheroidal shape particle. A_P is known as particle anisotropy (Cloude 2009) and it is bounded by (8.7)

$$\frac{1}{\varepsilon_s} < A_P < \frac{\varepsilon_s + 1}{2} \tag{8.7}$$

Volume scattering matrix [$\boldsymbol{S}_{vol}$] can be written for single particle with rotation about line of sight by angle θ as

$$[\boldsymbol{S}_{vol}] = S_{HH}^{vol}\begin{bmatrix}\cos\theta & \sin\theta \\ -\sin\theta & \cos\theta\end{bmatrix}\begin{bmatrix}1 & 0 \\ 0 & A_P\end{bmatrix}\begin{bmatrix}\cos\theta & -\sin\theta \\ \sin\theta & \cos\theta\end{bmatrix} \tag{8.8}$$

where γ_{HH} is the Fresnel transmission coefficient for HH polarization, γ_{VV} is the Fresnel transmission coefficient for VV polarization

$$\begin{cases}\gamma_{hh} = \dfrac{2\sqrt{\varepsilon_s - \sin^2\theta_i}}{\cos\theta_i + \sqrt{\varepsilon_s - \sin^2\theta_i}} \\[2ex] \gamma_{vv} = \dfrac{2\sqrt{\varepsilon_s - \sin^2\theta_i}}{\varepsilon_s\cos\theta_i + \sqrt{\varepsilon_s - \sin^2\theta_i}}\end{cases} \tag{8.9}$$

and θ is the orientation angle. Note the local incident angle θ_i should be converted into the local refractive angle θ_r by using Snell's law.

The volume coherency matrix of (8.8) can be written as

$$[T(\theta)]_{vol} = \frac{1}{2}\left|S_{HH}^{vol}\right|^2\begin{bmatrix}|1+A_P|^2 & (1+A_P)\cos2\theta & -(1+A_P)\sin2\theta \\ (1+A_P)^*\cos2\theta & |1-A_P|^2\cos^2 2\theta & -|1-A_P|^2\dfrac{\sin4\theta}{2} \\ -(1+A_P)^*\sin2\theta & -|1-A_P|^2\dfrac{\sin4\theta}{2} & |1-A_P|^2\sin^2 2\theta\end{bmatrix} \tag{8.10}$$

The volume scattering coherency matrix (8.10) is averaged over all possible angle θ for deriving volume scattering matrix of a random cloud of small spheroids particles in one resolution cell as

$$\langle[T]\rangle_{vol}^{snow} = \int [T(\theta)]_{vol}\, p(\theta) d\theta \tag{8.11}$$

With the uniformly distributed snow particles, the volume scattering coherency matrix is defined with

$$p(\theta) = \frac{1}{2\pi} \;\; ; \; 0 < \theta < 2\pi \tag{8.12}$$

as

$$\langle[T]\rangle_{vol}^{snow} = f_{vol} \begin{bmatrix} |\gamma|^2 & 0 & 0 \\ 0 & \frac{1}{2} & 0 \\ 0 & 0 & \frac{1}{2} \end{bmatrix} \tag{8.13}$$

$$f_{vol} = \frac{1}{2} |\gamma_{HH} - \gamma_{VV}|^2 . f(\theta_i, \theta_r, \omega, \tau, P) \tag{8.14}$$

and

$$|\gamma|^2 = \frac{|\gamma_{HH} + \gamma_{VV}|^2}{|\gamma_{HH} - \gamma_{VV}|^2} = \frac{|1 + A_P|^2}{|1 - A_P|^2} \tag{8.15}$$

Since A_P is bounded, therefore $|\gamma|^2$ can be bounded as

$$\left|\frac{\varepsilon_s + 1}{\varepsilon_s - 1}\right|^2 < |\gamma|^2 < \left|\frac{\varepsilon_s + 3}{\varepsilon_s - 1}\right|^2 \tag{8.16}$$

8.3.3 Bare wet snow discrimination

Here users have their own choice to use bare wet snow detection algorithm from Nagler (1996), Singh (2010) and/ or to develop a new algorithm for extracting bare wet snow areas. We have adopted algorithm Radar Snow Index *RSI* from Singh (2010) and [P7] in the Indian Himalayan region above the vegetation line.

8.3.4 Wet snow discrimination in vegetated areas

Wet snow cover can be mapped by SAR in areas with low vegetation but snow cover detection in dense vegetation areas is still a challenging task and need more research for developing an appropriate algorithm (Luojus *et al.* 2009). According to Forest Survey of India (FSI 2011) reports in 2011, Indian Himalaya has four major type vegetation-covered areas namely very dense forest, moderately dense forest, open forest and scrubs. We have five partly snow/glacier-covered states in India, which are situated in the Himalayan range namely Jammu & Kashmir, Himachal Pradesh, Uttarakhand, Sikkim and Arunachal Pradesh. These states statistics of non-vegetation-covered areas are 88.91%, 73.04%, 53.69%, 47.53%, and 19.36%, respectively. However the high-elevation zone (vegetation free zone (FSI 2011)) will probably remain snow covered for a longer period, and the low-elevation areas (vegetation area) will probably remain snow free below the vegetation line in melting season (May to

August/September) [for example see Fig. 8.2] especially for the Indian Himalayan region. However, wet snow can extent in vegetated areas of the Indian Himalayan during snow season (e.g. from December to April) (Singh and Venkataraman 2010). In this case, G4U will be applicable.

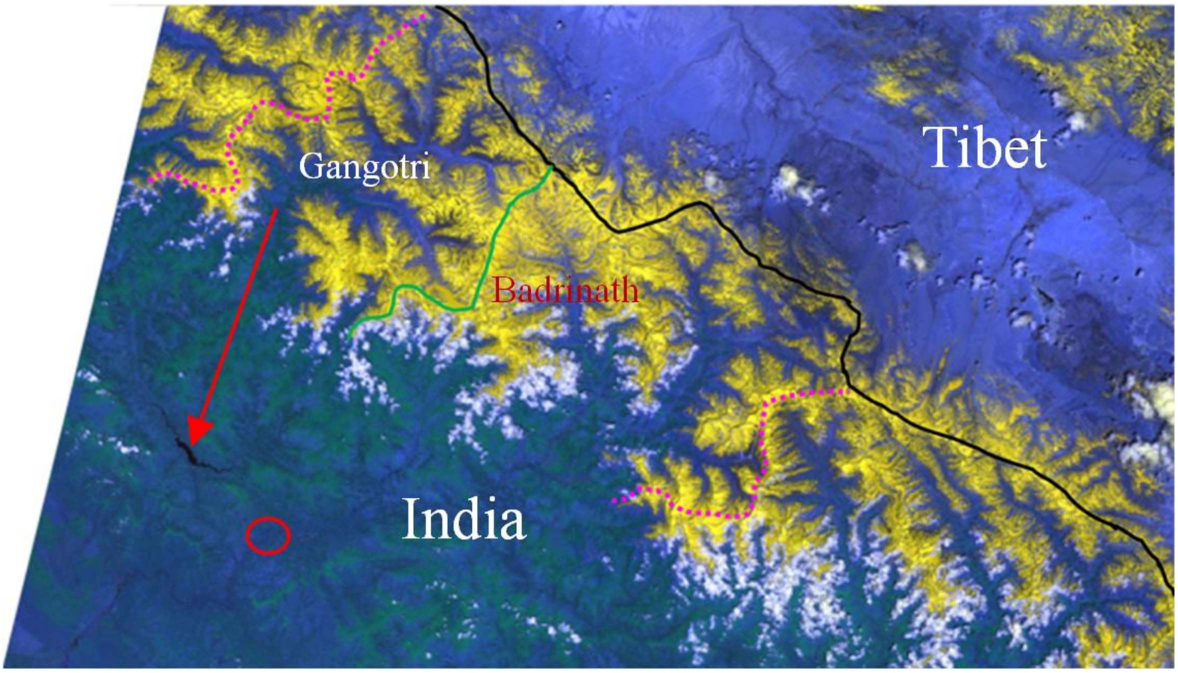

Fig. 8.2. Indian Remote Sensing Satellite P6 -Advanced Wide Field Sensor (IRS-P6-AWiFS) image of May 10, 2007 over Uttarakhand Glaciated terrain: Green color interprets the vegetation cover, blue color elucidates the bare surface, deep blue shows water body, white patches represent cloud cover and golden color demonstrates the bare snow-covered area. Red arrow indicates Tehri reservoir of the Bhagirithi River (Bhagirithi River is originating from the snout of Gangotri glacier). Red circle locates a junction of the Bhagirthi River and Alaknanda River (origin from the Satopanth glacier in Badrinath region).

8.3.5 Extended Decomposition scheme of (8.1) over wet snow

The coherency matrix can be expanded in surface and volume coherency sub matrices plus helix scattering (in case reflection symmetry breaks) and double-bounce scattering (if exist) over the wet snow area as

$$\begin{bmatrix} T'_{11} & T'_{12} & T'_{13} \\ T'_{21} & T'_{22} & 0 \\ T'_{31} & 0 & T'_{33} \end{bmatrix} = [U(\varphi)]\big(\langle[T]\rangle_{surface} + \langle[T]\rangle_{double} + [\langle[T]\rangle_{vol}^{snow} + \langle[T]\rangle_{helix}\big)[U(\varphi)]^{\dagger} \tag{8.17}$$

where $\langle[T]\rangle_{surface}$ is used as given in existing decompositions literature as

$$\langle[T]\rangle_{surface} = f_{surface} \begin{bmatrix} 1 & \beta^{*} & 0 \\ \beta & |\beta|^{2} & 0 \\ 0 & 0 & 0 \end{bmatrix} \tag{8.18}$$

where

$$f_{surface} = \frac{1}{2} |\alpha_{HH} + \alpha_{VV}|^2 \,.\, f(\theta_i, s, \boldsymbol{k}).\boldsymbol{W} \tag{8.19}$$

$$|\beta|^2 = \left|\frac{\alpha_{HH} - \alpha_{VV}}{\alpha_{HH} + \alpha_{VV}}\right|^2 \tag{8.20}$$

$$\begin{cases} \alpha_{HH} = \dfrac{\cos\theta_i - \sqrt{\varepsilon_s - \sin^2\theta_i}}{\cos\theta_i + \sqrt{\varepsilon_s - \sin^2\theta_i}} \\ \alpha_{VV} = (\varepsilon_s \text{ -1}) \dfrac{\sin^2\theta_i - \varepsilon_s(1 + \sin^2\theta_i)}{\left[\varepsilon_s \cos\theta_i + \sqrt{\varepsilon_s - \sin^2\theta_i}\right]^2} \end{cases} \tag{8.21}$$

s is snow surface rms height and $\boldsymbol{k}$ is wave number. $\boldsymbol{W}$ is Fourier transform component of surface correlation length (Fung 1994; Ulaby *et al.* 1986).

Therefore, (8.17) is rewritten as

$$\begin{bmatrix} T'_{11} & T'_{12} & T'_{13} \\ T'_{21} & T'_{22} & 0 \\ T'_{31} & 0 & T'_{33} \end{bmatrix} = [U(\varphi)] \left(f_s \begin{bmatrix} 1 & \beta^* & 0 \\ \beta & |\beta|^2 & 0 \\ 0 & 0 & 0 \end{bmatrix} + f_d \begin{bmatrix} |\alpha|^2 & \alpha & 0 \\ \alpha^* & 1 & 0 \\ 0 & 0 & 0 \end{bmatrix} \right.$$
$$\left. + f_v \begin{bmatrix} |\gamma|^2 & 0 & 0 \\ 0 & \frac{1}{2} & 0 \\ 0 & 0 & \frac{1}{2} \end{bmatrix} + \frac{\boldsymbol{f_c}}{2} \begin{bmatrix} 0 & 0 & 0 \\ 0 & 1 & \pm j \\ 0 & \mp j & 1 \end{bmatrix} \right) [U(\varphi)]^\dagger \tag{8.22}$$

Arrangement of the element relations in (8.22) provides five equations

$$T'_{11} = f_s + f_d|\alpha|^2 + f_v|\gamma|^2 \tag{8.23}$$

$$T'_{22} + T'_{33} = f_s|\beta|^2 + f_d + f_v + f_c \tag{8.24}$$

$$T'_{22} - T'_{33} = (f_s|\beta|^2 + f_d)\cos 4\varphi \pm f_c \sin 4\varphi \tag{8.25}$$

$$T'_{12} + T'_{13} = (f_s\beta^* + f_d\alpha)\, e^{-j2\varphi} \tag{8.26}$$

$$(f_s|\beta|^2 + f_d)\sin 4\varphi = \pm f_c \cos 4\varphi \tag{8.27}$$

From (8.27) and (8.25) together (8.24), f_c and f_v can be derived

$$f_c = |(T'_{22} - T'_{33})\sin 4\varphi| = 2|Im\{T_{33}(\theta)\}| \tag{8.28}$$

$$f_v = (T'_{22} + T'_{33}) - (T'_{22} - T'_{33})\cos 4\varphi - f_c = 2\,T_{33}(\theta) - f_c \tag{8.29}$$

If we assume, double-bounce scattering is negligible in wet snow, then we can derive the generalized Cloude volume parameter $|\gamma|^2$ as

$$|\gamma|^2 = \frac{T'_{11}}{(T'_{22} + T'_{33}) - (T'_{22} - T'_{33})\cos 4\varphi - f_c} - \frac{\dfrac{|T'_{12} + T'_{13}|^2}{(T'_{22} - T'_{33})\cos 4\varphi}}{(T'_{22} + T'_{33}) - (T'_{22} - T'_{33})\cos 4\varphi - f_c}$$
$$= \frac{T_{11}(\theta)}{2\,T_{33}(\theta) - f_c} - \frac{|T_{12}(\theta) + T_{13}(\theta)|^2}{(2\,T_{33}(\theta) - f_c)\,\left(T_{22}(\theta) - T_{33}(\theta)\right)} \tag{8.30}$$

The parameter $|\gamma|^2$ can be inverted for estimating the volume $|\varepsilon_s|$ of the media. However, the parameter $|\gamma|^2$ can be bounded for a certain range based on relation (8.30) by using the average possible value of dielectric constant of the medium (Table 8.1). In case, the average dielectric constant value is available, the bounded value of $|\gamma|^2$ will be generated by using (8.31) instead of constrain (ad-hoc) method of exceeding values for both extreme cases (Table 8.1). The bounded $|\gamma|_b^2$ is defined as a function of $|\gamma|^2$ as

$$|\gamma|_b^2 = f(|\gamma|^2) = \frac{|\gamma|^2{}_u - |\gamma|^2{}_l}{1 + e^{-\delta(|\gamma|^2 - |\gamma|^2{}_m)}} + |\gamma|^2{}_l \tag{8.31}$$

where

$$|\gamma|^2{}_l = \left|\frac{\varepsilon_s + 1}{\varepsilon_s - 1}\right|^2 \tag{8.32}$$

$$|\gamma|^2{}_u = \left|\frac{\varepsilon_s + 3}{\varepsilon_s - 1}\right|^2 \tag{8.33}$$

$$|\gamma|^2{}_m = \frac{|\gamma|^2{}_u + |\gamma|^2{}_l}{2} \tag{8.34}$$

By taking the first derivative of (30) at $|\gamma|^2{}_m$, the δ can be determined. The first derivative of $f(|\gamma|^2)$ can be written as

$$f'(|\gamma|^2) = \frac{e^{-\delta(|\gamma|^2 - |\gamma|^2{}_m)} . \delta\, (|\gamma|^2{}_u - |\gamma|^2{}_l)}{\left[1 + e^{-\delta(|\gamma|^2 - |\gamma|^2{}_m)}\right]^2} \tag{8.35}$$

The first derivative of $f(|\gamma|^2)$ at $|\gamma|^2 = |\gamma|^2{}_m$ should be unity *i.e.* $f'(|\gamma|^2{}_m) = 1$. Thus,

$$f'(|\gamma|^2{}_m) = \frac{\delta\, (|\gamma|^2{}_u - |\gamma|^2{}_l)}{4} = 1 \tag{8.36}$$

and

$$\delta = \frac{4}{(|\gamma|^2{}_u - |\gamma|^2{}_l)} \tag{8.37}$$

When *prior* information of dielectric constant is not available, the satisfaction of (8.38) [the rearrangement of (8.23) and (8.26)], then, can be considered to assign adaptive value of (8.30)

$$T_{11}(\theta) - f_v|\gamma|^2 > |T_{12}(\theta) + T_{13}(\theta)|\ ; [\because\ |\beta| < 1\,] \tag{8.38}$$

Since the double-bounce scattering magnitude is negligible in this case, it can be assumed $|\alpha| \ll 1$ and fixed $\alpha = 0$. This condition leads to solve a set of 3 equations with 4 unknowns

$$f_s + f_d|\alpha|^2 = S \tag{8.39}$$

$$f_s|\beta|^2 + f_d = D \tag{8.40}$$

$$(f_s\beta^* + f_d\alpha) = C \tag{8.41}$$

where

$$S = T'_{11} - f_v|\gamma|^2 = T_{11}(\theta) - f_v|\gamma|^2 \tag{8.42}$$

$$D = T'_{22} + T'_{33} - f_v - f_c = T_{22}(\theta) + T_{33}(\theta) - f_v - f_c \tag{8.43}$$

$$C = (T'_{12} + T'_{13})\, e^{j2\varphi} = T_{12}(\theta) + T_{13}(\theta) \tag{8.44}$$

The generalized Freeman surface parameter is derived in (8.45)

$$\beta^* = \frac{T_{12}(\theta) + T_{13}(\theta)}{T_{11}(\theta) - f_v|\gamma|^2} \tag{8.45}$$

$$P_s = f_s(1 + |\beta|^2) = S + \frac{|C|^2}{S} \tag{8.46}$$

$$P_d = f_d(1 + |\alpha|^2) = D - \frac{|C|^2}{S} \tag{8.47}$$

$$P_c = f_c \tag{8.48}$$

$$P_v = f_v(1 + |\gamma|^2) \tag{8.49}$$

So, due to non-availability of the *prior* information dielectric constant during the FULL-POL-SAR acquisition, the satisfaction of (8.38) is adopted to assign the adaptive value of (8.30) for the further analysis in this chapter.

Table 8.1. The bounding range of $|\gamma|^2$ for dry snow, moist snow, wet snow, water

	Dielectric constant	Lower bound $|\gamma|^2_l$	Upper bound $|\gamma|^2_u$
Dry snow	1.50	25.00	81.00
Moist Snow	2.20	6.25	17.36
Wet Snow	3.00	4.00	9.00
Ice	3.15	3.72	8.18
Very Wet Snow	4.00	2.78	5.44
Wet Soil	10.00	1.49	2.08
Water	80.00	1.05	1.10

8.3.6. Generalized FULL-POL-SAR Decomposition Implementation Scheme

The procedures in Sections 8.3.1 to 8.3.5 are summarized for implementation to FULL-POL-SAR images. The corresponding flowchart of the generalized FULL-POL-SAR decomposition algorithm is shown in Fig. 8.3. In the first stage before the decomposition, the measured coherency matrix is rotated about the line of sight (Yamaguchi *et al.* 2011), and then a unitary transformation is applied on the rotated coherency matrix. Decomposition starts by retrieving the helix scattering power at this stage. Then, the *RSI* is checked for extracting bare wet snow area. The *RSI* is specifically implemented for retrieving scattering powers by the spheroidal volume scattering model (cloud of generalized spheroidal shape snow particles) over bare wet snow areas. Once the bare wet snow-covered area is extracted based on *RSI* satisfaction, the generalized spheroidal expansion matrix (8.13) is used for volume scattering. On the other hand, if *RSI* is not satisfied, G4U, as derived in Singh *et al.* (2013b), is used for FULL-POL-SAR images decomposition. Then, four scattering power values are obtained. This new decomposition accounts for inclusion of all the elements of the coherency matrix.

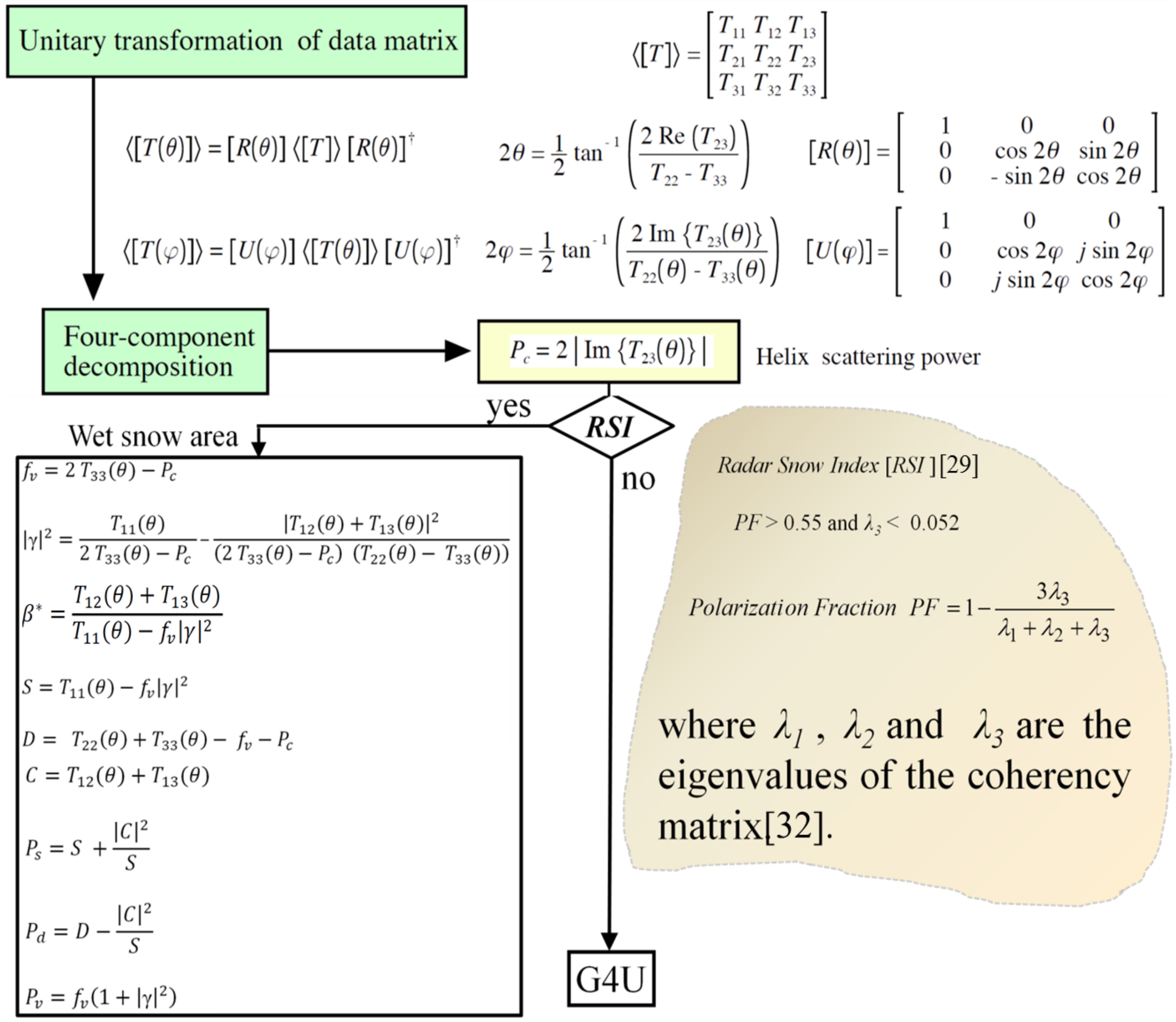

Fig. 8.3. Flowchart of generalized FULL-POL-SAR decomposition over wet snow. In this method, volume scattering power values are generated by dipole scattering plus dihedral scattering plus spheroidal particle scattering. All calculations can be executed from the elements of the coherency matrix.

8.4. Interpretation of Results and Discussion

8.4.1 Interpretation of Advanced G4U Results

G4U, as given in Chapter 6, considers the cloud of dipole and oriented dihedral to determine volume scattering power in the decomposition. However, the wet snow particle shape becomes rounded, and therefore, the spheroidal shape assumption has been considered rather than the dipole in the snowpack. When we apply the spheroidal case for snow-covered terrain, the volume scattering power is increased and surface scattering power is decreased as compared to dipole case scattering mechanism (see Fig. 8.4 as compared to Fig. 8.1). It is also known from literature that these two components are sensitive to the snow properties, i.e., liquid water content, ice particle size and shape, and surface roughness (Shi and Dozier 1995). The presence of liquid water content increases the absorption coefficient. Therefore, the volume scattering albedo is inversely correlated to snow wetness and snow density. At constant wetness and density, the volume scattering albedo increases as the size of the scatterers or their size variation increases, because, as Rayleigh scattering theory explains, the scattering coefficient is proportional to the third power of the scatterer's radii for a given volume fraction. Surface roughness affects the backscattering components. For low wetness (<3%) the dielectric contrast between air and snow is small and volume scattering dominates, so backscattering is not sensitive to surface roughness and decreases as wetness increases. However, for wetter snow, backscattering becomes sensitive to surface roughness, because the surface-scattering component increases while the volume scattering component decreases.

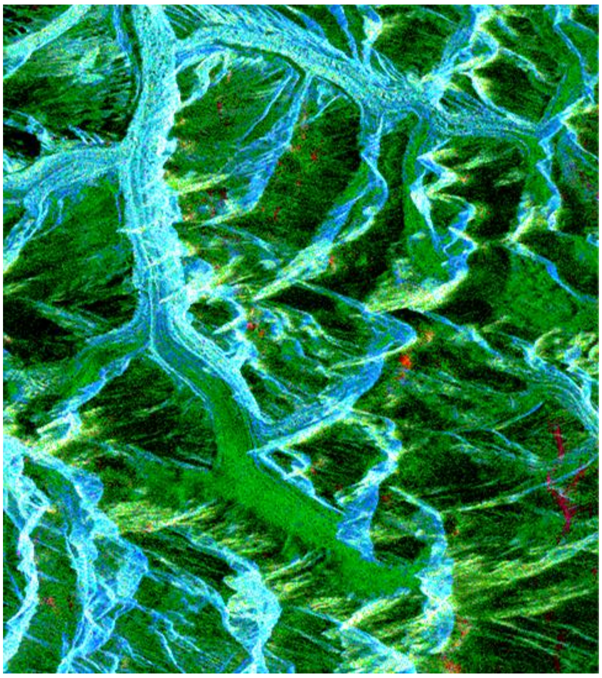

Fig.8.4 Generalized FULL-POL-SAR decomposition FCC with 12 × 2 multi-look (azimuth × range) factors of 06-06-2010 over Gangotri glacier (Red: double-bounce scattering, Green: volume scattering, Blue: surface scattering).

8.4.2 Interpretation of Generalized Volume and Surface parameters

The volume $|\gamma|^2$ and surface $|\beta|$ parameters are derived, as shown in Fig. 8.5. The $|\gamma|^2$ shows high value over snow (Fig. 8.5) while $|\beta|$ over snow shows lower value than other objects based on used fully polarimetric PALSAR data (Fig.8.5). The higher value of $|\gamma|^{\mathbf{2}}$ is responsible for higher volume scattering power contribution in Fig.8.4 rather than the dipole case ($|\gamma|^2$=1) in G4U images (Fig.8.1). Now a question arises that whether $|\gamma|^2$ is determined wrongly or not? To check and answer this question, the theoretical values (minimum and maximum values) are checked over snow for all possible states of snow from dry to very wet condition (see Table 8.1). It is seen that the minimum value of very wet snow case could not be equal to the value of the dipole case. Now it is clear from Table 8.1 that, the value of $|\gamma|^2$ for wet snow case should be greater than 2.78 and less than 17.36. To compare these values over the snow area, a subset over glacier area has been taken to avoid the disturbance of topography on the POL-SAR measurements (however, there will be topographically disturbances yet small due to gentle slope on valley glacier compared to the moderate to steep sloped surface of the mountainous area) (Singh *et al.* 2012). This subset is divided into three categories of glacier area: ablation zone (AZ), transition zone (TZ) and snow-covered area (SCA), as shown in Fig.8.1 and Fig.8.6. Since the ablation zone is covered by debris (soil layer + moraine), the value of $|\gamma|^2$ is observed to be less than 2.78 (Fig.8.6). The transition zone is dominated by the value between 2.78 to 6.25; it means that there may be a very wet snow layer converting into the bare ice zone. The value of $|\gamma|^2$ over SCA (as interpreted by

G4U and AVNIR-2 RGBs) are dominant in between 6.25 to 17.36 including a few pixel ranges from 17.36 to 21 (Fig.8.6). However, the value of $|\gamma|^2$ over SCA in between the range 6.25 to 9 covers a small area, and the areas above the range 17.36 are negligible. The value from 9 to 17.36 of the $|\gamma|^2$ over the SCA indicates that the SCA may be in moist condition. Moreover, the trend from wet to moist condition of SCA toward the accumulation area of glacier might easily be argued by the fact that temperature is decreasing toward higher elevation zone of the glacier.

The value of the surface parameter $|\beta|$ varies in between 0 to 1. Low value (less than 0.05) of $|\beta|$ may be interpreted as the snow-covered area. The value range from 0.1 to 0.3 indicates the debris covered glacier area. These interpretations of $|\beta|$ image, as shown in Fig. 8.5, are confirmed by using the optical ALOS-AVNIR-2 image, as presented in Fig. 8.1. The surface parameter can be utilized for the snow-covered area discrimination in the glaciated terrain of the Indian Himalayan region. Moreover, both generalized volume and surface parameters have one unknown parameter, i.e., the dielectric constant of the media. Therefore, these generalized volume and surface parameters will be useful for the development of a snow dielectric constant retrieval inversion algorithm over the wet snow area, which can be further related to wetness. At present due to lack of synchronous FULL-POL-SAR and ground truth data available to us, the estimation and validation of snow wetness will be done in near future. Although the proposed inversion algorithm schemes of snow wetness estimation are verified by Surendar *et al.* (2013) with the implementing RADARSAT-2 (C-band) FULL-POL-SAR data and near-real-time field observations over the Manali-Dundhi region (Indian Himalayan seasonally snow-covered areas), Himachal Pradesh, India, they observed the improved snow wetness estimation by using this proposed inversion algorithm [based on (8.30) and (8.45)] as compared with the Shi and Dozier (1995) inversion algorithm.

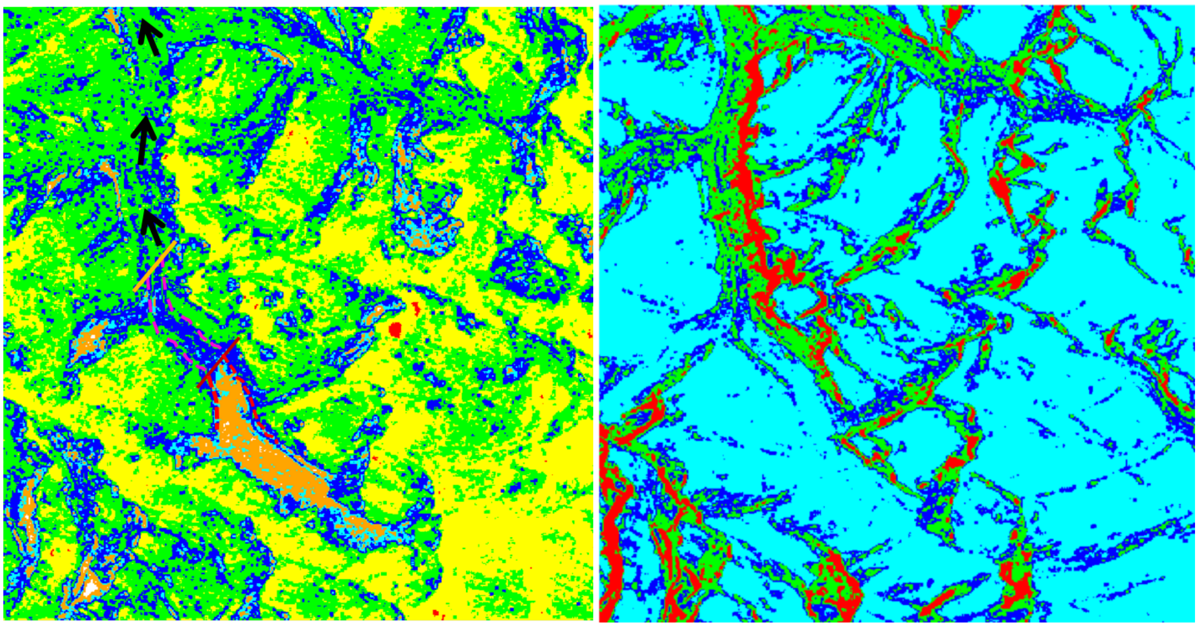

Fig.8.5 (**Left**) the generalized Cloude volume parameter $|\gamma|^2$ (Red: <0.1, Yellow: 0.1 to 1, Green: 1 to 2.78, Blue: 2.78 to 6.25, Cyan: 6.25 to 9 and Orange: 9 to 17.36). (**Right**) generalized Freeman's surface parameter $|\beta|$ (Cyan: <0.05, Blue: 0.05 to 0.1, Green: 0.1 to 0.3, and Red: 0.3 to 0.99). The magenta dashed lines cover the transition zone in between snow accumulated area behind the red line (across the glacier) and the ablation area below the golden line. Black arrows indicate the flow direction of the glacier.

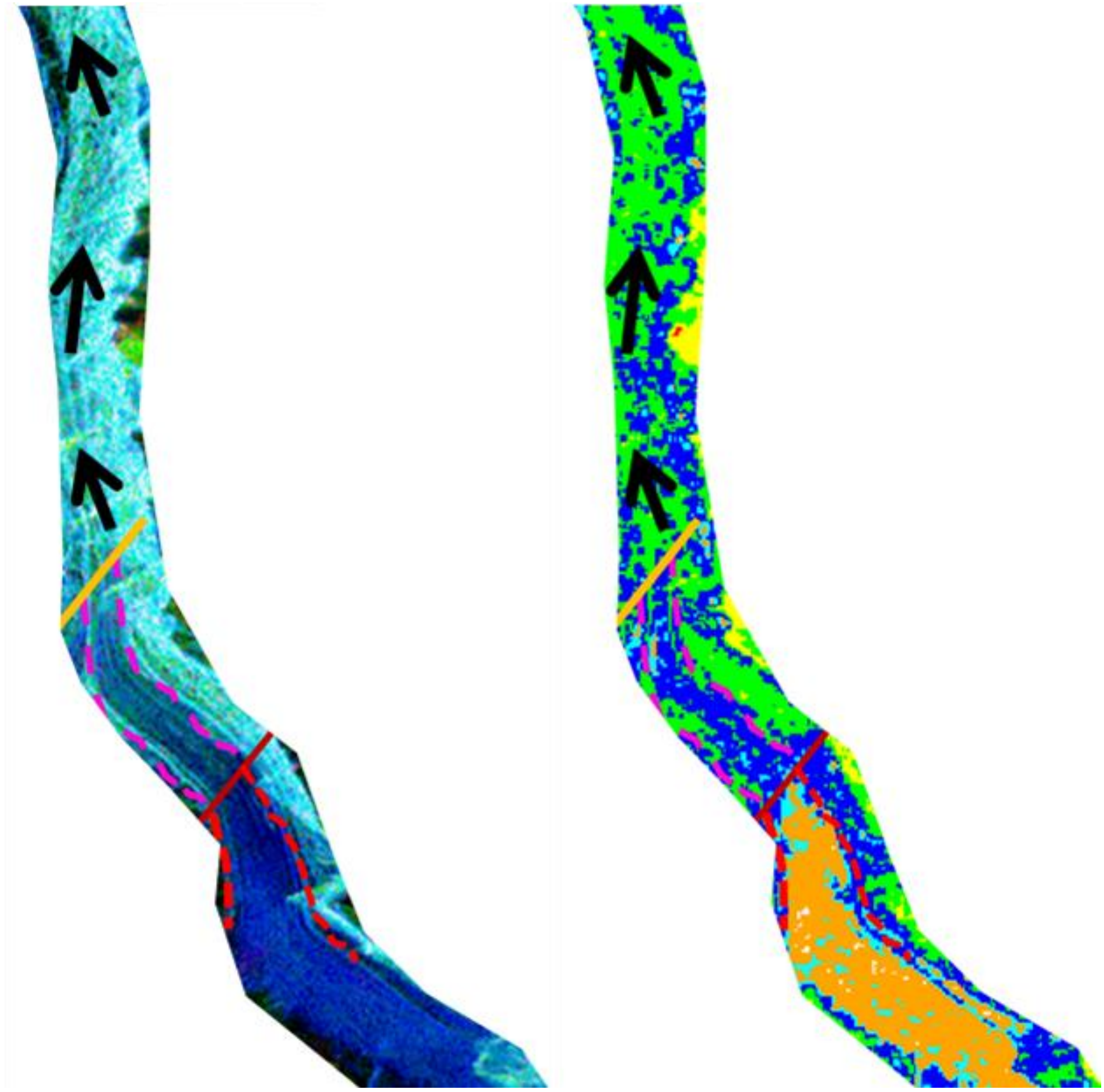

Fig.8.6 (**Left**) Sub-set of G4U FCC with 12 × 2 multi-look (azimuth × range) factors of 06-06-2010 over the Gangotri glacier (Red: double-bounce scattering, Green: volume scattering, Blue: surface scattering). (**Right**) the generalized Cloude volume parameters $|\gamma|^2$ (Red: <0.1, Yellow: 0.1 to 1, Green: 1 to 2.78, Blue: 2.78 to 6.25, Cyan: 6.25 to 9, Orange: 9 to 17.36). The magenta dashed lines cover the transition zone in between snow accumulated area behind the red line (across the glacier) and the ablation area below the golden line. Black arrows indicate the flow direction of the glacier.

8.5 Summary and Conclusions

The G4U decomposition scheme has been applied to several fully polarimetric ALOS-PALSAR data sets, which were acquired during the wet snow season over various parts of the Indian Himalaya. The G4U method accounts for the fully polarimetric information. In addition, it is noticed that G4U provides very good capability for delineation the snow line with the L-band POL-SAR data over the glaciated terrain of the Indian Himalayan region during the wet snow season. However, improved comparisons for simultaneously acquired L-

Band versus S-Band, C-Band and X-Band FULL-POL-SAR image data would be essential for further clarification, which could be achieved with the implementation of the airborne multi-band DLR F-SAR for which any three bands can be operated simultaneously. Furthermore, an advanced procedure of G4U has been proposed especially for the wet snow case. Under this new procedure, the generalized Cloude volume and Freeman surface parameters have been proposed for snow volume dielectric constant estimation and snow surface dielectric constant estimation respectively. When the dielectric constant (wetness) is low, volume scattering is the dominant scattering source. As snow wetness increases, both the volume parameters and the transmission coefficients decrease (Abe *et al.* 1990) and the surface parameter increases. This study will be extended to snowpack wetness estimation and snowpack states (melt/freeze conditions) detection based on generalized volume and surface parameter methods, which will be treated in future works.

Chapter 9 Conclusions

The beginning is always learning; the learning never ends

Key parameters of the Earth surface play important roles in environmental assessments. Remote Sensing with fully polarimetric radar is one of the most promising approaches for achieving the goal. From 1980's several methods have been developing for experimental POL-SAR data analysis to monitor the Earth. Hence, the aim of the thesis was to bridge the intellectual gap at the radar polarimetry method terminus—where radar polarimetry theories/methods developments traditionally ends— and earth surface parameters monitoring traditionally begins.

Key findings and linkages of this thesis are summarized using the answers of the following research questions under main subtasks

1. **Needs for physical scattering mechanism model-based scattering power decomposition of FULL-POL-SAR**:

   Why is the scattering model-based decomposition required in POL-SAR data interpretation?

   Physical scattering mechanism model-based Decomposition (Y4O & Y4R) outputs are directly recognizable and easy to interpret for understanding POL-SAR data. Chapter 2 and Chapter 3 show the examples of the interpretation of the four-component scattering power decomposition over glaciated terrain. It is elucidated in Chapter 2 and Chapter 3 that scattering power decompositions are useful for direct POL-SAR data interpretation pertinent to snow and ice.

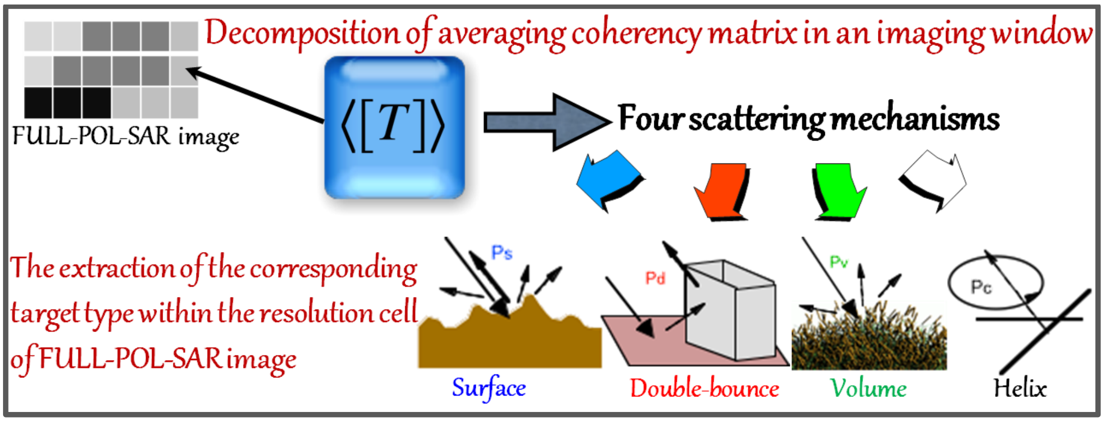

Fig. 9.1. Decomposition scattering powers for understanding FULL-POL-SAR data

   How can the model-based decomposition be utilised in terrain features categorization?

   Model based decomposition can easily be implemented on FULL-POL-SAR data with straight forward interpretation. The interpretation of the decomposition output for FCC images help to recognize the dominant scattering type. Further, the interpretation of decomposition FCC images and probabilities of decomposition components can be utilized to delineate or categorize the terrain features. Chapter 2 highlights the utilization of the model based decomposition Y4O for the categorization of the terrain features over the highly rugged mountainous region.

How can the model-based decomposition be aided in improvement of the terrain classification results?

It is found that the supervised algorithm shows high accuracy performance for obtaining terrain classification results of POL-SAR data but discriminations of transition zones in between two types of scattering features are still ambiguous. Scattering power decomposition components provide a source of knowledge to resolve this type of ambiguity from classified results. An example is shown in Chapter 2 by utilization of model based decomposition components means for avoiding ambiguous result in the final classified map are obtained using the newly proposed $Y4O_w$ method.

2. **Effects of volume scattering selection on decomposition and the results of decomposition components**:

   How will dipole, oriented dihedral and spheroid volume scattering models effect the decomposition results?

   The effect of the volume scattering model can be seen in the four-component scattering power decomposition method (Y4O), which is an extension of the three-component scattering method (FDD) for the extended volume scattering case with non-random uniformly distributed dipoles (Chapter 2). After decomposing the total power into four components, it has been found that the method Y4O has the problem of overestimating volume scattering in urban areas and orientated surface features; and is resulting in negative power occurrence in the processing caused by a large cross-polarization component (Chapter 3).

   Next improvement is introduced in the Y4R method results by minimizing the cross-polarized (HV) components. This minimization of HV reduces the negative power occurrence in the surface scattering and the double-bounce scattering components. A comparison of Y4O with Y4R is described in Chapter 3 for an example. However, there was still a problem of discrimination between vegetation and oriented buildings within the same volume scattering area. This ambiguity was caused by the assignment of the HV component. The volume scattering power is evaluated by the HV component due to vegetation only in the Y4O and Y4R. To resolve the discrimination ambiguity, we assessed the HV component whether it was created by vegetation (single bounce object) or by edges of oriented buildings (double-bounce structures). In Chapter 4, it was proposed to use a new volume scattering model that accounts for the HV component caused by double-bounce structures versus vegetation scatter and to improve the Y4R for additional more accurate classification. It is shown that vegetation area and oriented urban building area are well discriminated compared to those resulting from direct implementation of the Y4O and Y4R.

   How does the response vary in different scattering models?

   The volume scattering power is evaluated based on the three kinds of scatterers geometrical shapes include dipoles, dihedral and spheriodal in volume scattering model of the decomposition. These different volume scattering models are summarized in Fig. 9.2, with their corresponding geometrical shapes and probability distributions. The volume scattering power is calculated by the cross-polarized *HV* component caused by vegetation (cloud of dipole scattrers) in FDD, Y4O and Y4R. When the *HV* component is assigned to the dipole and dihedral scattering according to extended volume scattering model in Fig. 9.2, double-bounce scattering power was exaggerated and volume scattering power was reduced in the urban areas with the corresponding proposed decomposition methods in Chapter 4-6. Therefore, the discrimination in between the man-made structures and vegetation areas becomes simple due to conversion of the depolarization process into re-polarization process by using dihedral volume scattering model in man-made structures. However, the assumption of cloud of dipole scatteres and oriented dihedral scatteres is not suitable to determine volume scattering power in wet snowpack, because wet snow particle geometrical shape becomes rounded. Therefore, the spheroidal shape assumption was considered than the dipole or dihedral in the snowpack. When we apply the spheroidal case for wet snow area, the volume scattering power was amplified as compared to dipole and/or dihedral case scattering mechanism (e.g. G4U). This exaggeration of volume scattering power in wet snowpack was because of the converting polarization process into de-polarization process by using spheroidal shape scatteres volume scattering model.

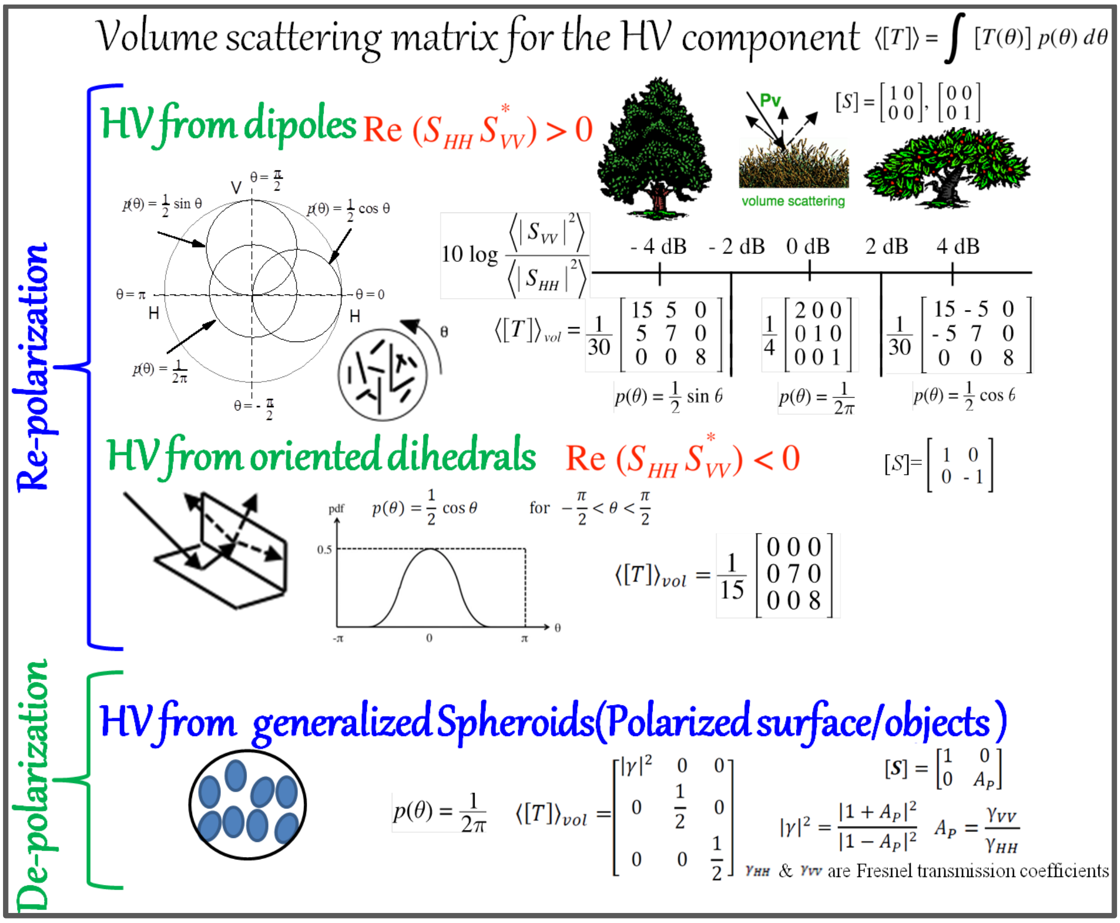

Fig.9.2 The summary of different volume scattering models with their corresponding geometrical shapes (dipole, dihedral, and spheroidal) and probability distributions.

3. Incorporation of FULL-POL-SAR information in scattering power decomposition:

How can the complete FULL-POL-SAR information be utilized in decomposition models?

The utilization of 100% polarimetric relative phase information in the model-based decomposition was one of the main issues in Radar Polarimetry research for the past two decades. It resulted from extracting only 55.5% polarimetric phase information (5 independent polarimetric parameters out of 9 independent polarimetric parameters of coherency matrix) under the reflection symmetry assumption for the FDD method; next the extraction of 66.6% polarimetric phase information was possible under non-reflection symmetric assumption in Y4O. Results of FDD and Y4O are illustrated in Chapter 2. The number of independent polarimetric parameters of the coherency matrix is increased from 66.6% to 75% in Y4R. Results of Y4R are presented in Chapter 3 and Chapter 4, respectively. The remaining 25% polarimetric information can be included by proposing double unitary transformations as mentioned in Chapter 5. The number of independent polarization parameters of coherency matrix from nine to seven can be achieved by implementing the double unitary transformations. Double unitary transformations eliminate the T_{23} element of the coherency matrix. Finally, 100% polarimetric information extraction is incorporated in G4U; and its developments are described in Chapter 5 and Chapter 6. Utilization of 100% polarimetric information is one of major contributions of this thesis.

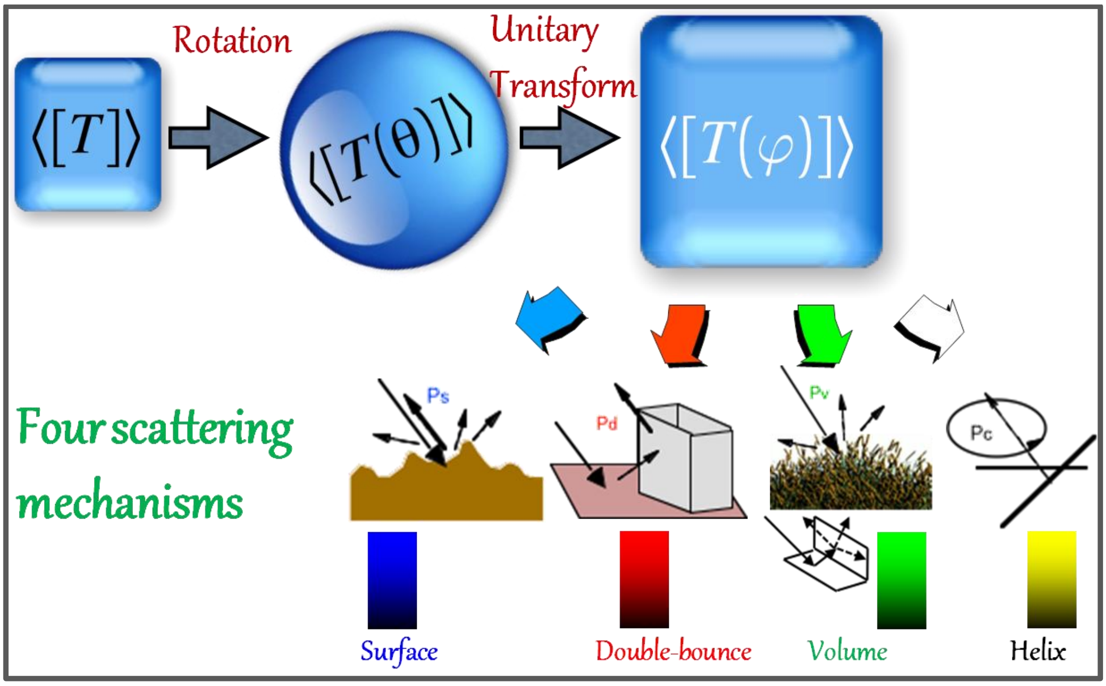

Fig. 9.3. Concept of the double unitary transformations to extract the four types of scattering mechanisms.

How can decomposition performance be improved?

It is known that the Y4R method reduces the number of observation parameters from 9 to 8 by rotation of the coherency matrix, and that it accounts for 6 parameters out of 8, leaving 2 parameters (i.e., real and imaginary part of T_{13} component) un-accounted for (Chapter 3). After the unitary transformation, the new four-component decomposition is carried out accounting for all parameters in the coherency matrix including the remaining T_{13} component. Therefore, the proposed G4U method makes use of full utilization of polarimetric coherency phase information in the decomposition. It is found that the G4U method enhances the double-bounce scattering contributions over the urban areas compared to those of the existing four-component decomposition, resulting from the full utilization of polarimetric phase information (Chapter 6). Additionally, these improvements reduce the negative power values of decompositions.

4. **Decomposition components as information repositories for earth surface parameters retrieval modelling**:

What kind of information can be extracted from decomposition that can aid earth surface parameters retrieval modelling?

This question is answered in Chapter 2, Chapter 3 and Chapter 7(the detailed evaluations of the use of the scattering power decomposition are described). The most important advantage of scattering power decomposition is that the scattering powers can be inverted to geo-/bio-physical parameters of the earth surface cover with least unknowns. (see Fig. 9.4).

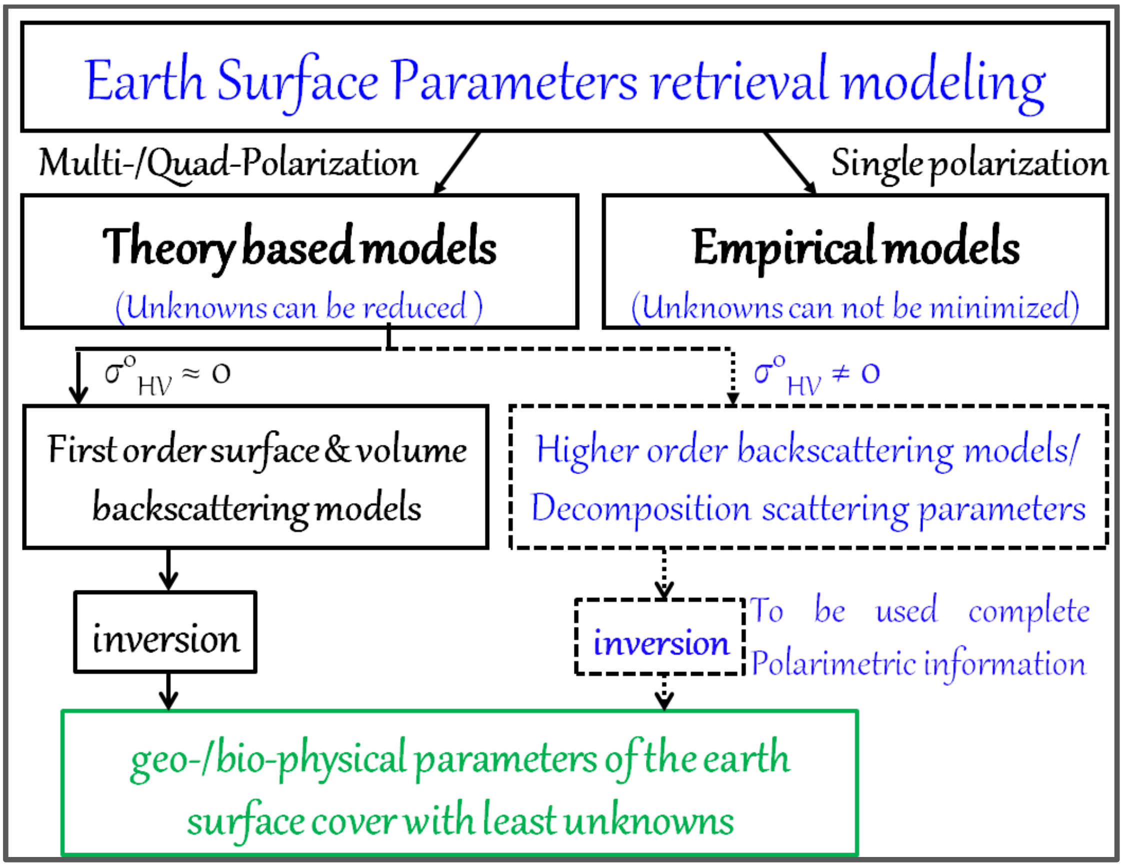

Fig. 9.4. Earth surface parameters retrieval modelling

How can decomposition components help to constrain model parameters or provide model input?

Development of simple theoretical inversion techniques with least unknown parameters for retrieving earth surface parameters (see Fig. 9.4) for example snow wetness is one of necessarily parts in FULL-POL-SAR research. Chapter 8 presents the generalized FULL-POL-SAR decomposition scheme over wet snow area. In proposed decomposition scheme, generalized spheroidal (ellipsoid) shape is considered for volume scattering model derivation. Furthermore, generalized the Cloude volume and the Freeman surface parameters are derived over wet snow areas. These generalized volume and surface parameters will be useful for the development of a snow dielectric constant retrieval inversion algorithm with one unknown parameter, i.e., the dielectric constant of snowpack.

Future Work and Recommendations

Based on the key findings of this research and applicability of general FULL-POL-SAR methodology, there still exist some potential unresolved issues deserving further research to improve the proposed method for the estimation of Earth surface parameters.

Radar Polarimetry

The presently developed model-based target decompositions scheme (e.g. G4U) can separate the signal maximum into four scattering components such as surface, double-bounce, volume and helical scattering, but there is need to solve the problem for discriminating double-bounce scattering from vegetation to double-bounce scattering from manmade features and similarly volume scattering from vegetation to volume scattering from underlying surface and oriented surface structures. Since aforesaid issues constitute the main challenge to microwave remote sensing community, this study recommends for resolving the aforesaid ambiguities to develop new target and/or modify the existing decomposition theorems. It is also envisaged that after including the present recommendations in future decomposition schemes, it will be the most suitable approach to provide consistent and reliable information on the land cover features. Furthermore, the effects of reflection symmetric depolarization and accounting for all polarimetric phase information in the decomposition schemes by extending monostatic to bistatic scattering need to be assessed and derived.

Although complete use of all relative polarimetric Covariance/coherency matrix phase components for the 2 × 2 Sinclair matrix is shown in G4U but the use of 9/9 coherency matrix information is not yet complete. We ought to focus in future studies on how to integrate first the 3 × 3 Gelfand matrix group (8/9 terms) in extension to the 2 × 2 Pauli group (3/4 terms), and finally the 4 × 4 Cartan group (15/16 terms) for the full non-symmetric reciprocal cases.

High Topography effects on POL-SAR Data

Due to the topography relief and side-looking geometry of SAR, the FULL-POL-SAR data suffer geometric distortions such as layover, foreshortening and shadow. For example, due to the low incidence angle and side looking geometry of ALOS-PALSAR and the high topography of the Indian Himalayan terrain, the layover affected areas are an inevitable image-distorting attribute to the image; and therefore we cannot obtain full information of the inherent scattering mechanisms. Moreover, the orientation angles become noisy at steep slopes due to layover distortion in PALSAR images. Therefore, orientation compensation method cannot help too much for correctly discriminating targets in steep slope areas with single flight direction. Both fusion of both ascending and descending configuration SAR images as well as the novel beam shaping angle of incidence extending antenna configurations will be used for future work to retrieve improved terrain information from the opposite viewing geometry with a wide range of incident angle image acquisitions.

Cryosphere

The proposed methodology of Chapter 2 will be assessed with addition of more time series data to check the resolving capability of the ambiguity between vegetation and glacier snow/ice.

The G4U method will also be analyzed for the detection of changes in the glaciated terrain features during two temporal POL-SAR images making use of multi-band fully polarimetric sensor systems.

The study, in Chapter 8, will be extended to snowpack wetness estimation and snowpack states (melt/freeze conditions) detection based on generalized volume and surface parameter methods.

We are planning to carry out ground-truth measurements of snow and glacier ice cover parameters concurrent with this acquisition period. We conjecture to optimize these algorithms not only for ALOS-PALSAR-2 data and will evaluate corresponding automated value-added glaciated-parameter products in line with the ALOS RA-4 goals and other forthcoming S-Band FULL-POL-SAR sensor systems.

Biosphere

Utilization of SAR data for the estimation of sole crop parameters are being used at massive level. In recent years, the trend of sole cropping systems has been rapidly expanding to Agroforestry (intercropping) systems in North-West India. The first step of crop parameter estimation is that the discrimination of different crops should become more accurate which definitely will require simultaneous multi-band fully polarimetric POLSAR sensor implementation, currently available only for airborne systems such as the F-SAR of DLR and the RAMSES (Radar Aéroporté Multi-Spectral d'Etudes de Signatures) and SETHI (Système Expérimental de Télédétection Hyperfréquence Imageur) of ONERA (Office National d’Etudes et Recherches Aérospatiales). Therefore, it is necessary to address the new challenge by mobilizing the younger radar polarimetry community for paying increased attention to crop parameter estimation under current agro-forestry (intercropping) methodologies and its extensions.

Hydrosphere

Considerable research needs to be extended in predicting secondary scattering and depolarization effects for overcoming the current imprecise soil moisture estimation approaches as ever advanced those may be. The approaches will be developed by integrating varying vegetation and roughness effects in the scattering behavior, and including the use of complete polarimetric and multiple incidence-angle information for soil moisture estimation.

Disaster Monitoring

In recent decades, natural disasters have frequently occurred, leading to significant loss of life, major environmental and socio-economic costs. Therefore, disaster monitoring will be continued by exploring the potential of G4U's secondary parameters (see Annexure B for G4U's secondary parameters) especially caused by volcano eruptions, earthquakes, tsunami, floods, landslides and debris flows, droughts, and wild-fires in Asia.

Annexure A. Coherency Unitary Transformation Matrices

Unitary transformation preserves the information contained in the matrix. Using this mathematical property, it is possible to transform the measured coherency matrix. Since there are many unitary transformation matrices, we tried specific three types among them:

The first one is to eliminate T_{12} component

$$\langle[T']\rangle = \begin{bmatrix} T'_{11} & 0 & T'_{13} \\ 0 & T'_{22} & T'_{23} \\ T'_{31} & T'_{32} & T'_{33} \end{bmatrix} \tag{A.1}$$

The second one is to eliminate T_{13} component,

$$\langle[T']\rangle = \begin{bmatrix} T'_{11} & T'_{12} & 0 \\ T'_{21} & T'_{22} & T'_{23} \\ 0 & T'_{32} & T'_{33} \end{bmatrix} \tag{A.2}$$

The third one is to eliminate T_{23} component,

$$\langle[T']\rangle = \begin{bmatrix} T'_{11} & T'_{12} & T'_{13} \\ T'_{21} & T'_{22} & 0 \\ T'_{31} & 0 & T'_{33} \end{bmatrix} \quad . \tag{A.3}$$

The elimination purpose is to reduce the number of polarimetric parameters from 9 to 8 or 7, in order to match the number of theoretical model parameters. Firstly, the T_{13} and T_{12} elimination methods have been tried but it produces poor decomposition image as compared to T_{23} elimination method. Therefore, we have concentrated T_{23} elimination method, assuming, at first, 3-component decomposition because of no-helix source by T_{23} element. However, the 3-component decomposition expansion was found ill-posed, i.e., it cannot account for all 7 parameters by the T_{23} method. Therefore we used 4-component decomposition to account for all 7 parameters as shown in the Chapter 6. It is important to note that the information of T_{23}=0 after the double transformations is utilized in the present GU4 decomposition method to account for all polarimetric parameters, even if we eliminate T_{23} element.

1) In order to achieve $T_{12} = 0$, the unitary transformation is implemented twice on $[\langle[T]\rangle]$ as

$$\begin{bmatrix} T_{11}(\theta) & T_{12}(\theta) & T_{13}(\theta) \\ T_{21}(\theta) & T_{22}(\theta) & T_{23}(\theta) \\ T_{31}(\theta) & T_{32}(\theta) & T_{33}(\theta) \end{bmatrix} = [R(\theta)] \begin{bmatrix} T_{11} & T_{12} & T_{13} \\ T_{21} & T_{22} & T_{23} \\ T_{31} & T_{32} & T_{33} \end{bmatrix} [R(\theta)]^{\dagger} \tag{A.4}$$

with the unitary rotation matrix,

$$[R(\theta)] = \begin{bmatrix} \cos 2\theta & -\sin 2\theta & 0 \\ \sin 2\theta & \cos 2\theta & 0 \\ 0 & 0 & 1 \end{bmatrix} \tag{A.5}$$

with the angle

$$2\theta = \frac{1}{2}\tan^{-1}\left(\frac{2\mathrm{Re}\,\{T_{12}\}}{T_{22}-T_{11}}\right) \tag{A.6}$$

T_{12} component becomes purely imaginary. $T_{12}(\theta) = j\ \mathrm{Im}\ \{T_{12}\}$ (A.7)

After this rotation (A.4), the elements of the coherency matrix become

$$\begin{aligned}
&T_{11}(\theta) = T_{11}\cos^2 2\theta + T_{22}\sin^2 2\theta - \mathrm{Re}(T_{12})\sin 4\theta \\
&T_{12}(\theta) = T_{21}^{*}(\theta) = j\ \mathrm{Im}\ \{T_{12}\} \\
&T_{13}(\theta) = T_{31}^{*}(\theta) = T_{13}\cos 2\theta - T_{23}\sin 2\theta \\
&T_{22}(\theta) = T_{22}\cos^2 2\theta + T_{11}\sin^2 2\theta + \mathrm{Re}(T_{12})\sin 4\theta \\
&T_{23}(\theta) = T_{32}^{*}(\theta) = T_{23}\cos 2\theta - T_{13}\sin 2\theta \\
&T_{33}(\theta) = T_{33}
\end{aligned} \tag{A.8}$$

Then, the second unitary transformation is employed such that

$$\langle [T']\rangle = \begin{bmatrix} T_{11}(\varphi) & T_{12}(\varphi) & T_{13}(\varphi) \\ T_{21}(\varphi) & T_{22}(\varphi) & T_{23}(\varphi) \\ T_{31}(\varphi) & T_{32}(\varphi) & T_{33}(\varphi) \end{bmatrix} = [U(\varphi)] \begin{bmatrix} T_{11}(\theta) & T_{12}(\theta) & T_{13}(\theta) \\ T_{21}(\theta) & T_{22}(\theta) & T_{23}(\theta) \\ T_{31}(\theta) & T_{32}(\theta) & T_{33}(\theta) \end{bmatrix} [U(\varphi)]^{\dagger} \tag{A.9}$$

with a special unitary transform matrix

$$[U(\varphi)] = \begin{bmatrix} \cos 2\varphi & j\sin 2\varphi & 0 \\ j\sin 2\varphi & \cos 2\varphi & 0 \\ 0 & 0 & 1 \end{bmatrix} \tag{A.10}$$

The angle φ is derived so as to minimize the T_{33} element in a way similar to θ

$$2\varphi = \frac{1}{2}\, tan^{-1}\left(\frac{2\ \mathrm{Im}\ \{T_{12}(\theta)\}}{T_{22}(\theta) - T_{11}(\theta)}\right) \tag{A$\cdot$11}$$

This unitary transformation yields the coherency matrix element as

$$\begin{aligned}
&T_{11}(\varphi) = T_{11}(\theta)\cos^2 2\varphi + T_{22}(\theta)\sin^2 2\varphi + \mathrm{Im}\ \{T_{12}(\theta)\}\sin 4\varphi \\
&T_{12}(\varphi) = T_{21}^{*}(\varphi) = \mathrm{Re}\ \{T_{12}(\theta)\} = \mathrm{Re}\ \{j\ \mathrm{Im}\ \{T_{12}\}\} = 0 \\
&T_{13}(\varphi) = T_{31}^{*}(\varphi) = T_{13}(\theta)\cos 2\varphi + j\ T_{23}(\theta)\sin 2\varphi \\
&T_{22}(\varphi) = T_{22}(\theta)\cos^2 2\varphi + T_{11}(\theta)\sin^2 2\varphi - \mathrm{Im}\ \{T_{12}(\theta)\}\sin 4\varphi \\
&T_{23}(\varphi) = T_{32}^{*}(\varphi) = T_{23}(\theta)\cos 2\varphi + j\ T_{13}(\theta)\sin 2\varphi \\
&T_{33}(\varphi) = T_{33}(\theta) = T_{33}
\end{aligned} \tag{A.12}$$

2) In order to achieve $T_{13} = 0$, the unitary transformation is implemented twice on $[\langle [T]\rangle]$ as

$$\begin{bmatrix} T_{11}(\theta) & T_{12}(\theta) & T_{13}(\theta) \\ T_{21}(\theta) & T_{22}(\theta) & T_{23}(\theta) \\ T_{31}(\theta) & T_{32}(\theta) & T_{33}(\theta) \end{bmatrix} = [R(\theta)] \begin{bmatrix} T_{11} & T_{12} & T_{13} \\ T_{21} & T_{22} & T_{23} \\ T_{31} & T_{32} & T_{33} \end{bmatrix} [R(\theta)]^{\dagger} \tag{A.13}$$

with the unitary rotation matrix,

$$[R(\theta)] = \begin{bmatrix} \cos 2\theta & 0 & -\sin 2\theta \\ 0 & 1 & 0 \\ \sin 2\theta & 0 & \cos 2\theta \end{bmatrix} \tag{A.14}$$

with the angle

$$2\theta = \frac{1}{2}\tan^{-1}\left(\frac{2\mathrm{Re}\,\{T_{13}\}}{T_{33} - T_{11}}\right) \tag{A. 15}$$

T_{13} component becomes purely imaginary. $T_{13}(\theta) = j\ \mathrm{Im}\,\{T_{13}\}$ (A.16)

After this rotation (A.13), the elements of the coherency matrix become

$$T_{11}(\theta) = T_{11}\cos^2 2\theta + T_{33}\sin^2 2\theta - \mathrm{Re}(T_{13})\sin 4\theta$$

$$T_{12}(\theta) = T_{12}\cos 2\theta - T_{23}^{*}\sin 2\theta$$

$$T_{13}(\theta) = j\ \mathrm{Im}\,\{\,T_{13}\}$$

$$T_{21}(\theta) = T_{12}^{*}(\theta)$$

$$T_{22}(\theta) = T_{22}$$

$$T_{23}(\theta) = T_{23}\cos 2\theta + T_{12}^{*}\sin 2\theta$$

$$T_{31}(\theta) = T_{13}^{*}(\theta)$$

$$T_{32}(\theta) = T_{23}^{*}(\theta)$$

$$T_{33}(\theta) = T_{33}\cos^2 2\theta + T_{11}\sin^2 2\theta + \mathrm{Re}(T_{13})\sin 4\theta \tag{A.17}$$

Then, the second unitary transformation is employed such that

$$\langle [T']\rangle = \begin{bmatrix} T_{11}(\varphi) & T_{12}(\varphi) & T_{13}(\varphi) \\ T_{21}(\varphi) & T_{22}(\varphi) & T_{23}(\varphi) \\ T_{31}(\varphi) & T_{32}(\varphi) & T_{33}(\varphi) \end{bmatrix} = [U(\varphi)] \begin{bmatrix} T_{11}(\theta) & T_{12}(\theta) & T_{13}(\theta) \\ T_{21}(\theta) & T_{22}(\theta) & T_{23}(\theta) \\ T_{31}(\theta) & T_{32}(\theta) & T_{33}(\theta) \end{bmatrix} [U(\varphi)]^{\dagger} \tag{A.18}$$

with a special unitary transform matrix

$$[U(\varphi)] = \begin{bmatrix} \cos 2\varphi & 0 & j\sin 2\varphi \\ 0 & 1 & 0 \\ j\sin 2\varphi & 0 & \cos 2\varphi \end{bmatrix} \tag{A.19}$$

The angle φ is derived so as to minimize the T_{33} element in a way similar to θ

$$2\varphi = \frac{1}{2}\ tan^{-1}\left(\frac{2\ \mathrm{Im}\,\{T_{13}(\theta)\}}{T_{33}(\theta) - T_{11}(\theta)}\right) \tag{A. 20}$$

This unitary transformation (A.18) yields the coherency matrix element as

$$T_{11}(\varphi) = T_{11}(\theta)\cos^2 2\varphi + T_{33}(\theta)\sin^2 2\varphi + \text{Im}\{T_{12}(\theta)\}\sin 4\varphi$$

$$T_{12}(\varphi) = T_{12}(\theta)\cos 2\varphi + j\ T_{23}^{*}(\theta)\sin 2\varphi$$

$$T_{13}(\varphi) = \text{Re}\{T_{13}(\theta)\} = \text{Re}\left\{j\ \text{Im}\{T_{13}\}\right\} = 0$$

$$T_{21}(\varphi) = T_{12}^{*}(\varphi)$$

$$T_{22}(\varphi) = T_{22}(\theta) = T_{22}$$

$$T_{23}(\varphi) = T_{23}(\theta)\cos 2\varphi + j\ T_{13}(\theta)\sin 2\varphi$$

$$T_{31}(\varphi) = T_{13}^{*}(\varphi)$$

$$T_{32}(\varphi) = T_{23}^{*}(\varphi)$$

$$T_{33}(\varphi) = T_{33}(\theta)\cos^2 2\varphi + T_{11}(\theta)\sin^2 2\varphi - \text{Im}\{T_{13}(\theta)\}\sin 4\varphi \qquad \text{(A.21)}$$

3) In order to achieve $T_{23} = 0$, the unitary transformation is implemented twice on $[\langle[T]\rangle]$ as The first one is the rotation of about the line of sight (Yamaguchi *et al.* 2011)

$$\begin{bmatrix} T_{11}(\theta) & T_{12}(\theta) & T_{13}(\theta) \\ T_{21}(\theta) & T_{22}(\theta) & T_{23}(\theta) \\ T_{31}(\theta) & T_{32}(\theta) & T_{33}(\theta) \end{bmatrix} = [R(\theta)] \begin{bmatrix} T_{11} & T_{12} & T_{13} \\ T_{21} & T_{22} & T_{23} \\ T_{31} & T_{32} & T_{33} \end{bmatrix} [R(\theta)]^{\dagger} \qquad \text{(A.22)}$$

with a unitary rotation matrix,

$$[R(\theta)] = \begin{bmatrix} 1 & 0 & 0 \\ 0 & \cos 2\theta & \sin 2\theta \\ 0 & -\sin 2\theta & \cos 2\theta \end{bmatrix} \qquad \text{(A.23)}$$

The angle θ is chosen as to minimize the T_{33} element

$$2\theta = \frac{1}{2}\ tan^{-1}\left(\frac{2\ \text{Re}\{T_{23}\}}{T_{22} - T_{33}}\right) \qquad \text{(A}\cdot\text{24)}$$

After this rotation, the T_{23} element becomes purely imaginary,

$$T_{23}(\theta) = j\ \text{Im}\{T_{23}\}. \qquad \text{(A.25)}$$

After this rotation (A.22), the elements of the coherency matrix become

$$T_{11}(\theta) = T_{11}$$

$$T_{12}(\theta) = T_{21}^{*}(\theta) = T_{12}\cos 2\theta + T_{13}\sin 2\theta$$

$$T_{13}(\theta) = T_{31}^{*}(\theta) = T_{13}\cos 2\theta - T_{12}\sin 2\theta$$

$$T_{22}(\theta) = T_{22}\cos^2 2\theta + T_{33}\sin^2 2\theta + \text{Re}(T_{23})\sin 4\theta$$

$$T_{23}(\theta) = T_{32}^{*}(\theta) = j\,\mathrm{Im}\,\{\,T_{23}\}$$

$$T_{33}(\theta) = T_{33}\cos^{2}2\theta + T_{22}\sin^{2}2\theta - \mathrm{Re}(T_{23})\sin 4\theta. \tag{A.26}$$

Then, the second unitary transformation is employed such that

$$\langle[T']\rangle = \begin{bmatrix} T_{11}(\varphi) & T_{12}(\varphi) & T_{13}(\varphi) \\ T_{21}(\varphi) & T_{22}(\varphi) & T_{23}(\varphi) \\ T_{31}(\varphi) & T_{32}(\varphi) & T_{33}(\varphi) \end{bmatrix} = [U(\varphi)] \begin{bmatrix} T_{11}(\theta) & T_{12}(\theta) & T_{13}(\theta) \\ T_{21}(\theta) & T_{22}(\theta) & T_{23}(\theta) \\ T_{31}(\theta) & T_{32}(\theta) & T_{33}(\theta) \end{bmatrix} [U(\varphi)]^{\dagger} \tag{A.27}$$

with a special unitary transform matrix

$$[U(\varphi)] = \begin{bmatrix} 1 & 0 & 0 \\ 0 & \cos 2\varphi & j\sin 2\varphi \\ 0 & j\sin 2\varphi & \cos 2\varphi \end{bmatrix} \tag{A.28}$$

The angle φ is derived so as to minimize the T_{33} element in a way similar to θ (see Chapter 3)

$$2\varphi = \frac{1}{2}\,tan^{-1}\left(\frac{2\,\mathrm{Im}\,\{T_{23}(\theta)\}}{T_{22}(\theta) - T_{33}(\theta)}\right) \tag{A$\cdot$29}$$

This unitary transformation (A.27) yields the coherency matrix element as

$$T_{11}(\varphi) = T_{11}(\theta) = T_{11}$$

$$T_{12}(\varphi) = T_{21}^{*}(\varphi) = T_{12}(\theta)\cos 2\varphi - j\; T_{12}(\theta)\sin 2\varphi$$

$$T_{13}(\varphi) = T_{31}^{*}(\varphi) = T_{13}(\theta)\cos 2\varphi - j\; T_{12}(\theta)\sin 2\varphi$$

$$T_{22}(\varphi) = T_{22}(\theta)\cos^{2} 2\varphi + T_{33}(\theta)\sin^{2} 2\varphi + \mathrm{Im}\,\{\,T_{23}(\theta)\}\sin 4\,\varphi$$

$$T_{23}(\varphi) = T_{32}^{*}(\varphi) = \mathrm{Re}\,\{\,T_{23}(\theta)\} = \mathrm{Re}\{\,j\,\mathrm{Im}\,\{\,T_{23}\}\,\} = 0$$

$$T_{33}(\varphi) = T_{33}(\theta)\cos^{2} 2\varphi + T_{22}(\theta)\sin^{2} 2\varphi - \mathrm{Im}\{\,T_{23}(\theta)\}\sin 4\,\varphi. \tag{A.30}$$

Annexure B. Generation of the Child/Secondary Parameters of G4U

1) Probabilities of Decomposed Scattering Powers

Surface scattering power probability $$p_s = \frac{P_s}{TP} \tag{B.1}$$

Double bounce power scattering probability $$p_d = \frac{P_d}{TP} \tag{B.2}$$

Volume scattering power probability $$p_v = \frac{P_v}{TP} \tag{B.3}$$

Helix scattering power probability $$p_c = \frac{P_c}{TP} \tag{B.4}$$

2) Scattering Mechanism Entropy

The scattering mechanism entropy of G4U is defined as

$$H = -p_s \log_4 p_s - p_d \log_4 p_d - p_v \log_4 p_v - p_c \log_4 p_c \tag{B.5}$$

3) Radar Vegetation Index/ Depolarization Index

Since the dominant probability of G4U over the vegetation areas is p_v, the radar vegetation index can be considered as

$$RVI = p_v\,; \qquad 0 < RVI < 1 \tag{B.6}$$

4) Scattering Mechanism Anisotropy

$$A_{s-v} = \frac{p_s - p_v}{p_s + p_v} = \frac{P_s - P_v}{P_s + P_v}\,; \qquad -1 < A_{s-v} < 1 \tag{B.7}$$

$$A_{d-v} = \frac{p_d - p_v}{p_d + p_v} = \frac{P_d - P_v}{P_d + P_v}\,; \qquad -1 < A_{d-\mathrm{v}} < 1 \tag{B.8}$$

$$A_{s-c} = \frac{p_s - p_c}{p_s + p_c} = \frac{P_s - P_c}{P_s + P_c}\,; \qquad -1 < A_{s-c} < 1 \tag{B.9}$$

$$A_{s-d} = \frac{p_s - p_d}{p_s + p_d} = \frac{P_s - P_d}{P_s + P_d}\,; \qquad -1 < A_{s-d} < 1 \tag{B.10}$$

$$A_{d-c} = \frac{p_d - p_c}{p_d + p_c} = \frac{P_d - P_c}{P_d + P_c}\,; \qquad -1 < A_{d-c} < 1 \tag{B.11}$$

5) Volume minus Surface/Surface –trunk scattering mechanism probability

$$VmS_{v-s} = p_v - p_s\,; \quad -1 < VmS_{v-s} < 1 \tag{B.12}$$

$$VmS_{v-d} = p_v - p_d\,; \quad -1 < VmS_{v-d} < 1 \tag{B.13}$$

6) Surface/Surface –trunk/ helix scattering over Volume scattering mechanism:

$$\mu_s = SoV = P_s / P_v \tag{B.14}$$

References

1. Abe, T., Y. Yamaguchi and M. Sengoku, 1990, “Experimental study of microwave transmission in snowpack,” *IEEE Trans. Geosci. Remote Sens.*, vol. 28, no. 5, pp. 915-921.
2. Agrawal, A. P., 1986, *A polarimetric rain back-scattering model developed for coherent polarization diversity radar applications*, Ph.D. thesis, UIC-GC, University of Illinois, Chicago, IL.
3. Agrawal, A.P. and W-M. Boerner, 1989, “Redevelopment of Kennaugh's target characteristic polarization state theory using the polarization transformation ratio formalism for the coherent case”, *IEEE Trans. Geosci. Remote Sens.*, vol. 27, no.1, pp. 2-14.
4. Arii, M., J. J. van Zyl, and Y. J. Kim, 2011, “Adaptive model-based decomposition of polarimetric SAR covariance matrices,” *IEEE Trans. Geosci. Remote Sens.*, vol. 49, no. 3, pp. 1104–1113.
5. Barnes, R.M., 1988, “Roll invariant decompositions for the polarization covariance matrix”, *Polarimetry Technology Workshop*, Redstone Arsenal, AL.
6. Beckmann, P. and A. Spizzichino, 1963, *Scattering of Electromagnetic Waves from Rough Surfaces*, MacMillan, New York.
7. Bickel, S. H. and J. F. A. Ormsby, 1965, “Error analysis, calibration, and the polarization scattering matrix”, *Proc. IEEE*, vol. 53, pp.1087-1089.
8. Bickel, S. H., 1965, “Some invariant properties of the polarization scattering matrix”, *Proc. IEEE*, vol. 53, pp. 1970-1072.
9. Boerner, W-M. *et al.* (eds), 1985, *Inverse Methods in Electromagnetic Imaging*, Proceedings of the NATO-Advanced Research Workshop, (18-24 Sept. 1983, Bad Windsheim, FR Germany), Parts 1&2, NATO-ASI C-143, (1,500 p.), D. Reidel Publ. Co., Jan. 1985.
10. Boerner, W-M. *et al.* (eds.), 1992, *Direct and Inverse Methods in Radar Polarimetry*, NATO- ARW, Sept. 18-24, 1988, Proc., Chief Editor, 1987-1991, (1,938 pages), NATO-ASI Series C: Math & Phys. Sciences, vol. C-350, Parts 1&2, D. Reidel Publ. Co., Kluwer Academic Publ., Dordrecht, NL, 1992 Feb. 15.
11. Boerner, W-M., 2003, “Recent advances in extra-wide-band polarimetry, interferometry and polarimetric interferometry in synthetic aperture remote sensing, and its applications”, *IEEE Proc.-Radar Sonar Navigation, Special Issue of the EUSAR-02*, vol. 150, no. 3, June 2003, pp. 113-125.
12. Boerner, W-M., 1981, “Use of polarization in electromagnetic inverse scattering”, *Radio Science*, vol. 16, no.6 (Special Issue: 1980 Munich Symposium on EM Waves), pp. 1037-1045.

13. Boerner, W-M., 1995, “Polarimetry in remote sensing and imaging of terrestrial and planetary environments”, *Proceedings of Third International Workshop on Radar Polarimetry* (JIPR-3, 95), IRESTE, Univ-Nantes, France, pp. 1-38.

14. Boerner, W-M., and A.-Q. Xi, 1990, “Characteristic radar target polarization state theory for the coherent monostatic and reciprocal case using the generalized polarization transformation ration formulation”, *ARCHIV DER ELEKTRISCHEN UBERTRAGUNG, AEU*, vol. 44, no.4, pp. 273-281 (Special Issue for the 60th Birthday of Prof. Hans Brand, UEN-IHFT).

15. Boerner, W-M., B.Y. Foo, and H.J. Eom, 1987, “Interpretation of the polarimetric co-polarization phase term (φ_{HH} - φ_{VV}) in high resolution SAR imaging using the JPL CV-990 polarimetric L-band SAR data”, *IEEE Trans. Geosci. Remote Sens.*, vol. 25, no. 1, pp. 77-82(Special IGARSS Issue).

16. Boerner, W-M., *et al.*, (Guest Eds.), 1981, IEEE Transactions on the Antennas & Propagation Society, vol. 29, no.2, Special Issue, *Inverse Methods in Electromagnetics*, (417 p.)

17. Boerner, W-M., H. Mott , E. Luneburg , C. Livingstone , B. Brisco , R.J. Brown, J.S. Paterson, S.R. Cloude, E. Krogager, J.S. Lee, D.L. Shuler, J.J. Van zyl , D. Randall , P. Budkewitsch and E. Pottier,1998, “Polarimetry in radar remote sensing: basic and applied concepts,” In Manual of remote sensing: principles and applications of Imaging Radar. Edited by F. M. Henderson and A. J. Lewis. John Wiley & Sons, Inc. New York. vol. 2, ch.5, pp. 271-356.

18. Brunner, D., G. Lemoine, and L. Bruzzone, 2010, “Earthquake damage assessment of buildings using VHR optical and SAR imagery,” *IEEE Trans. Geosci. Remote Sens.*, vol. 48, no. 5, pp. 2403-2420.

19. Cameron, W.L., N. Youssef, and L.K. Leung, 1996, “Simulated polarimetric signatures of primitive geometrical shapes,” *IEEE Trans. Geosci. Remote Sens.*, vol. 34, pp. 793–803.

20. Chandrasekhar, S., 1960, *Radiative Transfer,* Dover Publications Inc, New York.

21. Chaudhuri, S. K., and W.-M. Boerner,1987, “A polarimetric model for the recovery of high frequency scattering centers from bistatic --- monostatic scattering matrix data,” *IEEE Trans. Antennas Propagat.*, vol. AP-35, no. 1, pp. 87-93.

22. Chauhan, N.S., and R.H. Lang, 1989, “Polarization utilization in the microwave inversion of leaf angle distributions”, *IEEE Trans. Geosci. Remote Sens.*, vol. 27, no. 4, pp. 395-402.

23. Chini, M, .N. Pierdicca, W. J. Emery, 2009, “exploiting SAR and VHR optical images to quantify damages caused by the 2003 Bam earthquake,” *IEEE Trans. Geosci. Remote Sens.*, vol. 47, no. 1, pp. 145-152.

24. Cloude, S. R., 1985, “Target decomposition theorems in radar scattering,” *Electron. Lett.*, vol. 21, no. 1, pp. 22-24.

25. Cloude, S. R., 1986, “Group theory and polarization algebra”, *OPTIK*, vol. 75, no. 1, pp. 26-36.

26. Cloude, S. R., 2009, *Polarisation: applications in remote sensing*. London, U.K.: Oxford Univ. Press.

27. Cloude, S. R., and E. Pottier, 1996, "A review of target decomposition theorems in radar polarimetry', *IEEE Trans. Geosci. Remote Sens.*, vol. 34, no. 2, pp. 498-518.

28. Cloude, S. R., and E. Pottier, 1997, "An entropy based classification scheme for land applications of polarimetric SAR," *IEEE Trans. Geosci. Remote Sens.*, vol. 35, no. 1, pp. 68-78.

29. Cloude, S. R.,1992, "Uniqueness of target decomposition theorems in radar polarimetry," in *Direct and Inverse Methods in Radar Polarimetry*, Part 1, NATO-ARW, W. -M. Boerner *et al.*, Eds. Norwell, MA: Kluwer, pp. 267-269.

30. Cloude, S.R., 1990, "Polarimetric optimization based on the target covariance matrix", *Electron. Lett.*, vol. 26, no.20, pp. 1670-1671.

31. Cloude, S.R., E. Pottier, W-M Boerner, 2002, "Unsupervised image classification using the entropy/alpha/anisotropy method in radar polarimetry*", NASA-JPL, AIRSAR-02 Workshop,* Double Tree Hotel, Pasadena, CA, 2002 March 04-06.

32. Copeland, J.R., 1960, "Radar target classification by polarization properties", *Proc. IRE*, vol. 48, pp. 1290- 1296.

33. Corr D.G. and A.F. Rodrigues, "Alternative basis matrices for polarimetric decomposition," In EUSAR 2002, *Proceedings of the 4th European Union Conference on Synthetic Aperture Radar,* 4–6 June 2002, Cologne, Germany.

34. Davidovitz, M., and W.-M. Boerner, 1986, "Extension of Kennaugh's optimal polarization concept to the asymmetric matrix case," *IEEE Trans. Antennas Propagat.*, vol. AP-34, no. 4, pp. 569-574.

35. Deschamps, G.A., 1951, "Geometrical representation of the polarization of a plane electromagnetic wave", *Proc. IRE*, vol. 39, pp. 540-544.

36. Dobson, M.C., L. Pierce, K.C. Mc. Donald and T. Sharik,1991, "Seasonal change in radar backscatter from mixed conifer and hardwood forests in northern Michigan", *Proc. Int. Geosci. Remote Sens. Symp.'91*, pp. 1121-1124.

37. Dozier, J., 1989, "Spectral signature of alpine snow cover from the Landsat Thematic Mapper," *Remote Sen. Environ.*, vol. 28, pp. 9-22.

38. Durden, S. L., J. J. van Zyl, and H. A. Zebker, 1989, "Modeling and observation of the radar polarization signature of forested areas," *IEEE Tans. Geosci. Remote Sens.*, vol. 27, no. 3, pp. 290-301.

39. Durden, S. L., J. J. van Zyl, and H. A. Zebker, 1990, "The unpolarized component in polarimetric radar observations of forested areas," *IEEE Tans. Geosci. Remote Sens.*, vol. 28, no. *2*, pp. 268-271.

40. Floricioiu, D., and H. Rott, 2001, "Seasonal and short-term variability of multifrequency, polarimetric radar backscatter of Alpine terrain from SIR-C/X-SAR and AIRSAR Data," *IEEE Trans. Geosci. Remote Sens.*, vol. 39, no. 12, pp. 2634–2648.

41. Freeman, A., and S. Durden, 1998, “A three-component scattering model for polarimetric SAR data”, *IEEE Trans. Geosci. Remote Sens*., vol. 36, no. 3, pp. 963-973.

42. FSI, *India State of Forest Report 2011*, Forest Survey of India (FSI), Derhadun, India (accessed 2012-04-03). [Online]. Available: http://www.fsi.org.in/sfr_2011.htm

43. Fung, A. K., Z. Li, and K. S. Chen, 1992 “Backscattering from a randomly rough dielectric surface,” *IEEE Trans. Geosci. Remote Sens*., vol. 30, no. 2, pp. 356–369.

44. Fung, A., 1994, Microwave scattering and emission models and their applications. Artech House, 1994.

45. Graves, C.D., 1956, “Radar polarization power scattering matrix”, *Proc. IRE*, vol. 44, no. 5, pp. 248-252.

46. GSI, 2011, Geospatial Information (GSI) Authority of Japan (accessed 2011-06-17). [Online]. Available: http://www.gsi.go.jp

47. Hajnsek, I., 2001, *Inversion of surface parameters (soil moisture & roughness) using polarimetric SAR*, Doctoral Thesis, FSU, Jena, Germany, 2001 October 17 (ISSN 1434-8485 ISRN DLR-FB-2001-30).

48. Hajnsek, I., E. Pottier, and S. R. Cloude, 2003, “Inversion of surface parameters from polarimetric SAR,” *IEEE Trans. Geosci. Remote Sens.*, vol. 41, no. 4, pp. 727-744.

49. Holm, W.A. and R.M. Barnes, 1988, “on radar polarization mixed state decomposition theorems”, *Proc. National Radar Conference*-1988, USA.

50. Huynen, J. R., 1970, *Phenomenological theory of radar targets*, Ph. D. Dissertation, Technical University, Delft, The Netherlands.

51. Huynen, J. R., 1992, “Theory and measurement of surface-torsion,” *Direct and Inverse Methods in Radar Polarimetry* (W.-M. Boerner *et al.* eds.), NATO ASI Series C, vol. 350, Kluwer Academic Publishers, Dordrecht/Boston/London, pp. 581-623.

52. Kennaugh, M., 1952, *Polarization properties of radar reflections*, M.Sc. thesis, The Ohio State University, Columbus.

53. Kitayama, K., Y. Yamaguchi, J. Yang and H. Yamada, 2001, “Compound scattering matrix of targets aligned in the range direction,” *IEICE Trans. Commun.*, vol. E84-B, no.1, pp.81-88.

54. Kostinski, A. B., and W.-M. Boerner, 1986, "On the foundations of radar polarimetry,” *IEEE Trans. Antennas Propagat*., vol. AP-34, no. 12, pp. 1395-1404.

55. Kostinski, A.B. and W.-M. Boerner, 1987, “On the polarimetric contrast optimization”, *IEEE Trans. Antennas Propagt.*, vol. AP-35, no.8, pp. 988-991.

56. Kostinski, A.B., B.D. James and W-M. Boerner, 1988, “On the optimal reception of partially polarized waves”, *Journal of the Optical Society of America, Part A, Optics & Image Sciences,* Series 2, vol. 5, no. l, pp. 58-64.

57. Krieger G., N. Gebert, M. Younis and A. Moreira, 2008, “Advanced Synthetic Aperture Radar Based on Digital Beamforming and Waveform Diversity”, In: *IEEE Radar Conference (RadarCon),* pp. 767-772, Rome, Italy.

58. Krogager, E, and W-M. Boerner, 1996, “On the importance of utilizing polarimetric information in radar imaging classification”, *AGARD Proc*. 582-17, pp. 1-13.

59. Krogager, E., 1990, “A new decomposition of the radar target scattering matrix,” *Electron. Lett.*, vol. 26, no. 18, pp. 1525−1526.

60. Leckie, D.G., and K. J. Ranson, 1998, “Forestry applications using imaging radar,” In *Manual of remote sensing: principles and applications of Imaging Radar*. Edited by F. M. Henderson and A. J. Lewis. John Wiley & Sons, Inc. *New York*. vol. 2**,** ch.9, pp. 435-509.

61. Lee, J. S., and E. Pottier, 2009, Polarimetric radar imaging from basics to applications, CRC Press.

62. Lee, J. S., D.L. Schuler, T.L. Ainsworth, E. Krogager, D. Kasilingam, and W. M. Boerner, 2002, “On the estimation of radar polarization orientation shifts induced by terrain slopes”, *IEEE Trans. Geosci. Remote Sens.*, vol. 40, no.1, pp. 30 41.

63. Lee, J. S., and T. Ainsworth, 2011, “The effect of orientation angle compensation on coherency matrix and polarimetric target decompositions,” *IEEE Trans. Geosci. Remote Sens*., vol. 49, no. 1, pp. 53-64.

64. Lee, J. S., D.L. Schuler, and T.L. Ainsworth, 2000, “Polarimetric SAR data compensation for terrain azimuth slope variation”, *IEEE Trans. Geosci. Remote Sens.*, vol. 38, no. 5, pp. 2153-2163.

65. Lee, J. S., M. R. Grues, and G. de Grandi, 1999, “Polarimetric SAR speckle filtering and its implication for classification”, *IEEE Trans. Geosci. Remote Sens*., vol. 37, pp. 2363-2373.

66. Lee, J. S., T.L. Ainsworth and Y. Wang, “Recent advances in scattering model-based decompositions: An overview”, *Proc. of IGARSS11*, Vancouver, Canada, Jul. 2011.

67. Luojus, J., A. Pulliainen, C. Blasco, S. Metsamaki and M. Hallikainen, 2009, “Comparison of SAR-based snow-covered area estimation methods for the boreal forest zone”, *IEEE Geosci. Remote Sens. Lett.* , vol. 6, no. 3, pp. 403-407.

68. Matsuoka, M., and S. Koshimura, 2010, “Tsunami damaged area estimation for the 2010 Maule, Chile earthquake using ASTER DEM and PALSAR images on the geo grid,” *8th Int. Workshop on Remote Sens. and Disaster Response* on Sept. 30- Oct. 1, 2010, Tokyo, Japan.

69. Matsuoka, M., and F. Yamazaki, 2004, “ Use of satellite SAR intensity imagery for detecting building areas damaged due to earthquakes, *Earthquake Spectra*, vol. 20, no. 3, pp. 975-994.

70. Mätzler, C., and E. Schanda, 1984, “Snow mapping with active microwave sensors,” *Int. J. Remote Sens.,* vol. 5, no. 2, pp. 409–422.

71. Michel R., and E. Rignot, 1999, "Flow of Glaciar Moreno, Argentina, from repeat-pass shuttle imaging radar images: comparison of the phase correlation method with radar Interferometry," *J. Glaciology*, vol. 45, no. 149, pp. 93-100.

72. Mohite, K., G. Singh, and G. Venkataraman, 2007, "Feasibility of various remote sensing data for mapping snow cover area around Gangotri Glacier," *Proc. SPIE-MIPPR*, 6787 (DOI:10.1117/12.753441).

73. Mott, H. and W-M. Boerner, 1992, editors, *"Radar Polarimetry, SPIE's Annual Mtg., Polarimetry Conference Series",* 1992 July 23-24, San Diego Convention Center, SPIE Conf. Proc., vol. 1748.

74. Mott, H. and W-M. Boerner, 1997, editors, *"Wideband Interferometric Sensing and Imaging Polarimetry*", SPIE's Annual Mtg., Polarimetry and Spectrometry in Remote Sensing Conference Series, 1997 July 27- Aug 01, San Diego Convention Center, SPIE Conf. Proc., vol. 3120.

75. Mott, H., 1992, *Antennas for radar and communications - a polarimetric approach*, John Wiley & Sons, New York, 521 p.

76. Mott, H., 2007, *Remote sensing with polarimetric radar*, John wiley and sons, Inc., Hoboken, New Jersey.

77. Nagler, T., 1996, *Methods and analysis of SAR data from ERS-1 and X-SAR for snow and glacier applications*, Ph.D. Thesis, University of Innsbruck.

78. Nagler, T., and H. Rott, 2000, "Retrieval of wet snow by means of multitemporal SAR data", *IEEE Trans. Geosc. Rem. Sens.*, Vol. 38, no.2, pp. 754–765.

79. Nainwal, H. C., B. D. S. Negi, M. Chaudhary K.S. Sajwan and A. Gaurav, 2008, "Temporal changes in rate of recession: Evidences from Satopanth and Bhagirath Kharak glaciers, Uttarakhand, using Total Station Survey," *Current Science*, vol. 94, no. 5, pp. 653-660.

80. Nghiem, S.V. , S.H. Yueh, R. Kwok and F.K. Li,1992, "Symmetry properties in polarimetric remote sensing," *Radio Science*, vol. 27, no. 5, pp. 693-711.

81. NPA, 2012, Damage situation and Police countermeasures associated with 2011Tohoku district - off the Pacific Ocean earthquake on September 10, 2012. National Police Agency (NPA) of Japan, (Accessed 2012-09-11).

82. Partington, K. C., 1998, "Discrimination of glacier facies using multi-temporal SAR data," *J. Glaciology*, vol. 44, no. 146**,** pp. 42-53.

83. Peake, W. H., and T. L. Oliver, 1971, *The response of terrestrial surfaces at microwave frequencies*, Technical Report AFAL-TR-70301, Electroscience Laboratory, Ohio State University, Columbus, Ohio.

84. Poelman, A.J., and J.R.F. Guy, 1985, "Polarization information utilization in primary radar"; in Boerner, W-M. *et al.* (eds), 1985, "Inverse Methods in Electromagnetic Imaging", *Proceedings of the NATO-Advanced Research Workshop*, (18-24 Sept. 1983, Bad Windsheim, FR Germany), Parts 1&2, NATO-ASI C-143, (1,500 pages), D. Reidel Publ. Co., Part 1, pp. 521-572.

85. Pottier, E., 1998, “Unsupervised classification scheme and topology derivation of POLSAR digital image data based on the (H/A/α) polarimetric decomposition theorems”, *Proc. JIPR-4,* U. Nantes/IRESTE, Bretagne, 98 July 13-17, pp. 535-548.

86. Racoviteanu, A. E. , F. Paul, B. Raup, S.J.S. Khalsa, R. Armstrong, 2009, “Challenges and recommendations in mapping of glacier parameters from space: results of the 2008 Global Land Ice Measurements from Space (GLIMS) workshop, Boulder, Colorado, USA,” *Annals of Glaciology,* vol. 50, no. 53, pp. 53-69.

87. Reigber, A. , M. Jäger, J. Fischer, R. Horn, R. Scheiber, P. Prats, and A. Nottensteiner, 2011, “System status and calibration of the F-SAR air-borne SAR instrument,” *Proc. IGARSS 2011*, Vancouver, BC, 2011 August, pp.1520 - 1523.

88. Rice, S. O., 1951, ‘‘Reflection of electromagnetic waves from slightly rough surfaces,’’ *Communications on Pure and Applied Mathematics,* vol. 4, pp. 361–378.

89. Rott, H., 1994, “Thematic studies in alpine areas by means of polarimetric SAR and optical imagery,” *Adv. Space Res.,* vol. 14, no. 3, pp. 217-226.

90. Rott, H., and T. Nagler, 1992, “Snow and glacier investigations by ERS-1 SAR: First results,” in *Proc. 1st ERS-1 symposium,* ESA SP-359., Nov. 4-6, 1992, ESA, pp. 577-582.

91. Rott, H., R. Davis, and J. Dozier, 1992, “Polarimetric and multi-frequency SAR signatures of wet snow”, in *Proc. IEEE IGRASS,* Houston, TX, May 26-29, 1992, vol. 2, pp.1658-1660.

92. Rott, H., S. Yueh, Cline D., C. Duguay, R. Essery, C. Haas, F. Hélière, M. Kern, G. Macelloni, E.Malnes, T. Nagler , J. Pulliainen, H. Rebhan, and A. Thompson, 2010, "Cold Regions Hydrology High-Resolution Observatory for snow and cold land processes," *Proc. IEEE,* vol. 98, no.5, pp. 752-765.

93. Sato, A., Yoshio Yamaguchi, G. Singh, and S.-E. Park, 2012, “Four-component scattering power decomposition with extended volume scattering model”, *IEEE Geosci. Remote Sens. Lett.,* vol. 9, no. 2, pp. 166 – 170.

94. Shi J., and J. Dozier, 1995, “Inferring snow wetness using C-band data from SIR-C’s polarimetric synthetic aperture radar,” *IEEE Trans. Geosci. Remote Sens.,* vol. 33, no. 4, pp. 905-914.

95. Shi, J., and J. Dozier, 1997, “Mapping of seasonal snow with SIR C/X-SAR in mountainous areas”, *Remote Sens. Environ.,* vol. 59, no. 2, pp.294-307.

96. Shi, J., and J. Dozier, 2000, “Estimation of snow water equivalence using SIR-C/X SAR Part I: inferring snow density and subsurface properties,” *IEEE Trans. Geosci. Remote Sens.,* vol.38, no. 6, pp. 2465–2474.

97. Shi, J., J. Dozier, and H. Rott, 1993, “Deriving snow liquid water using C-band polarimetric SAR,” in *Proc. IEEE IGRASS*, Tokyo, Japan, Aug. 18-21, 1993, pp. 1038-1041.

98. Shi, J., J. Dozier, and H. Rott, 1994, “Snow mapping in alpine regions with synthetic aperture radar,” *IEEE Trans. Geosci. Remote Sens.,* vol. 32, no.1, pp. 152–158.

99. Sinclair, G., 1950, "The transmission and reception of elliptically polarized wave," *Proc. IRE*, vol. 38, no. 2, pp. 148-151, 1950.

100. Singh, G., G. Venkataraman, V. Kumar, Y.S. Rao and Snehmani, 2008, "The H-A-Alpha decomposition theorem and Wishart distribution for snow cover monitoring in Himalayan region," *Proc. IEEE IGRASS'08*, vol.4, pp1081-1084.

101. Singh, G., 2010, *SAR polarimetry techniques for snow parameters estimation*. Ph.D. Thesis, Indian Institute of Technology Bombay, India.

102. Singh, G., and G. Venkataraman, 2008, "LOS PALSAR data analysis of snow cover area in Himalayan region using four-component scattering decomposition model,". *Proc. IEEE Micowave08*, Jaipur, India, pp. 772-774.

103. Singh, G., and G. Venkataraman, 2010, "Snow permittivity retrieval inversion algorithm for estimating snow wetness," *Geocarto International*, vol. 25, no. 3, pp. 187-212.

104. Singh, G., and G. Venkataraman, 2012, "Application of incoherent target decomposition theorems to classify snow cover over the Himalayan region," *Int. J. Remote Sens.*, vol. 33, no. 13, pp. 4161–4177.

105. Singh, G., G. Venkataraman, Y. Yamaguchi and S.-E. Park, 2013a, "Capability assessment of fully Polarimetric ALOS PALSAR data to discriminate wet snow from other targets", *IEEE Trans. Geosci. Remote Sens.* (in press).

106. Singh, G., Y. Yamaguchi and S.-E. Park and G. Venkataraman, 2010, Glaciated terrain classification using modified four-component scattering decomposition model, *IEICE Tech. Rep.*, vol. 110, no. 250, SANE2010-70, pp. 13-17.

107. Singh, G., Y. Yamaguchi and S.-E. Park, 2011, "Utilization of four-component scattering power decomposition method for glaciated terrain classification using fully polarimetric PALSAR data", *Geocarto International*, vol. 26, no. 5, pp., 377-389.

108. Singh, G., Y. Yamaguchi and S.-E. Park, 2012, "Evaluation of modified four-component scattering power decomposition method over highly rugged glaciated terrain, *Geocarto International*, vol. 27, no. 2, pp. 139-151.

109. Singh, G., Y. Yamaguchi and S.-E. Park, 2013b, "General four-component scattering power decomposition using unitary transformation," *IEEE Trans. Geosci. Remote Sens.*, (in Press).

110. Singh, G., Y. Yamaguchi, S.-E. Park, Y. Cui and H. Kobayashi, 2013c, "Hybrid Freeman/eigenvalue model with extended volume scattering model", *IEEE Geosci. Remote Sens. Lett*, vol. 10, no. 1, pp. 81-85.

111. Stiles, W.H., and F.T. Ulaby, 1980, "The active and passive microwave response to snow parameters – 1. Wetness," *J. Geophys. Res.*, vol. 85, no. C2, pp. 1037–1044.

112. Surendar, M., G. Singh, A. Bhattacharya, G. Venkataraman, P. A. Bharathi, 2013 "Snow wetness estimation based on POL-SAR decomposition technique", *submitted to IGRASS 2013*, Melbourne, Australia, July 21-26, 2013.

113. Touzi, R., 2007, "Target scattering decomposition in terms of roll-invariant target parameters," *IEEE Trans. Geosci. Remote Sens.*, vol. 45, no. 1, pp. 73–84.

114. Touzi, R., and F. Charbonneau, "Characterization of target symmetric scattering using polarimetric SARs," *IEEE Trans. Geosci. Remote Sens.*, vol. 40, pp. 2507– 2516, 2002.

115. Touzi, R., W. M. Boerner, J S Lee, E. Lueneburg, 2004, "A review of polarimetry in the context of synthetic aperture radar: concepts and information extraction", *Can. J. Remote Sens.,* vol. 30, no. 3, pp. 380-407.

116. Ulaby F.T., and W.H Stiles, 1981, "Microwave response of snow", *Adv. Space Res.,* vol.1, no. 10, pp. 131–149.

117. Ulaby, F.T. , R. K. Moore and A.K. Fung,1986, *Microwave remote sensing, active and passive, from theory to applications.* Vol. III, Addison-Wesley Publishing Company: Reading.

118. Ulaby, F.T., and W.H. Stiles, 1980, "The active and passive microwave response to snow parameters – 2. Water equivalent of dry snow," *J. Geophys. Res.,* vol. 85, no. C2, pp. 1045–1049.

119. vanZyl, J. J. , and Y. Kim, 2010, *Synthetic aperture radar polarimetry,* John wiley and sons, Inc., Hoboken, New Jersey.

120. vanZyl, J. J., M. Arii, and Y. Kim, 2008, "Requirements for model-based polarimetric decompositions," *Proc. IGARSS,* Boston, MA, Jul. 2008, pp. V-417–V-420.

121. vanZyl, J. J., 1989, "Unsupervised classification of scattering behavior using radar polarimetry data," *IEEE Trans. Geosci. Remote Sens.*, vol. 27, no. 1, pp. 36-45.

122. vanZyl, J.J., 1985, *On the importance of polarization in radar scattering problems,* Ph.D. thesis, California Institute of Technology, Pasadena, CA, December 1985.

123. Wishart, J., 1928. "The generalised product moment distribution in samples from a normal multivariate population". *Biometrika,* vol. 20A (1-2), pp. 32–52.

124. Xu, F., and Y. Q. Jin, 2005 "Deorientation theory of polarimetric scattering targets and application to terrain surface classification," *IEEE Trans. Geosci. Remote Sens.,* vol. 43, no. 10, pp. 2351-2364.

125. Yajima,Y., Y. Yamaguchi, R. Sato, H. Yamada, and W -M. Boerner, "POLSAR image analysis of wetlands using a modified four-component scattering power decomposition," IEEE Trans. Geosci. Remote Sens., vol. 46, no. 6, pp. 1667-1773, June 2008.

126. Yamaguchi, Y., 2007, *Radar polarimetry from basics to applications: radar remote sensing using polarimetric information* (in Japanese). Japan: IEICE. ISBN 978-4-88552-227-7.

127. Yamaguchi, Y., A. Sato, W.-M. Boerner, R. Sato, and H. Yamada, 2011, "Four-component scattering power decomposition with rotation of coherency matrix," IEEE Trans. Geosci. Remote Sens., vol. 49, no. 6, pp. 2251-2258.

128. Yamaguchi, Y., G. Singh, S.-E. Park and H. Yamada, 2012, "Scattering power decomposition using fully polarimetric information," in *Proc. IEEE IGRASS,* Munich, Germany, July 22-27, 2012, pp.91-94.

129. Yamaguchi, Y., T. Moriyama, M. Ishido, and H. Yamada, 2005, "Four-component scattering model for polarimetric SAR image decomposition," IEEE Trans. Geosci. Remote Sens., vol. 43, no. 8, pp. 1699-1706.

130. Yamaguchi, Y., Y. Yajima, and H. Yamada, 2006, "A four-component decomposition of POLSAR images based on the coherency matrix," *IEEE Geosci. Remote Sens. Lett.*, vol.3, no. 3, pp.292–296.

131. Yamazaki, F., and M. Matsuoka, 2007, "Remote sensing technologies in post-disaster Damage assessment," *Journal of Earthquake and Tsunami*, vol. 01, no. 03, pp. 1-17.

132. Yang, J., 1999, *On Theoretical Problems in Radar Polarimetry*, Ph.D. Thesis, Niigata University, Japan.

133. Yonezawa, C., and S. Takeuchi, 2001, "Decorelation of SAR data by urban damage caused by the 1995 Hoyogoken-Nanbu earthquek", *Int. J. Remote Sens.*, vol. 22, no. 8, pp. 1585-1600.

134. Zoughi, R., L.K. Wu and R.K. Moore, 1986, "Identification of major backscattering sources in trees and shrubs at 10GHz," *Remote Sens. Environ.*, vol. 19, no. 3, pp. 269-290.

List of Publications

1.1 Publications in International Journal (Refereed) by Gulab Singh

P1. Gulab Singh, Yoshio Yamaguchi and Sang-Eun Park, "Utilization of four-component scattering power decomposition method for glaciated terrain classification using fully polarimetric PALSAR data", *Geocarto International,* vol. 26, no. 5, pp. 377-389, 2011.

P2. Gulab Singh, Yoshio Yamaguchi and S.-E. Park, "Evaluation of modified four-component scattering power decomposition method over highly rugged glaciated terrain, *Geocarto International,* vol. 27, no. 2, pp. 139-151, 2012.

P3. A. Sato, Yoshio Yamaguchi, Gulab Singh, and Sang-Eun Park,"4-component scattering power decomposition with extended volume scattering model", *IEEE Geoscience and Remote Sensing Letters,* vol. 9, no. 2, pp. 166-170, Mar. 2012.

P4. Gulab Singh, Yoshio Yamaguchi, Sang-Eun Park, Yi Cui and H. Kobayashi "Hybrid Freeman/eigenvalue model with extended volume scattering model", *IEEE Geosci. Remote Sens. Lett*, vol. 10, no. 1, pp. 81-85, 2013.

P5. Gulab Singh, Yoshio Yamaguchi and Sang-Eun Park, "General four-component scattering power decomposition using unitary transformation," *IEEE Trans. Geosci. Remote Sens.*, vol. 51, no.4, pp., 2013. (*in press*)

P6. Gulab Singh, Yoshio Yamaguchi, Wolfgang-Martin Boerner and Sang-Eun Park, Monitoring of the 2011 March 11 Off-Tohoku 9.0 Earthquake with Super-Tsunami Disaster by Implementing fully polarimetric high resolution POLSAR Techniques, *Proc. IEEE*, vol. 101, no.3, pp. 831-846, 2013.

P7. Gulab Singh, G. Venkataraman, Yoshio Yamaguchi and Sang-Eun Park, "Capability assessment of fully polarimetric ALOS PALSAR data to discriminate wet snow from other targets", *IEEE Trans. Geosci. Remote Sens.*, DOI 10.1109/TGRS.2013.2248369, (in press at the time of submission).

P8. Gulab Singh, Yoshio Yamaguchi, Sang-Eun Park, Yi Cui, Wolfgang-Martin Boerner and G. Venkataraman, FULL-POL-SAR decomposition over wet snow, *IEEE Trans. Geosci. Remote Sens.* (To be submitted).

1.2 Publications in International Proceedings (Refereed) By Gulab Singh

1. Gulab Singh, Yoshio Yamaguchi and Sang-Eun Park, "4-component scattering power decomposition with phase rotation of coherency matrix", *Proc. IEEE IGRASS*-2011, Vancouver, Canada
2. Gulab Singh, Yoshio Yamaguchi, G.Venktaraman, and Sang-Eun Park, "Potential assessment of SAR in compact and full polarimetry mode for snow detection", *Proc. IEEE IGRASS*-2011, Vancouver, Canada
3. Gulab Singh, Yoshio Yamaguchi and Sang-Eun Park, "4-CSPD with unitary transformation of coherency matrix", *Proc. APSAR-2011,* Seoul, South Korea, 2011.

4. Gulab Sinngh, Priyanka, H. Kobayashi, Yoshio Yamaguchi and Sang-Eun Park, “Crop monitoring using ALOS-AVNIR-2 and ALOS-PALSAR”, presented in ICSANE-2011, Oct.16-19, 2011, Bali, Indonesia.

5. Gulab Singh, Yoshio Yamaguchi, Hirokazu Kobayashi, Sang-Eun Park “Advanced Hybrid eigenvalue/freeman model”, presented in ICSANE-2011, Oct.16-19, 2011, Bali, Indonesia.

6. H. Kobayashi , Gulab Singh Sang-Eun Park, Yoshio Yamaguchi, “Polarimetric RCS prediction code for wide area surface with vegetation”, presented in ICSANE-2011, Oct.16-19, 2011, Bali, Indonesia.

7. Gulab Singh, Hirokazu Kobayashi, Yoshio Yamaguchi, Sang-Eun Park and G. Venkataraman “ Snow facies mapping in the end of the ablation season using SAR data”, presented in ICSANE-2011, Oct.16-19, 2011, Bali, Indonesia.

8. Gulab Singh, Yoshio Yamaguchi and Sang-Eun Park, “Three-component scattering power decomposition with phase rotation of coherency matrix”, *Proc. ISAP-2011*, Oct. 25-29, 2011, Jeju, Korea, 2011.

9. Yoshio Yamaguchi, Gulab Singh, and Sang-Eun Park, “Scattering power decomposition using fully polarimetric information”, *presented in IGRASS 2012*, July 22-27, 2012, Munich, Germany.

10. Gulab Singh, Sang-Eun Park, Yoshio Yamaguchi, Wolfgang-Martin Boerner and G. Venkataraman, “FULL-POL-SAR decomposition over wet snow”, *presented in IGRASS 2012*, July 22-27, 2012, Munich, Germany.

11. Gulab Singh, Yoshio Yamaguchi, Yi Cui, Sang-Eun Park and Ryoichi Sato, “New four-component scattering power decomposition method”, *Proc. EUSAR-2012*, pp. 521-522, 2012.

Acknowledgement

I believe I am one of a few who can share the experience, or should I say privilege, of writing second doctoral thesis. I had the enriching experience of living in Japanese cultures. None of this would have been possible without one truly amazing person who is to be ‘blamed’ for opening the door into the world of Radar Polarimetry. This person is **Prof. Yoshio Yamaguchi**, my mentor, Faculty of Engineering, Niigata University, who will probably never forget my first ‘contribution’ in Radar Polarimetry when I proudly revealed “G4U, good for you!” **Yamaguchi Sensei**, thank you for recognizing and believing in my potential (despite that revelation) and for motivating me from the very beginning with all your shared knowledge, amazing enthusiasm and support. Most of all, thank you for taking care us as best guardian.

I am indeed grateful to **Prof. Wolfgang-Martin Boerner**, University of Illinois at Chicago, USA, for his excellent technical guidance, patience, assistance and tireless encouragement in my research work and for being strongest supporter.

I would also like to express my sincere thanks and appreciation to my first mentor of radar remote sensing and the advisor of “IITB-Ph.D. Thesis”, **Prof. Gopalan Venkataraman**, Centre of Studies in Resources Engineering (CSRE), Indian Institute of Technology Bombay (IITB), Mumbai, India, for his continuous support and help. I have greatly benefited from my technical discussions about polarimetric decomposition methods with **Dr. Shane R. Cloude**, AEL Consultant, Scotland, United Kingdom.

I express my thanks and appreciation for the constructive suggestions received from **Prof. Hiroyoshi Yamada**, Faculty of Engineering, Niigata University, **Prof. Keisuke Nakano,** Faculty of Engineering, Niigata University, **Prof. Kentaro Nishimori,** Faculty of Engineering, Niigata University, **Prof. Hirokazu Kobayashi,** Faculty of Engineering, Niigata University, and **Prof. Ryoichi Sato,** Faculty of Education and Human Sciences, Niigata University. I am thankful to **Dean**, Graduate School of Science and Technology, Niigata University for extending all the facilities and providing administrative support. I am also thankful to **Dr. Sang-Eun Park,** for hid kind support and help.

I am grateful to **JAXA** for providing ALOS-PALSAR data sets under JAXA-555 & 599 and also to Association of Japanese Geographers, and Geospatial Information, Authority of Japan for providing ground truth data. In addition, I express my sincere gratitude for being provided the excellent VHR X-Band TerraSAR-X and S-Band F-SAR fully polarimetric POLSAR image data sets by **DLR** Oberpfaffenhofen, Germany.

I take this opportunity to express my deep sense of love to my father, **Mr. Ram Pal Singh**, my sister **Mrs. Mamtesh Malik**, and my younger brother **Mr. Ankit** for their unceasing enragement, support, and love. Thank you all for your belief in me. **Mom**, we miss you a lot.

I would like to express adequately my feeling of gratitude and indebtedness form the bottom of my heart to my beloved wife, **Dr. Priyanka**, for her love and full cooperation, and her encouraging nature.

Last but not least, a million of thanks to almighty God (*Nature*), who made my task a success. I humbly offer my salutation at the feet of **Lord Shiva** and **Maa Parvati** who enable me to complete this endeavour successfully.